NARROW-BEAM MONOPULSE TECHNIQUE
FOR BATHYMETRY
AND SEAFLOOR ACOUSTIC BACKSCATTER IMAGERY
WITH A VOLUME SEARCH SONAR

BY

DANIEL STUART BROGAN

B.S. in Electrical Engineering, University of New Hampshire, 2001

A.E.T. in Electronic Engineering Technology, New Hampshire Technical Institute, 1999

THESIS

Submitted to the University of New Hampshire

In Partial Fulfillment of

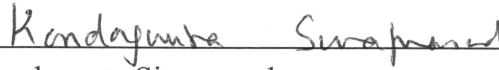The Requirements for the Degree of

Master of Science

In

Electrical Engineering

December, 2004

This thesis has been examined and approved.

Thesis Director, Christian P. de Moustier,
Professor of Electrical and Computer Engineering and
Ocean Engineering

Kondagunta Sivaprasad,
Professor of Electrical and Computer Engineering

Kent A. Chamberlin,
Professor of Electrical and Computer Engineering

17 September 2004

Date

ACKNOWLEDGEMENTS

TABLE OF CONTENTS

LIST OF TABLES

LIST OF FIGURES

x

ABSTRACT

NARROW-BEAM MONOPULSE TECHNIQUE
FOR BATHYMETRY AND SEAFLOOR ACOUSTIC BACKSCATTER IMAGERY
WITH A VOLUME SEARCH SONAR

by

Daniel Stuart Brogan

University of New Hampshire, December, 2004

The potential to obtain environmental information, specifically seafloor relief and texture, from a volume search sonar designed for mine countermeasure applications is demonstrated. This capability is explored using the volume search sonar of the AQS-20 mine countermeasure system, which transmits a stepped FM pulse over a 243° vertical fan beam centered on nadir and receives with twenty-seven pairs of beams symmetrically steered about nadir in the fore-aft direction and spaced at 7.16° intervals across-track. The receive beam pair geometry allows simultaneous views of the seafloor in forward, vertical, and rear profiles.

Pulse compression, monopulse processing techniques, and temporal and spatial filtering are used prior to the seafloor detection algorithm in order to improve the temporal and spatial resolution of the data. Three monopulse techniques are reviewed: conjugate-product, difference-over-sum, and narrow-beam. These techniques are used on both along-track and across-track pairs of adjacent beams. A seafloor detection algorithm using the data from narrow-beam monopulse processing applied to along-track beam pairs is derived in order to estimate the bathymetry and seafloor acoustic

backscatter imagery. The along-track beam pairs were chosen for this proof of concept because they provide results which are the simplest to represent spatially. Because of the unavailability of phase information in the monopulse results for along-track pairs (resulting from a common phase center for each pair of beams) the narrow-beam monopulse technique was chosen due to its superior magnitude response compared to the other two monopulse techniques reviewed. The detection algorithm employed detects targets within each narrow-beam beam separately while separating signal from noise using a constant threshold following the application of several normalization processes.

Results are presented for data collected in two test areas while surveying at roughly 25 knots, showing the combined effects of acoustic geometry and survey speed on the derived bathymetry and seafloor acoustic backscatter imagery and on bottom coverage over an across-track swath width of roughly 140°.

CHAPTER 1

INTRODUCTION

The United States Navy employs various sonar systems for use in mine countermeasure (MCM) operations. One example of the use of this type of system was for clearing the waterway into Umm Qasr during Operation Iraqi Freedom [HAB04]. In order to minimize the time required to measure the environmental parameters necessary for tactical decisions in operationally relevant areas for MCM operations, the Naval Research Laboratory, Stennis Space Center (NRL-SSC) is pursuing the development of Through-the-Sensors (TTS) technology. TTS technology extracts environmental data from sonars that are designed for other purposes, e.g. mine detection. This presents signal processing challenges due to the frequently suboptimal ability of these sonars to measure environmental characteristics [Bib04]. In addition to aiding in tactical decisions, obtaining these environmental characteristics from the MCM data eliminates the need for performing time consuming environmental surveys prior to opening an area to ship traffic. Since historical sources of data for these environmental characteristics are often outdated or non-existent for areas of interest for MCM operations, obtaining such information in near real-time can be critical for operational success [H+02], [HAB04].

This document focuses on the AQS-20 MCM system (Figure 1.1), "a variable depth, mine hunting sonar designed to detect, classify, and identify moored and bottom

mines" [HAB02]. This system can be towed through the water by a helicopter or a ship [Bib04]. The use of a helicopter-based system allows for safe operation in areas of unknown conditions in terms of both natural and man-made obstacles, e.g. mines. The AQS-20 system contains five sonars in addition to several other sensors [Ray99]. These sonar subsystems include a volume search sonar, two sidescan sonars in one subsystem, with a downward-looking sonar between them to fill in the gap, and a forward looking sonar in the nose of the AQS-20 towed body. Within the AQS-20 system, the multibeam volume search sonar (VSS), which is designed to detect mines in the water column [HAB04], is of particular interest because of its broad across-track coverage and the angular spatial resolution afforded by its multiple beams. These characteristics make it possible to obtain bathymetry and co-registered seafloor acoustic backscatter imagery.
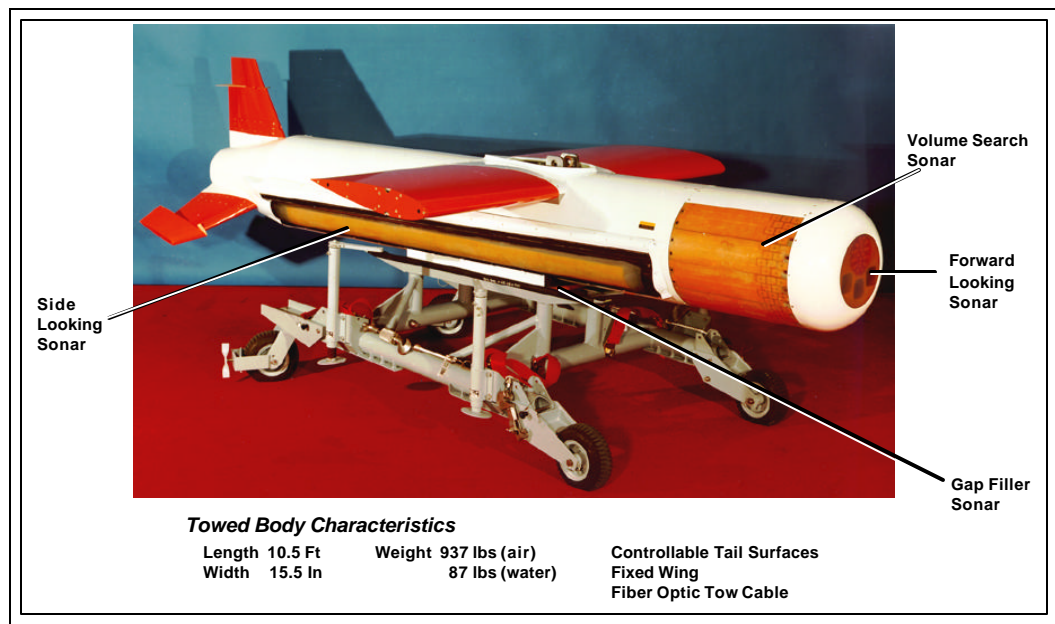
Figure 1.1. AQS-20 Towed Body.

1.1   <u>Research Objectives</u>

The bathymetric capability of the VSS has been demonstrated by Harris, et al. [H⁺01], [H⁺02] for near-nadir beams out to roughly 45° on either side of nadir (a 90° swath width). The research contained in this thesis seeks to expand on that work by addressing the following question:

- Is it possible to increase the swath width over which bathymetry and co-registered seafloor acoustic backscatter can be obtained with the VSS beyond 90°, and if so, by how much?

The approach followed is dictated by the nature of the basebanded broadband beamformed samples produced by the VSS, and by the beam geometry, which lends itself to monopulse processing for angle of arrival estimation. Given these constraints, the approach chosen to accomplish an increase in swath width uses pulse compression, monopulse techniques and a specialized seafloor detection algorithm. These techniques are meant to increase the signal-to-noise ratio (SNR) through the processing gain derived from the broadband time-bandwidth product of the pulse [CB67], and through an increase in directivity index and gain from the monopulse processing.

There are three monopulse techniques described in the literature [Rho59], [She84]: conjugate-product, difference-over-sum and narrow-beam. A goal is this research is to select which of these three techniques is best suited to the VSS beam geometry. Bathymetry estimation requires a time of arrival corresponding to each angle of arrival estimated by the monopulse technique chosen. To this end, another goal of this research is to determine what processing steps can be combined into a usable seafloor

detection algorithm designed specifically for obtaining bathymetry and seafloor acoustic backscatter from the VSS data.

The main contribution of this work is the extension of the swath width beyond 90° and the processing scheme used to obtain this increased swath width, which combines several preexisting techniques to achieve the specific objectives of this research.

The remainder of this chapter discusses the background information including a description of the VSS system, and prior art on the processing techniques to be used in this research. The VSS geometry and transmission pulse are reviewed in Chapters 2 & 3 in order to gain an understanding of the system operation and the constraints imposed by the format of the samples produced. The implementation of pulse compression and the choice of the monopulse technique chosen for the seafloor detection are discussed in Chapter 4. The seafloor detection algorithm used is derived in Chapter 5 through a trial and error method. Finally, Chapter 6 addresses conclusions and future work.

1.2 System Description

1.2.1 Array Geometry

Figure 1.2 shows the coordinate system used in this research. It is a conventional right handed spherical coordinate system [Wei99] rotated 90° around the y-axis. In this orientation the z-axis is nominally fore-aft (along-track), the y-axis is nominally across-track, and the x-axis is nominally pointed at nadir. The along-track angle, q, increases from 0° in the forward direction to 180° in the aft direction. Likewise, f, which is the

across-track angle, increases from -90° in the starboard direction through 0° at nadir to 90° in the port direction. Conventionally, the positive z-axis of the coordinate system is oriented upward. However, the variation of the coordinate system used here was chosen to simplify the calculations.
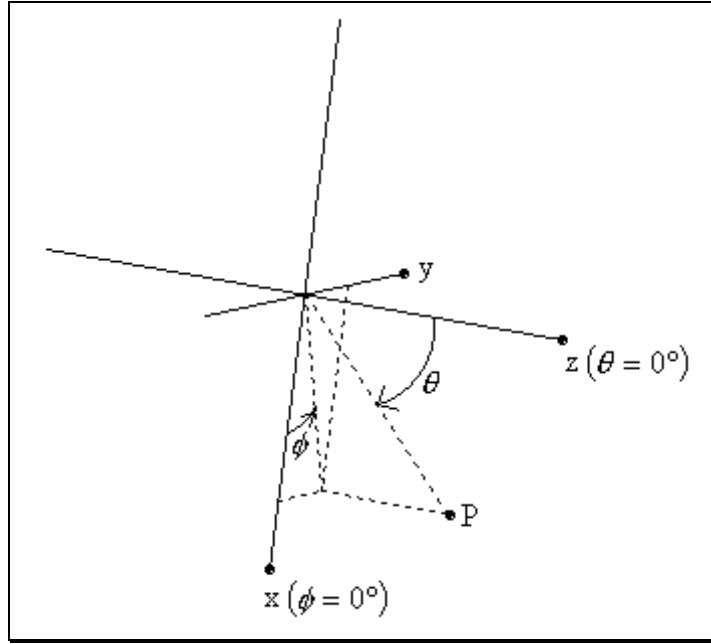
Figure 1.2. VSS Array Coordinate System Used in This Research.

Figure 1.3 shows the modeled VSS transducer array in its deployment orientation. The VSS array consists of forty staves uniformly spaced 7.16° apart on a cylinder 7.75 inches in radius. In this model, the array is centered at the origin with the z-axis as its central axis and staves symmetrically spaced in the xy-plane about the positive x-axis (ϕ = 0°). Each stave contains nine receive elements (tan) and either two or three transmit elements (teal). Adjacent staves are shifted along the cylinder's axis by one half of an element spacing in an alternating pattern. The physical array dimensions provided by the manufacturer, the Raytheon Systems Company, can be found in Table 1.1 [Ray99].
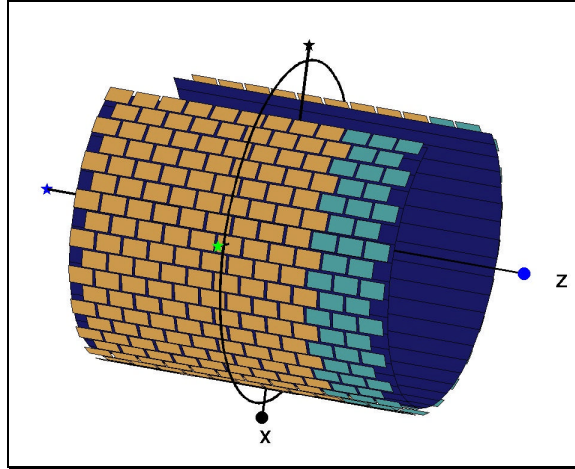
Figure 1.3. VSS Array Geometry as used in Simulation – Physical Orientation. (A circle represents a positive axis, and a star represents a negative axis.)

Stave Length	16.9 in ≡ 0.429 m
Cylinder Radius, R	7.75 in ≡ 0.197 m
Stave Angular Spacing, a	7.16° ≡ 0.125 rad
Element Spacing (Along-Track), h	1.4 in. ≡ 0.036 m
Receive Element Width (Across-Track)	0.89 in ≡ 0.023 m
Receive Element Height (Along-Track)	1.26 in ≡ 0.0320 m
Transmit Element Width (Across-Track)	0.84 in ≡ 0.021 m
Transmit Element Height (Along-Track)	1.27 in ≡ 0.0323 m

Table 1.1. VSS Array Dimensions.

1.2.2 Modes of Operation

There are two modes of operation of the VSS. The volume (VOL) mode, which covers an across-track swath below the VSS array, and the "SPD" mode, which covers as area 30° forward of nadir. The SPD mode is presumably used for obstacle avoidance and is not covered in this document.

The transmission beam of the VOL mode is created by firing all one hundred transmission elements simultaneously to cover a swath which is relatively narrow in the fore-aft direction and broad in the across-track direction (Section 2.2.2).

6

The fifty-four receive beams of the VOL mode form twenty-seven fore-aft beam pairs that cover overlapping areas of the swath illuminated by the transmission beam (Section 2.2.3). The orientations of the receive beams with respect to the towed body are shown in Figure 1.4.
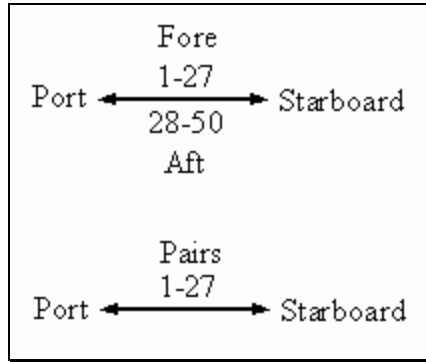
Figure 1.4. Receive Beam Orientation.

The receive elements on sixteen adjacent staves (shifting by one for each beam pair) are used for each of the twenty seven different beam pairs (except for the outer beams where only fourteen staves are used). Thus, the beam pairs are spaced every 7.16° across-track. Each pair of beams is produced by steering one beam slightly forward and one slightly aft. Amplitude weighting is applied to the elements that comprise each beam pair in both the fore-aft and along-track directions in order to reduce the sidelobes of the beam patterns. The receive element weights specified by the manufacturer are shown in Table 1.2 & Table 1.3. In the case where only fourteen staves are used the fourteen central weights are used.

0.082	0.102	0.164	0.289	0.453	0.665	0.841	1.00
↓←	←	←	←	←	←	←	↵
1.00	0.841	0.665	0.453	0.289	0.164	0.102	0.082

Table 1.2. Receive Stave Weighting Across-Track for One Beam Pair.

0.39	0.60	0.84	1.00	1.00	0.84	0.60	0.39	0.30

Table 1.3. Receive Element Weighting Along-Track (Aft to Fore) for One Stave.

There are two modes of receive beams within the VOL mode: short range (SR) and long range (LR). In VOL SR mode, only the central five receive elements in each stave and their associated weights are used. In this mode, receive beams are created 8° fore and aft of nadir. VOL LR mode uses all nine elements in each stave to produce receive beams 4° fore and aft of nadir. This combination of modes allows for larger coverage areas at small ranges while maintaining a reasonable coverage area for spatial discrimination at longer ranges. The combined coverage areas of the transmit beam and the receive beams determine the VSS sonar coverage of the water column, the sea surface and the seafloor.

1.2.3 Nominal Specifications

Table 1.4 contains the nominal beam widths of VOL mode beams given by the manufacturer. These are nominal values for a broadband transmission pulse whose center frequency is classified. When compared to simulated results, they provide an order-of-magnitude estimate of the operating frequency somewhere between 25 kHz and 50 kHz. A frequency of 37.5 kHz was chosen for the simulations presented here.

Receive Beamwidths	
Across-Track: VOL	9.5°
Along-Track: VOL SR	16.5°
Along-Track: VOL LR	8.25°
Transmit Beamwidths	
Across-Track: VOL	243°
Along-Track: VOL	29°

Table 1.4. Nominal Beamwidths for the Various Modes of VSS Operation in VOL Mode

The transmission pulse is a stepped FM approximation to an up-chirp with a duration of 4.32 ms (Chapter 3). The stepped FM pulse's theoretical spectrogram is shown in Figure 1.5. It consists of twelve frequencies equally spaced about the center

8

frequency in a 10.4 kHz bandwidth. Each of these frequencies occupies 0.36 ms of the transmission pulse. Processing internal to the towed body reduces the measured VSS data into digitized, quadrature demodulated, basebanded signals. After quadrature basebanding, the sampling frequency is $1/0.06\text{ms} \approx 16.67$ kHz. This is equivalent to taking six samples at each basebanded transmission frequency. The source level is stated to be 212 dB re 1 µPa @ 1 yd, which is 211 dB re 1 µPa @ 1 m.
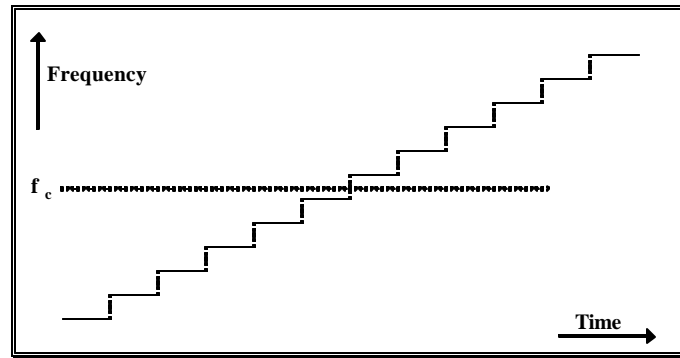
Figure 1.5. Theoretical Spectrogram of the Transmission Pulse.

1.3   Background Information

The remainder of this chapter discusses some of the previous work carried out on various aspects of the research contained in this document. Two general texts relating to multibeam sonars were written by de Moustier [Mou93] and Lurton [Lur02].

1.3.1   Beam Patterns for the VSS array

As preliminary steps to obtaining a better understanding of the VSS system operation, simulations of the beam patterns, their spherical and planar (seafloor) cross-sections and the transmission pulse were carried out in MATLAB and compared with sample data sets obtained with the AQS-20. The VSS consists of several rectangular elements arranged to form an array shaped like a large angular segment of a cylinder as

9

shown in Figure 1.1. The beam pattern of a rectangular element has the form of sinc function dependent on the major axis length multiplied by a sinc function dependent on the minor axis length, where the sinc functions are spatially orthogonal to each other. This type of transducer element is often referred to as a rigid piston in an infinite baffle in the literature.

A few authors ([Ber86], [Ols47] and [Tra66]) briefly mention the beam pattern of a rectangular transducer while Horton [Hor59] gives a few basic cross-sectional views for a square transducer. Hansen [Han83] provides the beam pattern of a rectangular transducer for a specific orientation using spherical coordinates, which was the coordinate system of choice for the present simulation. Swenson [Swe53] includes a short derivation of the beam pattern of a square transducer. More thorough derivations of the beam pattern of a rectangular transducer are given by Stenzel [Ste27] (in German, no English translation) and Freedman [Fre70]. Whereas, Stenzel follows the method of integrating a point source across the two-dimensional transducer surface, Freedman uses the method of breaking the rectangle into smaller geometrical sources, based on the position if interest in the far field. Although not discussed in Freedman's paper, this method relies on the underlying principles of point source integration that were used by Stenzel. The method used by Stenzel was followed in this research. However, no previous work was found for beam patterns of the specific element orientations applicable to the present research. The corresponding derivations are found in Appendix A. Note that in an earlier paper [Fre60], Freedman describes the near field of a rectangular piston source.

The beam pattern of an array of transducers may be determined by integrating over all transducer surfaces or by combining of the beam pattern of a single element with the array of element positions. The arrangement of the elements in this particular array is much like the staves of a barrel with a row of elements along each stave, and the elements on one stave are shifted along the stave by one half of an element length from those on the adjacent staves. The composite beam pattern simulation performed here combined the elements by summing their effects. This method takes advantage of the geometry of the element positions to reduce the calculations, but it is not a full reduction to the combination of the element beam pattern and positions as found in [RD82], [VT02], [Que70], [HHT85a], [HHT85b], [MPG71], [BB72], [Bor83] and [RPS77].

Davies [Dav83] provides a summary of circular arrays of point sources, and Lee and Lo [LL65] address an approximate solution for circular arc arrays of point sources that are not full circles. Carter [Car43] investigates the placement of dipoles around a cylinder (parallel to the central axis) in electromagnetics and provides several beam pattern plots. Rahim and Davies [RD82] discuss the effect of the element beam pattern on the overall response of a circular array. All of these authors deal with a single ring of elements.

Van Trees [VT02] discusses a cylindrical array of point sources where all elements on a ring lie in the same plane. Queen [Que70] compares the beam patterns of a cylindrical array of point sources and a cylindrical shell. In his array a ring of elements lies in the same plane. This type of element arrangement, and one in which adjacent staves are shifted by one half of an element spacing, are discussed in a two-part paper by Herper, Hessel and Tomasic [HHT85a], [HHT85b]. Their array consists of

electromagnetic dipole radiators placed around a cylindrical electromagnetic ground shell. Munger, Provencher and Gladman [MPG71] investigate a similar pair of arrays where the elements are rectangular waveguide openings in a cylinder. The case of circular apertures with element centers forming equilateral triangles is covered by Borgiotti and Balzano [BB72]. A more general treatment of a cylindrical array of apertures is treated in [Bor83]. Finally, Rolleigh, Pruitt and Stokes [RPS77] discuss an array where adjacent staves are axially shifted by one full element spacing. In their case, the element spacing is roughly one half of a wavelength, which is similar to the along-track element spacing of the VSS array. This stave shift severely reduces the axial end lobes that would otherwise be created when the elements are activated in phase simultaneously.

Although the transmission pulse used in the VSS was specified, Stokes and Koehler [SK79] give the minimum pulse length for effective operation with a cylindrical array.

A weighting function is applied to the VSS array elements both axially and radially (along staves and across staves). Two excellent fundamental papers on weighting functions are those by Harris [Har78] and Nuttall [Nut81]. Gallaudet and de Moustier [GM00] discuss how to apply standard weighting functions to elements on curved arrays.

VSS beam patterns are presented in Chapter 2.

1.3.2 <u>Stepped FM & chirp signals and Pulse Compression</u>

The VSS transmission pulse is a stepped FM approximation to a linear FM signal, i.e. a chirp. The technique of using a chirp signal to obtain a large time-bandwidth product was developed at Bell Telephone Laboratories in 1951. However, this information was not declassified for some time. It was first described publicly in a paper by Klauder, Price, Darlington and Albersheim [KPDA60]. Cook [Coo60], [Coo63] and Ramp and Wingrove [RW61] wrote three excellent articles on chirp signals and their applicability to pulse compression. Kochemasov [Koc83] has written the only text devoted entirely to linear FM signals. Unfortunately, the only version to be found is in Russian. *Radar Signals*, by Cook and Bernfeld [CB67] is a comprehensive reference on pulse compression and related signals. This book has been reprinted and is highly recommended for study in this area. Barton, Cook and Hamilton have edited a book [BCH91] that lists the advantages of using pulse compression waveforms. A short paper by Denisenko and Stetsenko [DS93] investigates the effect of non-linear distortions on linear FM signals.

Early stepped FM signals were produced by transmitting a sequence of time separated CW signals at different frequencies [Rih64], [RC68]. Concurrently, frequency shifting pulse trains without time separation began to appear in the literature as well. One early source for this was the text by Cook and Bernfeld mentioned above. This topic also appears later in a text by Wehner [Weh95].

Toomay [Too82] states that it is important for the system clock to be stable in order to maintain the phase coherence for LFM signals. While phase coherence was not the case for the VSS system, phase walking appears to have been negligible with respect

to the pulse length. One other significant concern for LFM signals is Doppler shift. Kinsler, et. al. [K$^+$00] provides a clear introduction to this topic.

The analysis of the VSS transmission pulse is discussed in Chapter 3.

1.3.3   Monopulse

Accurate measurement of seafloor characteristics is dependent on obtaining accurate time and angle of arrival estimates of the seafloor echoes. The comparison of arrivals received by adjacent beams is often referred to as a monopulse processing technique [Rho59]. Monopulse is a term that has its origin in radar. It refers to a system in which adjacent beams are compared to produce results over a large area from a single transmission pulse as opposed to previous technology that used beam scanning to cover an area. Monopulse techniques allow for a finer angular resolution than is available using the individual beams of the VSS system.

There are three major monopulse texts that have been used for the VSS research presented here. *Introduction to Monopulse* by Rhodes [Rho59] is probably the earliest text to try to summarize the topic. The second is *Volume 1 – Monopulse Radar* by Barton [Bar74], which is a collection of major papers on the topic. The last is *Monopulse Principles and Techniques* by Sherman [She84].

Rhodes breaks all monopulse techniques into two categories, phase comparison and magnitude comparison, using a strict set of classification rules. All other forms of beam comparison are termed 'pseudo monopulse' by Rhodes. Sherman later rejects Rhodes' classification as being too restrictive. However, it is beneficial to briefly discuss the two main categories. For convenience's sake, the adjacent beams to be compared are

labeled *A* and *B* respectively. Recall that each of these measured beams is still in its quadrature-sampled (complex) format, $|A|\exp(jf_A)$ and $|B|\exp(jf_B)$. The first category concerns two beams that are created from the same array but steered in different directions (Figure 1.6 (a)). These beams have the same phase shift to any point in the farfield (common phase center), but they have different magnitude responses in that direction. These beams are suitable for magnitude comparison because $f_A = f_B$. This is the relation of the beams in the along-track beam pairs (Figure 1.7 (a)). In the second case, two beams are created by equivalent but distinct arrays (Figure 1.6 (b)). In this case, the beams are spatially identical in magnitude (farfield approximation), but their phase center offset results in a phase shift between their beam patterns at a point in the farfield region. These beams are suitable for phase comparison because $|A|=|B|$. Sherman takes the view that a particular monopulse technique with a different beam geometry might fall partially into both categories. The across-track beam pairs are one such hybrid case (Figure 1.7 (b)) shown in Figure 1.6 (c). In this case, neither reduction applies, which implies that monopulse techniques based on magnitude and/or phase characteristics can be applied to these beams.
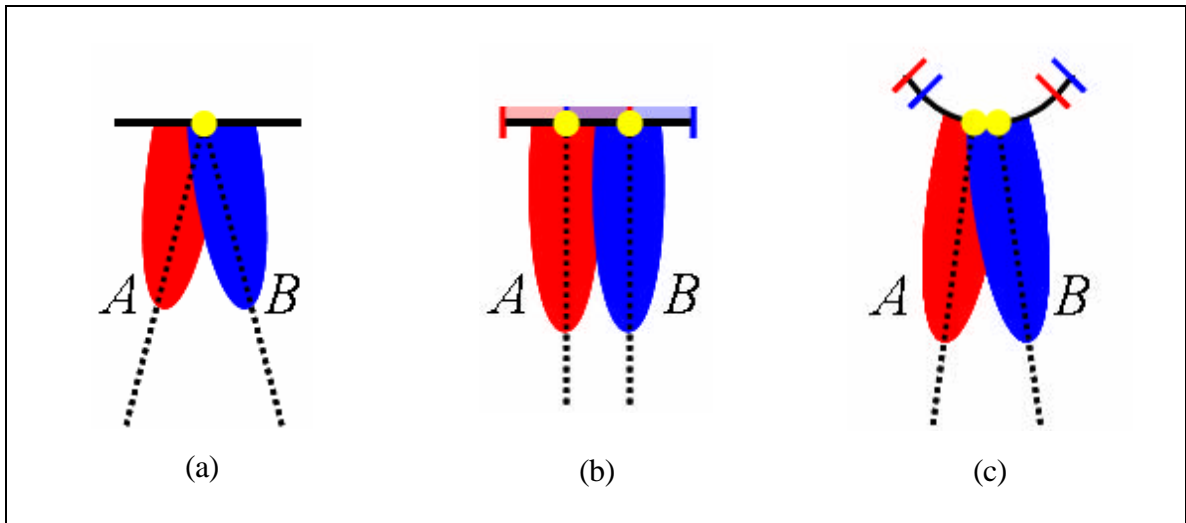
Figure 1.6. Monopulse Categories: (a) Magnitude Comparison – Common Phase Centers and Different Farfield Magnitude, (b) Phase Comparison – Phase Center Offset and Uniform Farfield Magnitude, (c) Hybrid Configuration - Phase Center Offset and Different Farfield Magnitude.
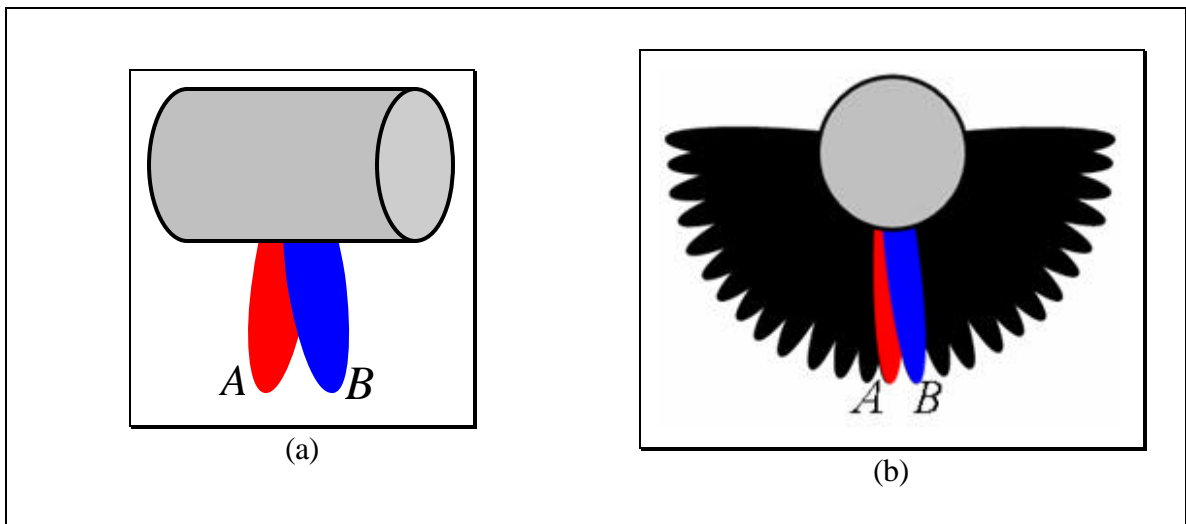
Figure 1.7 (a) VSS Side View – An Along-Track Pair, (b) VSS End View – Across-Track Pairs.

Before computer processing was available, the simplest way to combine adjacent radar beams was to add or subtract them, since they were radio signals in waveguides. As such, these monopulse texts focus, almost exclusively, on the ratio of the difference divided by the sum. This ratio has become so synonymous with monopulse that Sherman devotes a significant portion of his book to describing methods of approximating it.

Rhodes' text, being the earliest in the development process, does briefly mention a few other techniques which were used in the present research as well. One of these (the conjugate-product (CP) technique) produces a linear differential phase slope when there is a phase center offset as shown in Figure 1.8. This differential phase will be negative when the target is closer to the phase center of beam A than to the phase center of beam B (case (a)). The differential phase is zero when the target is equidistant from the phase centers (case (b)). Finally, when the target is closer to the phase center of beam B than to the phase center of beam A (case (c)), the differential phase will be positive. Henderson and Lacker [Hen87], [HL89] deal specifically with application of monopulse techniques to wideband sonar systems. The monopulse techniques used for VSS applications are covered in detail in Chapter 4
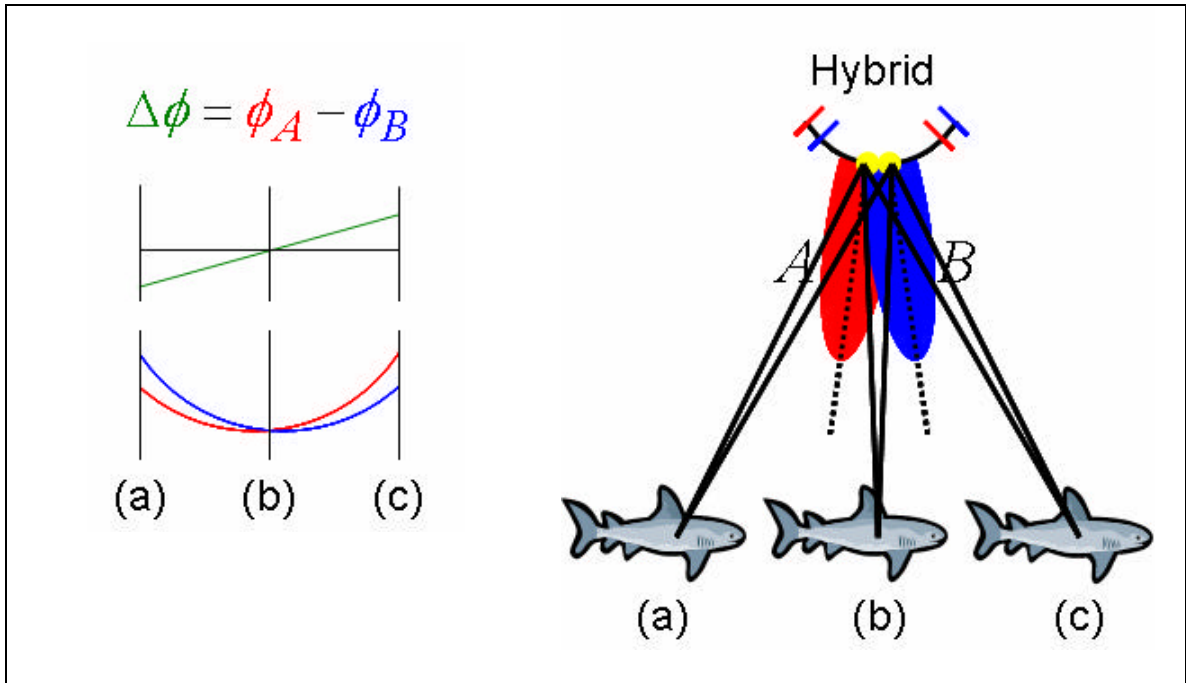
Figure 1.8. Differential Phase of the Conjugate-Product Monopulse Technique for the Hybrid Configuration of Across-Track Beam Pairs.

1.3.4 <u>Seafloor Characteristics</u>

Although there are several approaches to seafloor detection, they are categorized into the following three groups by de Moustier [Mou93]: estimation of a time of a arrival of a seafloor echo for data from a single angle of arrival using the echo magnitudes, estimation of angles of a arrival of seafloor echoes for data from a single time of arrival using the echo magnitudes, and a combined time and angle of arrival approach using a phase slope zero crossing detection process on data generated using the CP monopulse technique. Morgera [Mor76], Morgera and Sankar [MS84] and de Moustier and Alexandrou [MA91] each describe a different method of estimating a representative seafloor echo time of arrival from the returns in one direction. The phase slope classification had been briefly mentioned by de Moustier [Mou88]. Yang, Taxt and Albregtsen [YT97], [YTA97] discuss the combined use of the magnitude and phase for a CP detection technique called the *bottom image transform*.

De Moustier and Alexandrou [MA91] describe the angular dependence of a seafloor backscatter estimate for the data selected as the seafloor echo by their detection algorithm. Harris, Avera and Bibee [H^{+}02] discuss obtaining a seafloor acoustic backscatter estimate for the near-nadir beams of the VSS of the AQS-20 system. Several other VSS specific papers are referenced in Section 1.1.

The first of the three seafloor detection classifications is followed in this research. The application of monopulse techniques and the subsequent seafloor estimation for bathymetry and seafloor acoustic backscatter imagery covered in Chapter 5 are the portions of this research which contain the primary contribution to the field.

1.3.5 <u>Ray Tracing</u>

The last area of previous work to be covered here is that of ray tracing. In the final stage of processing before bathymetry and backscatter estimates were derived, the (time, angle) pairs of selected targets were corrected using a ray tracing method for simple horizontally layered media. Texts by Medwin and Clay [MC98] and Officer [Off58] were used in addition to course notes for the *34th UNB OMG / UNH CCOM Multibeam Sonar Training Course* [Mou04] to perform these calculations. Corrections for the towed body orientation [Mou93] are a necessary component of ray tracing calculations. The towed body orientation and ray tracing corrections are contained in Chapter 5.

CHAPTER 2

BEAM PATTERNS AND CROSS-SECTIONS

2.1 <u>Introduction</u>

As a first step in assessing the bathymetry and acoustical backscatter surveying capabilities of the VSS in VOL mode, a detailed beam pattern and cross-section analysis has been carried out with MATLAB software tools. The beam pattern is defined in three dimensions by the normalized free-space farfield intensity at a constant radial distance from the array's center, in which the magnitude of the intensity is used as a radial distance (Section 2.2). This magnitude can also be displayed as a spherical cross-section (Section 2.3.1) or as a planar cross-section representing the intersection of the beam with the sea floor (Section 2.3.2 & 2.3.3). The goals of this study were to provide visualization tools to describe the main lobe and sidelobe structures of the beams from the various VOL modes of operation used in the VSS. A nominal frequency of 37.5 kHz was chosen for this study, yielding realistic – though not exact – estimates of the spatial characteristics of the VSS operation. The speed of sound in water was arbitrarily chosen to be 1500 m/s for beam pattern simulations.

2.2 Beam Patterns in Free Space

2.2.1 Element Beam Pattern

In order to determine the beam pattern of an array, the beam pattern of an individual transducer element must be known. Each transducer element of the array was modeled as a piston radiator in an infinite planar baffle. This forces any signals more than 90° from the element normal to zero. However, since this array is not a large planar array, some minor edge effects appear in the simulation results that would not exist in the actual system response. For the array orientation described in the previous chapter, the derivation of the element's beam pressure pattern is derived in Appendix A to be

$$P(q,f) = G \cdot a \cdot b \cdot \text{sinc}((b/l)\cos(q)) \cdot \text{sinc}((a/l)\sin(q)\sin(f-f_N)) \cdot \exp\left(j\vec{k} \bullet \vec{r}_P\right) \qquad (2.1)$$

where G is a scalar gain, b and a are the length and width of the rectangular transducer respectively, l is the acoustic wavelength, f_N is the across-track component of the element normal, $\exp\left(j\vec{k} \bullet \vec{r}_P\right)$ is a phase component based on the location of the element center with respect to some arbitrary origin where $\vec{k}$ is the wavenumber vector and $\vec{r}_P$ is the vector from the origin to the element center, and

$$B(q,f) = 20 \log_{10}(abs(P(q,f))) \qquad (2.2)$$

is the beam pattern. Figure 2.1 and Figure 2.2 show the normalized (to a maximum of 0dB throughout this chapter) beam pattern and primary cross-sections of a transmission element located in the yz-plane, with its center at the origin and the z-axis as its major axis, for a transmission frequency of 37.5 kHz. At this frequency, the transmission element dimensions are roughly 0.81λ by 0.52λ. The receive element, with dimensions

of 0.80λ by 0.58λ, will have a nearly identical beam pattern. Note that, the back lobe has

been removed in order to match the piston radiator model.
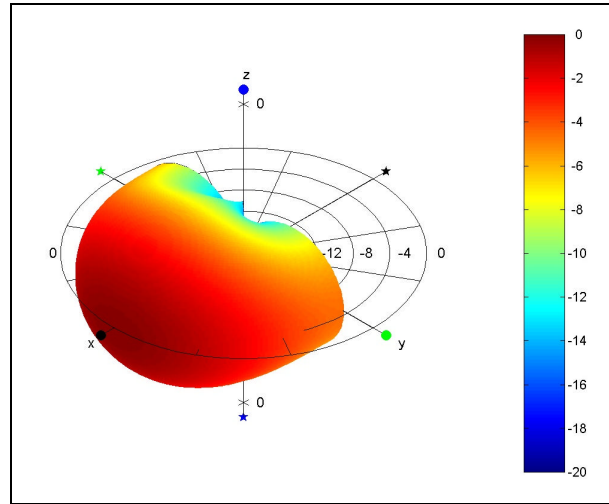
Figure 2.1. Normalized Transmission Element Beam Pattern on a Linear Scale – 37.5 kHz.
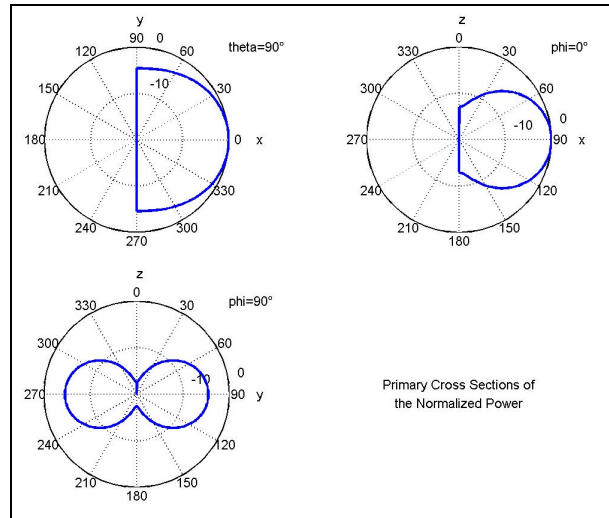
Figure 2.2. Normalized Transmission Element Beam Pattern Cross-Sections on a Linear Scale – 37.5 kHz.

2.2.2   <u>Transmission Beam Pattern</u>

The transmission beam pattern is calculated by combining the effects of the

transmission elements. For the transmission beam, the transmission elements in the forty

staves are synchronous in operation and uniformly weighted. The derivation in Appendix A yields a transmission pressure field of

$$
\begin{aligned}
P_T(\boldsymbol{q},\boldsymbol{f}) \;=\; & G\cdot a \cdot b \cdot \mathrm{sinc}\big((b/\boldsymbol{l})\cos(\boldsymbol{q})\big) \\[4pt]
& \times \sum_{q=-\frac{Q-1}{2}}^{\frac{Q-1}{2}}
\left[
\begin{array}{c}
\mathrm{sinc}\big((a/\boldsymbol{l})\sin(\boldsymbol{q})\sin(\boldsymbol{f}-q\boldsymbol{a})\big)\cdot \dfrac{\mathrm{Re}\left(\sqrt{\boldsymbol{p}/2-|\boldsymbol{f}-q\boldsymbol{a}|}\right)}{\sqrt{\boldsymbol{p}/2-|\boldsymbol{f}-q\boldsymbol{a}|}} \\[10pt]
\cdot \exp\big(jkR\sin(\boldsymbol{q})[\cos(\boldsymbol{f})\cos(q\boldsymbol{a})+\sin(\boldsymbol{f})\sin(q\boldsymbol{a})]\big) \\[8pt]
\cdot\{[1+2\cos(kh\cos(\boldsymbol{q}))]\cdot\mathrm{mod}(q+0.5,2)+[2\cos(0.5kh\cos(\boldsymbol{q}))]\cdot\mathrm{mod}(q-0.5,2)\}
\end{array}
\right]
\end{aligned}
\tag{2.3}
$$

where Q is 40 (number of staves), q is a counter for the stave separation from the across-track angular center of the array (nadir in this case) in units of the angular stave separation a (7.16°, Table 1.1), R (7.75 in) is the radius of the array cylinder, h (1.4 in) is the along-track separation between element centers on a stave and

$$
B_T(\boldsymbol{q},\boldsymbol{f}) = 20\log_{10}\big(abs(P_T(\boldsymbol{q},\boldsymbol{f}))\big)
\tag{2.4}
$$

is the beam pattern normalized to a maximum of 0 dB.

These results are shown in Figure 2.3 through Figure 2.5. The small variations seen in the across-track slice of Figure 2.4 are the result of the piston radiator model edge effects. Any other across-track scalloping is a frequency dependent effect, which is shown in detail in Section 2.4. This simulation shows an across-track beamwidth of roughly 243°, as expected. However, the amplitude of the upper portion (roughly 120° to 240°) of the across-track slice is only 7 to 15 dB below the maximum response. This may be the result of the inaccurate modeling of edge effects. Otherwise, it results in unwanted surface reflections in the VSS measurements. Figure 2.3 and Figure 2.5 show that there are also some unwanted along-track sidelobes at this frequency. These result from the along-track element spacing which is roughly 0.89λ at this frequency. The

23

benefit of the one half element-spacing shift between adjacent staves is shown in the fact that with a stave-to-stave shift of roughly 0.44λ, much of the energy along the z-axis is removed by destructive interference as was discussed in Section 1.2.
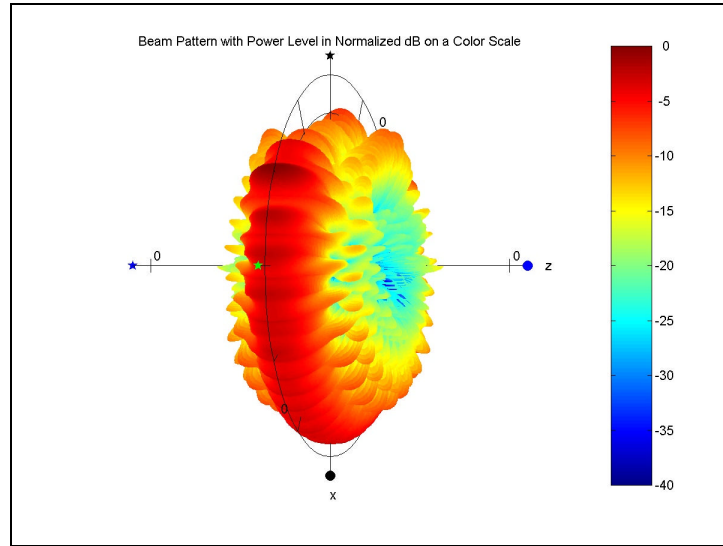
Figure 2.3. Normalized Transmit Beam Pattern , VOL Mode – 37.5 kHz.
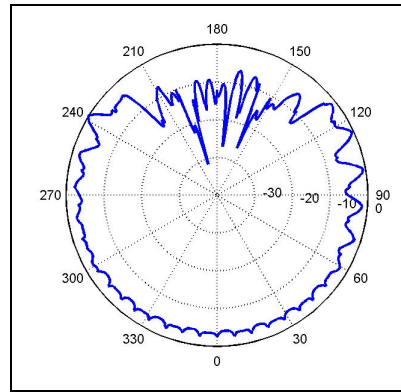
Figure 2.4. Normalized Transmit Beam Pattern Across-Track Slice ($q = 90°$), VOL Mode (Nadir At $\left(q = 90°, f = 0°\right)$) Cylinder Axis Out of Page – 37.5kHz.
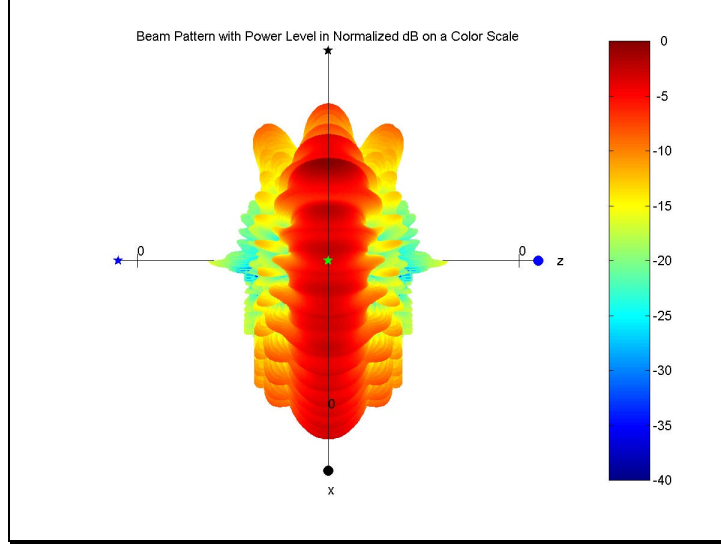
Figure 2.5. Normalized Transmit Beam Pattern – Side View, VOL Mode – 37.5 kHz.

2.2.3 Receive Beam Patterns

The configurations of the receive beams for both VOL modes including the selection and relative importance of individual receive elements for each beam were described in Section 0. The details of the derivations of these beam patterns are found in Appendix A. The resulting pressure fields for the all receiving modes are defined by

$$
\begin{aligned}
P_{R\_i}(\boldsymbol{q},\boldsymbol{f}) \;=\;& G \cdot a \cdot b \cdot \mathrm{sinc}((b/\boldsymbol{l})\cos(\boldsymbol{q})) \\
&\cdot \sum_{p=-(P-1)/2}^{(P-1)/2} \Big[W_h(p + P_{SHIFT}) \cdot \exp\big(jk \cdot (p+0.25) \cdot h[\cos(\boldsymbol{q}) \mp \sin(\boldsymbol{q}_S)]\big)\Big] \\
&\cdot \sum_{q=i-\frac{Q-1}{2}-\bar{i}\_cent}^{i+\frac{Q-1}{2}-\bar{i}\_cent}
\begin{bmatrix}
W_{\boldsymbol{a}}(q + Q_{SHIFT} - i) \cdot \mathrm{sinc}((a/\boldsymbol{l})\sin(\boldsymbol{q})\sin(\boldsymbol{f}-q\boldsymbol{a})) \\[6pt]
\cdot \dfrac{\mathrm{Re}\big(\sqrt{\boldsymbol{p}/2 - |\boldsymbol{f}-q\boldsymbol{a}|}\big)}{\sqrt{\boldsymbol{p}/2 - |\boldsymbol{f}-q\boldsymbol{a}|}} \\[10pt]
\cdot \exp\big(jk(R\cos(q\boldsymbol{a})[\sin(\boldsymbol{q})\cos(\boldsymbol{f})] + \sin(q\boldsymbol{a})[\sin(\boldsymbol{q})\sin(\boldsymbol{f})])\big) \\[6pt]
\cdot \exp\big(-j0.5k \cdot h[\cos(\boldsymbol{q}) \mp \sin(\boldsymbol{q}_S)] \cdot \mathrm{mod}(q+0.5,2)\big)
\end{bmatrix}
\end{aligned}
\tag{2.5}
$$

where the normalized beam pattern is again defined to be twenty times the base ten logarithm of the absolute value of the normalized (to a maximum of one) pressure field.

25

The counter i increments the across-track beam pair numbers and the counters p and q increment (along-track and across-track respectively) through the elements used to create each beam pair. The spatial weighting coefficients from Table 1.2 and Table 1.3 are contained in the vectors $W_a(q)$ and $W_h(p)$ respectively. Additionally, q_s is 8° for SR mode and 4° for LR mode, i_cent is 14, Q is 16 for beam pairs 2 through 26 and 14 for beam pairs 1 and 27 (number of staves used), Q_{SHIFT} is 22.5 $((length(W_a)+1)/2+i\_cent)$, P is 5 for SR mode and 9 for LR mode, and P_{SHIFT} is 5 $((length(W_h)+1)/2)$.

Figure 2.6 (a) and Figure 2.7 (a) show beams 14 and 41, respectively, for the VOL LR mode. These beams are the forward and rear beams, respectively, of central beam pair 14 (centered on nadir). Figure 2.8 (a) shows the along-track vertical slice through both beam maximum response axes. Note that the beams overlap near their half-power widths in the fore-aft plane, with sidelobes more than 25 dB below the main lobes. Figure 2.9 shows the beam pattern viewed from the front of the array. This shows that there are across-track sidelobes close to 20 dB below the main lobes. Of key importance will be the effect that the transmission pattern has on the receive beam sidelobes when the effects of transmit and receive beams are combined (Section 2.2.4).
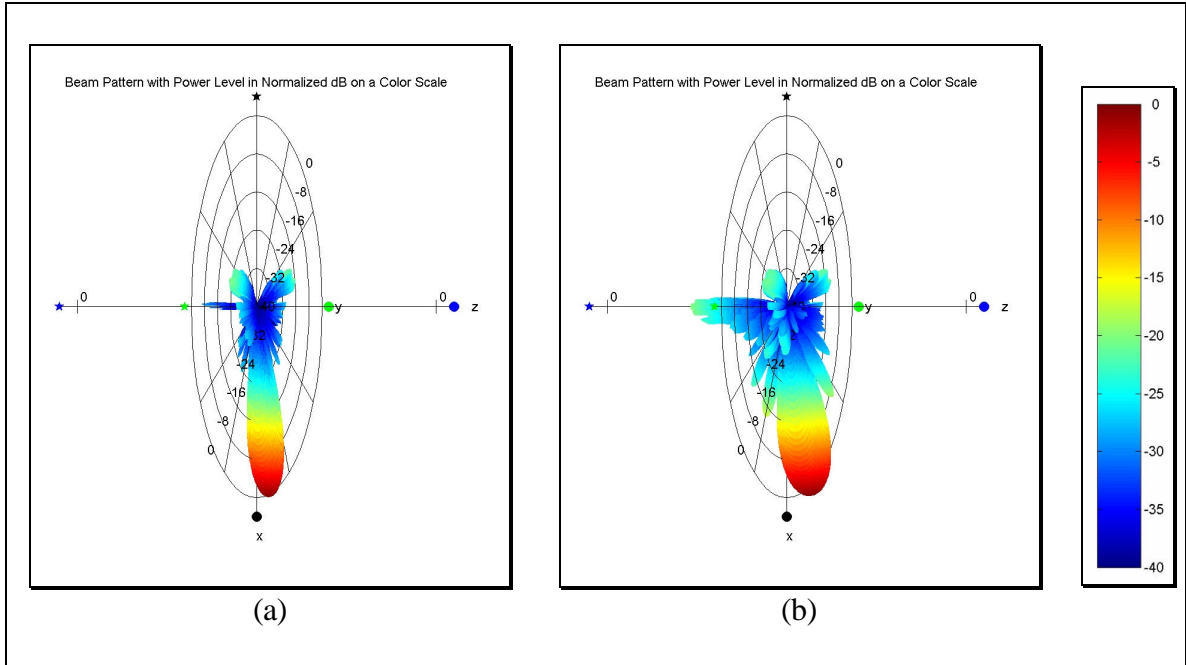
Figure 2.6. Normalized Receive Beam Pattern – Forward Beam 14, 37.5 kHz: (a) VOL LR (Steered 4° Forward of Nadir), (b) VOL SR (Steered 8° Forward of Nadir).
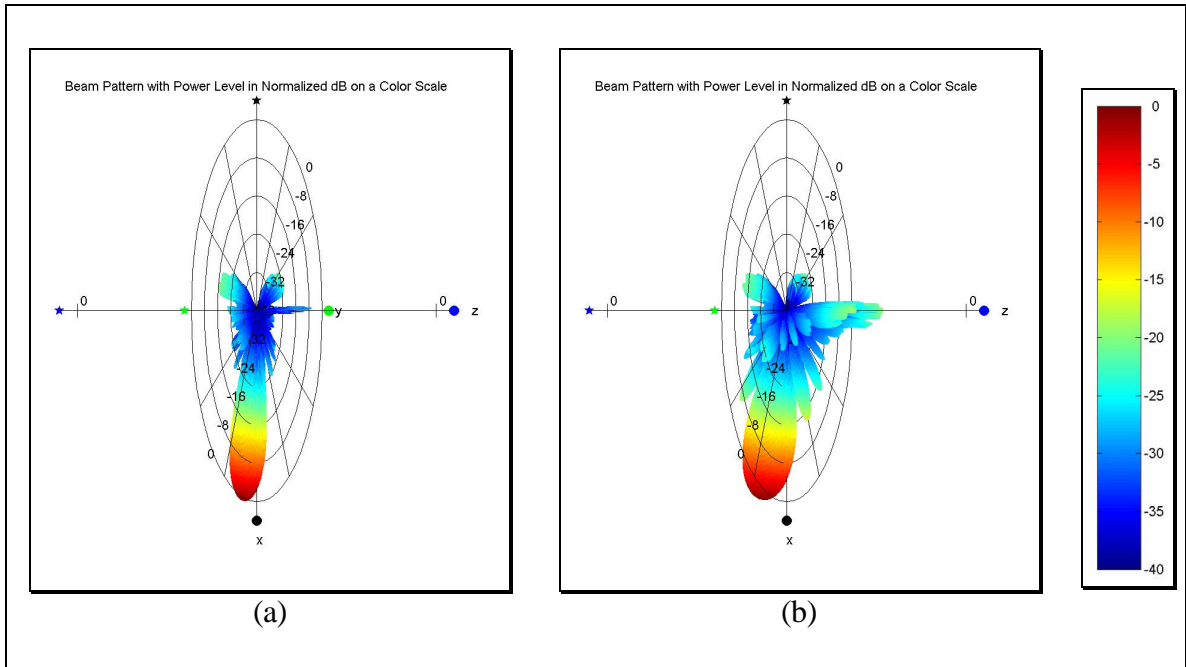
Figure 2.7. Normalized Receive Beam Pattern – Aft Beam 41, 37.5 kHz: (a) VOL LR (Steered 4° Forward of Nadir), (b) VOL SR (Steered 8° Forward of Nadir).
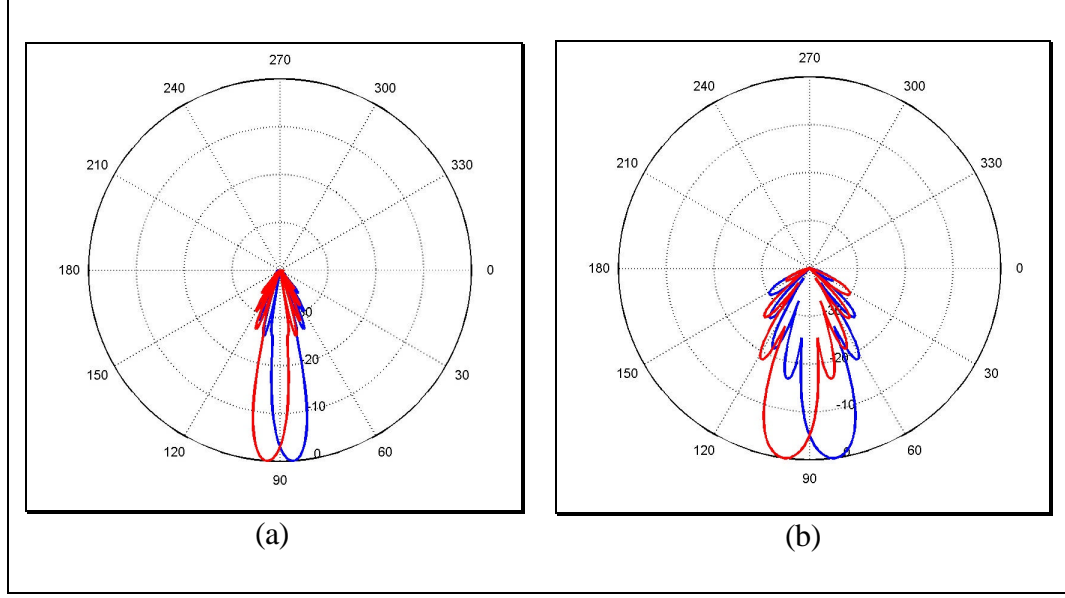
Figure 2.8. Lower Half of the Along-Track Slice ($f = 0°$) of the Normalized Receive Beam Pattern – Beam Pair 14 (Nadir At $(q = 90°, f = 0°)$) Cylinder Along 180° to 0° Axis – 37.5 kHz: (a) VOL LR, (b) VOL SR.
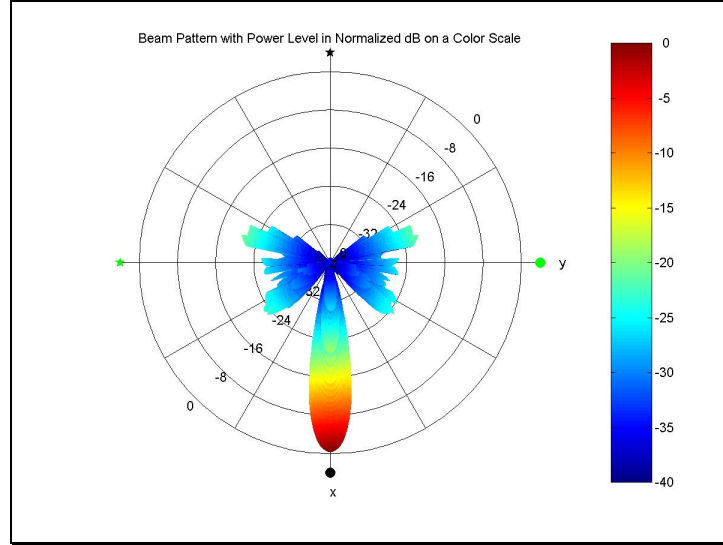
Figure 2.9. Normalized Receive Beam Pattern – Front View (Identical for both Receive Modes) for Beams 14 & 41 (Nadir At 0°) Cylinder Axis Out of Page – 37.5 kHz.

Figure 2.6 (b), Figure 2.7 (b) and Figure 2.8 (b) show the beam patterns of the forward and rear beams of beam pair 14 and their vertical along-track slice for VOL SR mode. Compared to the VOL LR beam patterns from part (a) of these three figures, the across-track sidelobes of the VOL SR beams are virtually unchanged in the along-track

dimension despite the shorter aperture of the VOL SR mode. However, the sidelobes in the along-track slice extend up to roughly 17 dB below the main lobes due to the shorter effective array aperture. What neither the along-track slices nor the front view show clearly are the pair of sidelobes that are nearly orthogonal to each main lobe but lying at angles between the cross-sectional and front views. These sidelobes are at roughly -30 dB for the VOL LR mode, but they are at roughly -19 dB for the VOL SR mode as is shown in Figure 2.6 and Figure 2.7. Simulation of the forward looking 'SPD' mode showed significant grating lobes of which the last sidelobes mentioned for the VOL mode may be the first indication. These sidelobes will also need to be monitored when the effects of transmit and receive beams are combined.

Figure 2.10 shows all fifty-four beams for VOL LR and VOL SR modes. The end lobes sticking out of the sides of these beam patterns along the fore-aft axis are the combined results of the off-axis sidelobes from all of the beams (forward end lobe from rear beams and rear end lobe from forward beams). Note that this is a much bigger issue for the SR mode than for the LR mode as mentioned previously. The other sidelobes occur between the main lobes and these end lobes. How effectively these end lobes are reduced by the transmission beam pattern will be seen in the next section.
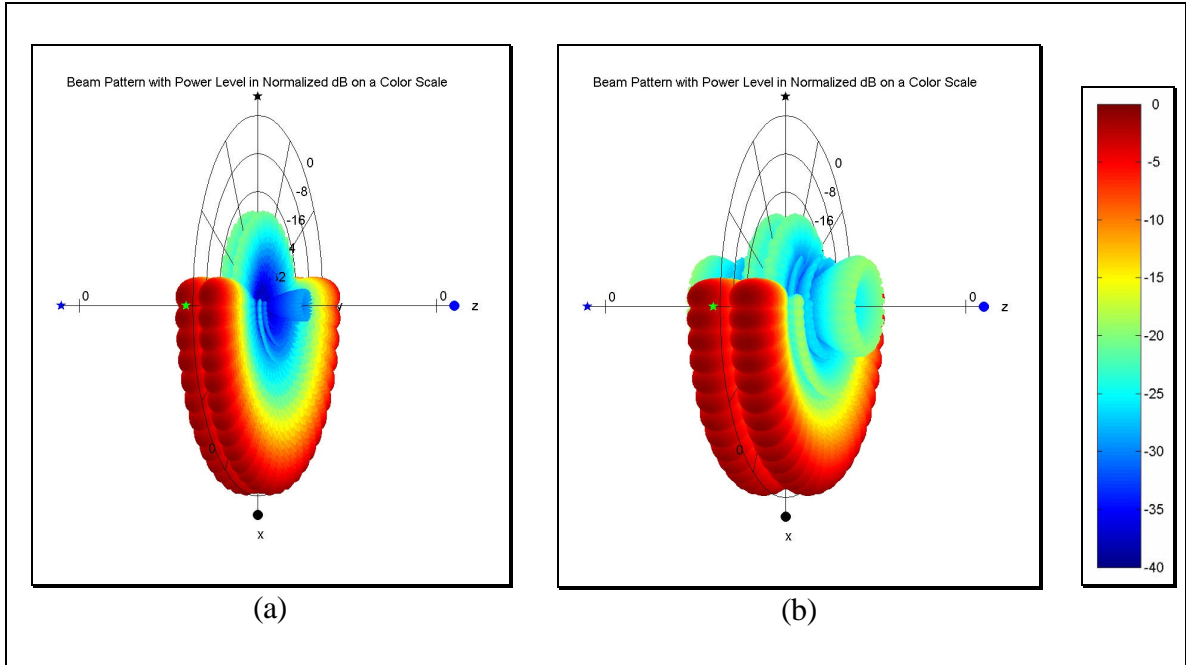
Figure 2.10. Normalized Receive Beam Pattern for all Beams – 37.5 kHz: (a) VOL LR, (b) VOL SR.

2.2.4   <u>Transmit and Receive Product Beam Patterns</u>

The combined transmit and receive beam patterns shown in Figure 2.11 through Figure 2.15 contain the full spatial sensitivity of the VSS array in VOL mode. They are created by adding the beam patterns (dB scale) of the transmit and receive beams. This is equivalent to multiplying the transmission pressure field by the receive pressure field.

With the exception of a few dB of scalloping, the main lobes of these beams look quite similar to those of the receive beams by themselves. However, the along-track and off-axis sidelobes are reduced below -40 dB in magnitude due to the weaker transmission beam in these directions. This is most clearly visible in Figure 2.15 where the end lobes have been reduced below the -40 dB threshold of the figures. There is still a relatively strong (-18 dB) along-track sidelobe remaining for each of the VOL SR beams shown in Figure 2.13 (b). These sidelobes will become significant in the monopulse processing of

30

Chapter 4. Note from Figure 2.14 that the across-track sidelobes are not noticeably reduced from those of the receive beams shown in Figure 2.9. Since the transmission pattern is broad in the across-track dimension, it has a minimal effect on these sidelobes.
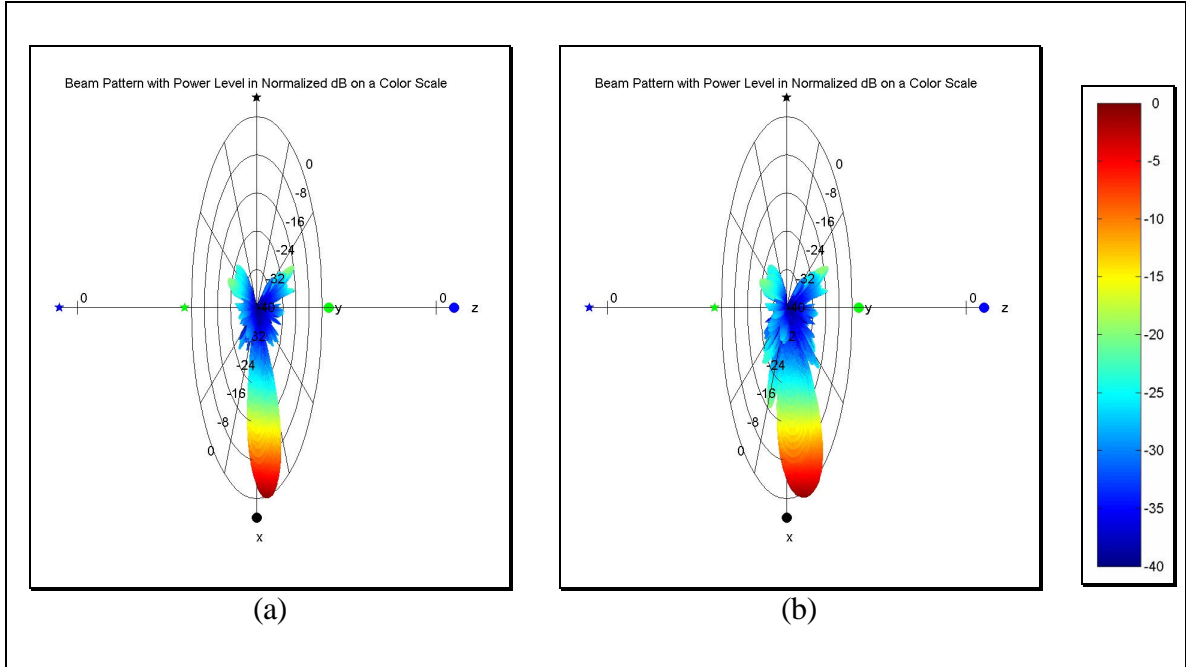
Figure 2.11. Normalized Combined Transmit and Receive Beam Pattern – Forward Beam 14, 37.5 kHz: (a) VOL LR (Steered 4° Forward of Nadir), (b) VOL SR (Steered 8° Forward of Nadir).
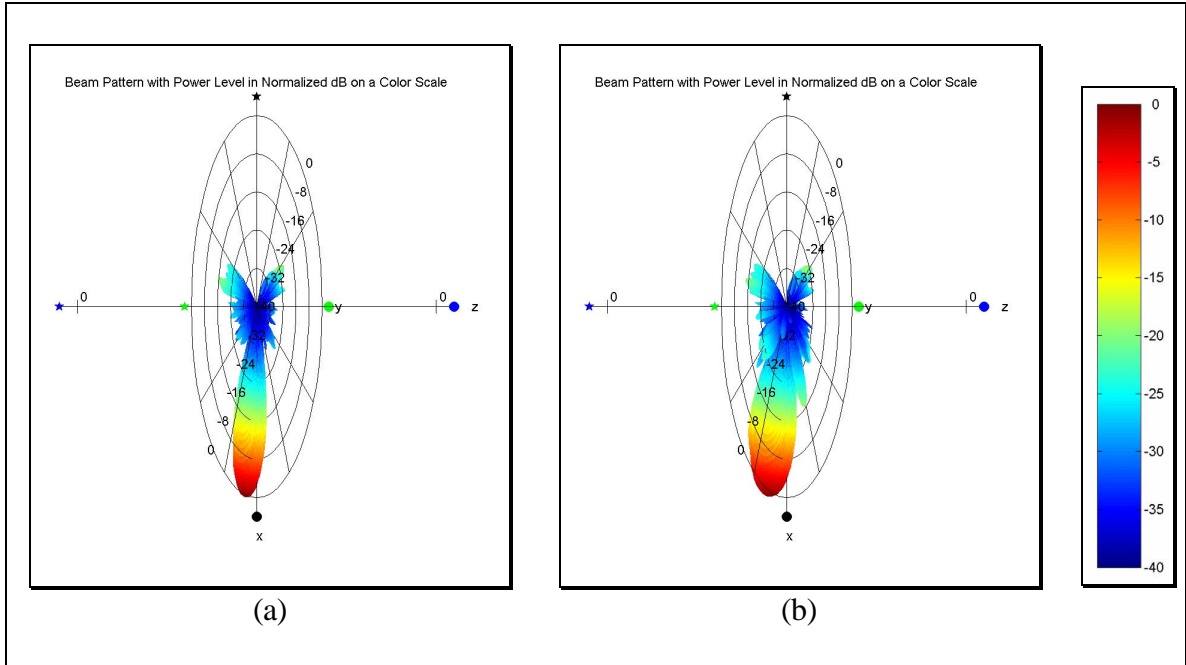
Figure 2.12. Normalized Combined Transmit and Receive Beam Pattern – Aft Beam 41, 37.5 kHz: (a) VOL LR (Steered 4° Forward of Nadir), (b) VOL SR (Steered 8° Forward of Nadir).
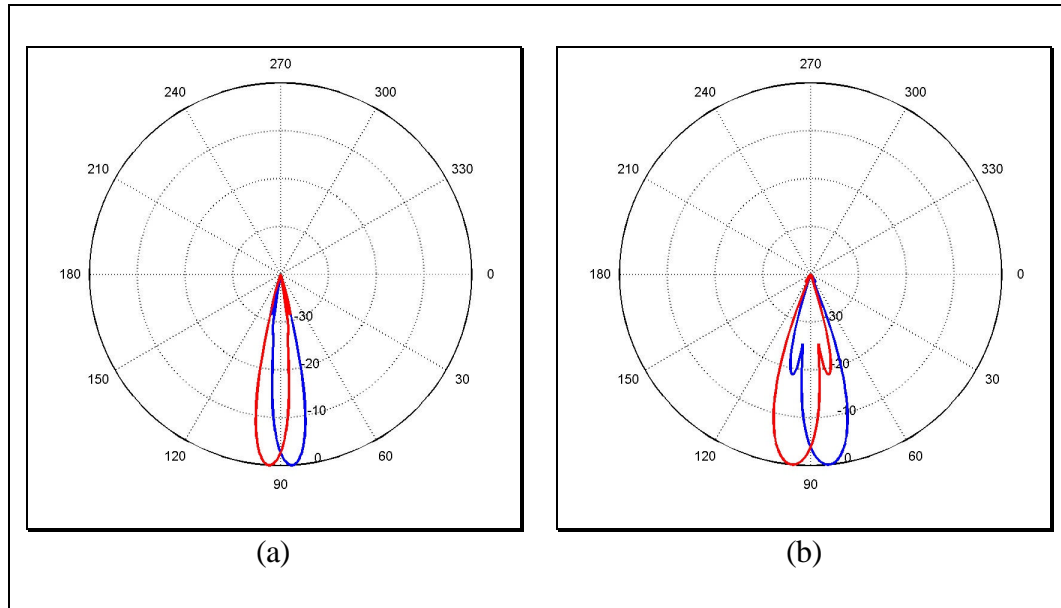
Figure 2.13. Lower Half of the Along-Track Slice ($\boldsymbol{f} = 0°$) of the Normalized Combined Transmit and Receive Beam Pattern – Beam Pair 14 (Nadir At $\left(\boldsymbol{q} = 90°, \boldsymbol{f} = 0°\right)$) Cylinder Along 180° to 0° Axis – 37.5 kHz: (a) VOL LR, (b) VOL SR.
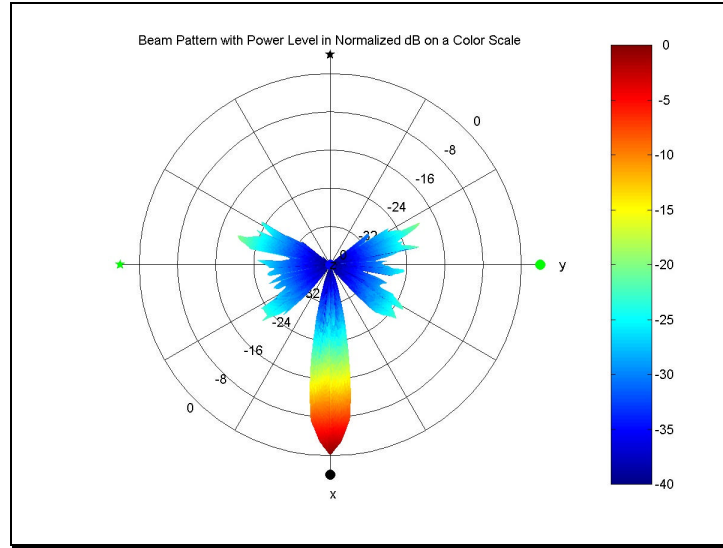
Figure 2.14. Normalized Combined Transmit and Receive Beam Pattern – Front View, All Receive Modes for Beams 14 & 41 (Nadir At $(q = 90°, f = 0°)$) Cylinder Axis Out of Page – 37.5 kHz.

(a) (b)
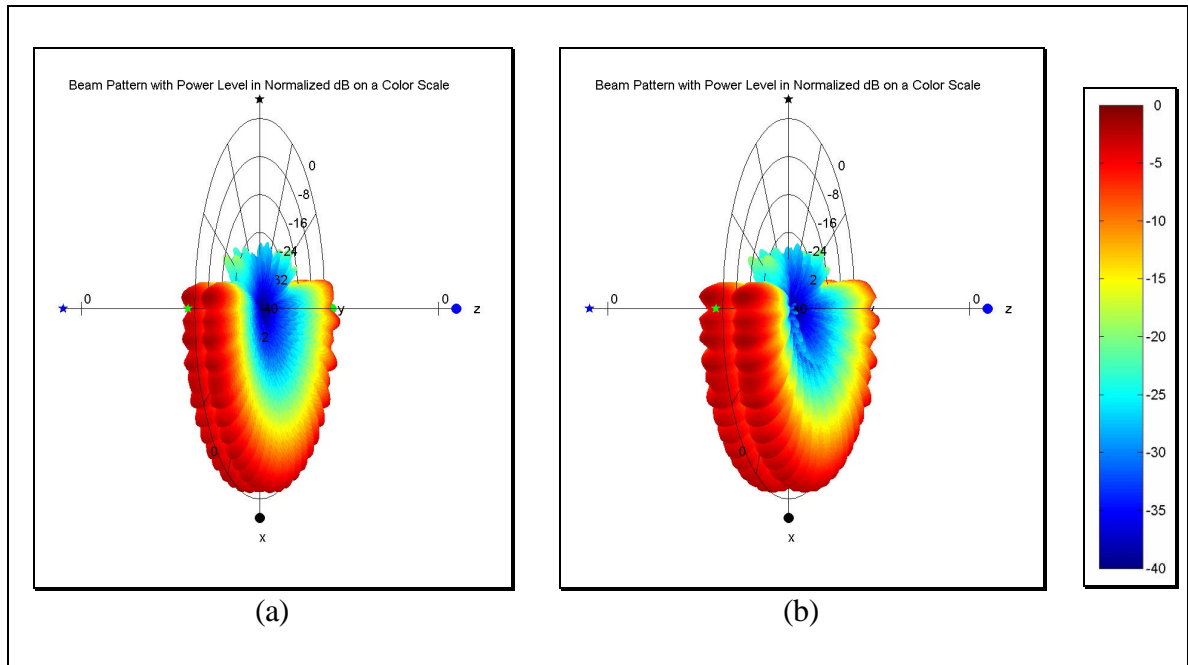
Figure 2.15. Normalized Combined Transmit and Receive Beam Pattern for all Beams – 37.5 kHz: (a) VOL LR, (b) VOL SR.

2.3   Cross-Sections

2.3.1   Spherical Cross-Sections

Spherical cross-sections of the transmit, receive and product beam patterns are presented in this section to highlight three characteristics that are not available in the beam pattern style of display. Spherical cross-sections provide (1) a spatially accurate method of visualizing the relative field intensity on a surface at a fixed distance from the origin, (2) a better visualization of the weaker field intensities near the viewing threshold, and (3) a visualization of the phase of a single beam. The phase visualizations cannot be produced in the three dimensional beam pattern plots since these plots are not well suited for displaying zero mean data. The orientation used for the spherical cross-section figures in this report is a view from nadir with the nose of the towed body pointed toward the top of the page. The spatial magnitude reference has been removed such that only the coloring scheme remains to show the normalized intensity of the field.

Figure 2.16 shows the normalized magnitude and the phase, respectively, of the spherical cross-section of the transmission signal. The along-track regions that have strong magnitude further away from the central across-track plane than the other along-track regions do are those from the staves with two transmit elements. These have wider main lobes than do the staves with three transmit elements. However, the staves with three elements have relatively strong sidelobes in the along-track dimension. As for the phase plot, shifts between sidelobes can be clearly seen. Slight changes appearing within the region of the main lobe correspond to slight variations in the interference patterns of the transmission elements.

34
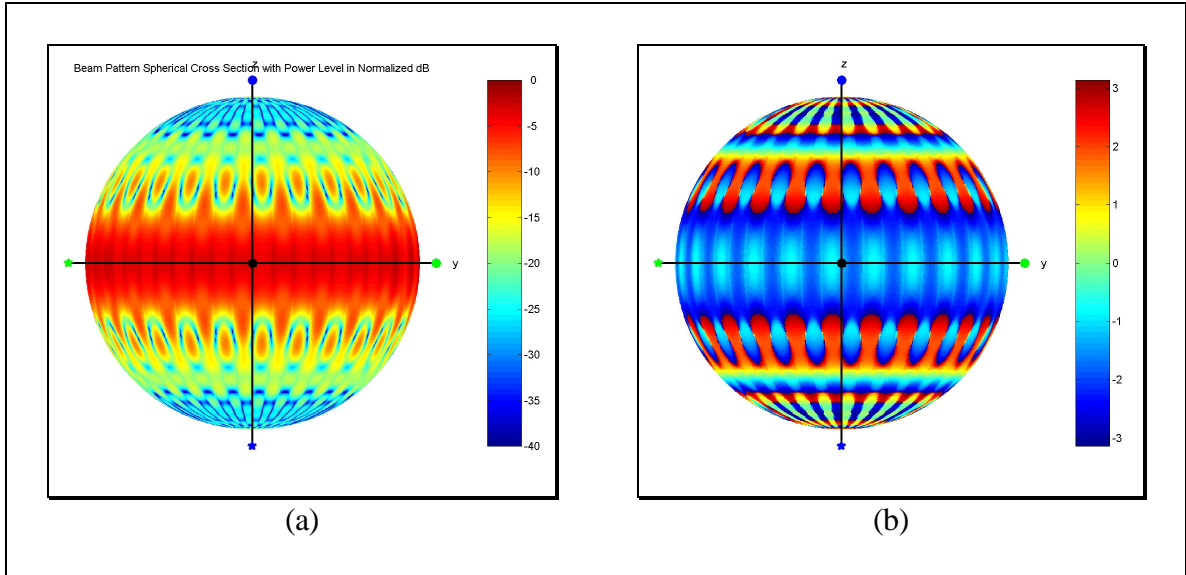
Figure 2.16. Transmit Spherical Cross-Section, VOL – 37.5 kHz: (a) Normalized Intensity in dB, (b) Phase in Radians.

Figure 2.17 shows the magnitude and phase respectively of beam 14 in VOL LR mode, and Figure 2.18 shows the show the magnitude and phase respectively of beam 41. Beams 14 and 41 combine to form beam pair 14. The magnitude plots show that the beam maximum response axes are four degrees fore and aft of nadir. It becomes clear from these plots that the off-axis sidelobes are the intersection of the across-track sidelobes and the along-track sidelobes. The across-track sidelobes extend above the towed body's nominally horizontal plane. Therefore, they are partially outside the visible region of these figures. The largest off-axis sidelobes that appear near the fore-aft axis are in what would be called the polar regions from a planetary view and are also nearly outside the visible region. One other interesting feature is the diagonal symmetry of some features in the across-track sidelobes. This symmetry results from the skewing effect of shifting adjacent staves by one half element-spacing in combination with using even numbers of staves to create the receive beams.

35

The phase patterns shown in the figures are created by the interference of two primary phase patterns. One of these patterns is a phase grid pattern of sharp along-track sidelobe transitions and broad across-track sidelobe transitions. These follow the same general pattern that is shown in the magnitude plots. The other pattern is caused by a displacement between the chosen receive array reference point and the acoustical centers of the portions of the array used to make the beams. Generally, the phase center of the segment of an array used to generate a beam would be chosen as that beam's reference point. However, in order to allow phase comparison between the receive beams, a single phase center has been chosen for them all on the central axis of the array (z-axis). The displacement occurs because the area bounded by the across-track arc of the subarray used to make any particular pair of receive beams and the arc's corresponding chord does not subtend a portion of the cylinder containing the central z-axis. As such, the distance to the effective phase center from the spherical surface is shortest along the bisector between the beams of the beam pair of interest. The bisector is nadir in the case of beam pair 14. At angles moving away from this bisector the distance to the effective center of the active subarray gradually increases until is reaches a maximum in the direction opposite from that of the shortest distance (toward the sea surface is this case).

Other variations occurring near the xy-plane (vertical across-track plane) are the result of the fore-aft stave skewing. These effects can be most clearly seen in the across-track sidelobes in the magnitude plots where they are manifested as a diagonal symmetry about a line passing through each beam's maximum response axis.
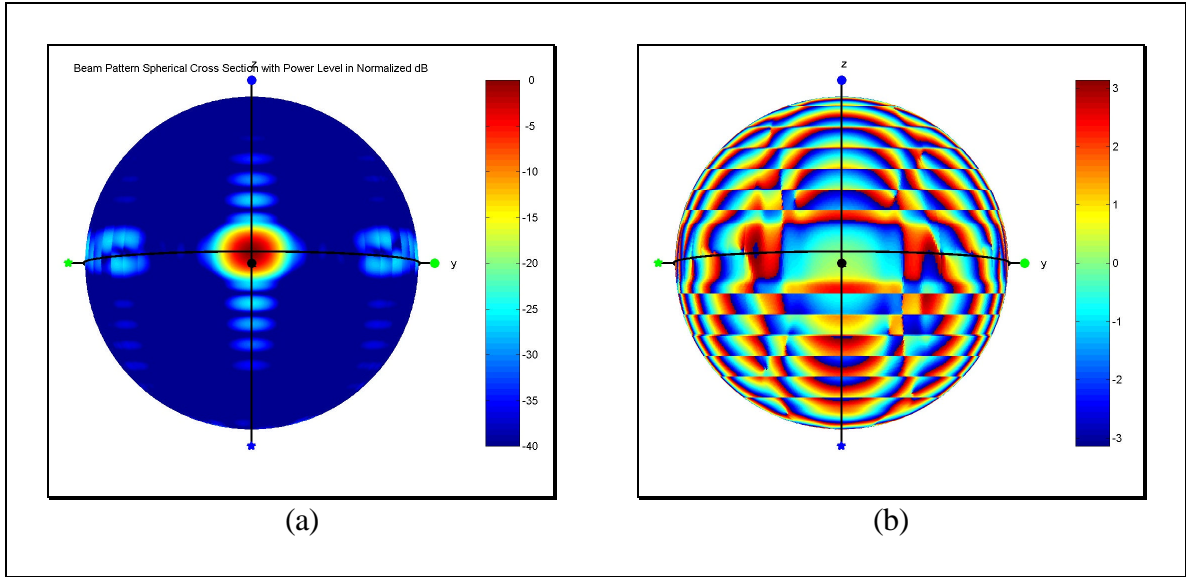
Figure 2.17. Receive Spherical Cross-Section – Forward Beam 14, VOL LR (Steered 4°
Forward of Nadir) – 37.5 kHz: (a) Normalized Intensity in dB, (b) Phase in Radians.
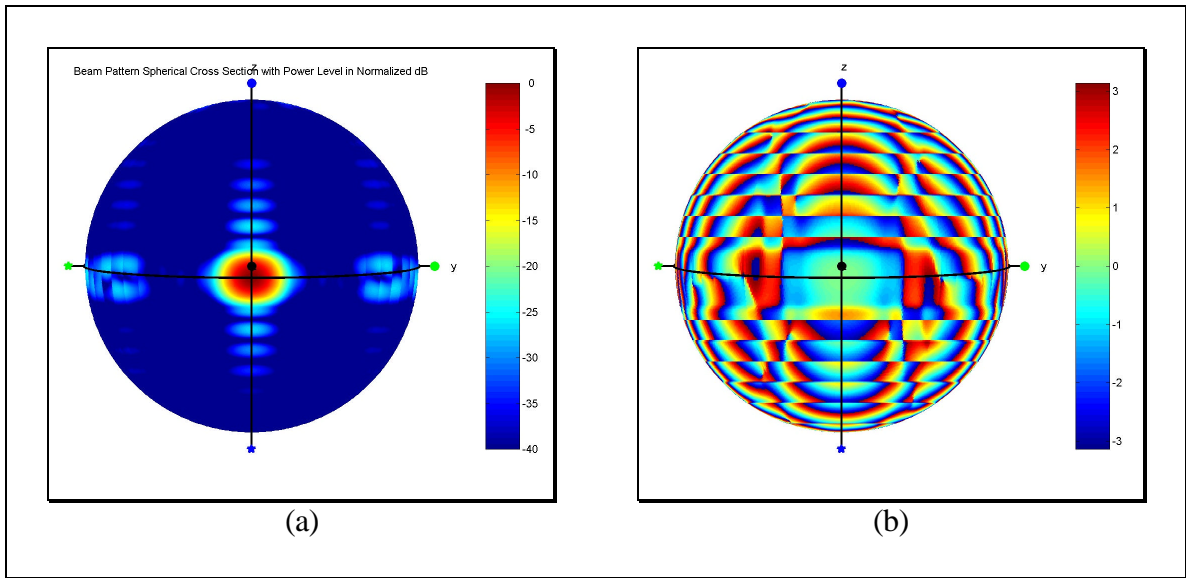
Figure 2.18. Receive Spherical Cross-Section – Aft Beam 41, VOL LR (Steered 4°
Forward of Nadir) – 37.5 kHz: (a) Normalized Intensity in dB, (b) Phase in Radians.

Figure 2.19 and Figure 2.20 repeat Figure 2.17 and Figure 2.18 for VOL SR data.

The beam maximum response axes appear at eight degrees fore and aft of nadir in this

case. Since the SR mode has a shorter aperture length (failure of constant first-sidelobe

height for an array length of 4.5 wavelengths in SR mode) and more uniform along-track

element amplitude weighting than the LR mode does, it has relatively stronger sidelobes

than the LR mode does. The strongest of these occur in the visible edge of the 'polar region' furthest away from the maximum response axis. Additionally, the shorter effective aperture of the SR mode creates fewer, wider sidelobes along-track than the LR mode does. The skewing effect of the stave shifts can be seen more strongly in the VOL SR mode figures than it was in the VOL LR mode figures since the sidelobes are relatively larger.

Recall that receive beams are steered along the fore-aft dimension but not along the across-track dimension. Consequently, the across-track sidelobes do not move as the steering angle changes, whereas the along-track sidelobes do. This is most clearly seen in the VOL SR phase plots, where the boundaries between along-track sidelobes appear as planes parallel to the xy-plane that are shifted so as to be symmetrical about the maximum response axes.

(a)   (b)
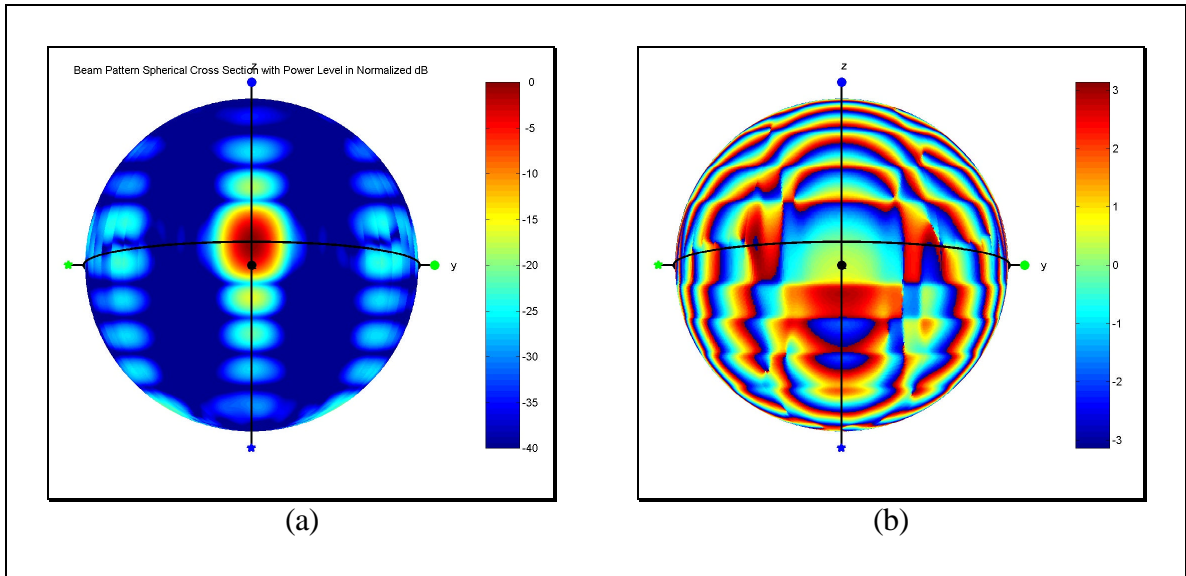
Figure 2.19. Receive Spherical Cross-Section – Forward Beam 14, VOL SR (Steered 8° Forward of Nadir) – 37.5 kHz: (a) Normalized Intensity in dB, (b) Phase in Radians.
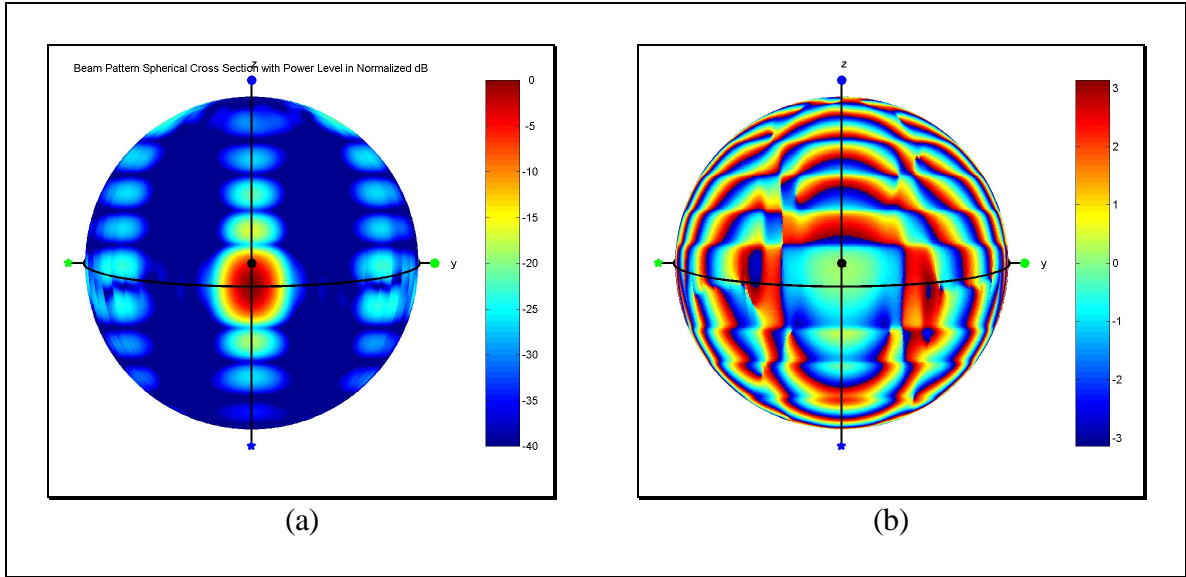
Figure 2.20. Receive Spherical Cross-Section – Aft Beam 41, VOL SR (Steered 8°
Forward of Nadir) – 37.5 kHz: (a) Normalized Intensity in dB, (b) Phase in Radians.

Figure 2.21 through Figure 2.24 show the combined effects of the transmit and
the receive spherical cross-sections for both VOL LR and VOL SR modes. As expected,
the magnitude in the fore-aft 'polar regions' has been greatly reduced. However, the
receive maximum response axes have been pulled toward the xy-plane by the shape of
the transmission pattern. Note that the aft sidelobe of beam 14 in the VOL SR mode is
aligned along-track with the main lobe of beam 41, whose forward sidelobe is aligned
with the main lobe of beam 14.   The phase of the combined spherical cross-sections
shows some characteristics of both the transmit and the receive phase patterns. These are
already beginning to look like noise, and this is a noise-free simulation using a
homogeneous media. As such, little usable phase information can be expected from the
measured data. This will be shown to be the case in Chapter 4.

Both the transmit and the receive phase patterns must be retained in order to
obtain an accurate representation of system operation. While the assumption used in the
spherical cross-section simulation that the target surface is always normal to the radii of

the sonar array is extremely unlikely to represent any physical environment, every patch of target surface can be modeled as a plane at the smallest level. The characteristics of a ray reflection from a plane are well known, and the resulting phase of the received signal will be the combined result of the phase of the transmit and receive beams, the path length of the ray in the medium, and any phase changes caused by the reflection from the target. As the reflecting surface becomes increasingly rough, it may be possible to model it with a statistical model. In such a case, it is possible that the effect of transmission phase might be lost. However, such is not the case in this simulation. Therefore the phase information is retained.
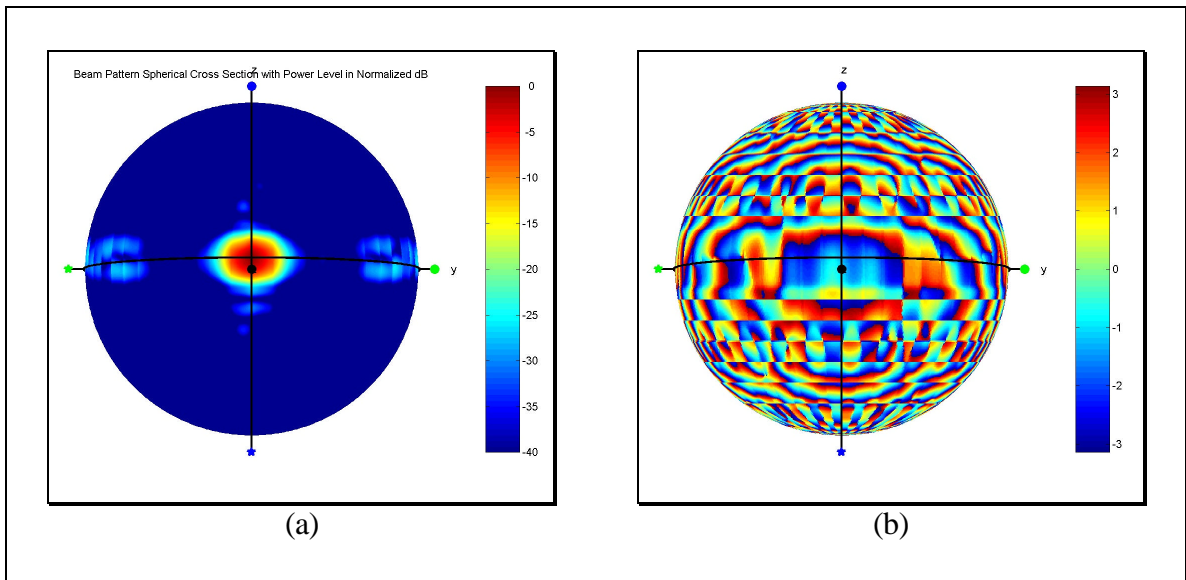
Figure 2.21. Combined Transmit and Receive Spherical Cross-Section – Forward Beam 14, VOL LR (Steered 4° Forward of Nadir) – 37.5 kHz: (a) Normalized Intensity in dB, (b) Phase in Radians.
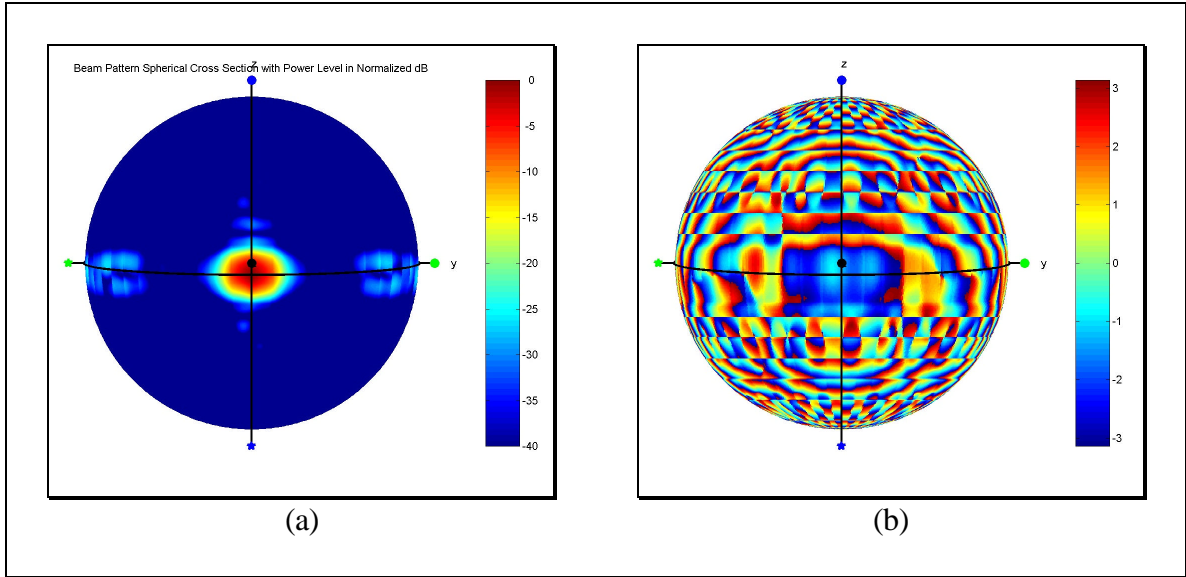
Figure 2.22. Combined Transmit and Receive Spherical Cross-Section – Aft Beam 41, VOL LR (Steered 4° Forward of Nadir) – 37.5 kHz: (a) Normalized Intensity in dB, (b) Phase in Radians.
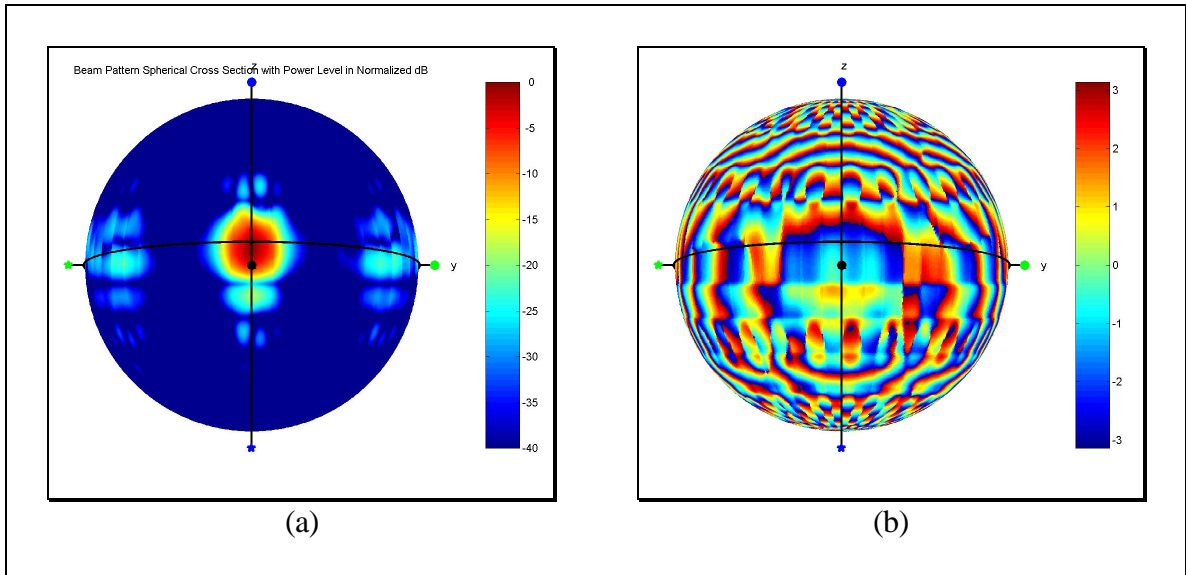
Figure 2.23. Combined Transmit and Receive Spherical Cross-Section – Forward Beam 14, VOL SR (Steered 8° Forward of Nadir) – 37.5 kHz: (a) Normalized Intensity in dB, (b) Phase in Radians.
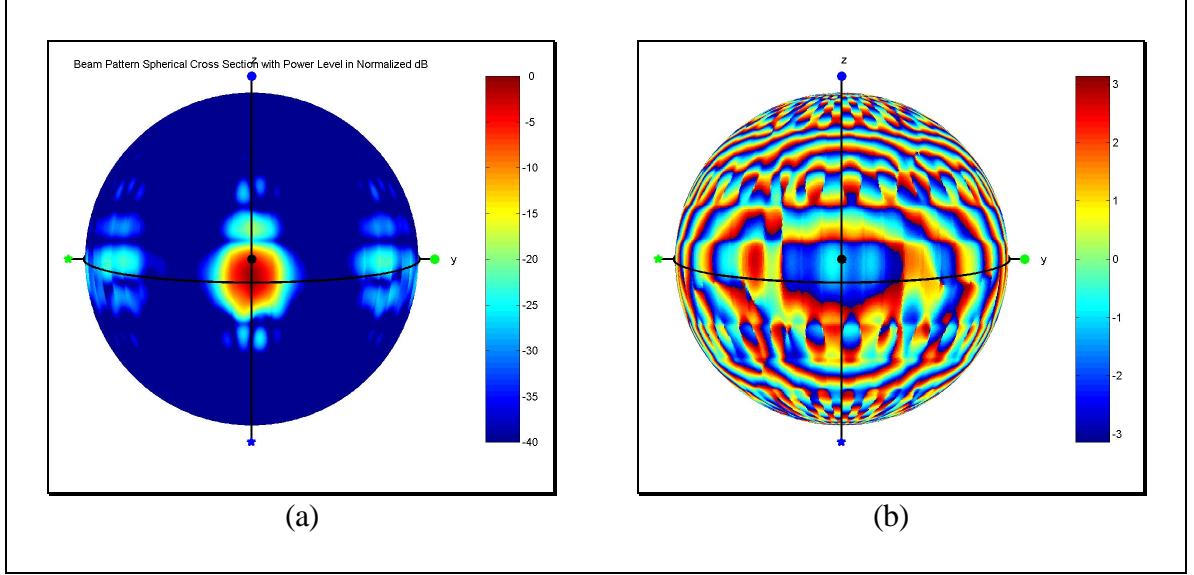
Figure 2.24. Combined Transmit and Receive Spherical Cross-Section – Aft Beam 41, VOL SR (Steered 8° Forward of Nadir) – 37.5 kHz: (a) Normalized Intensity in dB, (b) Phase in Radians.

2.3.2   <u>Planar Cross-Sections of a Flat Seafloor</u>

Beam pattern planar cross-sections represent the intensity of the projection, or footprint, of the beam pattern on a plane assuming no towed body motion and no refraction. The planar cross-sections contained in this report were derived by first calculating the acoustic intensity corresponding to a spherical cross-section at a unit radius and geometrically extrapolating each point along the line of its radius until it intersected a horizontal plane at a unit depth by means of the following method:

$$\left[x_{plane}, y_{plane}, z_{plane}\right] = \frac{1 depth}{x_{sphere}} \left[x_{sphere}, y_{sphere}, z_{sphere}\right] \tag{2.6}$$

A sample conversion is shown in Figure 2.25 for the case the $z_{plane} = z_{sphere} = 0$. In this case, point A is converted to point B. This forces the x component to be at 1 depth and the distances across the horizontal plane to be in units of depths. Because of the properties of similar triangles, The ratio of the distances OA and OB is equivalent to the

ratio of the distances x_A and $x_B = 1depth$. This method could represent a planar cross-section at any depth by simple scaling.
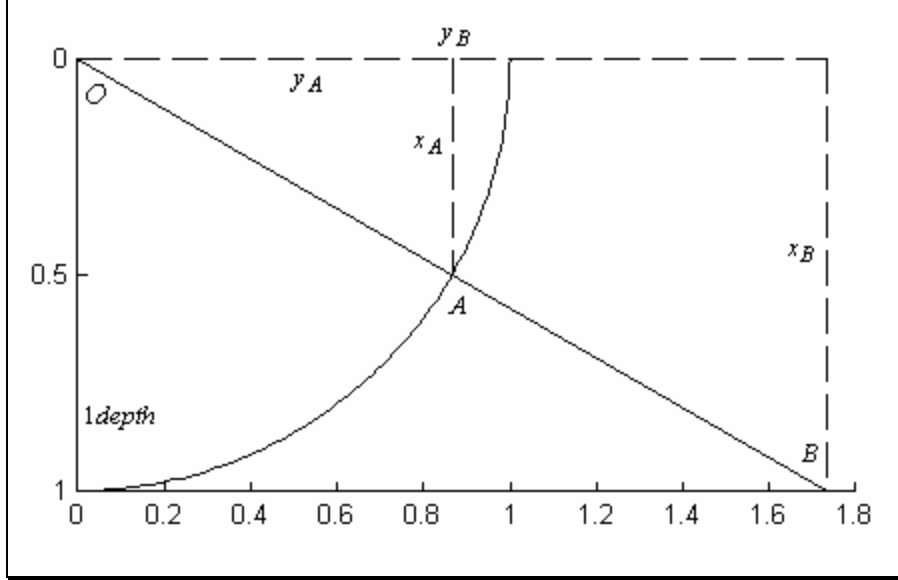
Figure 2.25. Sample Spherical Cross-Section to Planar Cross-Section Conversion.

The actual system beam patterns and cross-sections depend on the product of the transmit and receive patterns. All of the planar cross-section calculations account for geometrical spreading loss but no other losses, e.g. absorption or backscattering strength, which are dependent on spatially varying physical attributes. As such, these are the 'best case' planar cross-sections. The beam's footprint on a horizontal plane has increased spreading loss away from nadir due to the increasing distance from the transducer. The spreading loss is defined from the geometry of Figure 2.25 to be

$$20 * \log_{10}\left(\frac{OB}{OA}\right) = 20 * \log_{10}\left(\frac{x_B}{x_A}\right) = 20 * \log_{10}\left(\frac{1depth}{x_{sphere}}\right) \tag{2.7}$$

The spreading loss (in dB) is doubled for the combined transmit and receive beams since two-way travel is implied. Each plot is normalized to the maximum theoretical intensity which lies in the plane of interest. All planar cross-section figures in this report are

viewed from above with nose of the towed body pointed toward the top of the page. This is left-right reversed from the spherical cross-sections, which were viewed from below.

Figure 2.26 through Figure 2.30 show the planar cross-sections for the transmit, receive LR, receive SR, combined LR and combined SR modes out to six times the array center altitude (80° from nadir), and Figure 2.31 through Figure 2.35 show the same data out to only one time the array center altitude (45° from nadir) in order to show more detail in the near-nadir region. It can be clearly seen that the outer beams cover a larger area with a lower intensity than do the near-nadir beams. These are the result of the spreading and the spreading loss respectively. Note that that not all beams contain strong responses from the seafloor and that the main lobes from all beams are not contained in the visible region of the planar seafloor cross-section. From the receive plots it can be seen that the fore-aft beam pairs and their sidelobes ensonify hyperbolic regions of the seafloor. What had been the end lobes of the VOL SR receive patterns ensonify large areas of the seafloor fore and aft of the desired swath. While the transmit pattern greatly reduces the intensity of these sidelobes until they are not a problem, any noise producing sources in these extra regions will deteriorate the system response. The close-up combined SR magnitude response in Figure 2.35 clearly shows aspects of both the transmit and the receive SR fields.
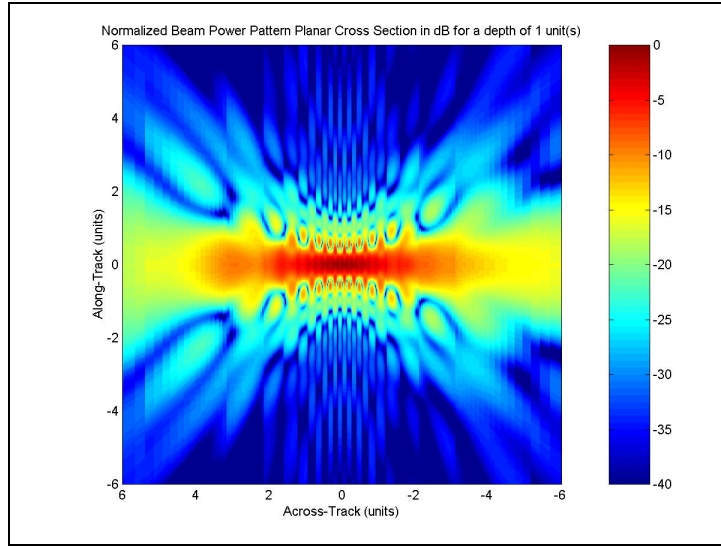
Figure 2.26. Normalized Transmit Beam Footprint on a Horizontal Plane at Unit Distance from the Transducer for VOL Mode (Viewed from Above) – Units are in Multiples of the Transducer Altitude, Forward ≡ Top of Image (Visibility > 80° from Nadir) – 37.5 kHz.
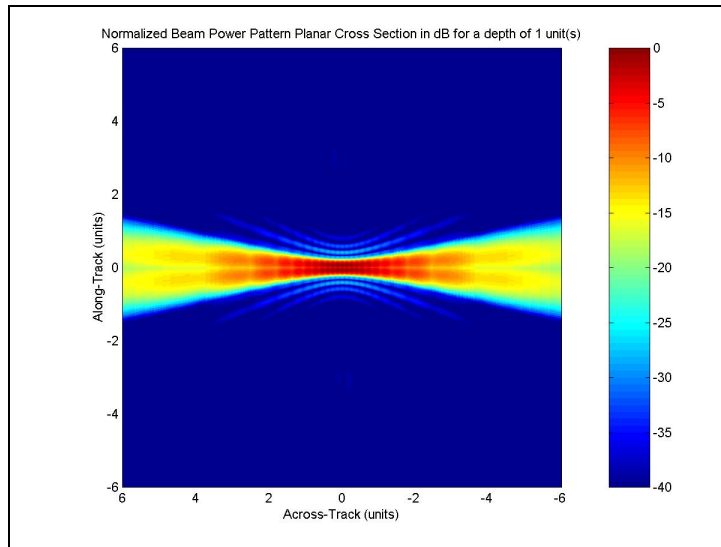
Figure 2.27. Normalized Receive Beam Footprints (for all Beams) on a Horizontal Plane at Unit Distance from the Transducer for VOL LR (Viewed from Above) – Units are in Multiples of the Transducer Altitude, Forward ≡ Top of Image (Visibility > 80.0° from Nadir) – 37.5 kHz.
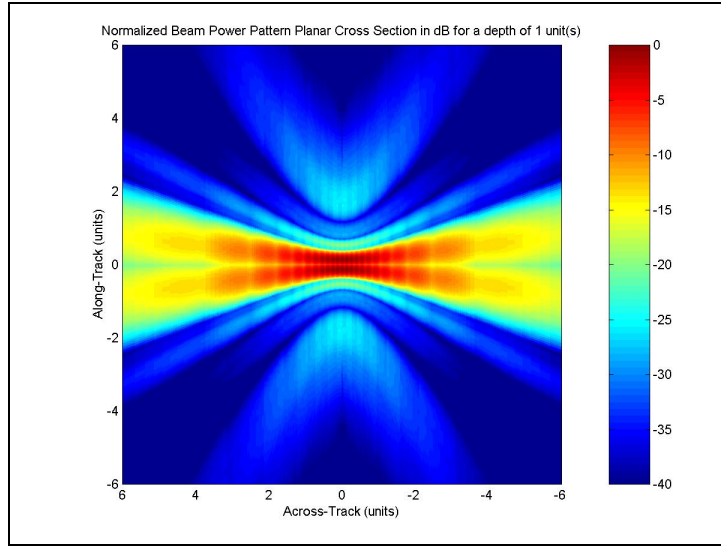
Figure 2.28. Normalized Receive Beam Footprints (for all Beams) on a Horizontal Plane at Unit Distance from the Transducer for VOL SR (Viewed from Above) – Units are in Multiples of the Transducer Altitude, Forward ≡ Top of Image (Visibility > 80.0° from Nadir) – 37.5 kHz.
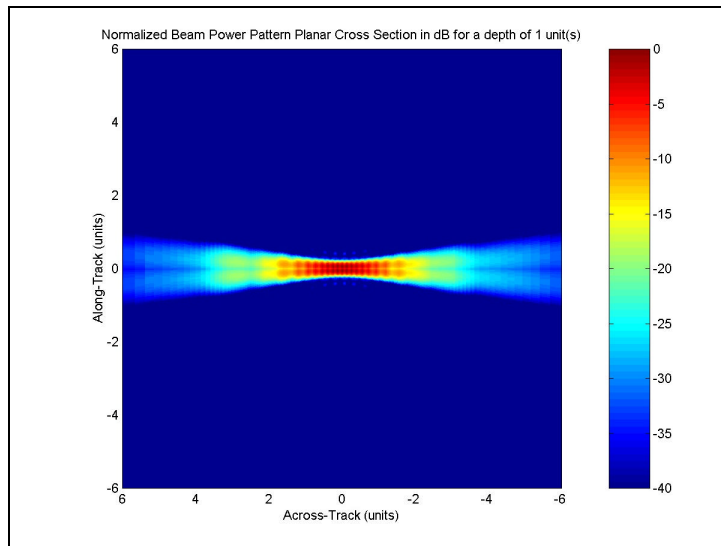
Figure 2.29. Normalized Combined Transmit and Receive Beam Footprints (for all Beams) on a Horizontal Plane at Unit Distance from the Transducer for VOL LR (Viewed from Above) – Units are in Multiples of the Transducer Altitude, Forward ≡ Top of Image (Visibility > 80.0° from Nadir) – 37.5 kHz.
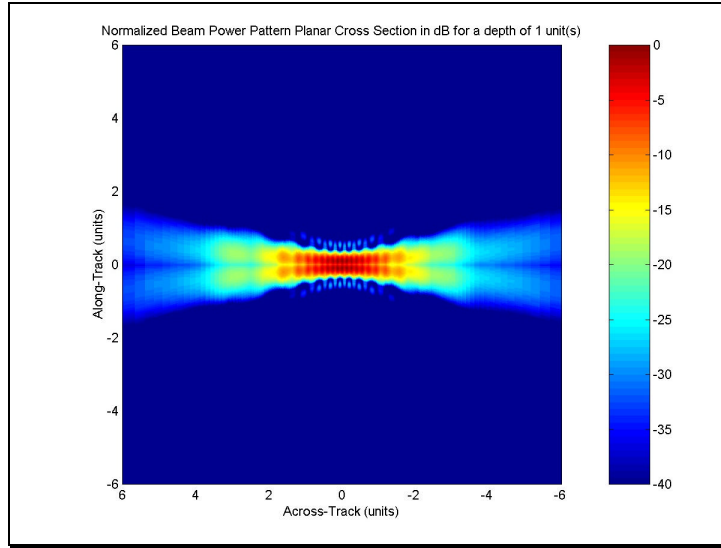
Figure 2.30. Normalized Combined Transmit and Receive Beam Footprints (for all Beams) on a Horizontal Plane at Unit Distance from the Transducer for VOL SR (Viewed from Above) – Units are in Multiples of the Transducer Altitude, Forward ≡ Top of Image (Visibility > 80.0° from Nadir) – 37.5 kHz.
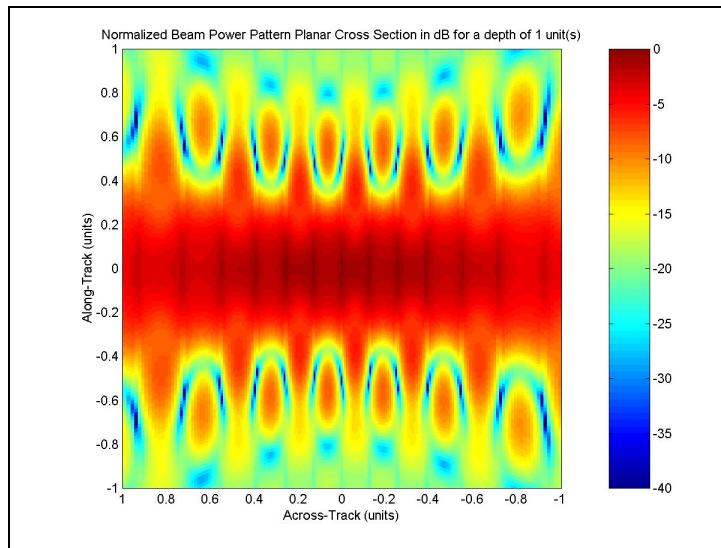
Figure 2.31. Normalized Transmit Beam Footprint on a Horizontal Plane at Unit Distance from the Transducer for VOL Mode (Viewed from Above) – Units are in Multiples of the Transducer Altitude, Forward ≡ Top of Image (Visibility > 80° from Nadir) – 37.5 kHz.
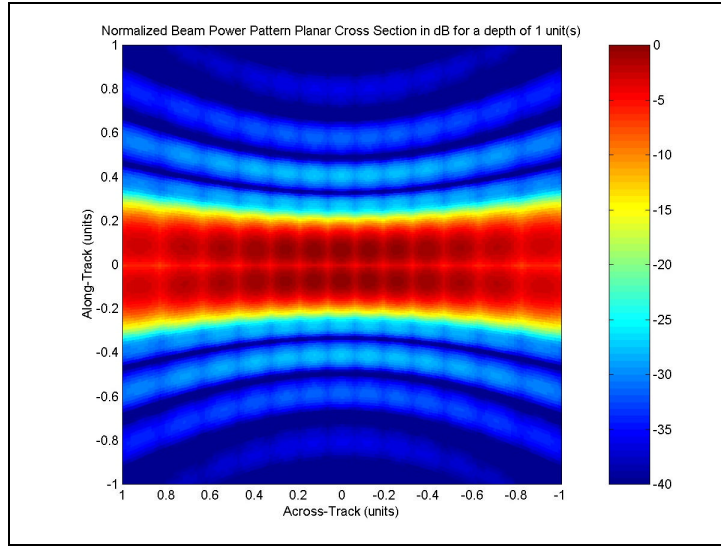
Figure 2.32. Normalized Receive Beam Footprints (for all Beams) on a Horizontal Plane at Unit Distance from the Transducer for VOL LR (Viewed from Above) – Units are in Multiples of the Transducer Altitude, Forward ≡ Top of Image (Visibility > 45.0° from Nadir) – 37.5 kHz.
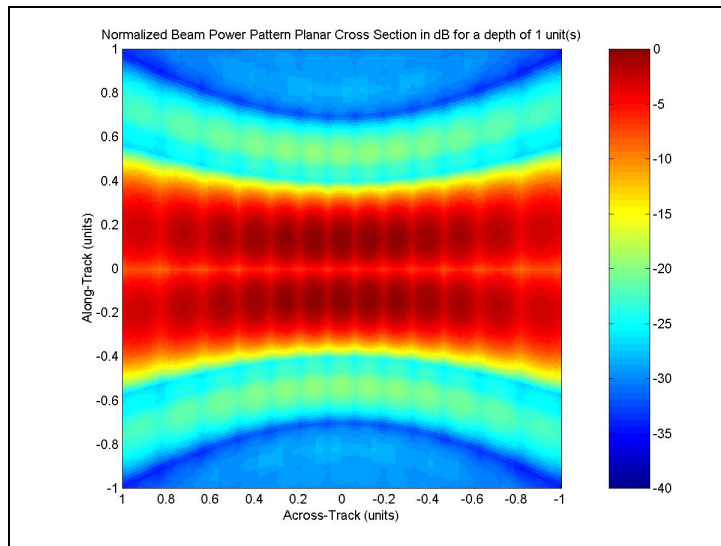
Figure 2.33. Normalized Receive Beam Footprints (for all Beams) on a Horizontal Plane at Unit Distance from the Transducer for VOL SR (Viewed from Above) – Units are in Multiples of the Transducer Altitude, Forward ≡ Top of Image (Visibility > 45.0° from Nadir) – 37.5 kHz.
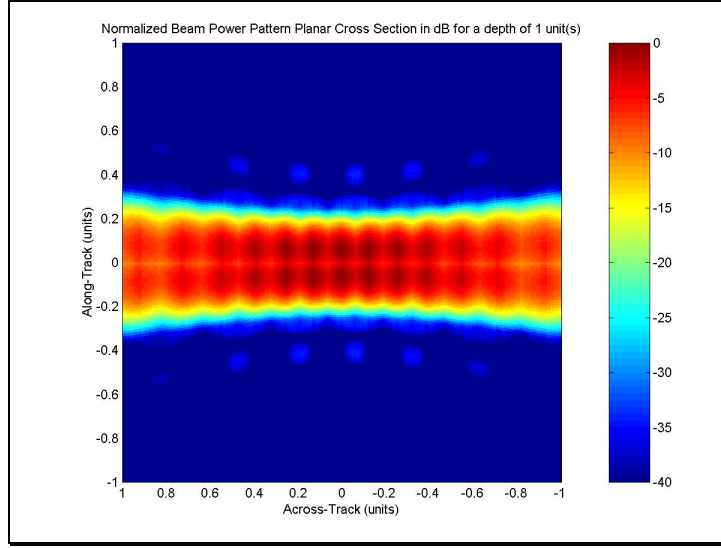
Figure 2.34. Normalized Combined Transmit and Receive Beam Footprints (for all Beams) on a Horizontal Plane at Unit Distance from the Transducer for VOL LR (Viewed from Above) – Units are in Multiples of the Transducer Altitude, Forward ≡ Top of Image (Visibility > 45.0° from Nadir) – 37.5 kHz.
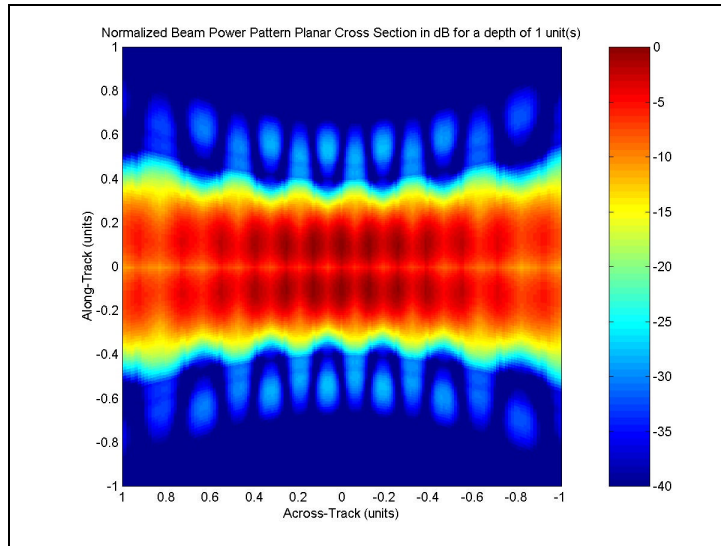
Figure 2.35. Normalized Combined Transmit and Receive Beam Footprints (for all Beams) on a Horizontal Plane at Unit Distance from the Transducer for VOL SR (Viewed from Above) – Units are in Multiples of the Transducer Altitude, Forward ≡ Top of Image (Visibility > 45.0° from Nadir) – 37.5 kHz.

2.3.3   <u>Planar Cross-Sections of a Sloped Seafloor</u>

Thus far, only planar cross-sections which are perpendicular to the x-axis, i.e. nadir, have been considered.   Equation (2.8) extends these results to cross-sectional

49

planes of arbitrary orientation, passing through the nominal unit distance immediately below the center of the transducer array at angles up to forty-five degrees from the horizontal. The angle g defines the steepest slope below the horizontal, and a is the horizontal direction of the steepest slope measured from the forward direction of the towed body:

$$[x_{plane}, y_{plane}, z_{plane}] = \frac{1depth \cdot \cos(g) \cdot [x_{sphere}, y_{sphere}, z_{sphere}]}{x_{sphere} \cdot \cos(g) - y_{sphere} \cdot \sin(g)\sin(a) - z_{sphere} \cdot \sin(g)\cos(a)} \quad (2.8)$$

When $g = 0$, equation (2.8) reduces to equation (2.6). The distances across the plane are again measured in multiples of the unit depth at nadir. The spreading loss can still be simplified to use the ratio of the x components in the case of equation (2.8). However, the upper x value from equation (2.7) is no longer limited to a value of $1depth$.

Figure 2.36 shows how a non-horizontal planar cross-section affects the receive pattern of VOL SR fore-aft beam pair 14. In this case, the seafloor falls away at 30° from the horizontal in a direction 45° to the port side of the towed body (upper left in the plot), and the horizontal plane containing the towed body is broken by the seafloor just beyond the lower right of the visible region. The distortion of the field intensity is clearly visible in this diagram. Such distortions may have significant implications for the processing of the measured data from rough seafloors. For example, the maximum response is likely to be skewed from its expected location toward the shallower water where the transmitted field is closer to perpendicular to the sea floor (stronger return) and geometrical spreading loss is reduced.
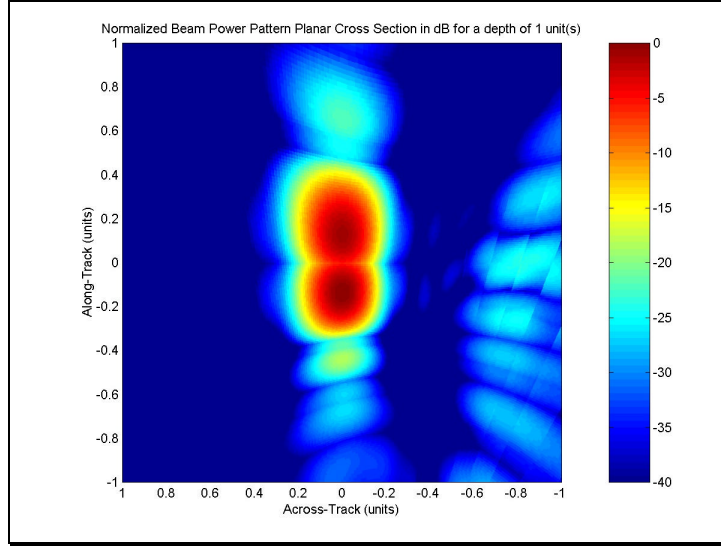
Figure 2.36. Normalized Receive Beam Footprints for Beams 14 and 41 on a Plane Falling Away from Horizontal at Thirty Degrees from the Upper Left to the Lower Right at Unit Distance (to Nadir) from the Transducer for VOL SR (Viewed from Above) – Units are in Multiples of the Transducer Altitude (at Nadir), Forward ≡ Top of Image (Visibility ≈ 45.0° from Nadir) – 37.5 kHz.

2.4 Frequency Response

Figure 2.37 and Figure 2.26 compare the frequency response of the transmit beam planar cross-section for the following operating frequencies: 26.0 kHz, 35.0 kHz, 40.0 kHz, and 50 kHz with that of the 37.5 kHz frequency used in simulation. Clearly the frequencies at the lower end of this range are not desirable since they ensonify large areas of the seafloor in the fore and aft regions and have relatively large main-swath along-track widths, which will decrease the spatial resolution of the array. When the frequency has increased to 35.0 kHz, the ensonification of the fore and aft regions is much weaker than at the lower frequencies. In the limit, one would want to increase the operating frequency indefinitely in order to increase the spatial resolution of the array. However, as the operating frequency approaches 50 kHz, sidelobes of the grating lobes begin to strongly ensonify regions fore and aft of the main swath. This is the result of the element

51

spacing as the half element-spacing between adjacent staves approaches one wavelength, which is a constructively interfering configuration in the end-fire directions. Thus a center operating frequency in the 35 to 40 kHz range seems to be a good choice.
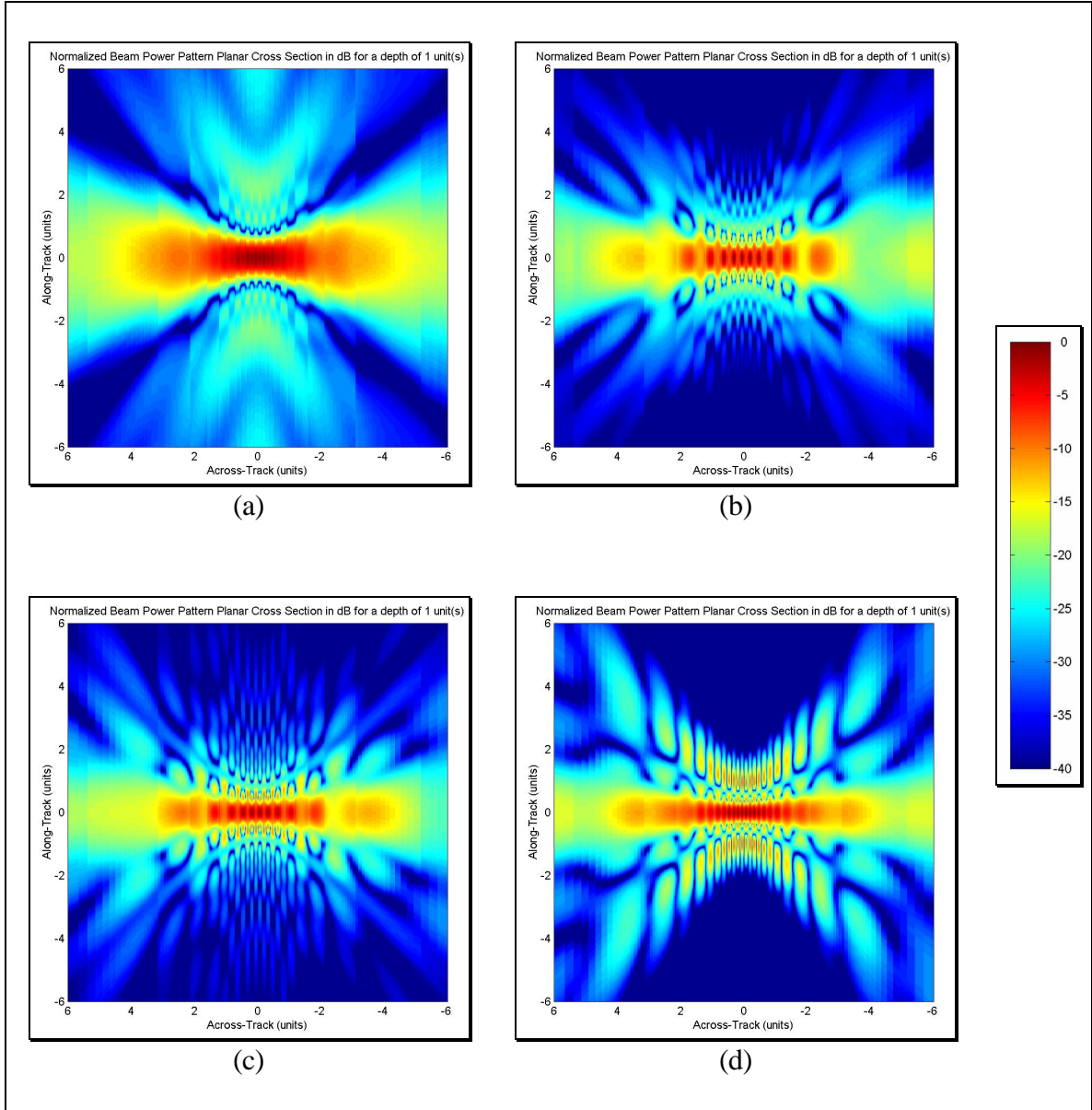
Figure 2.37. Normalized Transmit Beam Footprint on a Horizontal Plane at Unit Distance from the Transducer for VOL Mode (Viewed from Above) – Units are in Multiples of the Transducer Altitude, Forward ≡ Top of Image (Visibility > 80° from Nadir): (a) 26.0 kHz, (b), 35.0 kHz, (c) 40.0 kHz and (d) 50.0 kHz.

However, there is also the problem of across-track scalloping in the transmission pattern caused by interference between the transmission elements. This scalloping will

carry over into the combined transmit and receive response. Figure 2.38 shows an unwrapped version of the transmission beam across-track slice shown in Figure 2.4 versus frequency. This shows that at a frequency of 35.0 kHz, which was previously used in simulation, the scalloping is quite severe (6-8 dB) as shown in Figure 2.37 (b). There were, however, none of these scalloping effects visible in the measured data. The current simulation frequency of 37.5 kHz was chosen due to its relatively scallop-free across-track slice. It is important to remember that the actual system employs a transmission pulse with a bandwidth of 10.4 kHz. Careful observation of Figure 2.38 shows that across-track angles which have constructive interference at some frequencies have destructive interference at other frequencies. Thus, the scalloping effect might be averaged out by the use of an appropriately selected broadband pulse.
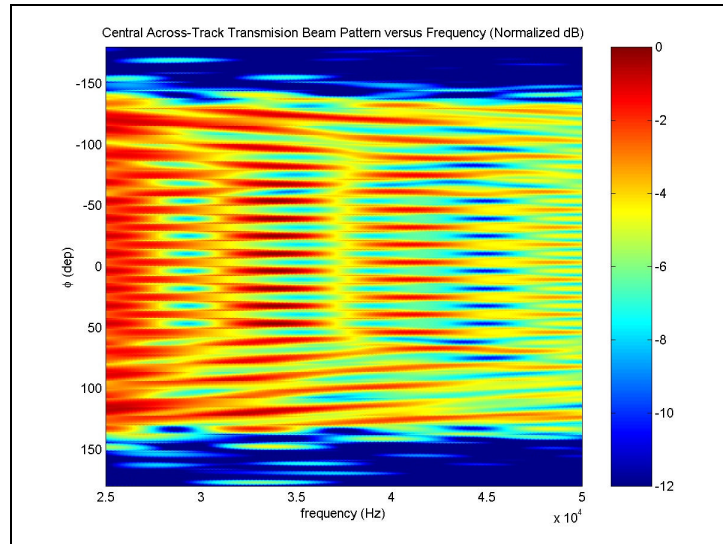
Figure 2.38. Normalized Transmit Beam Pattern Across-Track Slice Versus Frequency (Through Nadir), VOL Mode

2.5   Summary

Using simulation techniques, this chapter illustrates the farfield spatial characteristics of the transmit beams, the receive beams and their combinations. These

simulations show that the use of a 37.5 kHz transmission pulse center frequency produces minimal across-track scalloping and along-track sidelobes among frequencies in the range 25 kHz to 50 kHz. Additionally, they indicate that potential sources of error in the determination of seafloor relief and texture resulting from the VSS array geometry include noisy phase patterns and displacement of the combined transmit-receive beam pattern maximum response axes from the receive beam pattern maximum response axes due to the shape of the transmission pattern. The beam pattern and cross-section visualization techniques described here are used for the discussion of monopulse techniques in Chapter 4.

CHAPTER 3

SIGNAL ANALYSIS

3.1   Theoretical Signals

3.1.1   Stepped FM Pulse

Recall from Section 1.2.3 that the VSS uses a stepped FM transmission pulse. This is a stepped approximation to a linearly increasing chirp (up-chirp) consisting of twelve frequencies equally spaced in time and frequency. Since this is a real signal, the spectrum is mirrored in the negative frequency region, as shown in Figure 3.1 (a). The spectrum magnitude is symmetrical about 0 Hz. For the purposes of simulation, the center frequency of the transmission pulse was chosen to be 38.0 kHz.
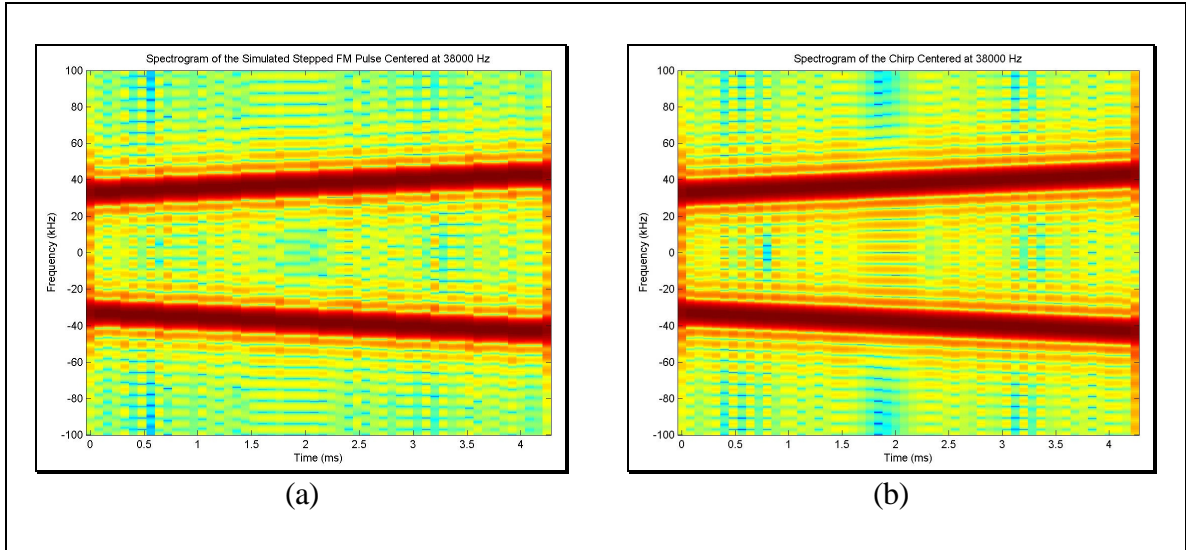
Figure 3.1. Spectrogram of the Simulated: (a) Double Sided Stepped FM Pulse, (b) Chirp.

Comparison with a linear FM chirp is also included; since the linear FM pulse is the optimal pulse compression signal [Coo60], [RW61] and pulse compression will be used in Chapter 4. Figure 3.1 shows the similarity of the transmitted signal to a linearly increasing chirp. All simulated pulse sequences have been padded with zeroes on both ends prior to displaying the spectrogram in order to produce the full time of the stepped FM signal. This results in some spreading of the spectra at the boundaries of the pulse time extent.

Figure 3.2 shows the spectrum of the simulated transmission pulse. Each expected frequency is shown as a black circle around a black 'x'. This is shown more clearly in the detailed spectrum of Figure 3.3 (a). Note that the expected frequency components are not aligned with those appearing in the simulated result. However, Figure 3.3 (b), which shows the equivalent spectrum for a linear FM signal, has the same characteristic. Cook relates these to the amplitude variations of the time domain envelope, which introduce "frequency components that do not occur at the times dictated by the linear sweep of the carrier frequency." [Coo60]

56
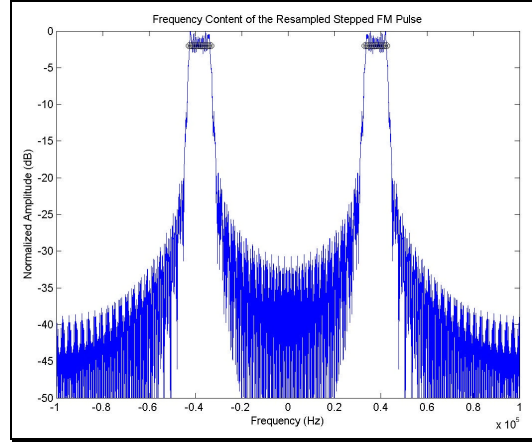
Figure 3.2. Nominal Frequency Spectra of the Simulated, Double Sided Stepped FM Pulse.

(a)

(b)
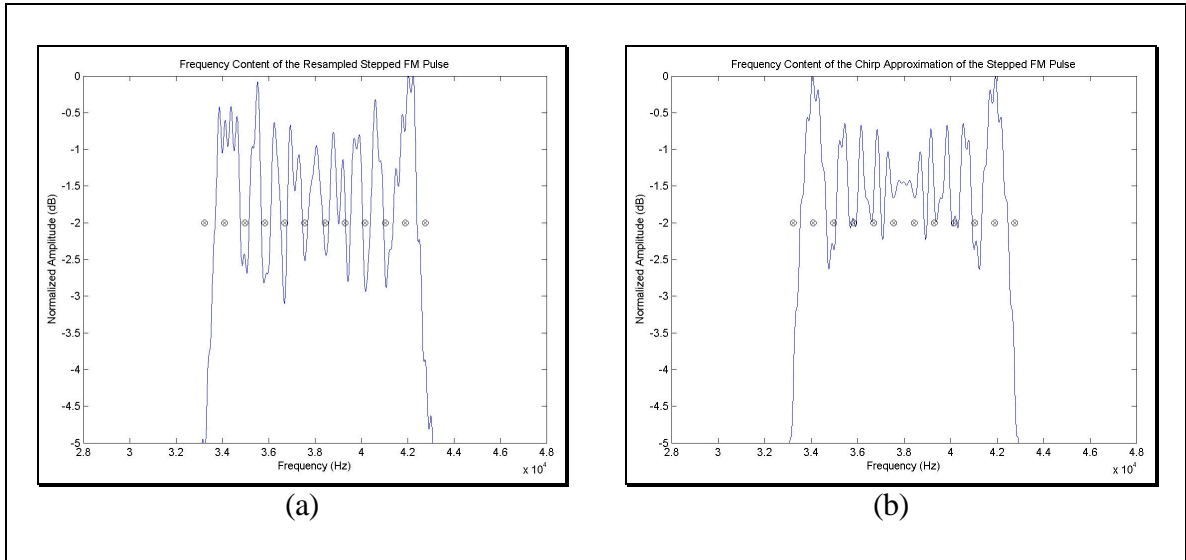
Figure 3.3. Nominal Frequency Spectra – with the Twelve Stepped FM Frequencies for Reference (Detailed View) – of (a) the Simulated, Double Sided Stepped FM Pulse (b) Simulated, Double Sided Linear FM Pulse.

3.1.2   <u>Conversion to a Single-Sided Basebanded Signal – Quadrature Sampling</u>

There are several methods by which a signal with a double-sided spectrum centered at some carrier frequency $\pm f_c$ can be converted into a single-sided, basebanded form. To be precise, this refers to a signal in which one side of the spectrum is removed, and the other side of the spectrum is shifted so as to be centered at 0 Hz. In this chapter,

57

two processing scenarios to achieve this result are compared. Simulation of these processes lead to nearly identical results.

The top-level block diagram of the simulation processes is shown in Figure 3.4. The two paths, (A) and (B), leading to the desired "ramp" pattern, yield nearly identical results.
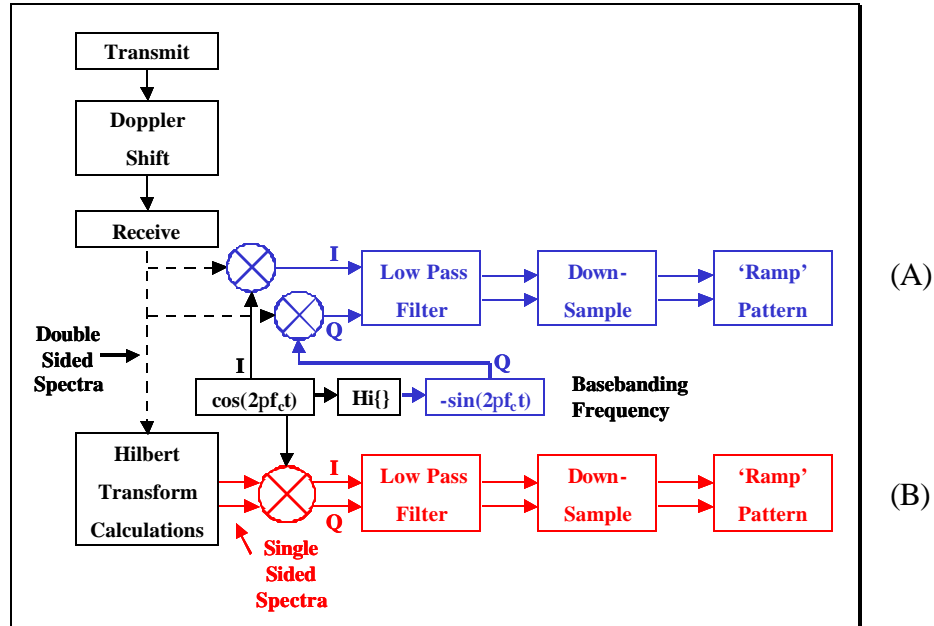
Figure 3.4. Top Level Block Diagram of the Data Processing Used to Simulate Actual Conditions.

After being received, the signals may undergo manipulations in order to place them in the required format for further processing, e.g. A/D conversion. This portion theoretically does not alter the information content and is represented by the dashed lines in Figure 3.4.

In the upper processing path (A) of Figure 3.4, the signal is mixed with a reference signal at its center frequency in order to baseband the original signal. Quadrature components are obtained during the basebanding process by multiplying the input signal with versions of the center frequency signal that are in quadrature to each

other. In order to obtain these quadrature signals, the original basebanding signal,

$\cos(2\mathbf{p}f_ct)$, is shifted by $\frac{\mathbf{p}}{2}$ radians in phase, yielding $\cos\left(2\mathbf{p}f_ct+\frac{\mathbf{p}}{2}\right)=-\sin(2\mathbf{p}f_ct)$.

Computationally, basebanding would be accomplished by using the two sinusoids just

mentioned (under the assumption that the signal is still analog) or with a Hilbert

transformed pair of sampled sinusoids (under the assumption that the signal has already

been digitized), as shown in the simulation diagram. Although the transmission pulse

does not meet the strict definition of a narrow band signal required for quadrature

sampling, it is treated as one throughout the simulation process.

The Hilbert transform produces a result which is 90 degrees out of phase with the

original signal such that when it is shifted another 90 degrees the resulting signal is

identical to the original signal for positive frequencies and inverted for negative

frequencies. Thus, when this signal is added to the original signal, the result contains

only positive frequency components. The method by which the Hilbert transform is used

to obtain a complex signal with a single sided spectrum from a real signal with a double

sided spectrum is shown in equations (3.1) and (3.2) [Bra00]:

$$SingleSided = [DoubleSided + j \cdot Hi\{DoubleSided\}] \tag{3.1}$$

$$g(t)+ j*Hi\{g(t)\}= \cos(2\mathbf{p}f_ct)- j \cdot \sin(2\mathbf{p}f_ct)= \exp(-i2\mathbf{p}f_ct) \tag{3.2}$$

Where $Hi\{\ \}$ is the Hilbert transform and $g(t)$ is $\cos(2\mathbf{p}f_ct)$. Thus the original double

sided signal in Figure 3.4 is effectively multiplied by a single sided carrier frequency of –

f_c Hz. The result is shift of $-f_c$ Hz from the spectrum of the double sided signal.

Figure 3.5 (a) and (b) and Figure 3.6 show how the basebanding process shifts the

spectrum by $-f_c$ Hz. The ramp increasing in frequency with time is the replica of the

positive spectrum of the original transmission pulse and the ramp decreasing with time is the replica of the negative spectrum of the original transmission pulse. Figure 3.5 (b) clearly shows the high frequency signal components around $-2f_c$ riding on the basebanded signal components. In this plot, the real and imaginary components are the quadrature samples, I and Q.
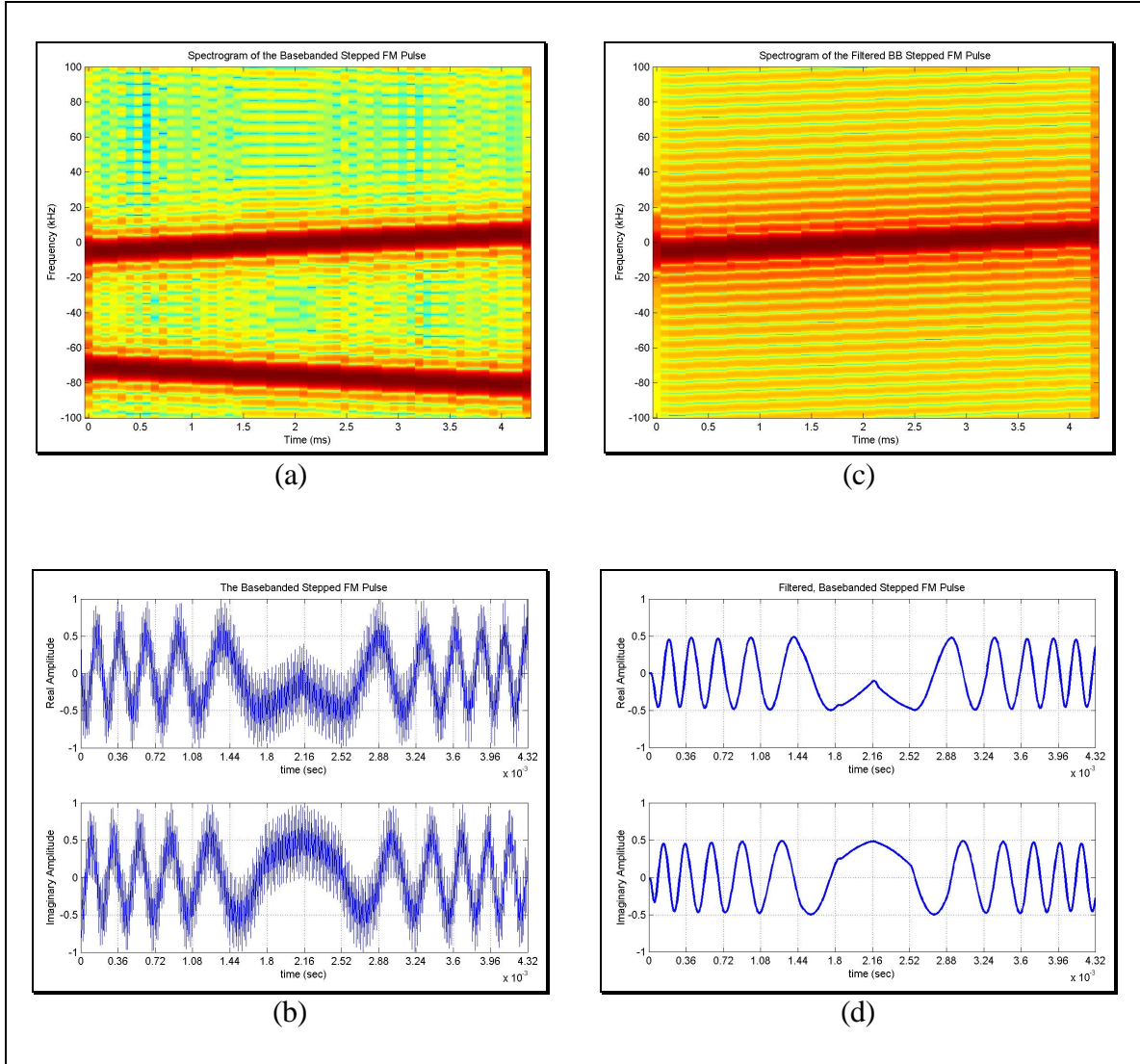
Figure 3.5. Simulated, Basebanded, Quadrature Sampled Stepped FM Pulse: (a) Spectrogram, (b) Time Domain, (c) Spectrogram after Filtering, and (d) Time Domain after Filtering.
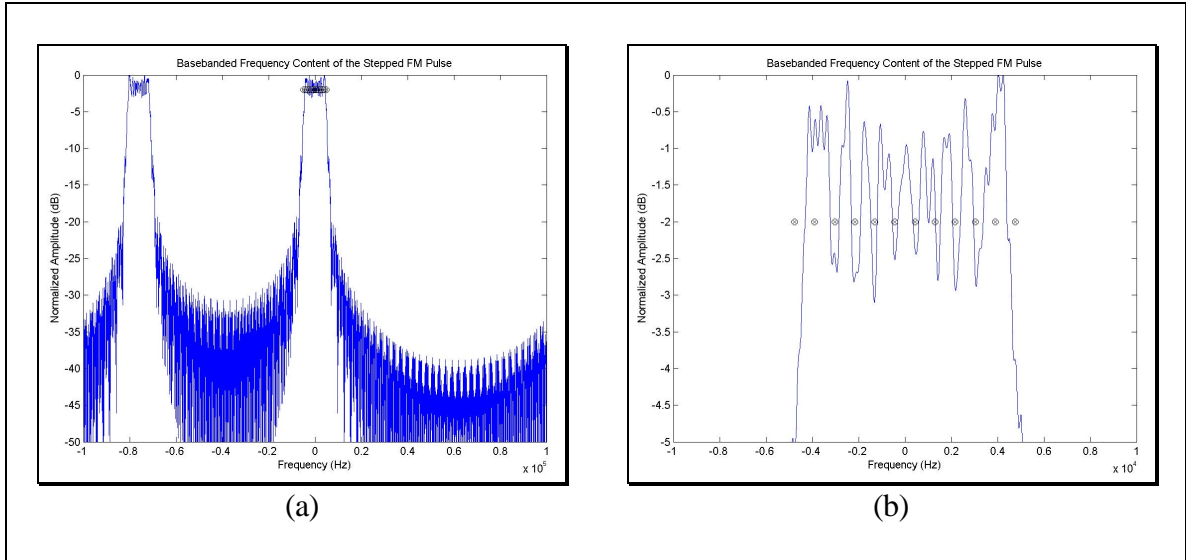
Figure 3.6. Nominal Frequency Spectra of the Simulated, Basebanded, Quadrature Sampled Stepped FM Pulse: (a) Normal View, (b) Detailed View.

Low pass filtering must be applied after basebanding in order to remove the high frequency (i.e. away from 0 Hz) components. In the case of the upper path (A), the signal centered at $-2f_c$ (-76 kHz) (Figure 3.6 (a)) must be removed. Figure 3.5 (c) and (d) and Figure 3.7 show how the particular filter used in simulation was able to remove the high frequency components. Note in Figure 3.5 (d) the transitions in the signal frequency every 0.36 ms. Because the signal is now centered at 0 Hz, the frequency ramp has the appearance of a down-ramp followed by an up-ramp versus time as it increases from -5.2 kHz to 5.2 kHz. Figure 3.7 shows the small amount (-48dB) of the high frequency data that is remaining near $-2f_c$ (-76 kHz).
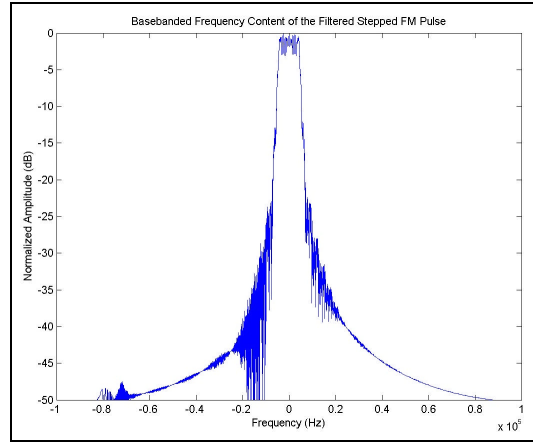
Figure 3.7. Nominal Frequency Spectra of the Simulated, Filtered, Basebanded, Quadrature Sampled Stepped FM Pulse.

The simulated signal is subsequently down-sampled to seventy-two samples, to match the actual system sampling rate. The results of this down-sampling are shown in Figure 3.8 and Figure 3.9. The intensity variations along the sides of the main signal that have the appearance of zipper teeth in Figure 3.8 are the only remnant of the frequency stepping of the original signal that are still visible in the spectrogram due to the information loss associated with downsampling. A comparison of Figure 3.9 (a) and (b) shows that the end result of the stepped FM pulse processing is very similar to that of a simple linear up-chirp.
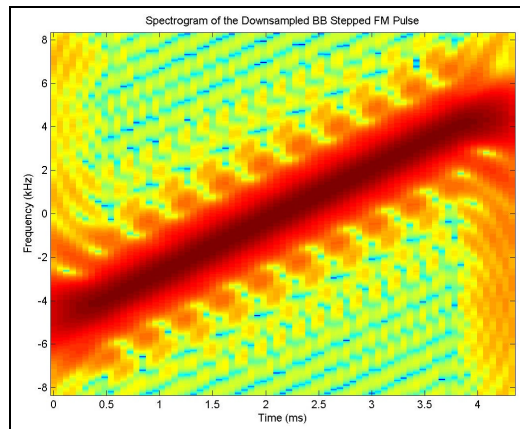
Figure 3.8. Spectrogram of the Simulated, Down Sampled, Filtered, Basebanded, Quadrature Sampled Stepped FM Pulse.
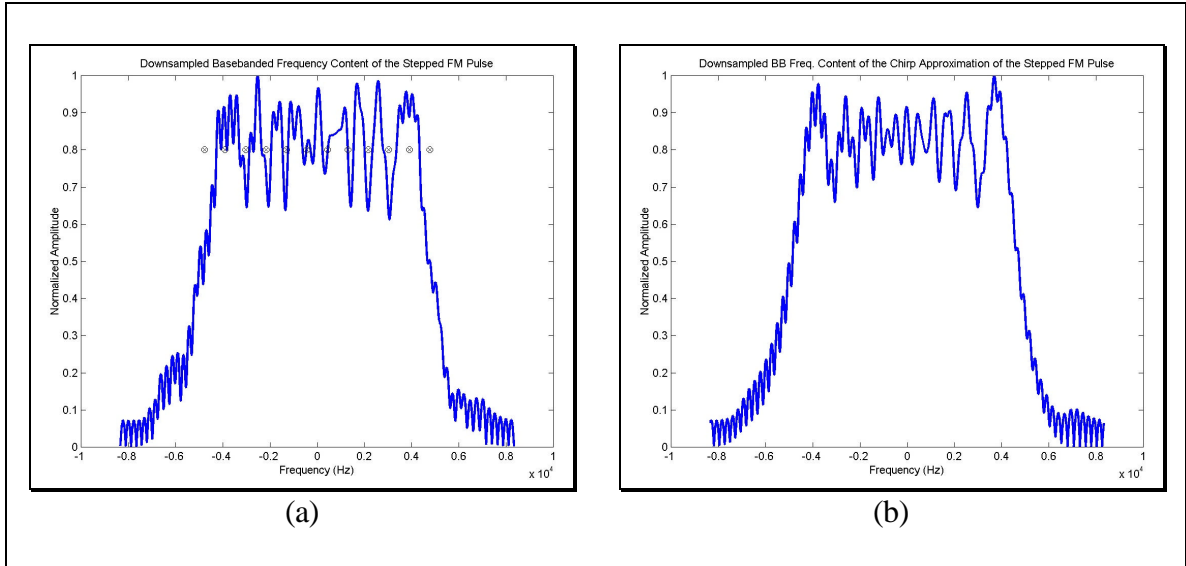
Figure 3.9. Frequency Spectra of the Simulated, Down Sampled, Filtered, Basebanded, Quadrature Sampled… (a) Stepped FM Pulse, (b) Chirp.

Figure 3.10 shows the phase of the simulated transmission pulse following the down-sampling operation. The phase has a nominally quadratic shape, but phase wrapping results in the style of display shown. Because this phase pattern is unlikely to occur randomly, it will be shown to be beneficial for signal detection (Chapter 4).
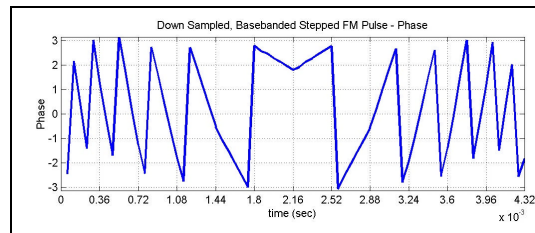
Figure 3.10. Phase in Radians of the Simulated, Down Sampled, Filtered, Basebanded, Quadrature Sampled Stepped FM Pulse.

3.1.3   Conversion to a Single-Sided Basebanded Signal – Hilbert Transform

In contrast to the process used in the previous section, the lower path in Figure 3.4 (B) uses the Hilbert transformation to produce a version of the original signal with a single sided spectrum directly from the double sided signal. Thus the signal has already been converted into complex, i.e. quadrature, components prior to basebanding. This

63

process leaves only the spectrally increasing transmission pulse centered at f_c. Figure 3.11 and Figure 3.12 contain the single sided spectra. These are identical to the double sided spectrogram and spectrum plots (Figure 3.1 (a), Figure 3.2 and Figure 3.3) for the positive frequencies and nearly non-existent for the negative frequencies. Note in Figure 3.12 that the Hilbert transform calculations do not completely remove the negative frequency components because of computational limitations.
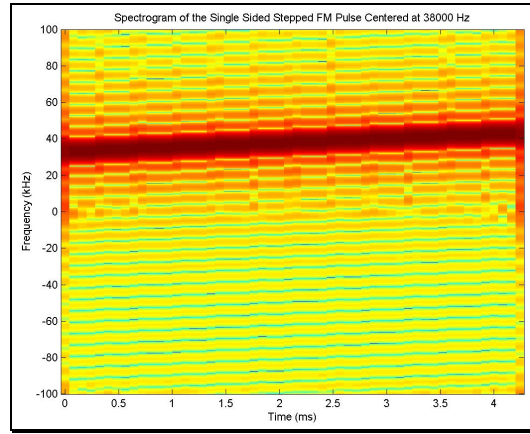
Figure 3.11. Spectrogram of the Hilbert Transformed Stepped FM Pulse.

(a)   (b)
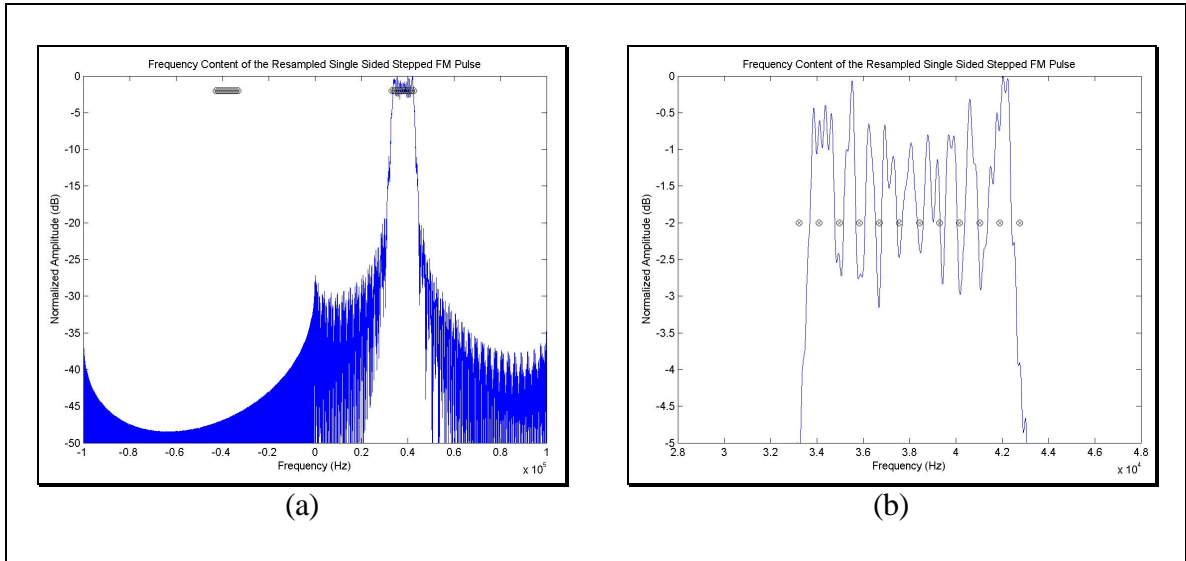
Figure 3.12. Nominal Frequency Spectra of the Simulated, Hilbert Transformed Stepped FM Pulse: (a) Normal View, (b) Detailed View.

Multiplication by $\cos(2\pi f_c t)$ places copies of the spectrum at 0 Hz and $2f_c$ Hz as seen in Figure 3.13 (a) and (b) and Figure 3.14. Note that these figures show a signal that is basically identical to that of the first process path (A) shown in Figure 3.5 through Figure 3.6 in the baseband region and symmetrically reversed about 0 Hz in the high frequency region. The unusual variations from -60 to -40 kHz and 20 to 40 kHz in Figure 3.14 are the remnants of the Hilbert transformation limitation that was seen in Figure 3.12.
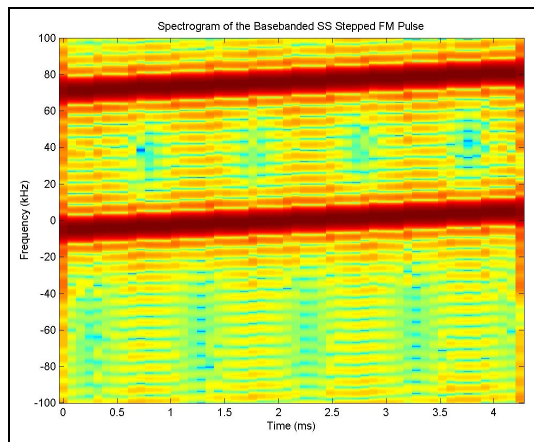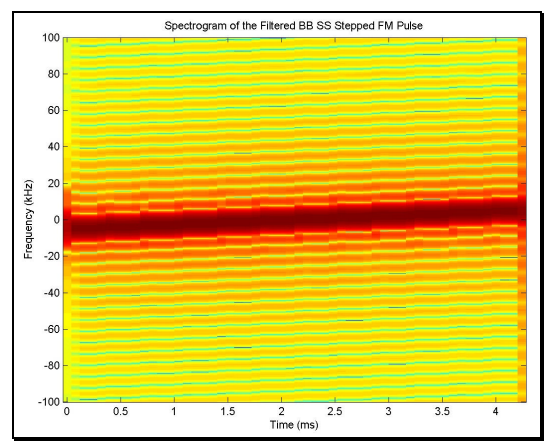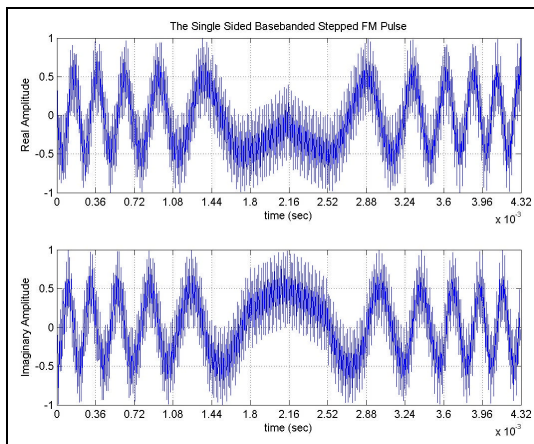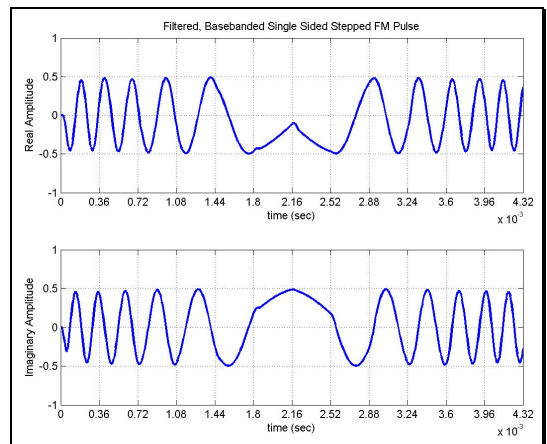
Figure 3.13. Simulated, Basebanded, Hilbert Transformed Stepped FM Pulse: (a) Spectrogram, (b) Time Domain, (c) Spectrogram after Filtering, and (d) Time Domain after Filtering.
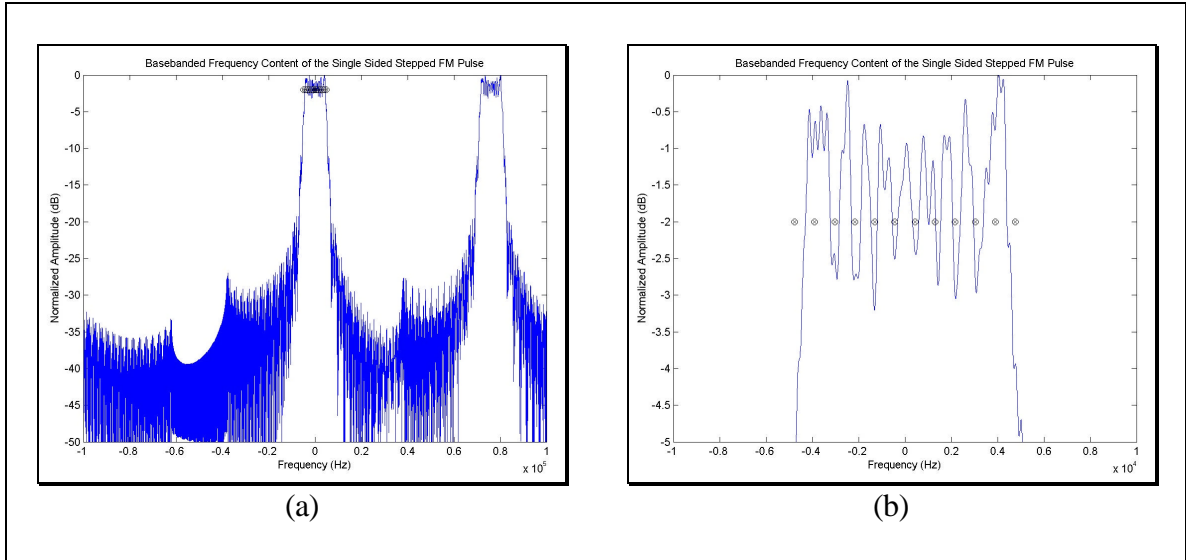
Figure 3.14. Nominal Frequency Spectra of the Simulated, Basebanded, Hilbert Transformed Stepped FM Pulse: (a) Normal View, (b) Detailed View.

Low pass filtering must be applied after basebanding in order to remove the high frequency component centered at $2f_c$ Hz. Provided that the filtering has effectively removed the high frequency components from the spectra on each processing path, the resulting signals are the same for each path following this processing stage. The results are shown in Figure 3.13 (c) and (d) and Figure 3.15. Note that these results are nearly identical to those of the quadrature-sampled results after filtering (Figure 3.5 (c) and (d) and Figure 3.7). This time, however, the remnant of the high frequency signal occurs at $2f_c$ (76kHz) instead of $-2f_c$.
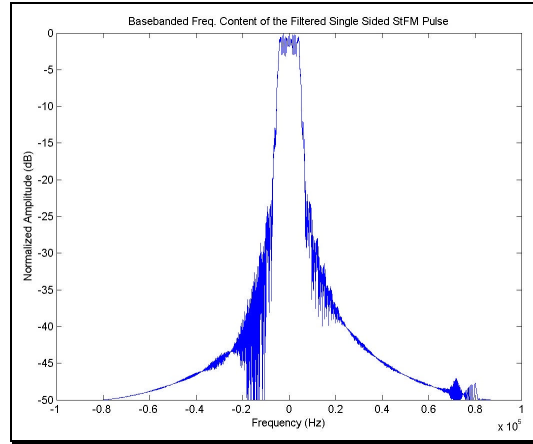
Figure 3.15. Nominal and Doppler Shifted Freque ncy Spectra of the Simulated, Filtered, Basebanded, Hilbert Transformed Stepped FM Pulse.

Figure 3.16 and Figure 3.17 show the signal after down sampling has been performed. As in the case of the low pass filtered signals, these results are basically identical to those for the quadrature-sampled signal (Figure 3.8 and Figure 3.9). Once again the end result of the stepped FM pulse processing is very similar to that of a simple linear up-chirp. This serves as a verification of the processing techniques used.
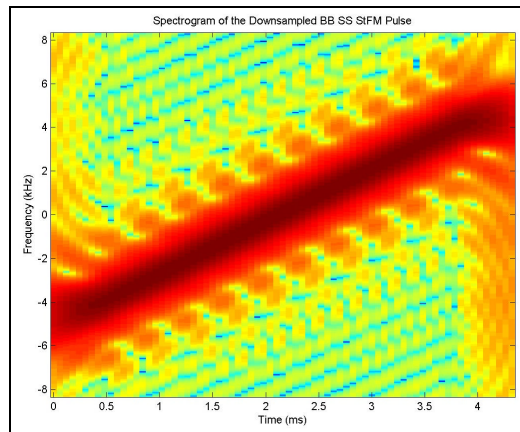
Figure 3.16. Spectrogram of the Simulated, Do wn Sampled, Filtered, Basebanded, Hilbert Transformed Stepped FM Pulse.
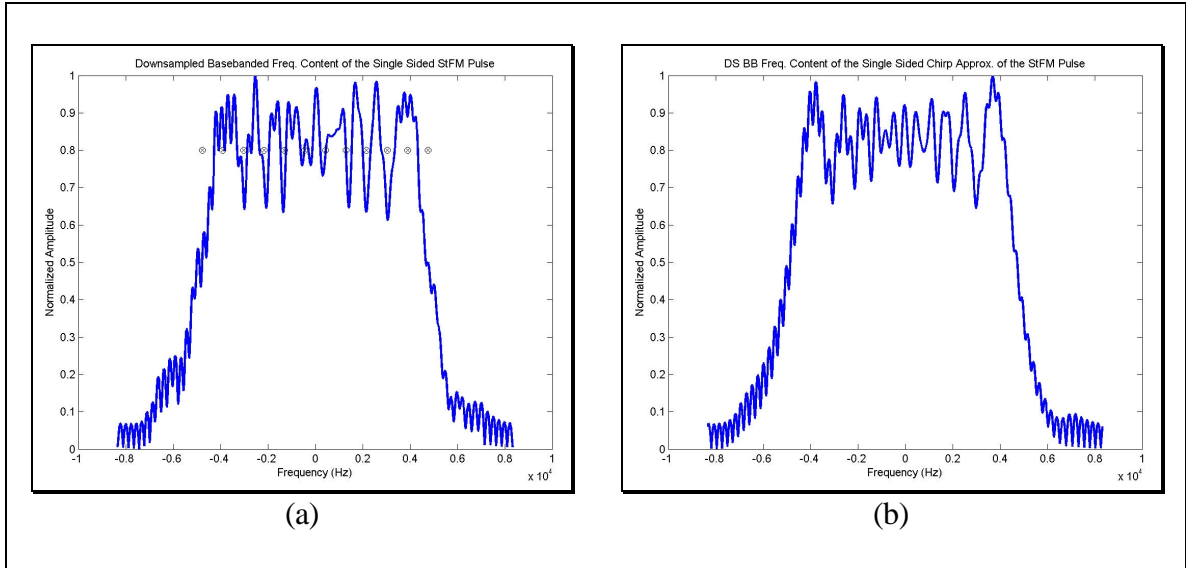
Figure 3.17. Frequency Spectra of the Simulated, Down Sampled, Filtered, Basebanded, Hilbert Transformed… (a) Stepped FM Pulse, (b) Chirp.

3.1.4 <u>Doppler Shift</u>

Due to the 86° and 94° (VOL LR) or 82° and 98° (VOL SR) orientation of beam directions with respect to the direction of travel, positive and negative Doppler shifts corrupt the forward and aft beams respectively. Doppler shifts occur in the water column prior to reception by the VSS array. Throughout this report, a positive Doppler shift is 'upshifted' in frequency and a negative Doppler shift is 'downshifted' in frequency. A towing speed of 100m/s was used in simulation in order to improve the visualization of the Doppler shift results. The Doppler effect shifts the positive and negative spectra toward or away from 0 Hz. In each case, a Doppler shift in the original signal will create the same shift in the basebanded signal that was produced in the positive spectrum of the original signal. Hence, a signal centered at $\pm(f_c + a)$ Hz will now be centered at a Hz. For both the original and Doppler shifted signals, low pass filtering must be applied after

69

basebanding in order to remove the high frequency components. However, care must be taken not to make the filter too narrow to retain a signal with strong Doppler shift.

Figure 3.18 through Figure 3.20 show some results of Doppler shift for the quadrature sampled case. Plots of the Hilbert Transformed case are nearly identical and are not included here. Note in Figure 3.18 that the frequency closest to 0 Hz is left of center (earlier in time) for the Doppler upshifted signal and right of center (later in time) for the Doppler downshifted signal. In this case, the ideal signal (noise free) is not corrupted by any type of spectral folding. Thus it should be possible to remove the Doppler component from the data. Had the signal not been converted into a single sided form prior to basebanding, the positive and negative replicas of the spectrum would have corrupted each other at baseband, and Doppler shift correction would not have been possible. The effect of the Doppler shift is shown clearly in the downsampled signal (Figure 3.19 through Figure 3.20). It can also be seen that the artificially large Doppler shift used in simulation is of the same order of magnitude as a stepped FM pulse frequency step. Preliminary testing of the measured data showed that the effect of Doppler shift was not detectable, i.e. the Doppler shift at the actual towing speed was negligible. Thus, no account of Doppler shift is taken when processing the measured data.
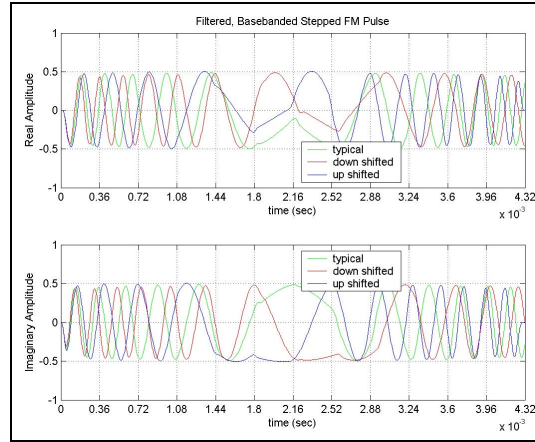
Figure 3.18. Nominal and Doppler Shifted Simulated, Filtered, Basebanded, Quadrature Sampled Stepped FM Pulse.
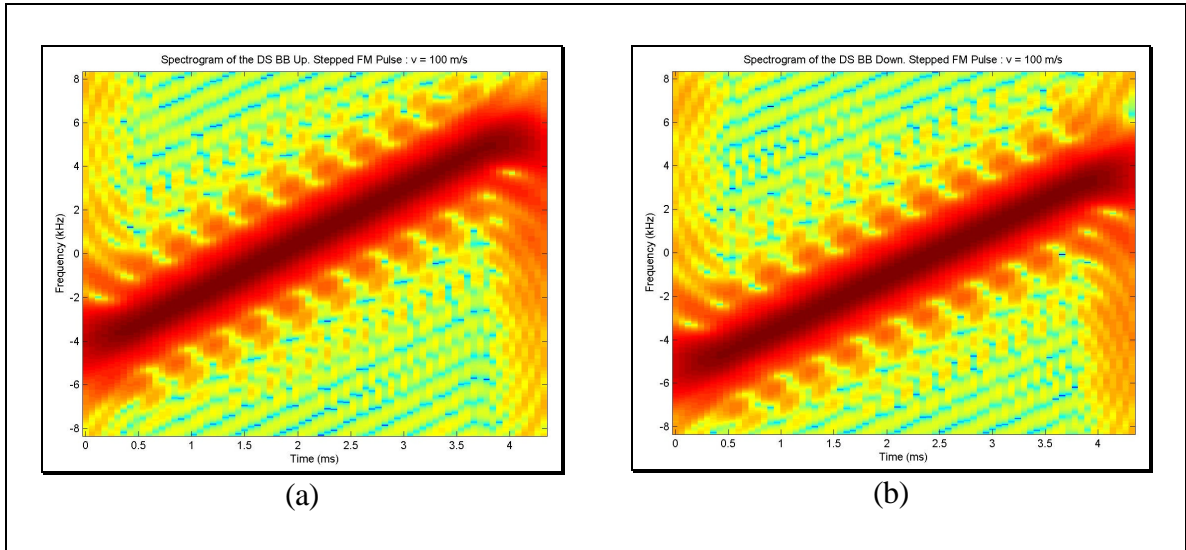
Figure 3.19. Spectrogram of the Simulated, Down Sampled, Filtered, Basebanded, (a) Doppler Upshifted and (b) Doppler Downshifted, Quadrature Sampled Stepped FM Pulse.
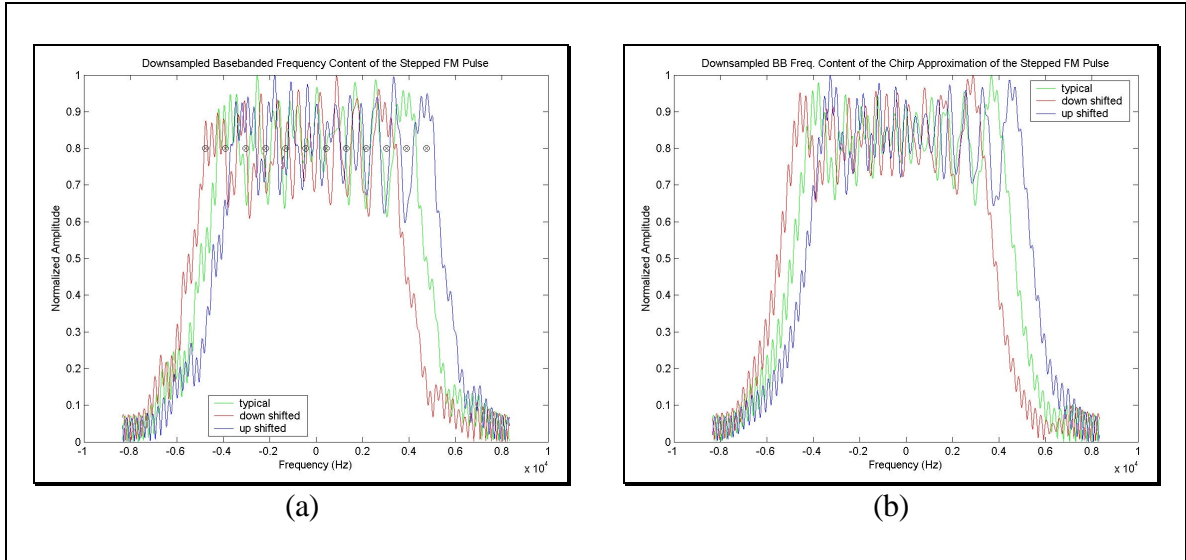
Figure 3.20. Nominal and Doppler Shifted Frequency Spectra of the Simulated, Down Sampled, Filtered, Basebanded, Quadrature Sampled… (a) Stepped FM Pulse, (b) Chirp.

3.2   Actual Signals

3.2.1   Stepped FM in the Transmission Pulse and Bottom Returns

The simulations in previous sections show steps that lead to the formation of the data that is contained in the received data sets. This section focuses on the appearance of what is believed to be the transmission portion of the measured data. This data occurs at the beginning of the time sequence of data for each ping and is several times stronger than the specular bottom return.

Figure 3.21 shows the spectrogram of the data received by beam 14 for a sample ping named sand3688 in a data set recorded during sea tests over a sandy seafloor. It is the receive beam direction closest to normal incidence backscatter from a nominally horizontal seafloor plane. A closer inspection of the first 80 ms in the time series (Figure 3.22) clearly shows the single-sided basebanded stepped FM pulse in both the

transmission pulse [0ms,5.5ms] and the bottom reflection [58ms,64ms]. Fainter replicas can also be seen throughout the rest of the data from multipath and scattering layers. The returns between 0.02 seconds and 0.03 seconds result from the sidelobes of the receive beam pattern in the direction of the sea surface. The transition around 0.3 seconds in Figure 3.21 is the result of the transition from VOL SR mode to VOL LR mode. The removal of this transition gain is discussed in Chapter 4. The faint broadband signal around 0.48 seconds is the result of some system noise that occurs at this time in every ping. The signal around 0.14 seconds is a bottom-to-surface to-bottom reflection.
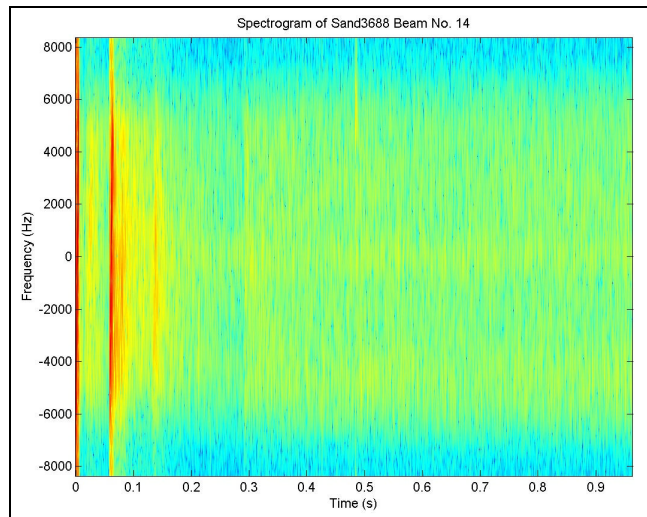
Figure 3.21. Spectrogram of Measured Data from Sand3688 Beam No. 14.
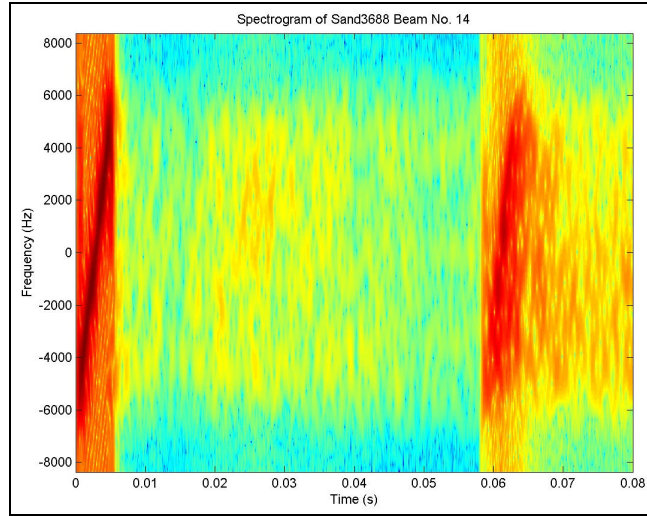
Figure 3.22. Spectrogram of Measured Data from Sand3688 Beam No. 14: Transmission Pulse and Bottom Reflection.

The close-up view of the transmission portion of the signal (sand3688 beam 14) in Figure 3.23 shows a distinct replica of the transmission pulse [0.7ms,5.0ms] with loss of signal strength at different times for different frequencies. There is also some noise immediately following the transmission pulse, which may be caused by reverberation at the face of the array. The same signal is shown for sand3688 beam 17 in Figure 3.24. Beam 17 is the forward beam for one of the beam pairs roughly 21.5° away from the fore-aft vertical plane. Although the signal strengths of these two beams from ping sand3688 vary in intensity with respect to each other, the stepped FM pattern is quite visible in each. Figure 3.25 shows the results from beam 14 of sample ping mud4000, which was measured during sea tests over a muddy seafloor. Comparison of this image with Figure 3.23 from beam 14 of sand3688 shows definite ping-to-ping repeatability within the system. However, while some of the signal after 5.5 ms resembles the possible reverberation signal in the sand3688 - beam 14 data, two scattering layers appear roughly 2 ms and 7.5 ms after the transmission pulse. The corresponding scatterers are most likely bubbles.
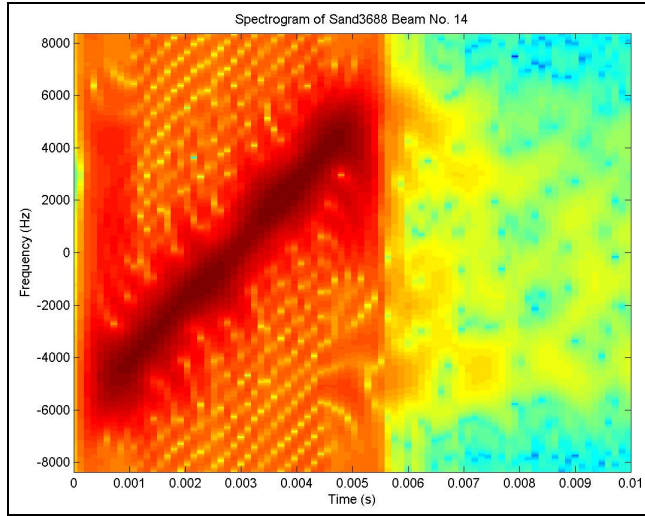
Figure 3.23. Spectrogram of the Transmission Pulse from the Measured Data in Sand3688 Beam No. 14.
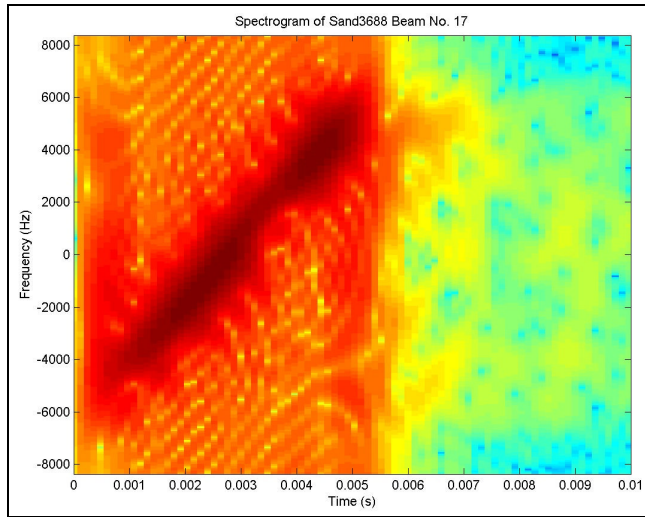
Figure 3.24. Spectrogram of the Transmission Pulse from the Measured Data in Sand3688 Beam No. 17.
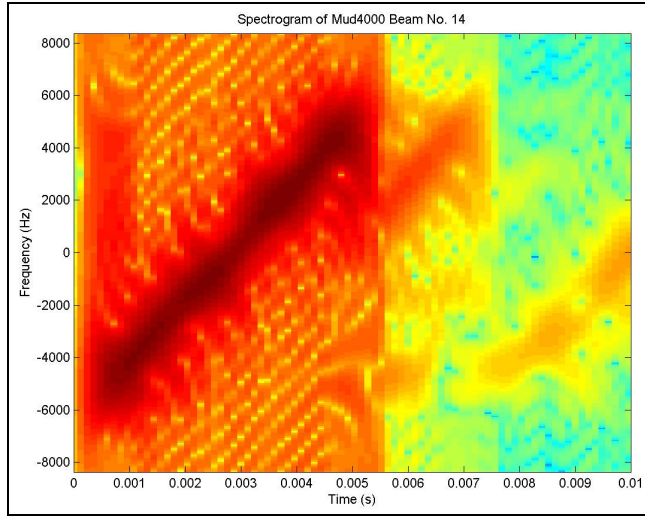
Figure 3.25. Spectrogram of the Transmission Pulse from the Measured Data in Mud4000 Beam No. 14.

3.2.2 Transmission Reverberation Distortions

Figure 3.26 through Figure 3.28 show comparisons between the transmission pulse portions (roughly equivalent to the time interval [0,5.5ms] in Figure 3.23 through Figure 3.25) of two pings from different data sets (sand3688, mud4000) in both the time and the frequency domains. Unlike the simulated spectra shown in Figure 3.9 and Figure 3.17, which are nearly symmetrical about 0 Hz, the frequency domain responses shown in Figure 3.26 are not symmetrical about 0 Hz. The amplitudes in this portion of the data appear to have undergone non-linear compression, which is probably due to saturation of the receiver by the high transmission power level. This compression varies from beam to beam as shown in Figure 3.27. However, it does not appear to vary from ping to ping. Since the transmission signal increases in frequency with time, the amplitude increase versus time results in an amplitude increase versus frequency. The variations in compression between the forward beams (1:27) and the rear beams (28:54) are of concern because they affect the quality of the matched filter response (Chapter 4) and do not yet

76

have a known cause. The phase (Figure 3.28) appears to wrap steadily with increasing time during each ping as expected from Figure 3.10. However, there are some unexpected variations across the beams where uniform phase is expected for any particular sample time. These variations may be the result of the compression, an element failure, some other phenomenon or a combination thereof. Note the phase variations from one ping to the next, which are also of concern, because the output is biased by the variable phase shift that exists at the beginning of the transmission pulse [Coo63].
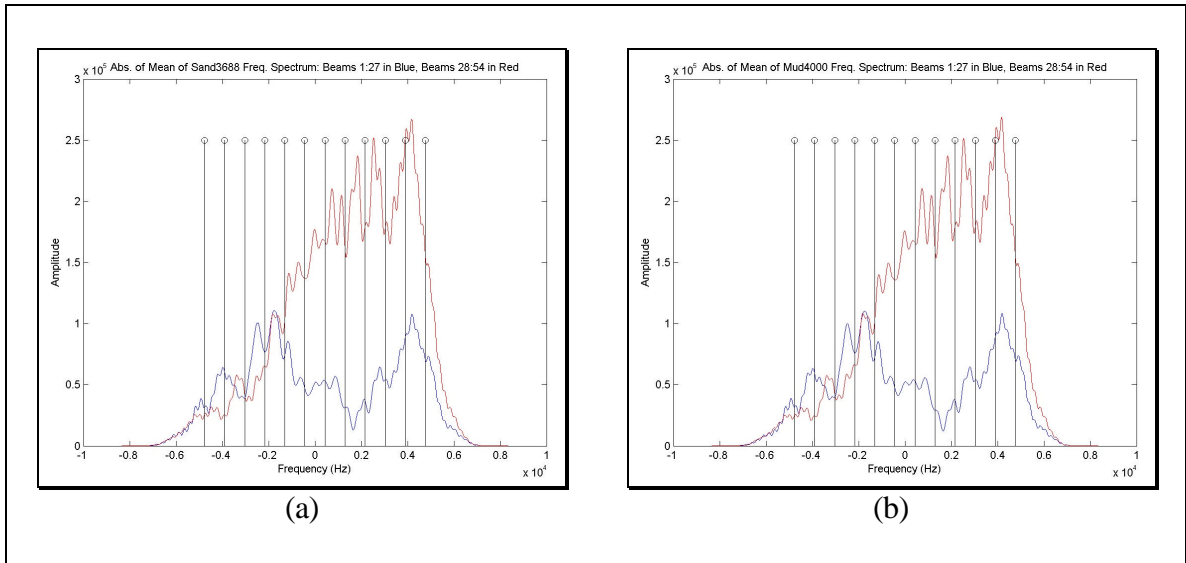
Figure 3.26. Absolute of the Mean of the Frequency Spectra of Beams 1 to 27 (in Blue) and Beams 28 to 54 (in Red) for the Transmission Pulse in the Measured Data: (a) Sand3688, (b) Mud4000.
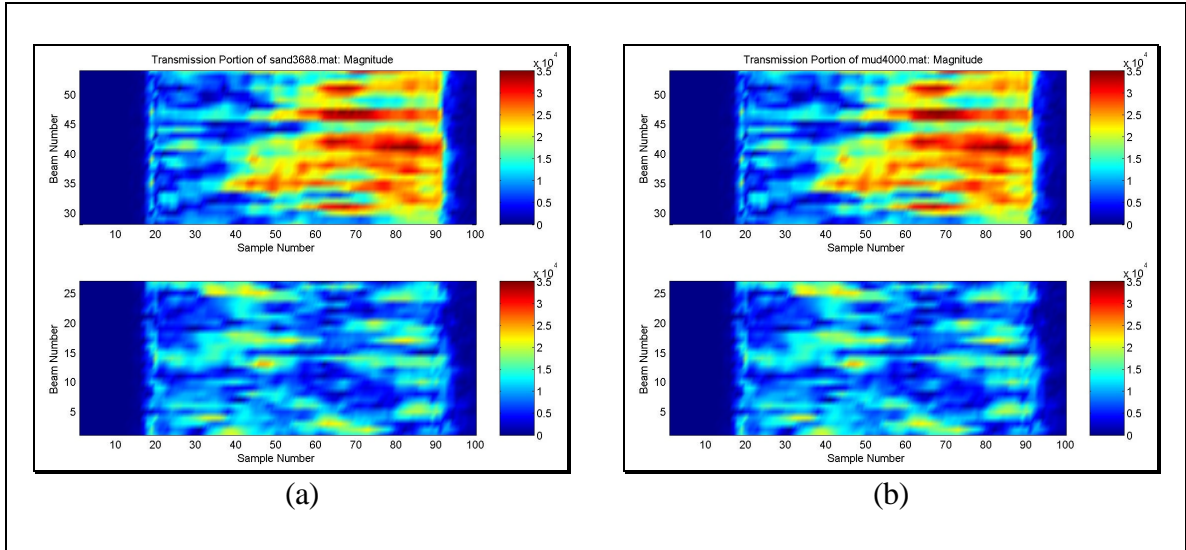
Figure 3.27. Magnitude of the Transmission Pulse in the Measured Data: (a) Sand3688, (b) Mud4000.
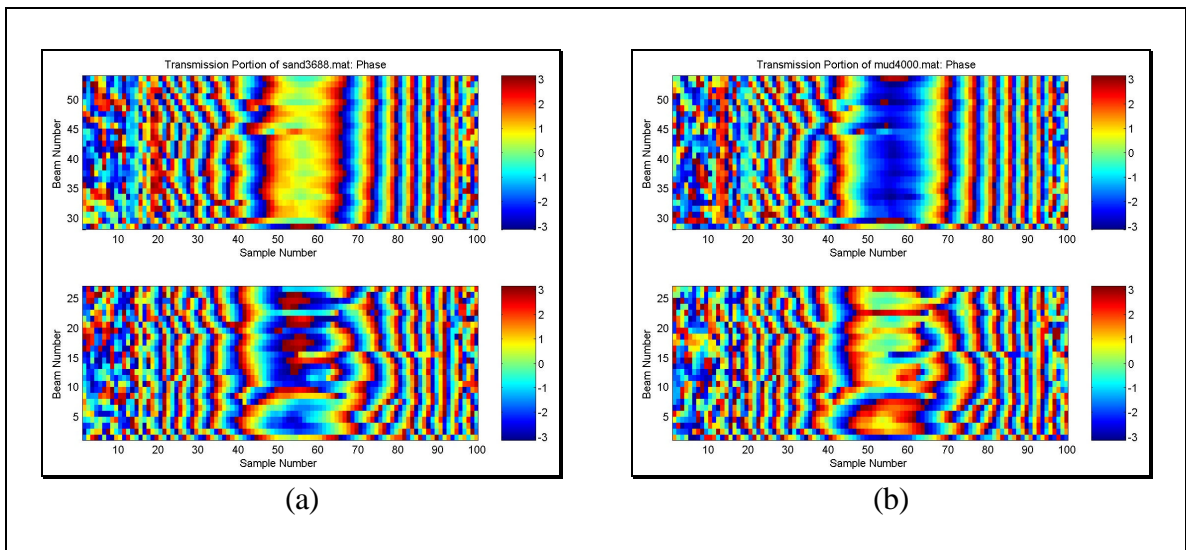
Figure 3.28. Phase of the Transmission Pulse in the Measured Data: (a) Sand3688, (b) Mud4000.

In order to determine whether the amplitude variations shown versus time and beam number were the result of transmission and reception or of some other phenomenon, such as non-linear compression due to relatively large magnitudes compared to the bottom returns, the bottom returns for each beam of each ping were aligned using the initial reflections of the near-nadir beams and the assumption of a seafloor with a horizontal across-track slope. Although the result of this alignment

78

contained higher reflective levels in the rear beams, like those seen in the transmission portion of the signals (Figure 3.27), they were inconclusive in determining whether the cause was from the signal itself, from the pitch of the towed body or from some other phenomenon.

3.3 <u>Summary</u>

This chapter shows two theoretical methods by which a quadrature basebanding process can be used to place the center frequency of a broadband signal at 0 Hz without corrupting it. Basebanding simulations for the stepped FM pulse indicate that it is a good approximation to the linear FM chirp (at least as far as the magnitudes of the frequency spectra are concerned), which is the optimal combination of high bandwidth, high range resolution and single filter phase matching [RW61]. Since the stepped FM signal does not have the "rectangular" spectrum amplitude of the linear FM pulse, its range resolution is inferior to that of the linear FM pulse [RW61]. However, since only six time domain samples are taken at each frequency, the deterioration in range resolution is insignificant. In addition to the magnitude approximation, the parabolic phase shift (versus frequency) that the linear FM signal has is approximated in the stepped FM signal to allow pulse compression (Section 4.3) to work correctly in the presence of Doppler shifts [RW61]. Using the assumption of an ideal linear FM signal, the best case increase in the SNR resulting from the pulse compression process is equal to the time-bandwidth product of the signal as defined by the following expression [CB67]:

$$10 \cdot \log_{10}(T \cdot \Delta f) = 10 \cdot \log_{10}(4.32ms \cdot 10.2kHz) \approx 10 \cdot \log_{10}(44.0) \approx 16.4dB \quad (3.3)$$

The sample measured results indicate that the system is non-ideal in its physical implementation. This is shown by the signal's variations in phase from ping to ping, resulting from a floating time base, and by variations in the signal's magnitude and phase from beam to beam, presumably due to the non-uniform nature of the transducers. Since the range resolution of a stepped FM signal is directly related to the quality of the pulse compression, these variations deteriorate the system range resolution.

CHAPTER 4

MONOPULSE

4.1 <u>Introduction</u>

As discussed in the introduction, monopulse techniques are used to improve angle of arrival estimates by comparing adjacent beams in various ways. Figure 4.1 shows three such techniques. The methods to be reviewed here are referred to as conjugate product (CP), difference-over-sum (DS) and narrow beam (NB). The names of the first two are derived from the forms of their respective mathematical expressions, and the name of the third type (NB) is derived from the reduction in beam width that is produced by this method [Rho59]. Both the CP and the NB techniques place a beam at the center of the pair of beams (assuming no distortion and similar beams). The DS technique, however, places a null at the center of the beams. The phase responses of these techniques will be described later in this report. Equations (4.1) through (4.4) expand the three monopulse expressions to include the phase terms where $\boldsymbol{f}_A$ and $\boldsymbol{f}_B$ are the phases of the signals measured on beams A and B respectively. These are discussed further in Appendix B.
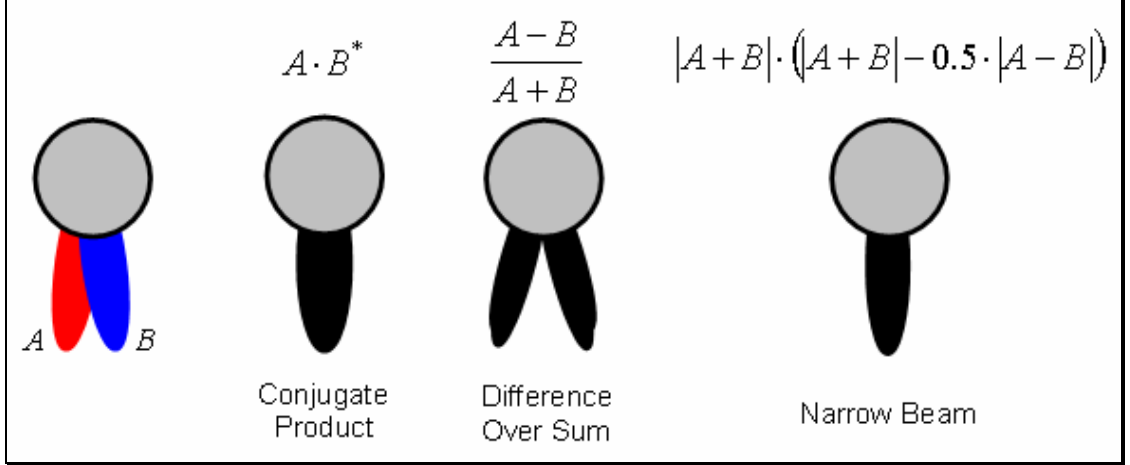
Figure 4.1. Monopulse Techniques.

$$CP = A \cdot B^* = |A||B| \cdot \exp\left(j(f_A - f_B)\right) \tag{4.1}$$

$$DS = \frac{A-B}{A+B} = \frac{|A| \cdot \exp(jf_A) - |B| \cdot \exp(jf_B)}{|A| \cdot \exp(jf_A) + |B| \cdot \exp(jf_B)} \tag{4.2}$$

$$DS = \sqrt{\frac{\left[|A|^2 + |B|^2\right] - 2|A||B|\cos(f_A - f_B)}{\left[|A|^2 + |B|^2\right] + 2|A||B|\cos(f_A - f_B)}} \angle \tan^{-1}\left(\frac{2|A||B|\sin(f_A - f_B)}{|A|^2 - |B|^2}\right) \tag{4.3}$$

$$NB = \left\| |A| \cdot \exp(jf_A) + |B| \cdot \exp(jf_B) \right\| \\ \cdot \left(\begin{array}{c} \left\| |A| \cdot \exp(jf_A) + |B| \cdot \exp(jf_B) \right\| \\ -0.5 \cdot \left\| |A| \cdot \exp(jf_A) - |B| \cdot \exp(jf_B) \right\| \end{array} \right) \tag{4.4}$$

Since the results of LR and SR modes are quite similar and the majority of the target echoes are in the SR portion of the data, for brevity only the SR mode is covered in detail in the remaining simulations in this chapter.

Prior to further discussing these three monopulse techniques, the format of the measured data from a single ping and the required pre-processing steps will be covered.

4.2   The Data from a Single Ping

Figure 4.2 and Figure 4.3 show the magnitude and phase for the measured data of sample ping sand3688 in both grid and rough positional formats.   The grid format displays the time sequence of beam measurements versus beam number. Two-way travel time has been converted into a rough distance estimate using a sound speed of 1500 m/s. The rough positional format places the time sequence of data from each beam along its theoretical maximum response axis. This method assumes a homogeneous medium (i.e. no ray tracing), a sound speed of 1500 m/s, nominal towed body orientation and a towed body depth of 9.5 meters (roughly the mean value of the sample data). Throughout this document, the 'normalized' magnitude data is normalized with respect to the maximum value occurring between time samples 200 and 5000. This corresponds to roughly 10 m to 220 m from the towed body. These values were chosen based on the particular data set of interest.   This normalization is used only for generating figures.   Thus its lack of robustness is not important here.

The grid format is optimal for performing computations and investigating phenomena that are coherent in time.   The rough positional format is preferred for investigating spatially coherent phenomena, e.g. bottom reflections.   This format may also be preferred for human perception of anomalies in the data, e.g. targets in unexpected locations.   In both formats, the phase plots appear to be random noise. However, one might perceive a slight increase in yellow in the area of the bottom echoes. The quality of the phase data is one of the major issues addressed by the monopulse techniques.

(a)   (b)
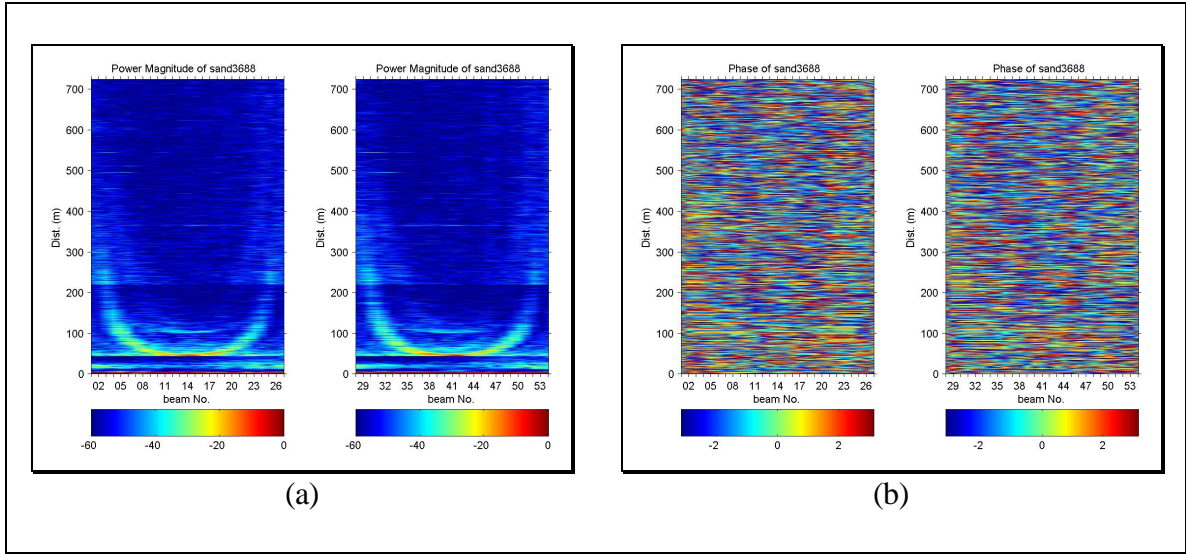
Figure 4.2. sand3688 (Grid Format): (a) Normalized Magnitude in dB, (b) Phase in Radians.

(a)   (b)
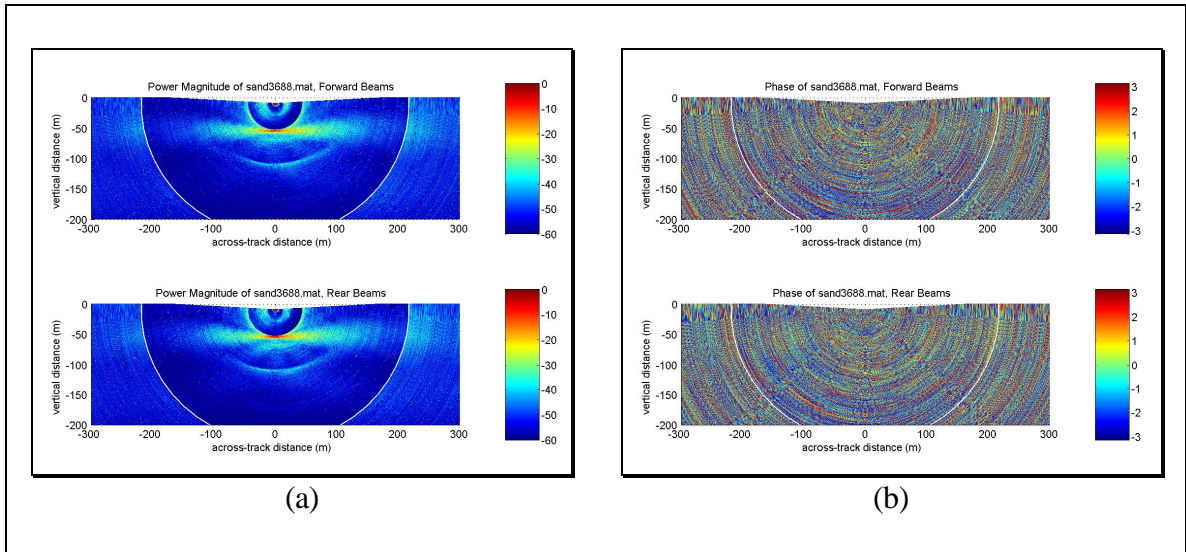
Figure 4.3. sand3688 (Rough Positional Format): (a) Normalized Magnitude in dB, (b) Phase in Radians.

Figure 4.4 shows the forward beams of Figure 4.3 (a) with labeling of significant targets. The distinctive semicircle of gain increase corresponds to the transition from VOL SR mode to VOL LR mode as was seen in the data of Figure 3.21. This corresponds to the straight line at roughly 210 m in Figure 4.2 (a). Figure 4.3 (a) clearly shows the bottom reflection (B) as a relatively linear horizontal stripe at roughly 55 m depth. This is shown as a 'u' shaped area in Figure 4.2 (a). The semicircular ring just

84

touching the bottom reflection in Figure 4.3 (a) is the initial bottom reflection at nadir being received by the sidelobes of the other beams. In Figure 4.2 (a) this appears as a straight line at 55m. Further down in Figure 4.3 (a), the first bottom multiple (BSB) reflection appears at roughly 110m depth. Figure 4.2 (a) reveals that this is the multiple of the nadir specular return and its sidelobes. The multiple of the other bottom returns is visible only in Figure 4.2 (a) as a fainter 'u' inside of the primary one. Other features in Figure 4.3 (a) are the sidelobes of the surface return (S), the surface-to-bottom multiple, and the transmission pulse and its reverberation (R).
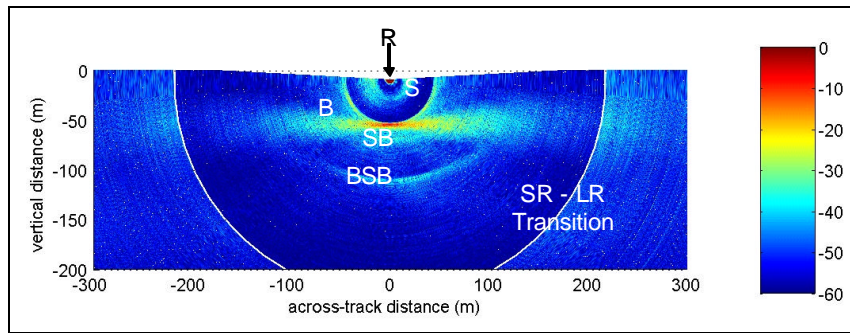
Figure 4.4. Normalized Magnitude of the Forward Beams of sand3688 in dB (Rough Positional Format) with Target Labeling.

4.3   Pre-Processing

4.3.1   VOL SR to VOL LR Transition Gain

The first issue to be addressed in preparing the data for monopulse processing is the gain change that occurs between VOL SR and VOL LR modes. This transition involves the change from beamforming with five elements per stave to beamforming with nine elements per stave. This transition provides a raw increase in signal strength of 1.8 times from SR mode to LR mode. Applying this level of amplitude gain reduction to the LR portions of the data (sample numbers 4881 to 16080 for each ping to be exact)

resulted in equalization of the noise floor between these two regions. However, in order to equalize the bottom returns through the main lobes of the beam patterns, the increase in directivity from SR to LR also has to be taken into account. For simplicity's sake, this was estimated to be $\sqrt{2}$, i.e. 3 dB. The combined effect is a reduction of the LR data by 2.55 times the pressure value or 8.11 dB. Figure 4.5 shows the data from sample ping sand3688 with '4881' scaling applied. Note how the magnitude transition shown in Figure 4.3 (a) is no longer visible.
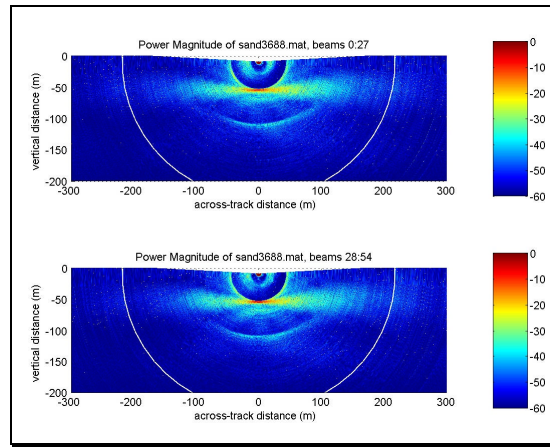
Figure 4.5. Normalized Magnitude of sand3688 in dB with SR-LR Correction Applied (Rough Positional Format).

4.3.2 High Pass Filter to Remove Near-DC Noise

It was discovered that some extra near-dc components were corrupting the signal as shown in Figure 4.6. A high pass filter was created that would pass all frequency components of the stepped FM pulse (shown as black lines) while reducing the near-dc signal components. The closest components of the basebanded signal are at ± 433 Hz. The magnitude and phase of the high pass filtered data are shown in Figure 4.7 (a) and Figure 4.7 (b). There is no perceptible visual difference between these plots and those from before the high-pass filtering. Note also from Figure 4.6 that the signal portion of

the spectrum already occupies nearly the entire spectrum at the 16.667 kHz sampling rate. Thus, low pass filtering can not be used for noise reduction.
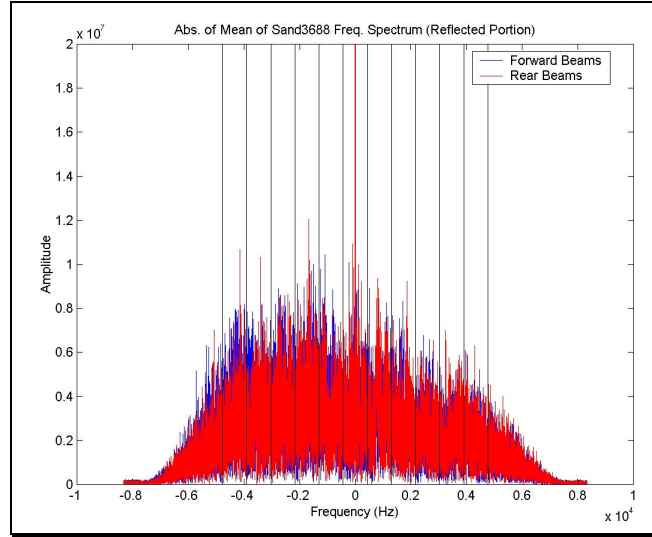
Figure 4.6. Spectrum of the non-Transmission Pulse Portion of the Average (Across Beams) Absolute of the Mean of sand3688.
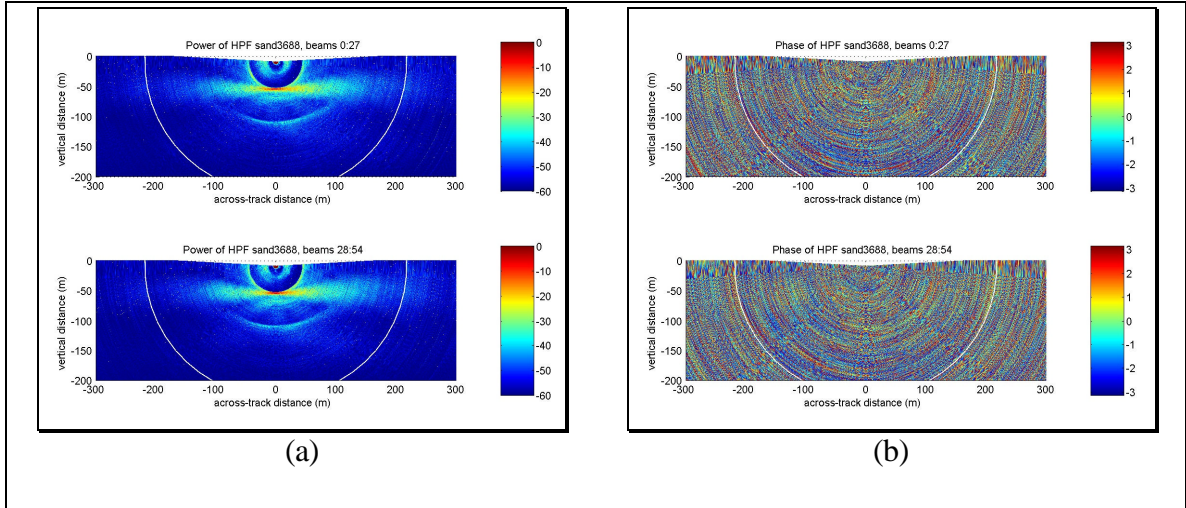
Figure 4.7. sand3688 with High-Pass Filtering Applied (Rough Positional Format): (a) Normalized Magnitude in dB, (b) Phase in Radians.

4.3.3   Pulse Compression via Matched Filtering

In order to improve the detection algorithms, the measured data is pulse compressed using the theoretical stepped FM transmission signal.   The theoretical

transmission pulse was provided as a data file with seventy-two complex (quadrature) samples. Figure 4.8 and Figure 4.9 illustrate that this signal is a stepped FM approximation to a down-chirp with phase that decreases away from 0 Hz. However, inspection of Figure 3.22 through Figure 3.25 and Figure 3.28 show that the measured data is a stepped FM approximation to an up-chirp with phase that increases away from 0 Hz.
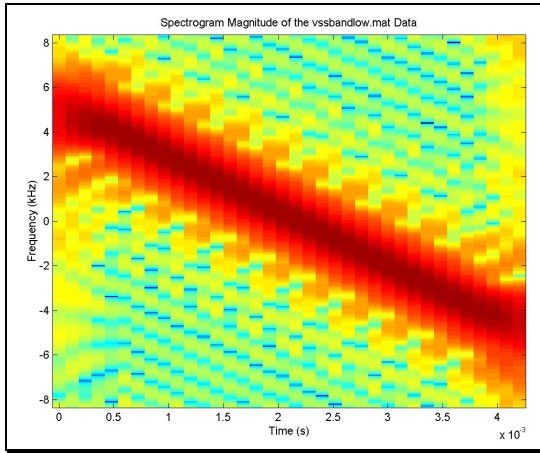
Figure 4.8. Spectrogram of the Theoretical
Transmission Pulse.
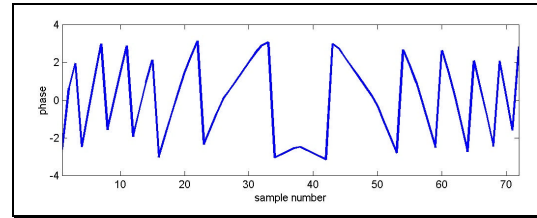
Figure 4.9. Phase in Radians of the
Theoretical Transmission Pulse.

From the magnitude patterns alone, one would assume that pulse compression could be carried out using a convolution process since this provides the necessary time reversal to align the theoretical transmission pulse with the measured data that a correlation process would not provide. However, this still leaves the problem of the inverted phase wrapping. For a real signal with a double-sided spectrum, this would present a very difficult problem, but for the single-sided signal the phase can be inverted by taking the conjugate of the theoretical transmission pulse. Because of the nature of the single sided signal centered at 0 Hz, this conjugation also reverses the spectrum about 0 Hz. This will be perfectly clear if the signal at any instant is thought of as a complex exponential, $\exp(i2\pi f t + g)$. Thus, when this conjugation is performed, the theoretical

88

transmission pulse takes on the form of the measured data as shown in Figure 4.10 and Figure 4.11. Note that the spectrogram of the conjugated theoretical transmission pulse has the same intensity variations along the sides of the main signal that were seen in simulation. Additionally, the phase plot closely resembles the phase plot of the simulated transmission pulse shown in Figure 4.12 (repeated from Figure 3.10).
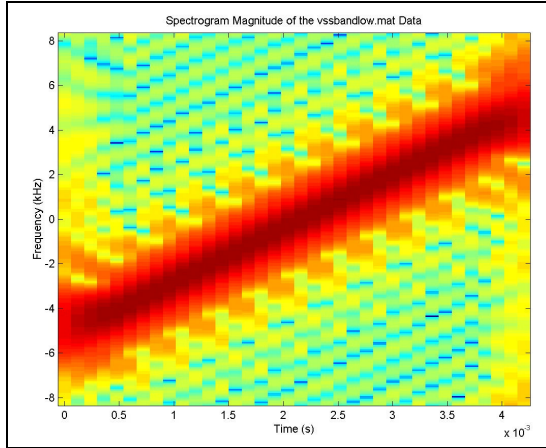
Figure 4.10. Spectrogram of the Complex Conjugate of the Theoretical Transmission Pulse.
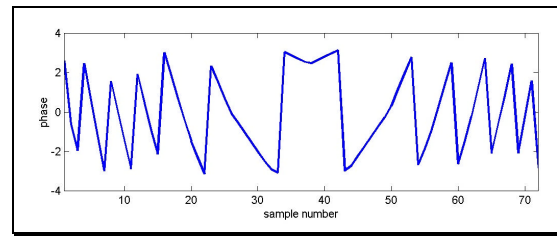
Figure 4.11. Phase in Radians of the Complex Conjugate of the Theoretical Transmission Pulse.
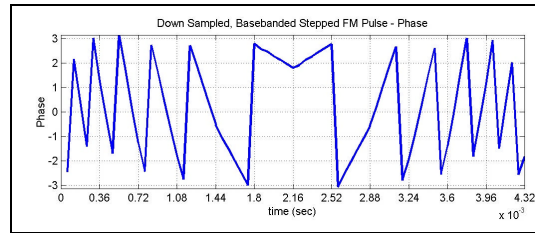
Figure 4.12. Phase in Radians of the Simulated, Down Sampled, Filtered, Basebanded, Quadrature Sampled Stepped FM Pulse.

The conjugated theoretical transmission pulse is used to pulse compress the measured data using a correlation function. Figure 4.13 shows the results of this method of pulse compression on the measured transmission pulse of Figure 3.23. The 'X' shaped energy remaining on either side of the compressed signal results from a mismatch between the theoretical transmission pulse and the measured data. In practice, the time sample at the middle of the pulse compression is then chosen as time zero. Thus, a

measure of the time at the peak of the pulse compressed seafloor echo will be relative to that of the outgoing transmission pulse.
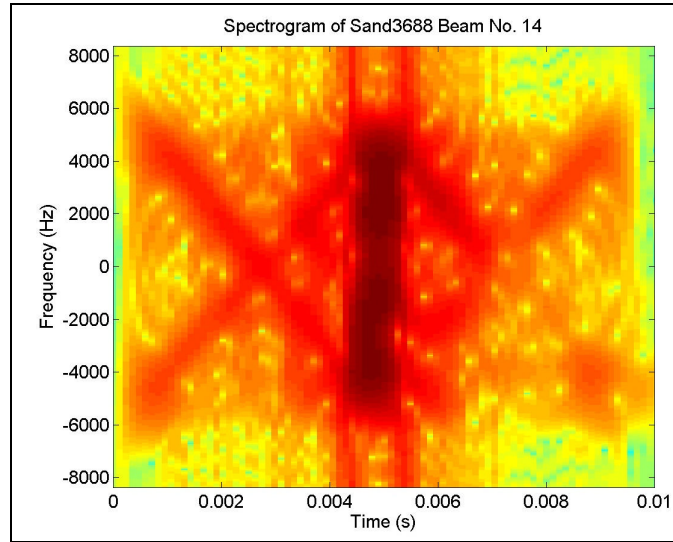
Figure 4.13. Spectrogram of the Pulse Compressed Transmission Pulse from the Measured Data in Sand3688 Beam No. 14.

Figure 4.14 (a) and Figure 4.14 (b) show the result of applying pulse compression to the high-pass filtered data in Figure 4.7 (a) and Figure 4.7 (b). Careful inspection of the magnitude plots from these two stages reveals that the target echoes are definitely reduced in time extent by the pulse compression. Additionally, since the near-specular returns match the theoretical signal better than the returns from broad grazing angles, the relative magnitudes of echoes away from nadir are reduced. Careful inspection of the phase plots reveals no more information content after pulse compression than was present previously.
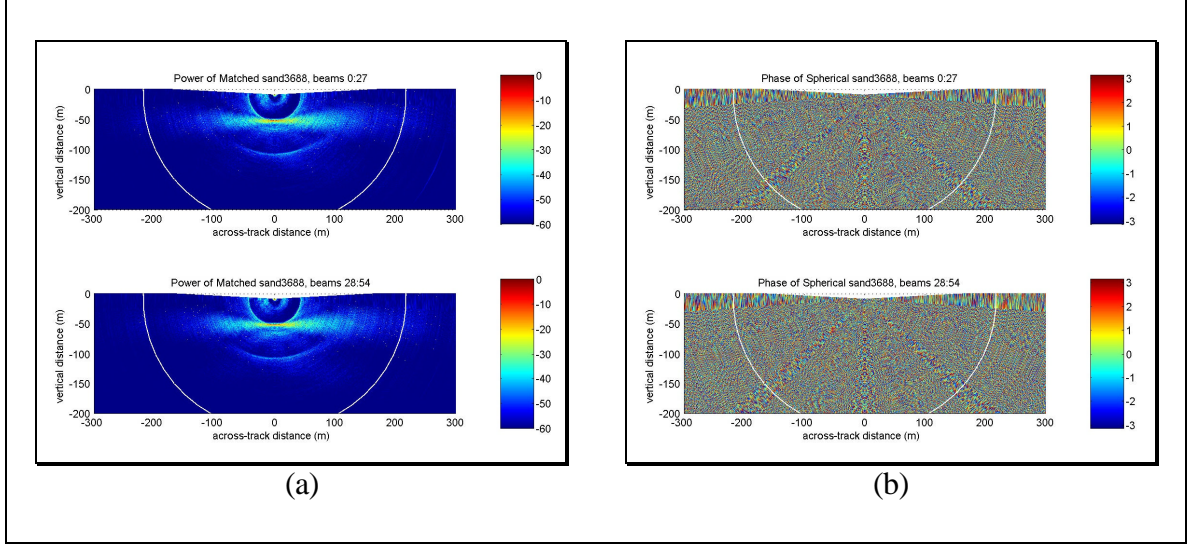
Figure 4.14. Matched sand3688 (Rough Positional Format): (a) Normalized Magnitude in dB, (b) Phase in Radians.

4.3.4 Spreading Loss Correction

One last correction has to be made prior to applying monopulse techniques to the data. Because of spreading loss, the magnitude of the data is reduced by $10 \cdot \log_{10}\left(R^2\right)$ for each direction of travel where R is the traveled distance. However, there is also a backscattering strength proportional to $10 \cdot \log_{10}(R)$. Thus the total spreading loss correction is

$$10 \cdot \log_{10}\left(R^2\right) + 10 \cdot \log_{10}\left(R^2\right) - 10 \cdot \log_{10}(R) = 30 \cdot \log_{10}(R) \tag{4.5}$$

Applying this correction brings the echo strength into a more uniform level as range increases. However, it also increases the noise at long ranges. The monopulse techniques will help to reduce some of this noise since the noise is uncorrelated. One other benefit of the spreading loss correction for bottom detection is that the portion of the data containing the transmission pulse is significantly reduced to the extent that it no longer interferes in detection schemes.
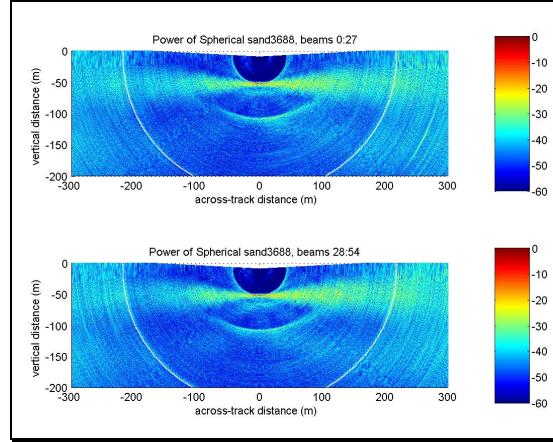
Figure 4.15. Normalized Magnitude of Matched sand3688 in dB with Spreading Loss Correction Applied (Rough Positional Format).

4.4   Conjugate Product

4.4.1   Theoretical Analysis

Prior to investigating the results of applying monopulse processing to the measured data, simulations of the techniques are carried out using the beam pattern and cross-section techniques from Chapter 2. Recall that the equation for combining adjacent beams is $A \cdot B^*$ for CP monopulse processing. As the name implies, this technique multiplies the field from one beam by the complex conjugate of the field from the other beam.

The beam pattern and primary cross-sections of the CP for VOL SR, along-track beam pair 14 (near nadir) are shown in Figure 4.16 through Figure 4.18, and the beam pattern for all twenty-seven such beams is shown in Figure 4.19. As expected, a beam is created in the center of the beam pair. However, it has two major along-track sidelobes. These can be traced back to the sidelobes of each beam that pointed in the direction of the maximum response axis of its fore-aft neighbor as seen in Figure 2.23 and Figure 2.24.

92

Since each of the input beams have similar across-track beam patterns, the CP across-track slice resembles that of the VOL SR product beams.
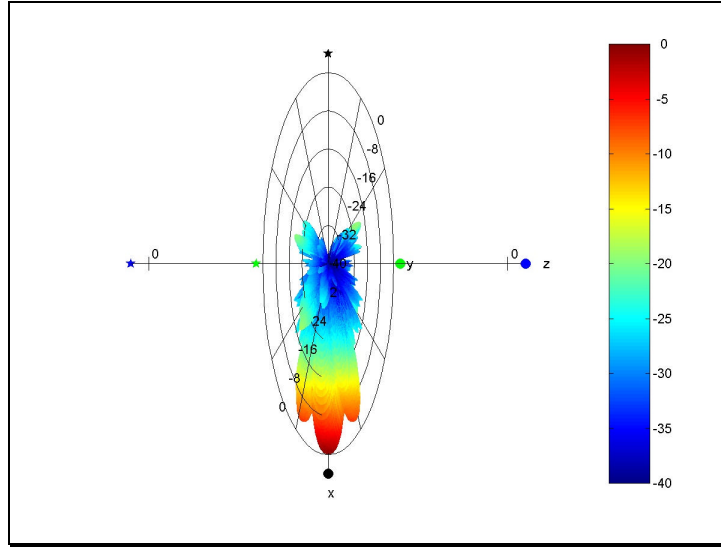
Figure 4.16. Normalized Conjugate Product Beam Pattern – Along-Track (Beams 14 & 41), VOL SR – 37.5 kHz.

Figure 4.17. Normalized Conjugate Product Beam Pattern Across-Track Slice ($q = 90°$) – Along-Track (Beams 14 & 41), VOL SR Mode (Nadir At $(q = 90°, f = 0°)$) Cylinder Axis Out of Page – 37.5kHz.

Figure 4.18. Lower Half of the Along-Track Slice ($f = 0°$) of the Normalized Conjugate Product Beam Pattern – Along-Track (Beams 14 & 41), VOL SR (Nadir At $(q = 90°, f = 0°)$), Cylinder Along 180° to 0° Axis – 37.5 kHz.

Figure 4.19. Normalized Conjugate Product Beam Pattern – Along-Track, VOL SR for all Beams – 37.5 kHz.

Figure 4.20 and Figure 4.21 show the spherical cross-section magnitude and phase plots respectively for along-track CP VOL SR beam 14, and Figure 4.22 shows the horizontal cross-section for all twenty-seven along-track CP VOL SR beams.[1] Recall

---

[1] A thorough explanation of the orientation of spherical and planar cross-section figures is given in Section 2.3.

from Section 2.3 that not all beams contain strong responses from the seafloor and that the main lobes from all beams are not contained in the visible region of the planar seafloor cross-section. As explained in Chapter 1, a pair of beams that has a common phase center (as this one does) should have no usable phase information. From Appendix B the CP expression reduces to $|A||B|$. In this case, the phase takes the form of a constant $\pm\pi$ radians (interfering sidelobes). Since this pair of beams is created by steering fore and aft, there should be no variations across-track. However, lobe interferences should create $\pm\pi$ radian variations along-track. Thus, the expected phase pattern should look like a series of across-track rings. This is the basic pattern in Figure 4.21. However, there are several areas where this pattern is not maintained. These result from the skewed shape of the array used to create the beams. This array shape causes the forward and rear beams to be inexact mirror images of each other, which results in the variations seen here. Figure 4.20 and Figure 4.22 highlight why the along-track sidelobes are an undesirable phenomenon: they ensonify swaths of the seafloor immediately in front of, and behind the main swath, which passes through nadir. The backscatter strength gain is not included in the simulation plots.

Figure 4.20. Normalized Conjugate Product Spherical Cross-Section in dB – Along-Track (Beams 14 & 41), VOL SR – 37.5 kHz.

Figure 4.21. Conjugate Product Spherical Cross-Section Phase in Radians – Along-Track (Beams 14 & 41), VOL SR – 37.5 kHz.

Figure 4.22. Normalized Along‑Track Conjugate Product Beam Footprints (for all Beams) on a Horizontal Plane at Unit Distance from the Transducer for VOL SR (Viewed from Above) – Units are in Multiples of the Transducer Altitude, Forward ≡ Top of Image (Visibility > 80.5° from Nadir) – 37.5 kHz.

Figure 4.23 shows the horizontal cross‑section of all twenty‑seven along‑track CP VOL LR beams. While the along‑track sidelobes do still exist in these plots, their effect is minimal compared to that of the SR case. This improves the effective spatial resolution of the LR results over the SR results for the along‑track CP beams.

Figure 4.23. Normalized Along‑Track Conjugate Product Beam Footprints (for all Beams) on a Horizontal Plane at Unit Distance from the Transducer for VOL LR (Viewed from Above) – Units are in Multiples of the Transducer Altitude, Forward ≡ Top of Image (Visibility > 80.5° from Nadir) – 37.5 kHz.

Figure 4.24 through Figure 4.26 show the VOL SR CP beam patterns for across‑track beam pairs. Comparison of these beam patterns with those of the combined transmit and receive beams shows no significant benefit other than creating beams in new directions. Figure 4.27 through Figure 4.29 show the various cross‑sections plots for the VOL SR CP across‑track beam pairs. The black circles in these figures pass through the theoretical maximum response axes of the beams shown. This arrangement is used throughout the remainder of this chapter wherever such circles appear. This is where the

true benefit of this technique is revealed. Since across-track beam pairs do not have common phase centers, the CP beams do not have constant phase. Rather, they have gradual phase shifts through the CP beams' maximum response axes. This is shown in Figure 4.28 where the color map has been shifted to emphasize the zero crossing. Thus a detection scheme could be built to look for the zero crossing of a gradual phase shift within the main lobe of the CP beam in order to determine the angle of arrival.
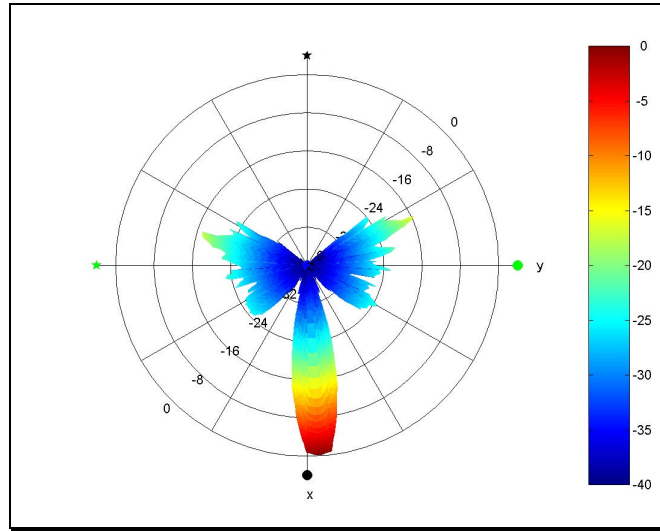
Figure 4.24. Normalized Conjugate Product Beam Pattern – Across-Track (Beams 13 & 14 (fore) and 40 & 41 (aft)), VOL SR, Front View Cylinder Axis Out of Page – 37.5 kHz.
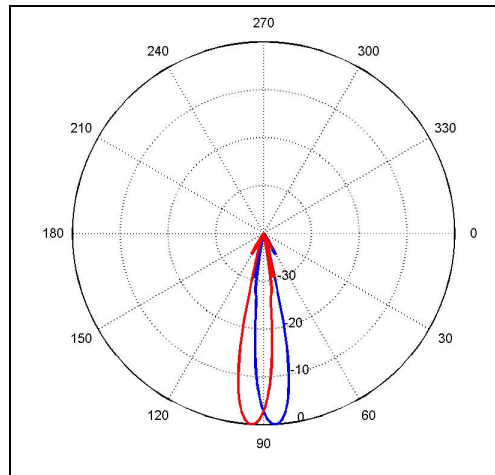
Figure 4.25. Lower Half of the Along-Track Slice ($f = 3.58°$) of the Normalized Conjugate Product Beam Pattern – Across-Track (Beams 13 & 14 (fore) and 40 & 41 (aft)), VOL SR (Nadir At $\left(q = 90°, f = 0°\right)$), Cylinder Along 180° to 0° Axis – 37.5 kHz.
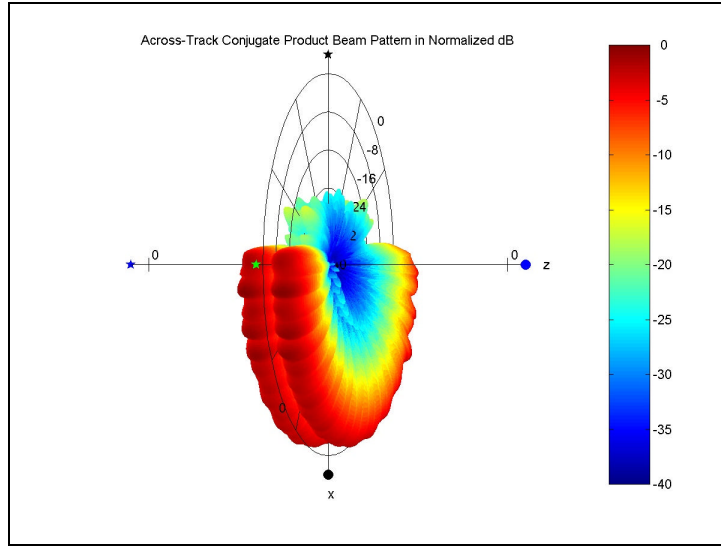
Figure 4.26. Normalized Conjugate Product Beam Pattern – Across-Track, VOL SR for all Beams – 37.5 kHz.
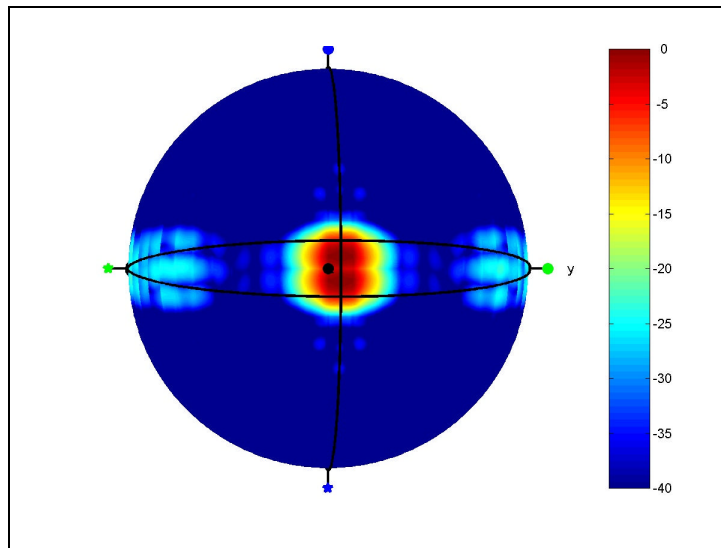
Figure 4.27. Normalized Conjugate Product Spherical Cross-Section Magnitude in dB – Across-Track (Beams 13 & 14 (fore) and 40 & 41 (aft)), VOL SR – 37.5 kHz.
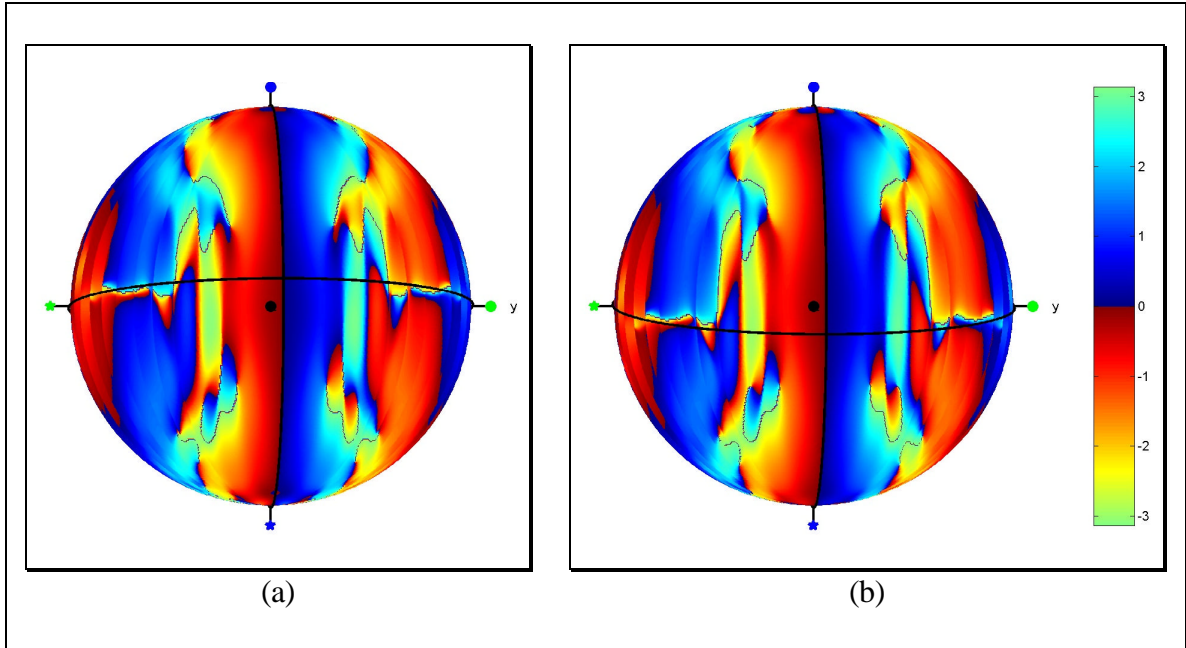
Figure 4.28. Conjugate Product Spherical Cross-Section Phase in Radians – Across-Track, VOL SR – 37.5 kHz: (a) Beams 13 & 14 (fore), (b) Beams 40 & 41 (aft).
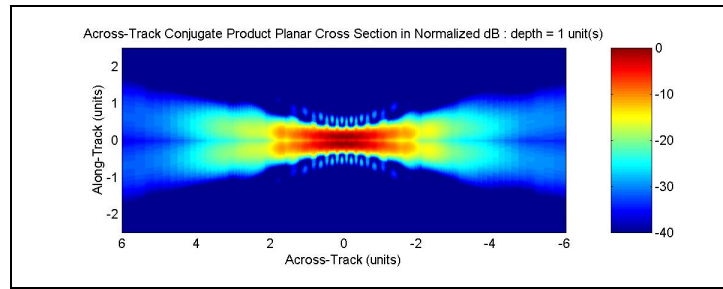
Figure 4.29. Normalized Across-Track Conjugate Product Beam Footprints (for all Beams) on a Horizontal Plane at Unit Distance from the Transducer for VOL SR (Viewed from Above) – Units are in Multiples of the Transducer Altitude, Forward ≡ Top of Image (Visibility > 80.5° from Nadir) – 37.5 kHz.

Figure 4.30 shows the horizontal cross-section of all twenty-seven across-track CP VOL LR beam pairs. Visually, Figure 4.29 and Figure 4.30 show a significant improvement in the effective spatial resolution (footprint size) of the LR results compared to the SR results for the across-track CP beams. As mentioned previously for the SR results, there is really no spatial resolution improvement in the magnitude response for the across-track CP LR results over that of the combined transmit and receive LR results.
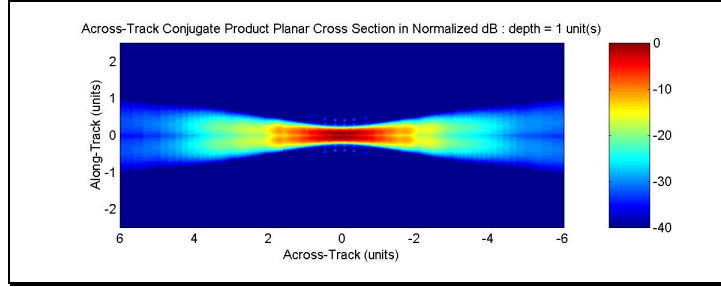
Figure 4.30. Normalized Across-Track Conjugate Product Beam Footprints (for all Beams) on a Horizontal Plane at Unit Distance from the Transducer for VOL LR (Viewed from Above) – Units are in Multiples of the Transducer Altitude, Forward ≡ Top of Image (Visibility > 80.5° from Nadir) – 37.5 kHz.

4.4.2 <u>Sample Results</u>

Figure 4.31 shows the results of applying the CP monopulse technique to along-track beam pairs. As predicted by the simulation, the magnitude response is quite similar to that of the spreading loss corrected data shown in Figure 4.15. While the phase plot appears to relate to the magnitude plot more than previous phase plots did (Figure 4.14 (b)), it contains no usable information. This is expected from the simulations shown above and the common phase center condition for each along-track beam pair.

The magnitude of the CP beams from forward and rear across-track beam pairs shown in Figure 4.32 and Figure 4.33 have the same lackluster quality as the along-track CP beams. However, a distinct transition between light blue and yellow (±1 radian) can be clearly seen in the primary echo returns. This is the gradual phase shift that was predicted by the simulation. The points where this linear phase slope passes through 0° is one estimate of the seafloor location for each CP across-track beam. Note, however, that this technique will not work well for near-specular returns. This is true of all phase comparison techniques because the travel time to each beam phase center is essentially identical for echoes from the near-specular region. Fortunately, this region generally has

101

a strong magnitude response, which makes it well suited to amplitude detection techniques.
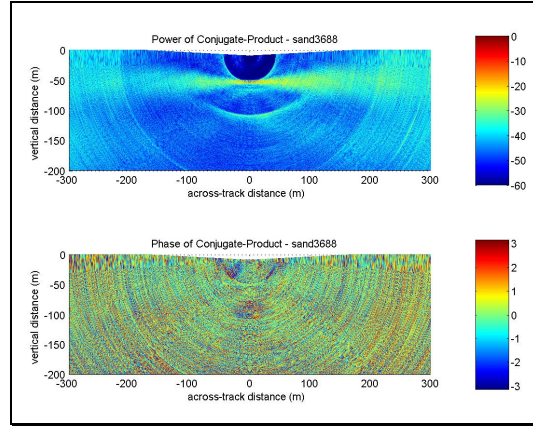
Figure 4.31. Normalized Magnitude in dB and Phase in Radians of the Conjugate-Product of sand3688 for Fore-Aft (Along-Track) Beam Pairs (Rough Positional Format).
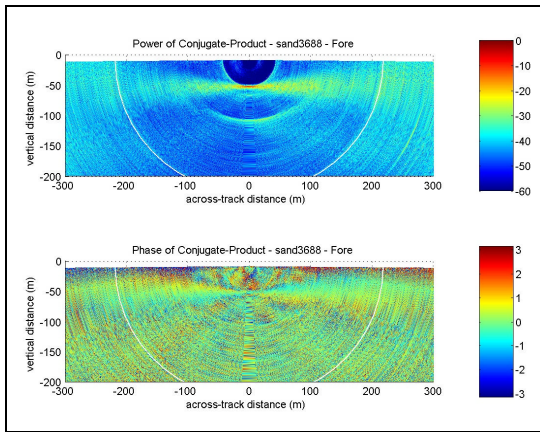
Figure 4.32. Normalized Magnitude in dB and Phase in Radians of the Conjugate-Product of sand3688 for Forward Across-Track Beam Pairs (Rough Positional Format).
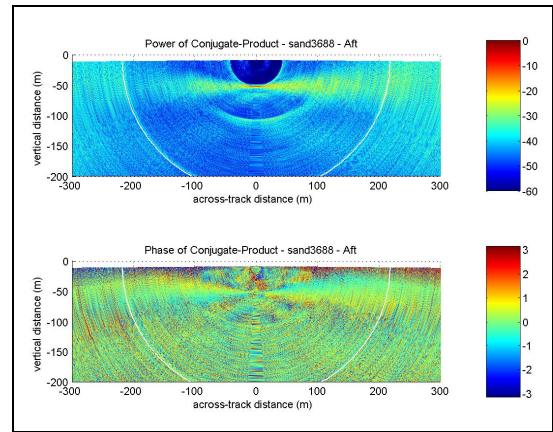
Figure 4.33. Normalized Magnitude in dB and Phase in Radians of the Conjugate-Product of sand3688 for Rear Across-Track Beam Pairs (Rough Positional Format).

4.5   Difference Over Sum

4.5.1   Theoretical Analysis

The difference-over-sum (DS) monopulse technique combines adjacent beams exactly as expected – their difference divided by their sum. Equation (4.3) is repeated here for convenience.

$$DS = \sqrt{\frac{\left[|A|^2 + |B|^2\right] - 2|A||B|\cos(f_A - f_B)}{\left[|A|^2 + |B|^2\right] + 2|A||B|\cos(f_A - f_B)}} \angle \tan^{-1}\left(\frac{2|A||B|\sin(f_A - f_B)}{|A|^2 - |B|^2}\right) \quad (4.6)$$

When a signal is received equally by both beams, the DS output approaches zero for closely spaced beams. A signal which is slightly stronger in one beam produces a result shifted by π radians from that of a signal which is slightly stronger in the other beam (denominator of phase term). The susceptibility of this technique to large errors from spatially separated signals results from the denominator of the magnitude term, which tends toward zero in such a case.

As in the previous case, the simulation data is distorted by the skewed nature of the VSS receive array. In this case, the results are signal spikes that would otherwise not exist in the noise-free simulation. Because a minimum, as opposed to a maximum, is sought in the magnitude pattern, DS beams do not lend themselves to displaying several beams on one plot. As such, only spherical cross-sections are included for DS results as shown in Figure 4.34 through Figure 4.39. The DS result for the along-track beam pair yields a slight across-track null and a corresponding phase inversion area. However the null is not very strong and other areas of the cross-sections contain similar features. The DS beams for across-track beam pairs, on the other hand, have strong, steep along-track

103

nulls and corresponding π-radian phase shifts for both forward and rear across-track beam pairs.
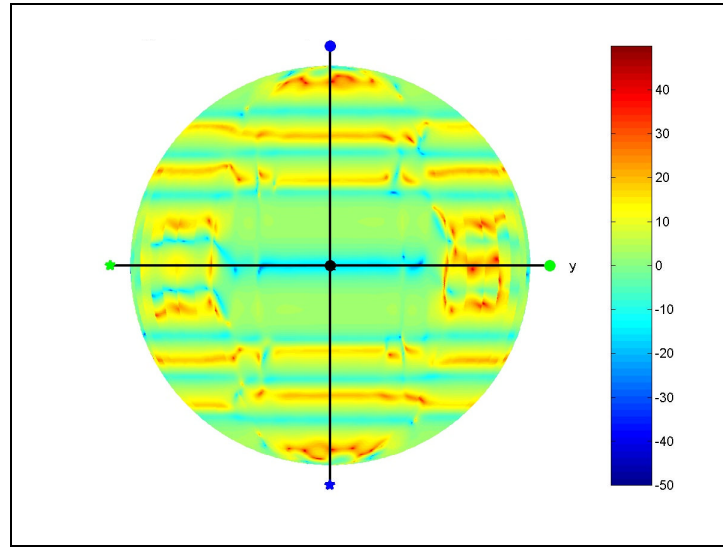
Figure 4.34. Difference-Over-Sum Spherical Cross-Section Magnitude in dB – Along-Track (Beams 14 & 41), VOL SR – 37.5 kHz.
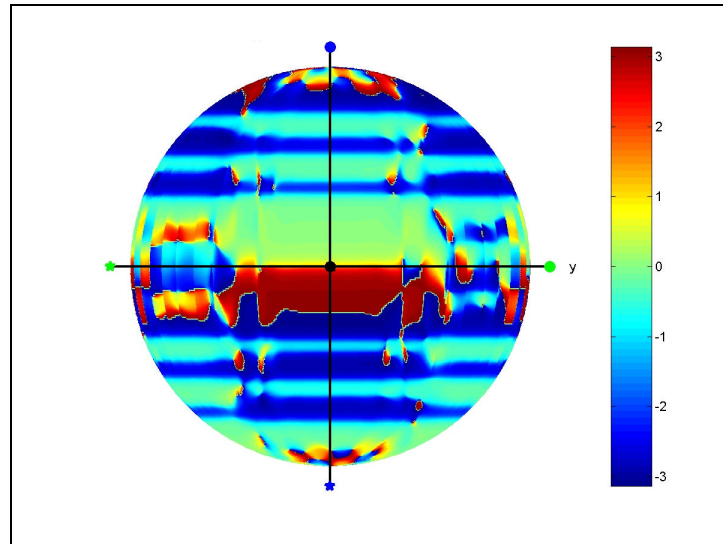
Figure 4.35. Difference-Over-Sum Spherical Cross-Section Phase in Radians – Along-Track (Beams 14 & 41), VOL SR – 37.5 kHz.
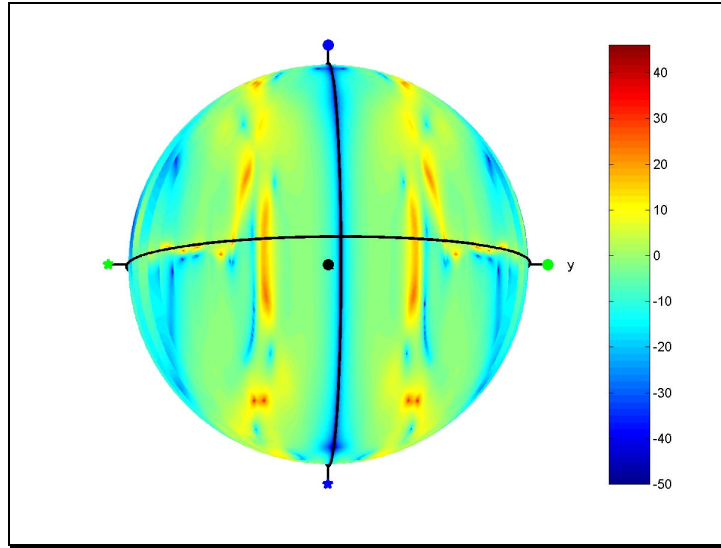
Figure 4.36. Difference-Over-Sum Spherical Cross-Section Magnitude in dB – Across-Track (Beams 13 & 14 (fore)), VOL SR – 37.5 kHz.
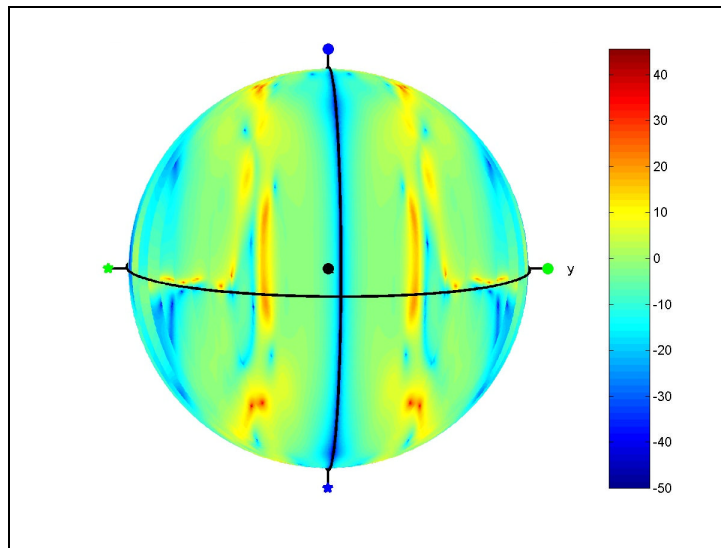
Figure 4.37. Difference-Over-Sum Spherical Cross-Section Magnitude in dB – Across-Track (Beams 40 & 41 (aft)), VOL SR – 37.5 kHz.
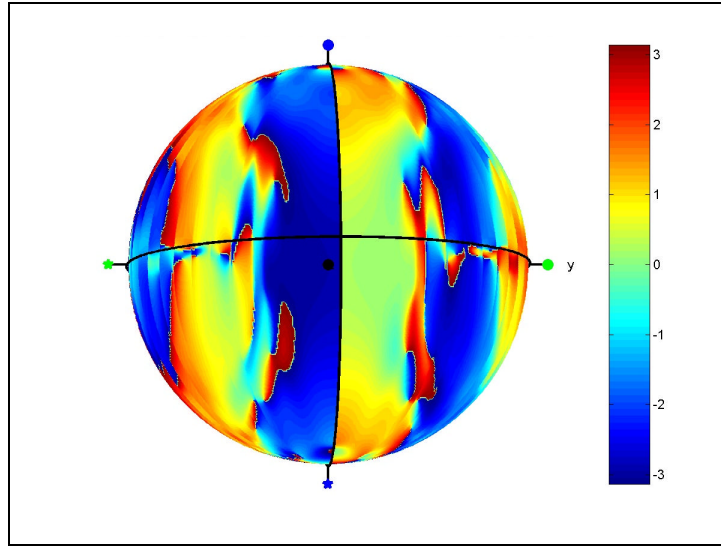
Figure 4.38. Difference-Over-Sum Spherical Cross-Section Phase in Radians – Across-Track (Beams 13 & 14 (fore)), VOL SR – 37.5 kHz.
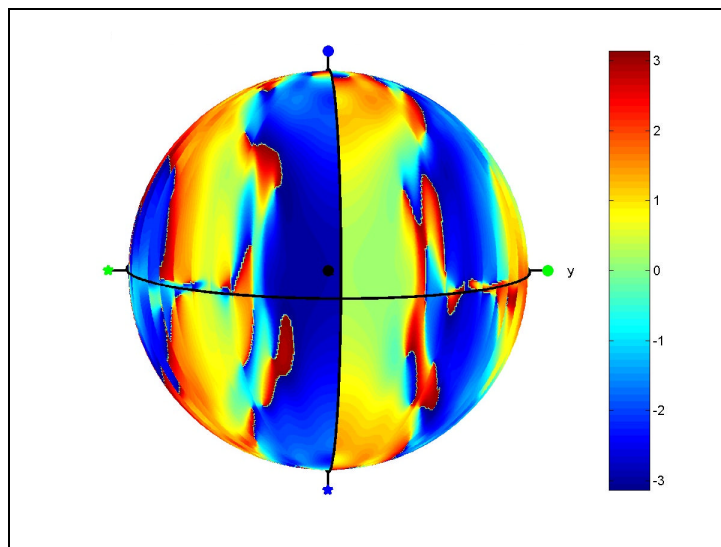
Figure 4.39. Difference-Over-Sum Spherical Cross-Section Phase in Radians – Across-Track (Beams 40 & 41 (aft)), VOL SR – 37.5 kHz.

4.5.2 <u>Sample Results</u>

Figure 4.40 through Figure 4.42 show the results of DS monopulse processing on the data of sample ping sand3688 in rough positional format. Clearly, there in no usable information in either the magnitude or the phase for the DS technique using the along-track beam pairs. This can, once again, be related to the common phase center, which

106

reduces returns from all targets to simply a ratio of amplitudes. The differences in the amplitudes by themselves are insufficient to produce a visual seafloor return.

The DS technique exhibits a null at the time of arrival of the seafloor echo for the forward and rear across-track beam pairs. Within this null is the π-radian transition in the DS phase. At ranges beyond the seafloor, faint multiples of this phase transition can be seen. While the across-track DS processing results in the measured data are somewhat noisy, the phase transitions are detectable by a well designed detection algorithm.
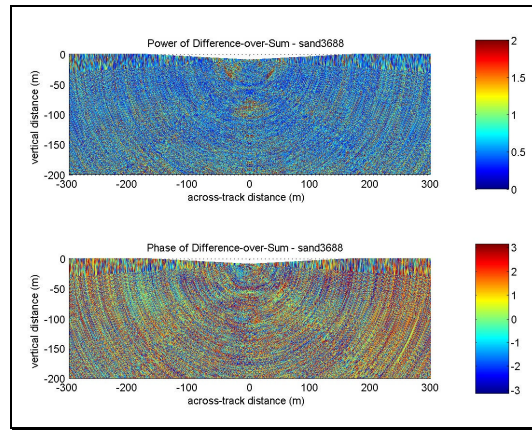
Figure 4.40. Normalized Magnitude in dB and Phase in Radians of the Difference-over-Sum of sand3688 for Fore-Aft (Along-Track) Beam Pairs (Rough Positional Format).
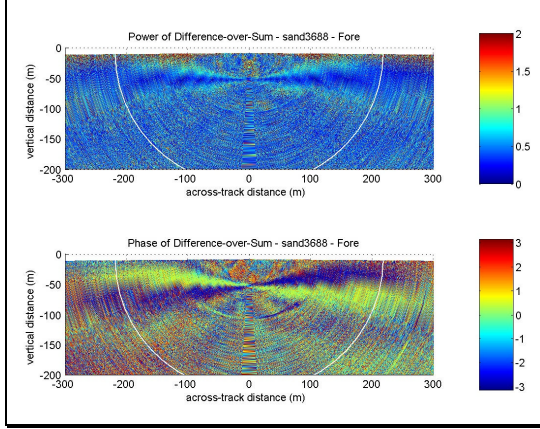
Figure 4.41. Normalized Magnitude in dB and Phase in Radians of the Difference-over-Sum of sand3688 for Forward Across-Track Beam Pairs (Rough Positional Format).
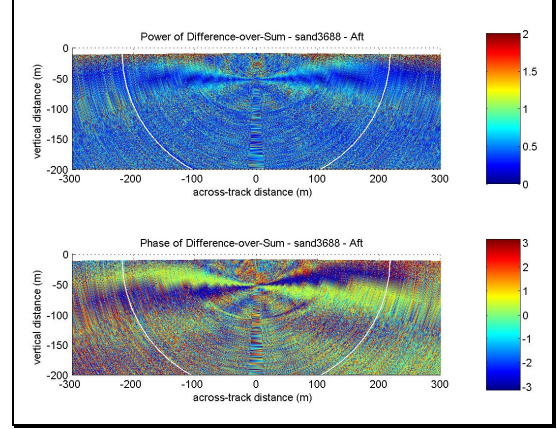
Figure 4.42. Normalized Magnitude in dB and Phase in Radians of the Difference-over-Sum of sand3688 for Rear Across-Track Beam Pairs (Rough Positional Format).

4.6   Narrow Beam

4.6.1   Theoretical Analysis

The name of the NB monopulse process comes from its effect on the beam pair. The NB simplified expression is

$$NB = |A + B| \cdot \left(|A + B| - 0.5 \cdot |A - B| \right) \tag{4.7}$$

Figure 4.43 shows how the narrow beam is produced using the SR simulation data at 37.5 kHz. This figure shows that the beam widths grow progressively narrower from $|A + B|$ to $\left(|A + B| - 0.5 \cdot |A - B| \right)$ to *Narrow Beam* with the aid of the difference signal. In this particular simulation, the beamwidth of the forward and rear beams is 10.6° and the beamwidth of the NB beam is 9.2° measured at their respective half power levels. These beamwidths are 7.2° and 7.0° respectively for LR mode.
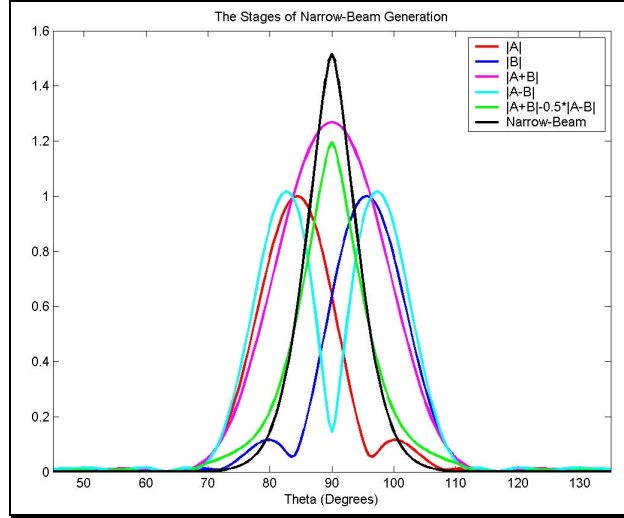
Figure 4.43. Central Along-Track Slice ($f = 0°$) for Various Stages of the Narrow-Beam Beam Pattern – Along-Track (Beams 14 & 41), VOL SR (Nadir At $(q = 90°, f = 0°)$), Cylinder Along 180° to 0° Axis – 37.5 kHz.

The along-track NB beams are not quite as narrow as those of the along-track CP technique in the along-track dimension (7.7° and 6.4° for SR and LR respectively). However, the NB beams do not have the along-track sidelobes (-6 dB) that the CP beams do (Figure 4.44).
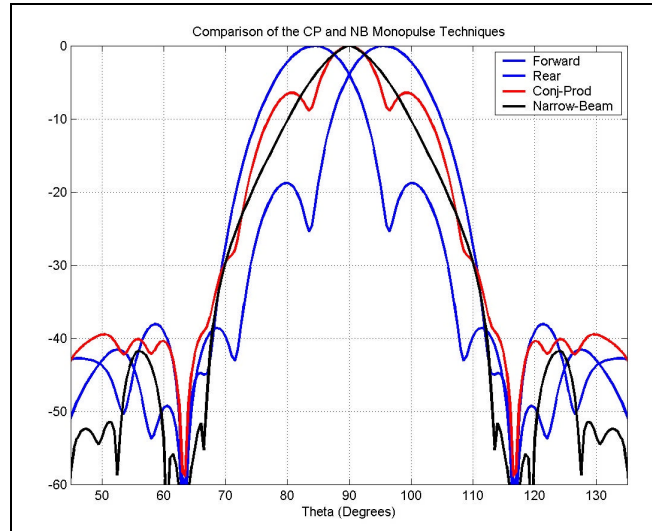
Figure 4.44. Central Along-Track Slices ($f = 0°$) for the Normalized Narrow-Beam Beam Pattern and the Conjugate-Product Beam Pattern – Along-Track (Beams 14 & 41), VOL SR (Nadir At $(q = 90°, f = 0°)$), Cylinder Along 180° to 0° Axis – 37.5 kHz.

109

Figure 4.45 through Figure 4.48 show the beam patterns for VOL SR along-track NB monopulse processing. These show that one advantage of the NB technique is severe sidelobe reduction.
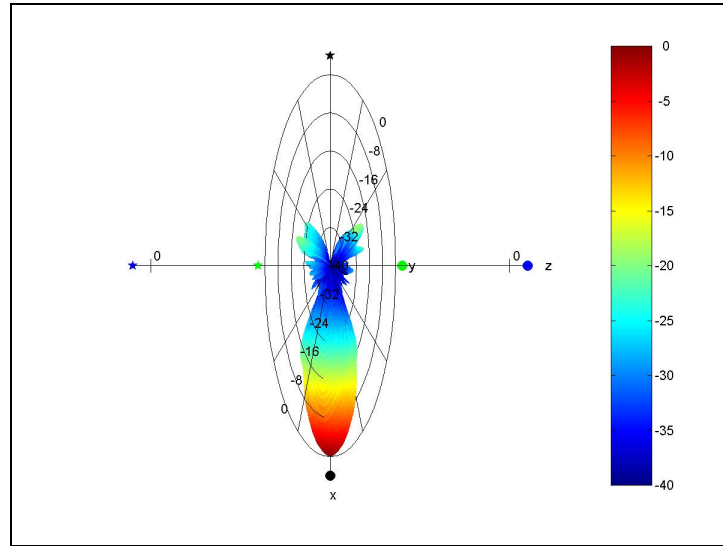
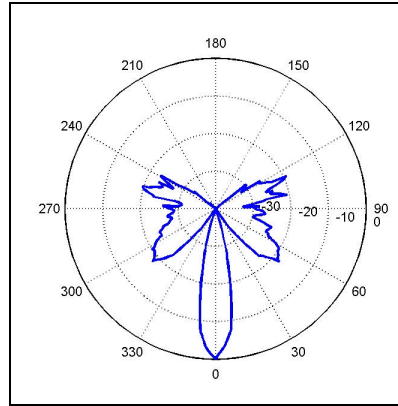Figure 4.45. Normalized Narrow-Beam Beam Pattern – Along-Track (Beams 14 & 41), VOL SR – 37.5 kHz.
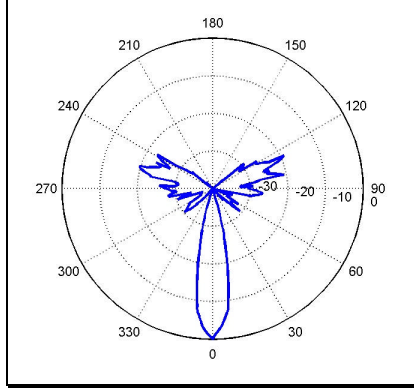
Figure 4.46. Normalized Narrow-Beam Beam Pattern Across-Track Slice ($q = 90°$) – Along-Track (Beams 14 & 41), VOL SR Mode (Nadir At $(q = 90°, f = 0°)$) Cylinder Axis Out of Page – 37.5kHz.
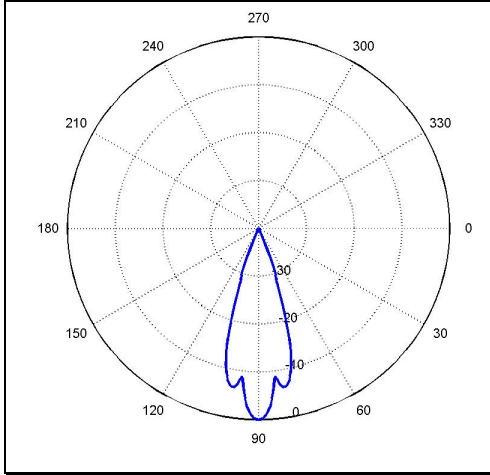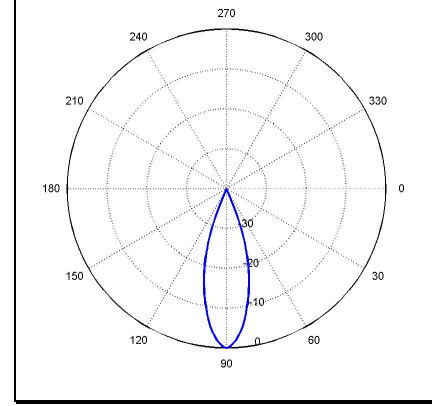
Figure 4.47. Lower Half of the Along-Track Slice ($f = 0°$) of the Normalized Narrow-Beam Beam Pattern – Along-Track (Beams 14 & 41), VOL SR (Nadir At $(q = 90°, f = 0°)$), Cylinder Along 180° to 0° Axis – 37.5 kHz.
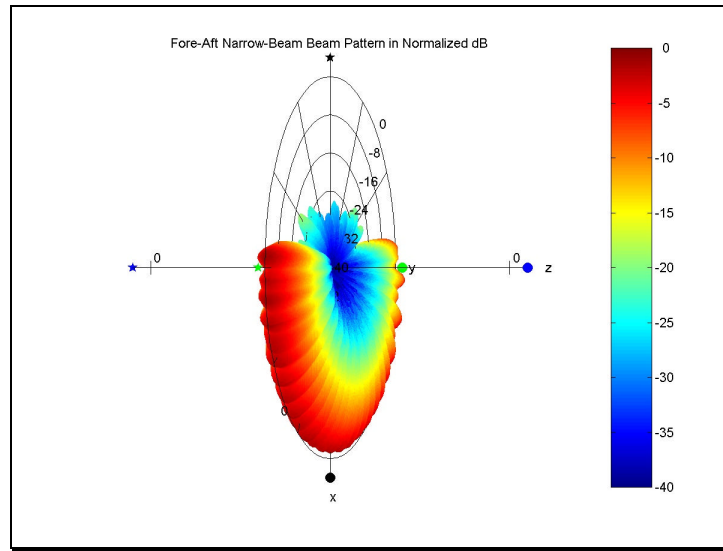
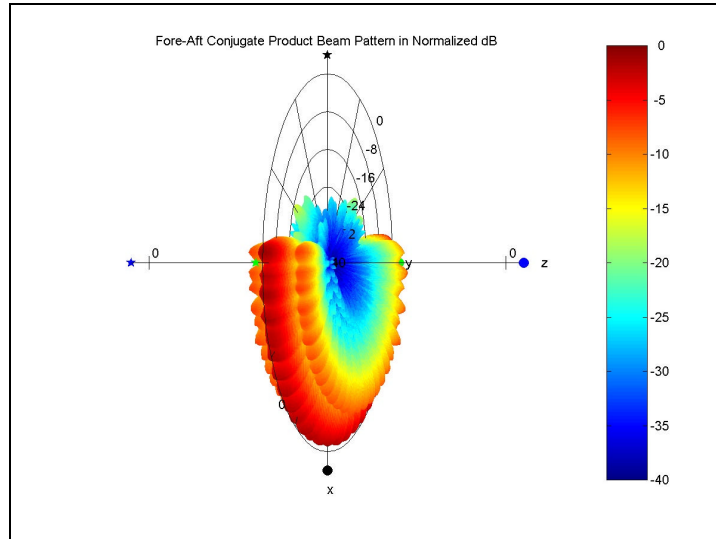Figure 4.48. Normalized Narrow-Beam Beam Pattern – Along-Track, VOL SR for all Beams – 37.5 kHz.

Figure 4.49 and Figure 4.50 show the spherical cross-sections for SR along-track NB pair 14, and Figure 4.51 shows the horizontal cross-section for all twenty-seven SR along-track NB beams. Note that the phase plot contains values of only 0 and π radians due to the absolute value signs in the NB expression. The only remaining phase information results from the comparison of the magnitude of the sum term with half the

111

magnitude of the difference term. From this figure, it appears that the phase of this comparison cannot be used to extract any usable information.
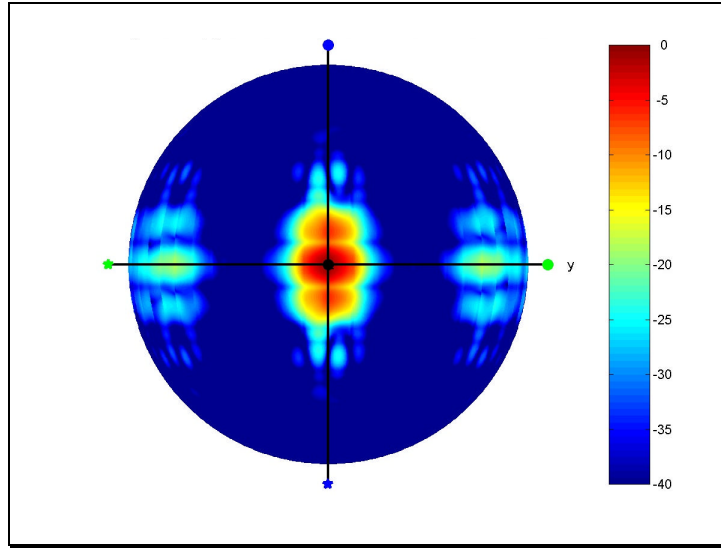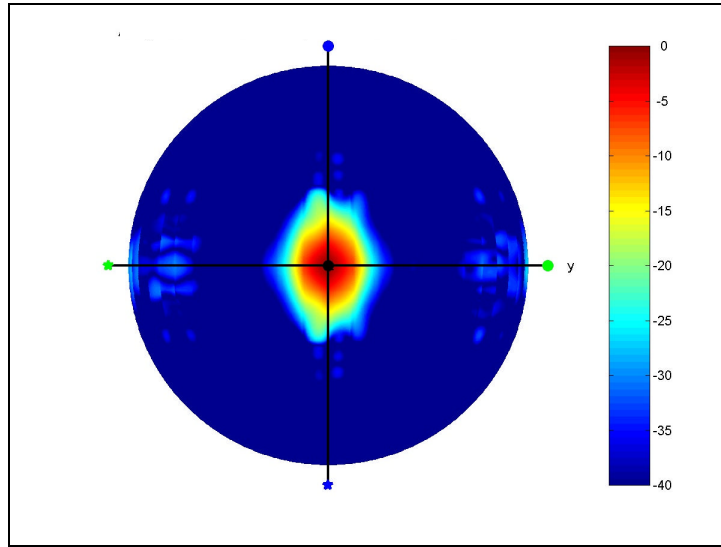

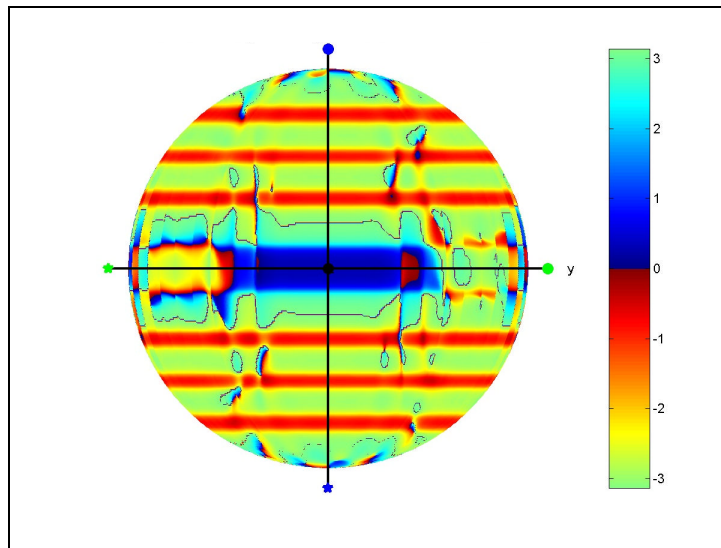Figure 4.49. Normalized Narrow-Beam Spherical Cross-Section in dB – Along-Track (Beams 14 & 41), VOL SR – 37.5 kHz.
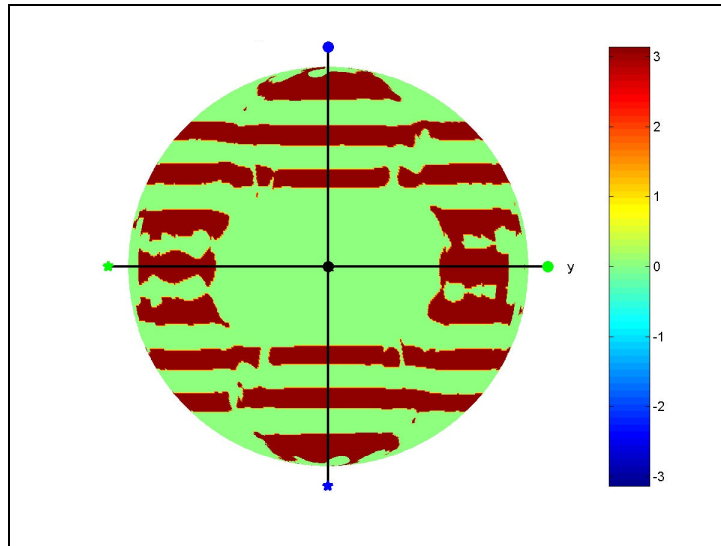
Figure 4.50. Narrow-Beam Spherical Cross-Section Phase in Radians – Along-Track (Beams 14 & 41), VOL SR – 37.5 kHz.
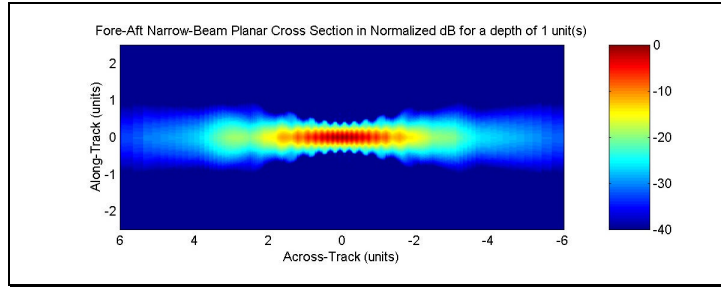
Figure 4.51. Normalized Along-Track Narrow-Beam Beam Footprints (for all Beams) on a Horizontal Plane at Unit Distance from the Transducer for VOL SR (Viewed from Above) – Units are in Multiples of the Transducer Altitude, Forward ≡ Top of Image (Visibility > 80.5° from Nadir) – 37.5 kHz.

Figure 4.52 shows the horizontal cross-section for all twenty-seven LR along-track NB beams. Although the difference is not as severe as the SR mode, the LR along-track NB results have a slightly wider along-track beam width than the LR along-track CP results do, but the results of the NB process do not exhibit the menacing sidelobes of the CP process results.
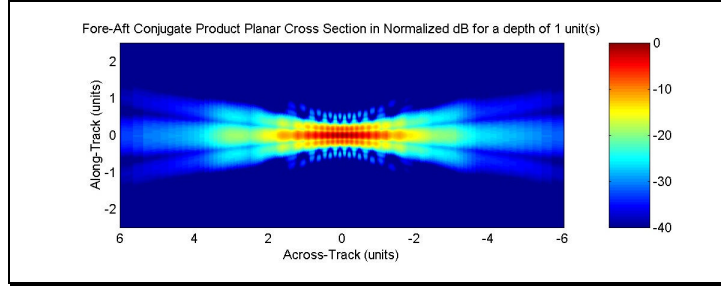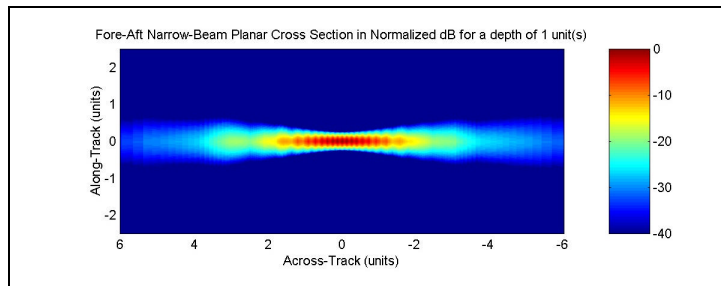

Figure 4.52. Normalized Along-Track Narrow-Beam Beam Footprints (for all Beams) on a Horizontal Plane at Unit Distance from the Transducer for VOL LR (Viewed from Above) – Units are in Multiples of the Transducer Altitude, Forward ≡ Top of Image (Visibility > 80.5° from Nadir) – 37.5 kHz.

Figure 4.53 through Figure 4.57 show the results of applying NB techniques to SR across-track beam pairs, and Figure 4.58 shows the results for LR across-track beam pairs. Comparison of these figures with those of the across-track CP figures shows nearly identical results for the magnitude responses. There is a small reduction in the across-track sidelobe magnitude for the NB case as was discussed previously (Figure 4.44). However, the key phase information of the CP case is completely lost in the NB

computations, which renders this particular processing combination overly computationally intensive for the limited results obtained.
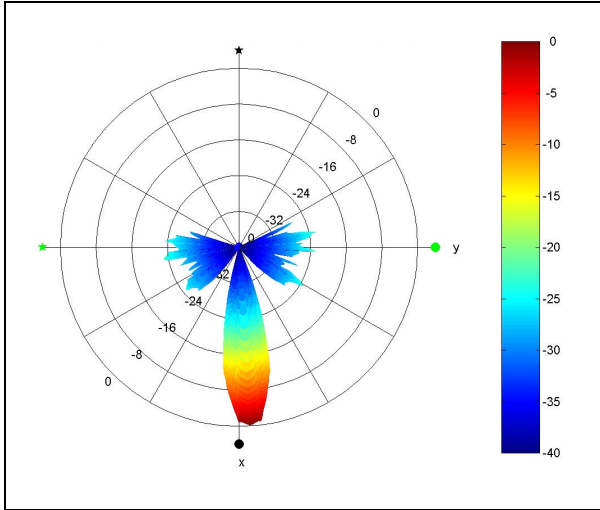
Figure 4.53. Normalized Narrow-Beam Beam Pattern – Across-Track (Beams 13 & 14 (fore) and 40 & 41 (aft)), VOL SR, Front View Cylinder Axis Out of Page – 37.5 kHz.
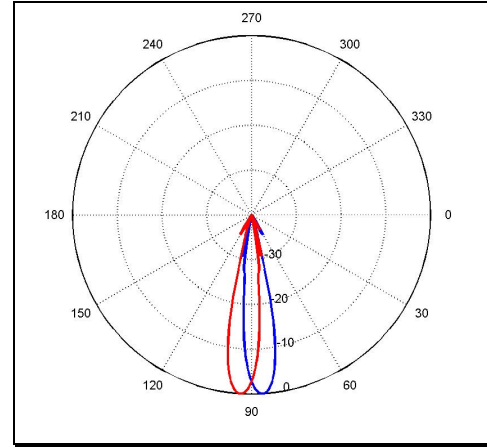
Figure 4.54. Lower Half of the Along-Track Slice ($\boldsymbol{f} = 3.58°$) of the Normalized Narrow-Beam Beam Pattern – Across-Track (Beams 13 & 14 (fore) and 40 & 41 (aft)), VOL SR (Nadir At $\left(\boldsymbol{q} = 90°, \boldsymbol{f} = 0° \right)$), Cylinder Along 180° to 0° Axis – 37.5 kHz.
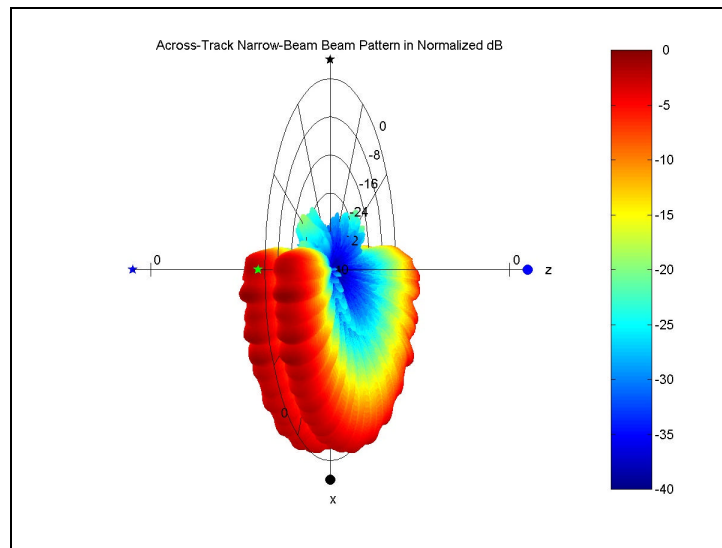
Figure 4.55. Normalized Narrow-Beam Beam Pattern – Across-Track, VOL SR for all Beams – 37.5 kHz.
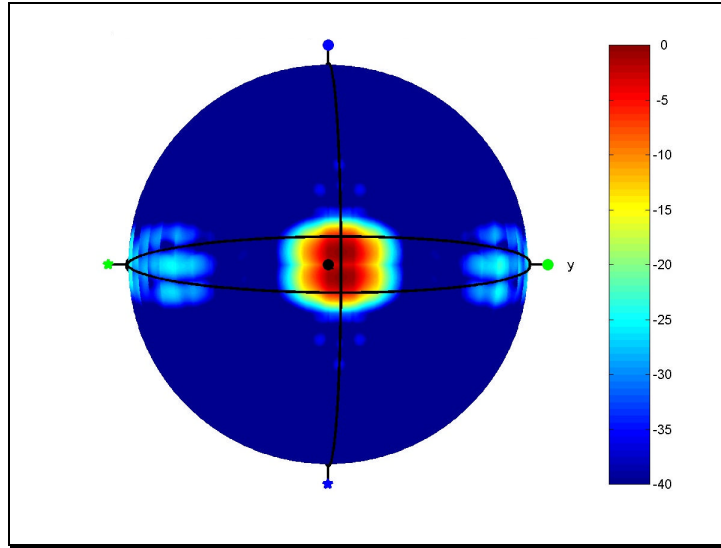
Figure 4.56. Normalized Narrow-Beam Spherical Cross-Section in dB – Across-Track (Beams 13 & 14 (fore) and 40 & 41 (aft)), VOL SR – 37.5 kHz.
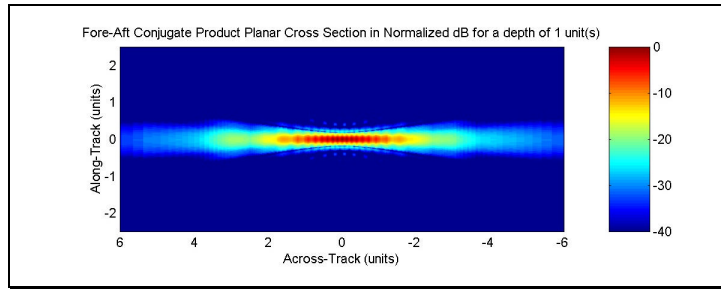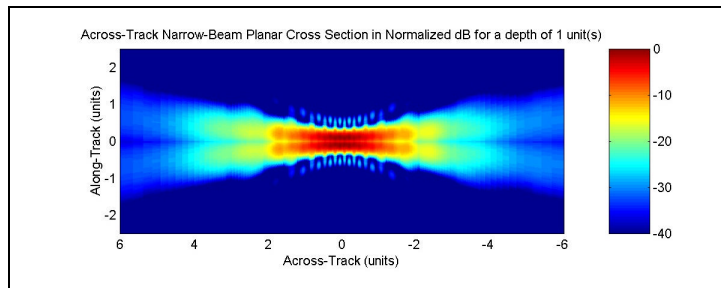

Figure 4.57. Normalized Across-Track Narrow-Beam Beam Footprints (for all Beams) on a Horizontal Plane at Unit Distance from the Transducer for VOL SR (Viewed from Above) – Units are in Multiples of the Transducer Altitude, Forward ≡ Top of Image (Visibility > 80.5° from Nadir) – 37.5 kHz.
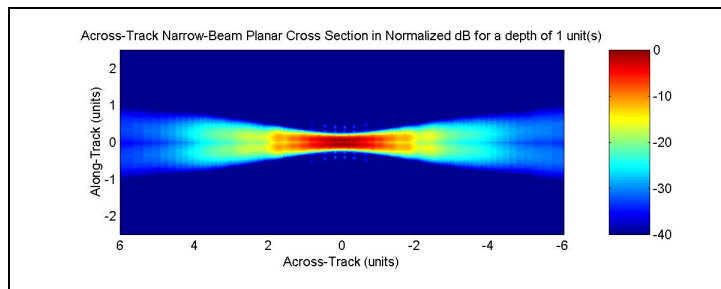
Figure 4.58. Normalized Across-Track Narrow-Beam Beam Footprints (for all Beams) on a Horizontal Plane at Unit Distance from the Transducer for VOL LR (Viewed from Above) – Units are in Multiples of the Transducer Altitude, Forward ≡ Top of Image (Visibility > 80.5° from Nadir) – 37.5 kHz.

4.6.2 **Sample Results**

The NB technique is applied to the along-track, forward across-track and rear across-track beam pairs in Figure 4.59 through Figure 4.61 in rough positional format. As discussed previously, there is no phase information that is usable in the NB case. However, the magnitude is still a viable parameter. The NB technique seems to produce the best results for along-track beam pairs from visual comparisons of the noise floors in the sample plots. Recall that there was no useful phase information for any of the monopulse techniques applied to along-track beam pairs. For the across-track beam pairs, however, these NB magnitude results prove to be no better than those of the CP technique. This was predicted by the planar cross-sections in the simulation results (Figure 4.29 and Figure 4.57).
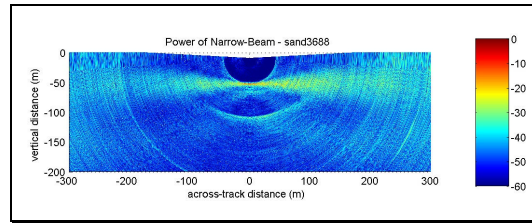
Figure 4.59. Normalized Magnitude in dB of the Narrow-Beam of sand3688 for Fore-Aft (Along-Track) Beam Pairs (Rough Positional Format).
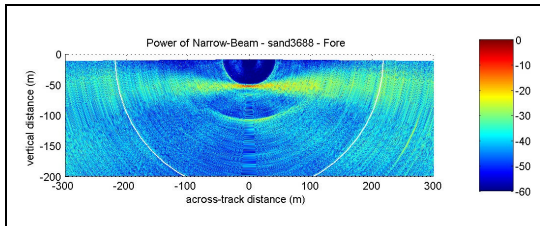
Figure 4.60. Normalized Magnitude in dB of the Narrow-Beam of sand3688 for Forward Across-Track Beam Pairs (Rough Positional Format).
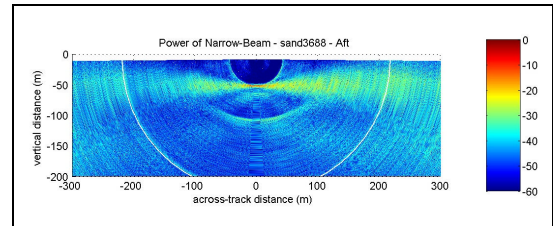
Figure 4.61. Normalized Magnitude in dB of the Narrow-Beam of sand3688 for Rear Across-Track Beam Pairs (Rough Positional Format).

4.7 <u>Summary</u>

The most important manipulation of the data prior to implementation of the monopulse techniques is pulse compression, which uses the large time-bandwidth product of the stepped FM transmission pulse to reduce the pulse's duration. This is equivalent to improving the system range resolution. Following pulse compression, the time-bandwidth product should have a value of one. However, the variations that deteriorate the range resolution also reduce the actual SNR increase produced by the pulse compression process. For example, the remaining time-bandwidth product measured from sample ping sand3688 is equivalent to

$$10 \cdot \log_{10}(T \cdot \Delta f) = 10 \cdot \log_{10}(0.18ms \cdot 10.2kHz) \approx 10 \cdot \log_{10}(1.84) \approx 2.64dB \quad (4.8)$$

The theoretical processing gain increase in the SNR is reduced by this amount to 13.8 dB.

Monopulse techniques combine the data from adjacent beams in order to improve angle of arrival estimates by effectively improving the signal-to-noise ratio. Due to the configuration of the VSS receive beams, both along-track and across-track beam pair combinations are available for use with the monopulse techniques. The common phase center of the beams in each along-track pair precludes the generation of any target response phase information by monopulse techniques. However, the phase center offset for the beams of each across-track pair provides the potential of obtaining both magnitude and phase information in the monopulse results when a target is present. These beam pair configurations are compared in Table 4.1 for the three monopulse processing techniques reviewed – conjugate-product (CP), difference-over-sum (DS) and narrow-beam (NB). The simulation of these monopulse techniques for each beam pair

configuration and their application to sample data collected with the VSS system produced equivalent results in both magnitude and phase.

	Along-Track Beam Pairs	Across-Track Beam Pairs
Beam Pair Phase Centers	Common (No Monopulse Phase)	Offset (Possible Monopulse Phase)
Resulting Beam Geometry	Ideal Maximum Response Axes in Plane	Ideal Maximum Response Axes in Cone
Conjugate-Product (CP) Target Response	Large Magnitude No Phase Information	Large Magnitude Linear Phase Transition
Difference-over-Sum (DS) Target Response	No Magnitude Information No Phase Information	Null Magnitude p-Radian Phase Step
Narrow-Beam (NB) Target Response	Large Magnitude No Phase Information	Large Magnitude No Phase Information

Table 4.1. Summary of Beam Geometries and Monopulse Techniques.

Due to the simple beam geometry of monopulse results from along-track beam pairs, these were chosen over the across-track beam pairs for this proof of concept. Since there is no target response phase information for the along-track beam pair configuration, the NB monopulse technique was chosen for the seafloor detection process of Chapter 5 due to its superior magnitude target response for this beam pair configuration compared to the other two monopulse techniques reviewed.

The SNR is increased by the change in directivity index resulting from switching to NB monopulse from the original beams. The directivity index increase is the ratio of the solid angle in radians [K$^+$00], which reduces to the ratio of the along-track beam widths of the two systems.

$$\Delta SNR = 10 \cdot \log_{10}\left(\frac{q_2}{q_{2\_NB}}\right) \qquad (4.9)$$

Despite it's superiority to the other monopulse techniques, the increase in the SNR due to the DI use of the NB technique is only 0.62 dB for SR and 0.12 dB for LR. Compared to the DI of a single beam, this presents a negligible gain. However, when

combined with the magnitude gain of roughly 2dB obtained through the NB processing, this yields a total SNR increase of roughly 2.5 dB. Thus the total SNR increase from applying pulse compression and narrow-beam monopulse processing is 17.3 dB.

CHAPTER 5

SEAFLOOR CHARACTERISTICS

5.1   Bottom Detection

5.1.1   Time Limitation for Noise Reduction

Monopulse techniques require a detection algorithm to make obtain angle of arrival estimates.[2] This chapter discusses a detection algorithm that works on the data that is produced when a narrow-beam (NB) monopulse technique is applied to along-track beam pairs. Recall that the NB monopulse process contains no usable phase information. The algorithm employed detects targets within each narrow-beam beam separately while separating signal from noise using a constant threshold following the application of several normalization processes. No prevailing theory is used for this bottom detection algorithm. Rather, a combination of fundamental concepts yields a relatively robust detection solution for the sample data sets tested here.

Recall from the beginning of the previous chapter that a spreading loss correction is applied to the data in order to reduce the dynamic range of the seafloor returns from

---

[2] Refer to Section 0 for beam orientations. Each fore-aft beam pair is used to create a NB beam at its spatial center.

several ranges. Recall also that this increases the noise floor dramatically at large ranges. While the NB processing aided in removing much of this noise, the noise magnitude at large ranges is still large enough to cause serious problems in the bottom detection process. In order to minimize the distorting effect that this noise causes, some of the data at longer ranges must be removed while maintaining minimal loss of usable signal.

Making the assumption of a horizontal seafloor, a maximum time sample number is chosen at some multiple of the time of the maximum amplitude return from all beams, based on the additional assumption that the maximum return is from the seafloor at its closest point to the sonar. All returns after this maximum time sample number, which corresponds to a maximum range, are discarded. The choice of a time multiplier needs to optimize the competing factors of long range noise and signal loss, which is equivalent to the across-track swath width for a flat seafloor. Using the assumption that the maximum angular extent from nadir of a beam's coverage area occurs midway between this beam's maximum response axis and the maximum response axis of the next beam away from nadir, beams 5 and 23 extend to 9.5 beam spacings from nadir, beams 4 and 24 extend to 10.5 spacings from nadir, and beams 3 and 25 extend to 11.5 spacings from nadir. These beam spacings correspond to roughly 68.0° (1.19 rad.), 75.2° (1.31 rad.), and 82.3° (1.44 rad.) from nadir respectively. Under the assumption of a horizontal sea floor and ideal ray paths (Section 5.2.2), these are equivalent to 2.48, 3.78 and 7.44 times the distance and travel time to the seafloor at nadir. However, since the seafloor is likely not to be a horizontal plane, all twenty-seven beams must be analyzed for potential targets.

Testing preformed using data out to 7.5 times the time of the maximum return proved to be unusable because of the noise at the longer ranges. Testing was also

preformed using time multipliers of 4.5 and 6.0. While the data from the multiplier of 6.0 does not provide any extra beams over the use of a range multiplier of 4.5 for a horizontal seafloor, it may add extra coverage for other seafloor shapes. In the end, the multiplier of 4.5 proved to be the most useful for the data tested. However, several plots are included using the multiplier of 6.0 because they better represent some of the issues that were faced for certain stages of the detection process.

Figure 5.1 shows NB data of Figure 4.59 out to a range of 6.0 times the maximum return for the ping sand3688 in 3D view with the normalized intensity on the vertical scale. The 4.5x range limit occurs near sample 4300 in this case. This figure is repeated in Figure 5.2 for another sample ping named mud4000. The 4.5x range limit for the data of mud4000 occurs near sample 5800. Note that mud4000 does indeed appear to have a more mud-like intensity pattern, i.e. sharp intensity drop off away from nadir [APL94], than sand3688 does.
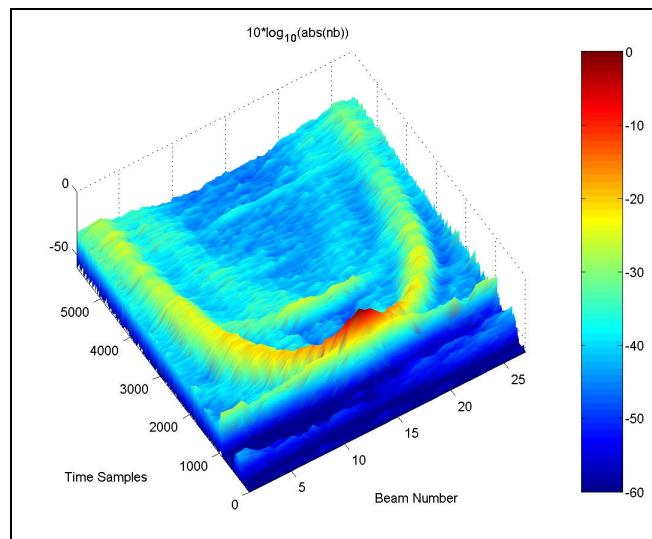
Figure 5.1. Normalized Magnitude in dB of the NB of Ping sand3688, 6x Cutoff – 3D View.
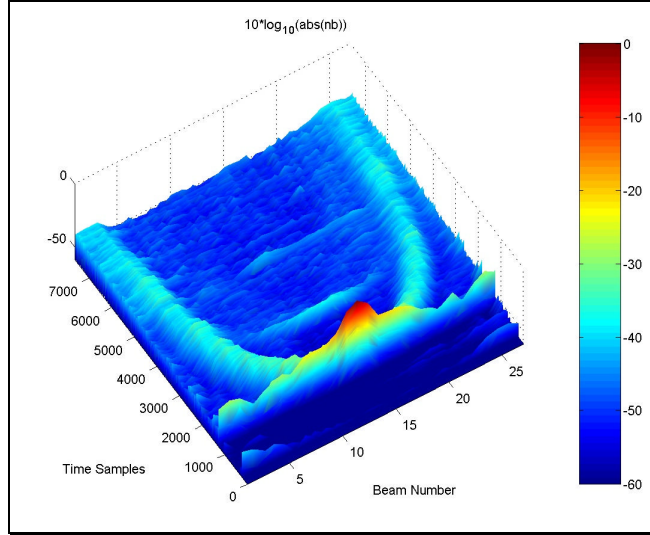
Figure 5.2. Normalized Magnitude in dB of the NB of Ping mud4000, 6x Cutoff – 3D View.

Figure 5.3 shows the normalized (to a maximum of one) cumulative square of the NB magnitude for the mud4000 data with a 4.5x time limit. This technique is a measure of gauging which regions of time contain target returns. A steeper slope corresponds to a region of more concentrated target returns. Since the NB signal already has units of signal squared, e.g. power or energy, this has units of signal strength to the fourth power. The near-specular returns will appear similar to step functions since the bulk of the energy is received within a narrow time extent. In this example, the near-specular returns occur near time sample 1500 for beams 13 through 15. The sidelobe specular returns (steps near sample number 1500) are likely to interfere with the seafloor detection process due to their relatively large magnitudes. Note that the portions of the curves not resulting from the specular sidelobes returns generally follow a cubic curve, e.g. beams 5 and 22, as the returns arrive from various portions of the intersection between the beam pattern main lobe and the seafloor. However, in the outer beams such as 1 through 3 and 25 through 27, the time cutoff occurs prior to any seafloor echoes. The curves for these beams follow a more parabolic shape due to the noise floor increase caused by the

123

spreading loss correction. Since there is little signal strength in these beams, the sidelobes of the near-specular returns sometimes comprise a large portion of their cumulative fourth order signal strength.
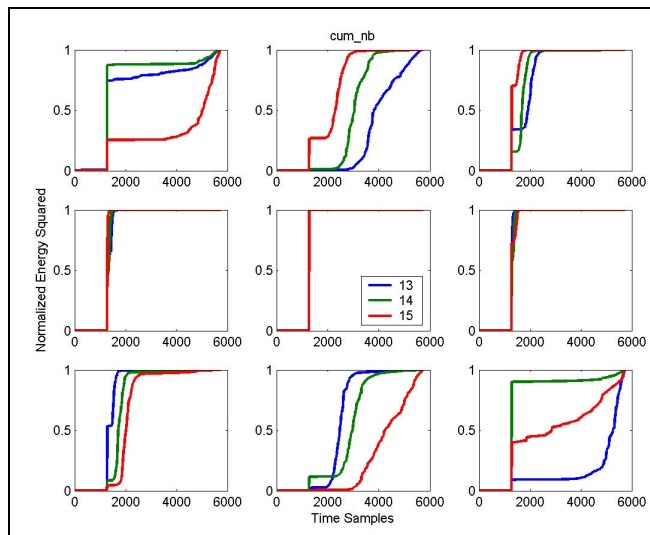
Figure 5.3. Normalized Cumulative Magnitude Squared of the NB of Ping mud4000, 4.5x Cutoff. (Following the color scheme of the central subplot containing beams 13 through 15, the beams follow progressively from beam 1 in blue in the upper left to beam 27 in red in the lower right.)

5.1.2 <u>Maximum Echo Sidelobe Removal</u>

From the results of the previous section it becomes clear that a method for the removal or reduction of the sidelobe specular returns would improve the detection process. Such a method was successfully employed by Alexandrou and de Moustier [AM88] by way of a correlation technique. In this method, the beam containing the strongest return was correlated with the other beams. Since the data was in a quadrature format, the portions of the other beams that were strongly correlated with the first beam could be removed. This technique has been modified to work with the envelope data produced by NB processing. Instead of correlating the entire time sequences of the beams, a moving sequence of three time samples from the beam of maximum response is

124

correlated with the same time samples of the adjacent beams. The central values of the correlations, i.e. equivalent to a sum of multiplications, are retained. This process is performed on all time sequences from ten samples prior to the time of maximum return to twenty samples after the time of maximum return. The result of this process for mud4000 is shown in Figure 5.4.
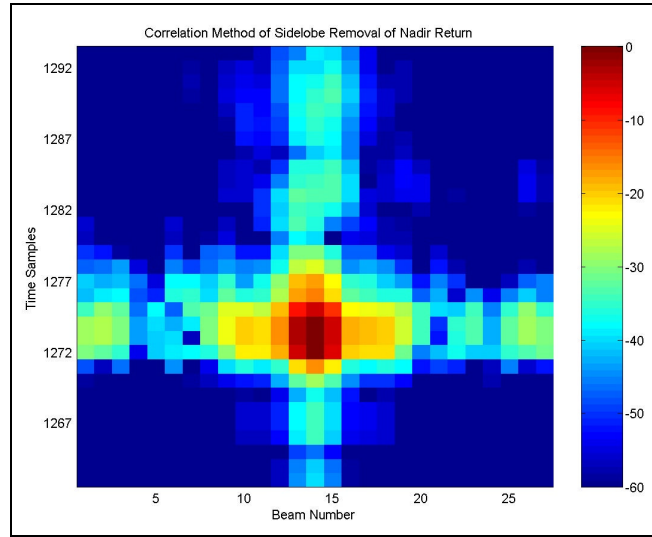
Figure 5.4. Results of Maximum Response Correlation – mud4000.

Since the object of interest is the energy in the sidelobes, the results for all beams except that of the maximum return are summed for each time slice as is shown in Figure 5.5. Since the original NB signal was normalized, its maximum value is one. If the summation value exceeds 0.05 (-13 dB from overall maximum), all beams except that of the maximum response are set to zero at that sample time. If the summation value exceeds 0.01 (-20 dB from overall maximum), all beams except that of the maximum response and those adjacent to it are set to zero at that sample time. These values were chosen by trial and error with the sample pings sand3688 and mud4000 and are not based on any theoretical analysis. They are most likely system dependent. The method of trial and error was to test a threshold visually to see if it was removing the sidelobes while

retaining the majority of likely target returns from non-sidelobe sources. The most

critical region of this process occur in the beams adjacent to that containing the maximum

return.
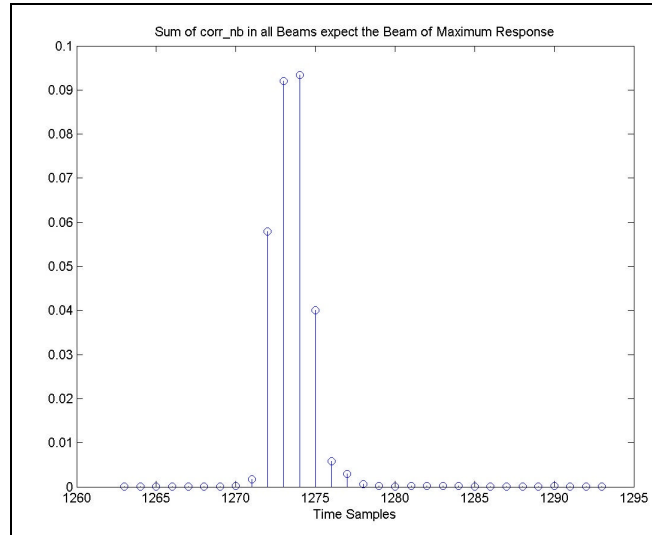
Figure 5.5. Non-Maximum Beam Summation of the Maximum Response Correlation
Results – mud4000.

Figure 5.6 shows a close-up version of the region of the maximum response of

mud4000, which is a specular seafloor return in this case. Figure 5.7 shows the same

data after the sidelobe suppression. While some of the sidelobes remain, the strongest

ones have been effectively removed. This portion of the detection code was added

subsequent to that covered later in this chapter because those portions could remove only

the smaller sidelobe values. Thus, the portions of the sidelobes that remain do not effect

the detection process. This method is not as robust as that of Alexandrou and de

Moustier [AM88] since it works only with magnitude data. However, it works

adequately enough to with the data set tested to remove the largest sidelobes as shown

below. If the more robust method employed by Alexandrou and de Moustier were

required, it would have to be applied prior to application of the NB monopulse technique.
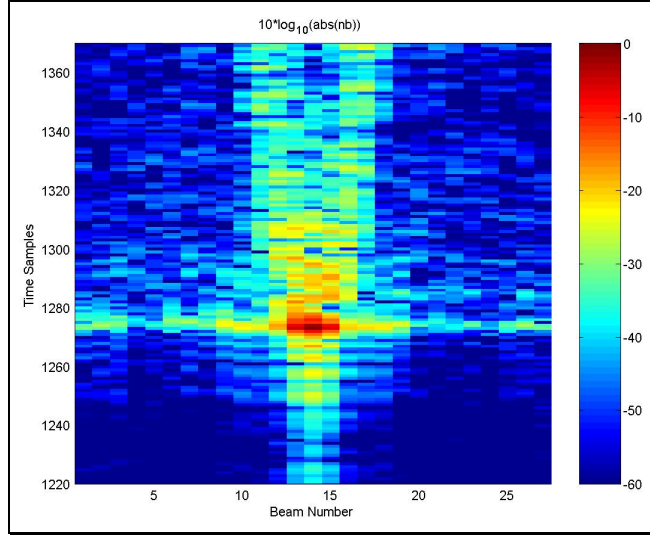
Figure 5.6. Normalized Magnitude in dB of the NB of Ping mud4000 – Close-Up.
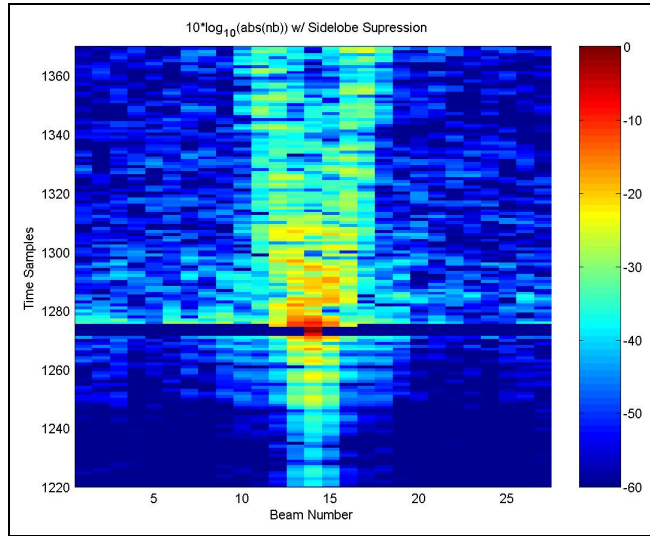
Figure 5.7. Normalized Magnitude in dB of the Sidelobe Suppressed NB of Ping mud4000 – Close-Up.

Figure 5.8 and Figure 5.9 show the 3D view of sample pings mud4000 and sand3688 after sidelobe suppression. Comparison of these figures with Figure 5.1 and Figure 5.2 shows that the largest sidelobes have been removed.
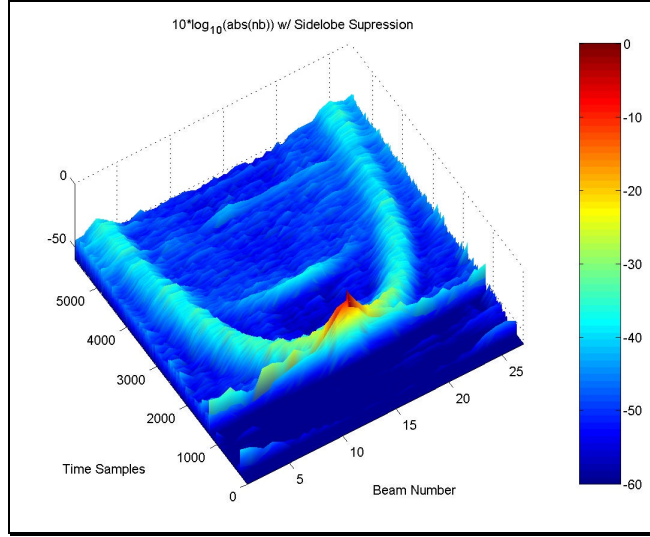
Figure 5.8. Normalized Magnitude in dB of the Sidelobe Suppressed NB of Ping mud4000, 4.5x Cutoff – 3D View.
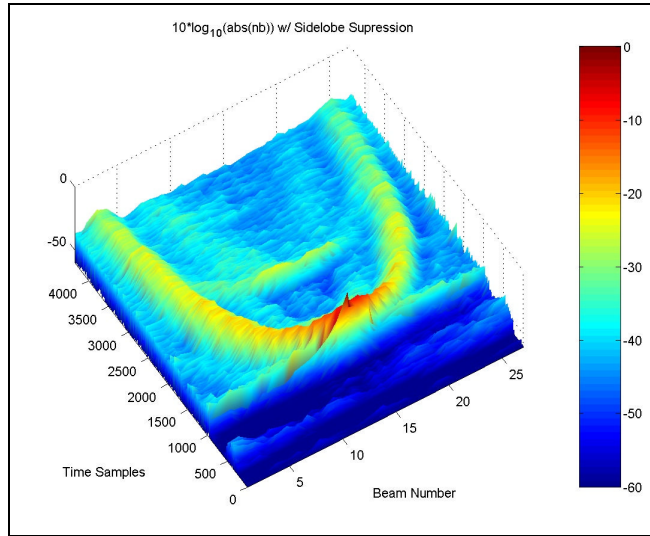
Figure 5.9. Normalized Magnitude in dB of the Sidelobe Suppressed NB of Ping sand3688, 4.5x Cutoff – 3D View.

Figure 5.10 shows the normalized cumulative NB magnitude squared for the mud4000 data with a 4.5x time limit after sidelobe suppression. Comparison with the previous plot in Figure 5.3 shows that the problems with signal energy in the sidelobes of the specular return have been reduced but are still present (size of step functions in non-specular beams).
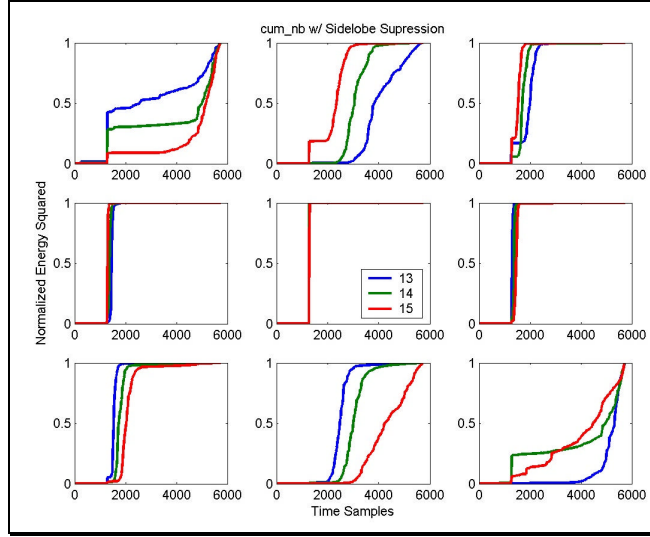
Figure 5.10. Normalized Cumulative Magnitude Squared of the Sidelobe Suppressed NB of Ping mud4000, 4.5x Cutoff.

5.1.3   Magnitude Scaling for Retaining Returns from Potential Targets Only

There are two major classifications of methods for separating signal from noise using a threshold detection process. The first is to apply a threshold that varies with space and time as the signal amplitude varies with space and time. The other is to normalize the data in such a manner that a constant threshold can be applied. The latter method is implemented here.

The first normalization process to be applied to the data normalizes each beam separately. This is accomplished by dividing the fourth order signal (NB^2) at each time sample by the sum of fourth order signals in the beam up to the time limit. This reduces the specular beam significantly with respect to the outer beams that contain significantly less signal strength. The results of this normalization are shown in Figure 5.11 for sand3688.

129
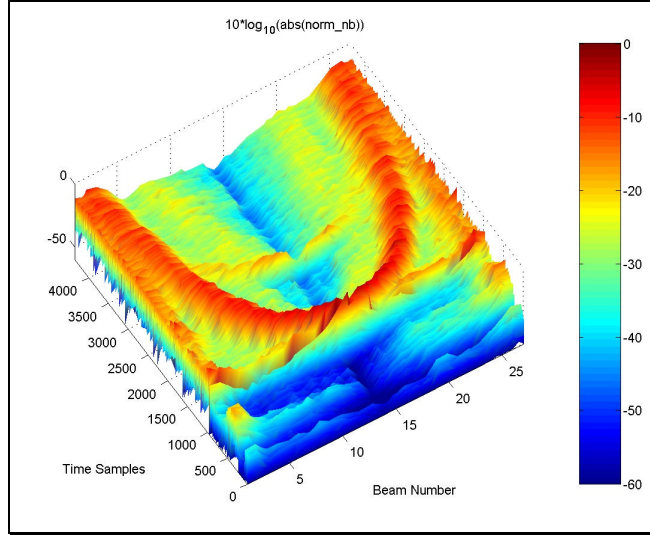
Figure 5.11. Normalized Magnitude in dB of the Beam-Normalized Ping sand3688, 4.5x Cutoff – 3D View.

The second type of normalization works on each time sample separately. In this process the data at each sample time is divided by the strongest signal in that time slice in the sidelobe suppressed NB data. This further reduces the sidelobes of any target return and increases the probability of having at least one usable return in every time slice. The results of this normalization are shown in Figure 5.12 for sand3688. This shows clearly that a threshold could be successfully applied for signal detection.
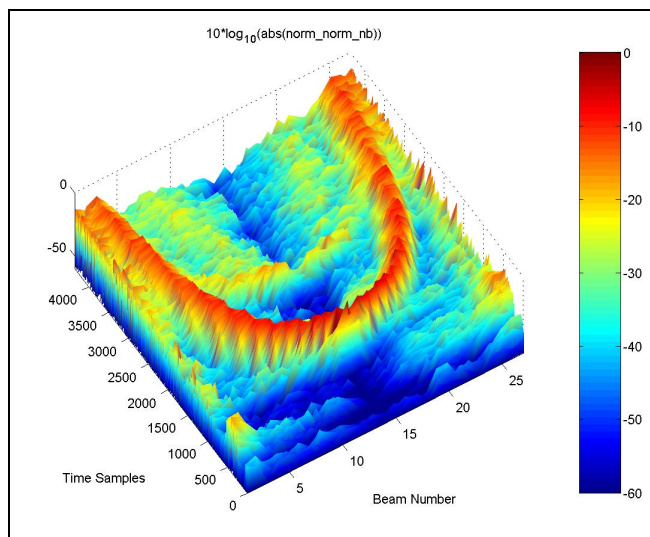
Figure 5.12. Normalized Magnitude in dB of the Beam-Normalized, Time-Normalized Ping sand3688, 4.5x Cutoff – 3D View.

The unit-normalized cumulative dual-normalized (vs. space and time) square of the NB magnitude for the mud4000 data with a 4.5x time limit is shown in Figure 5.13. Note that in this figure the sidelobes of the specular return have been severely reduced (reduction in step size) with respect to the other signal characteristics, which is the desired effect. Thus when this data is used to retain only points from potential targets, the points in the specular sidelobes are not included. Figure 5.14 shows the dual-normalized data from sand3688 on a linear scale where thresholding is represented by a change in color. A threshold of 0.01 (-20 dB) was chosen by trial and error and seems to produce a good result here.
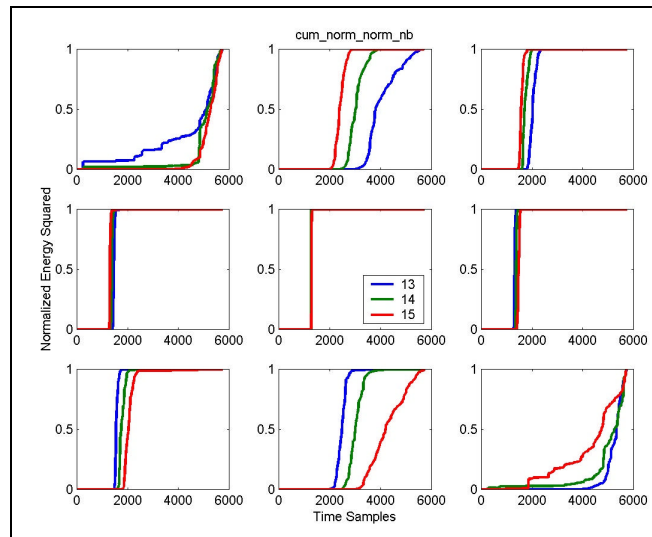
Figure 5.13. Normalized Cumulative Magnitude Squared of the Beam-Normalized, Time-Normalized Ping mud4000, 4.5x Cutoff.
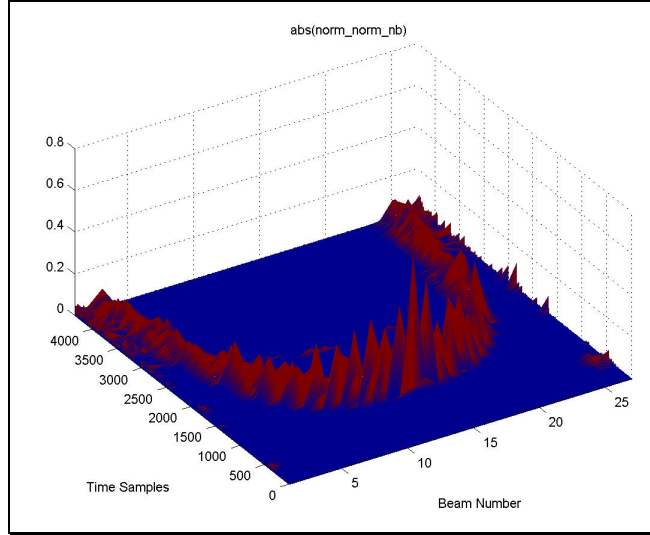
Figure 5.14. Normalized Magnitude of the Beam Normalized, Time Normalized Ping sand3688, 4.5x Cutoff – 3D View with Threshold Coloring.

5.1.4   Grouping of Potential Target Returns with Energy Thresholding

After the points are selected using the thresholding technique, these points are restored to their original NB values, and all other points are set to zero. Figure 5.15 and Figure 5.16 show the selected sand3688 data with 4.5x and 6.0x time thresholds respectively. These plots are repeated in Figure 5.17 and Figure 5.18 for the selected points in mud4000. Figures have been included for both the 4.5x and 6.0x time limits to show that choosing different time limits changes some of the points that are retained as potential target returns. This occurs because their dual-normalized magnitudes are altered with respect to the selection threshold. These four figures are directly comparable with the first two figures in this chapter. Such a comparison shows that the selected data contains the majority of the returns from the seafloor echoes but little of the sonar-induced pseudo targets [MG02]. There are still some troublesome noise returns included at longer ranges whose effect will be seen later.

132
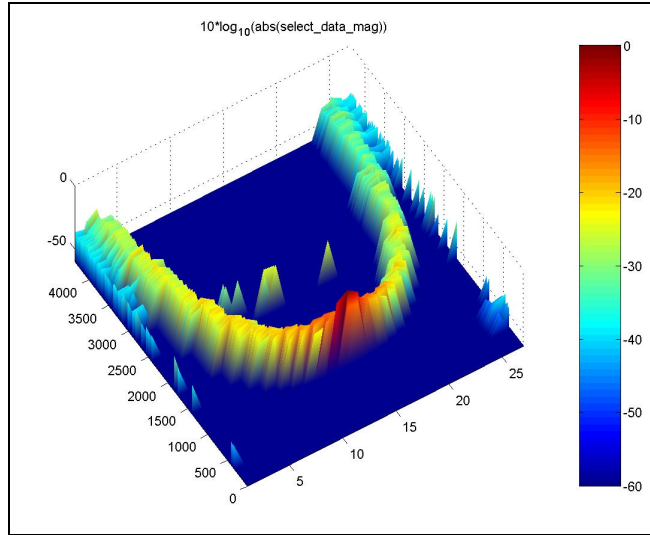
Figure 5.15. Normalized Magnitude in dB of the Selected Points from Ping sand3688, 4.5x Cutoff – 3D View.
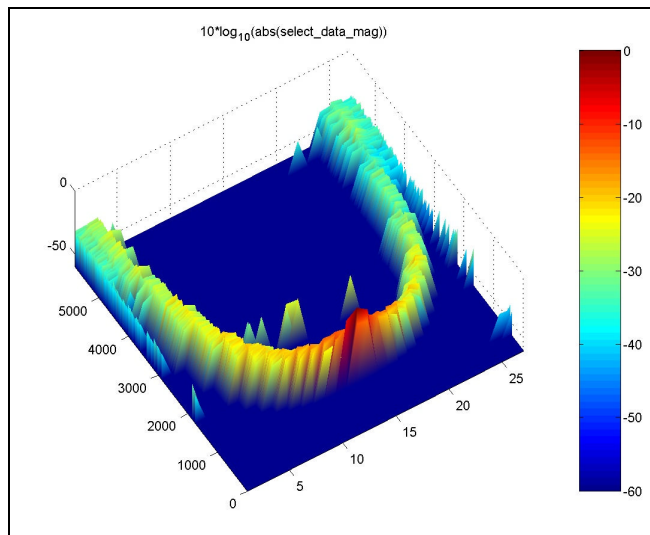
Figure 5.16. Normalized Magnitude in dB of the Selected Points from Ping sand3688, 6x Cutoff – 3D View.
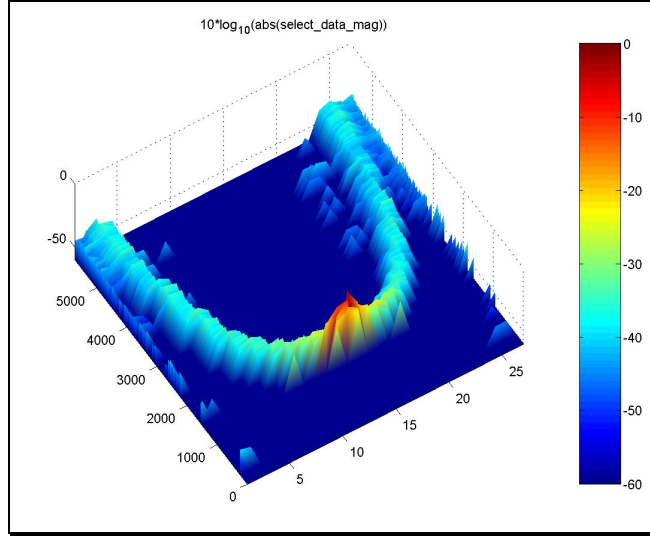
Figure 5.17. Normalized Magnitude in dB of the Selected Points from Ping mud4000, 4.5x Cutoff – 3D View.
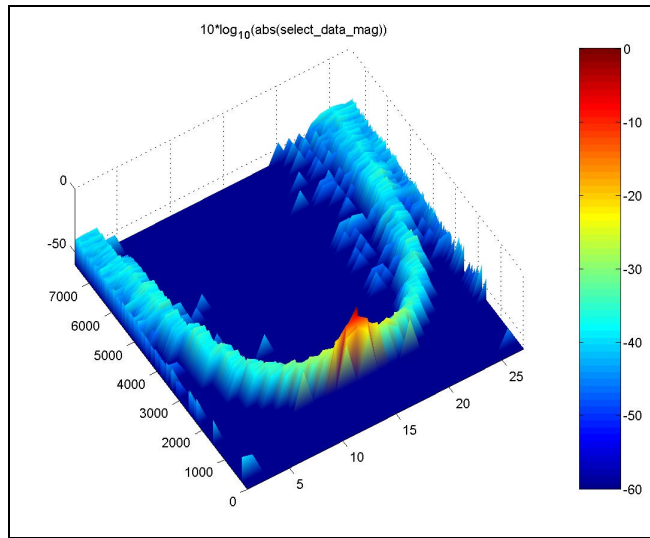
Figure 5.18. Normalized Magnitude in dB of the Selected Points from Ping mud4000, 6x Cutoff – 3D View.

Figure 5.19 and Figure 5.20 show the normalized cumulative magnitude squared of the selected NB points for the mud4000 data with 4.5x and 6.0x time limits respectively. The former is quite similar to that of the dual-normalized data shown in Figure 5.13. This is indicative of successful thresholding execution since the sidelobe returns from the specular echo (step functions around sample number 1500) are no longer problematic. One area of concern that still exists is shown in the curve for beam 24 (red,

134

bottom-center) for the 6.0x time limit. The gradual slope that occurs after that of the main return is noise that has been mistaken to be signal by the thresholding algorithm. A method of correcting this issue is discussed in the next section. Other than the change in time base, the greatest distinction between these figures occurs in the outer beams. The 6.0x time limit allows for more of the seafloor returns from these beams to be retained than the 4.5x time limit does. This alters the shapes of the curves for the outer beams.
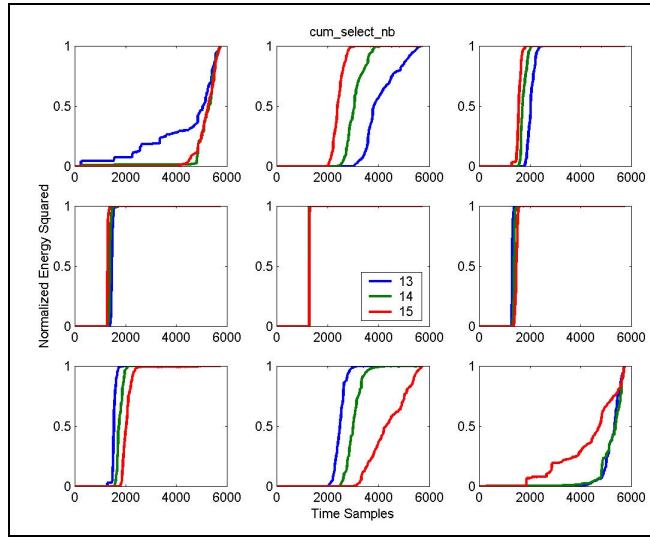
Figure 5.19. Normalized Cumulative Magnitude Squared of the Selected Points from Ping mud4000, 4.5x Cutoff.
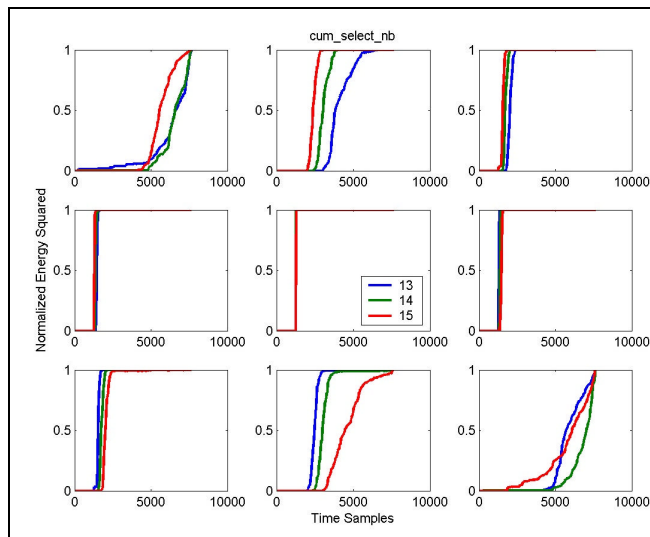
Figure 5.20. Normalized Cumulative Magnitude Squared of the Selected Points from Ping mud4000, 6x Cutoff.

These selected points are broken into potential targets by looking for separations between consecutive selected points that are greater than at least one of the following: (1) 500 time samples or (2) the standard deviation of all selected points in the beam divided by some constant such as two or five. The latter spacing limit works best on beams where one target provides the majority of the reflected energy. Using the standard deviation provides a method of grouping an elongated seafloor return from an outer beam as one target without losing resolution for near-specular beams. The 500-sample time limit corresponds to roughly twenty meters, which is more than twenty times the range resolution of the compressed transmission pulse. This method allows separation of targets in beams that contain more than one strong target or large amounts of noise. Of course, this method is not able to separate targets separated by less than twenty meters. Figure 5.21 shows an example of target separation from the mud4000 data. The black vertical lines correspond to target separations. Only targets containing more than 25% of the fourth order signal strength (NB^2) of the selected points in the beam are retained. Clearly, in this case, only the first target (group of points furthest left in the figure) is retained as a potential seafloor return. The reason for choosing the 25% (-3 dB) threshold is based on data processing rather than sonar theory. The choice of threshold level is discussed in Section 5.1.6.
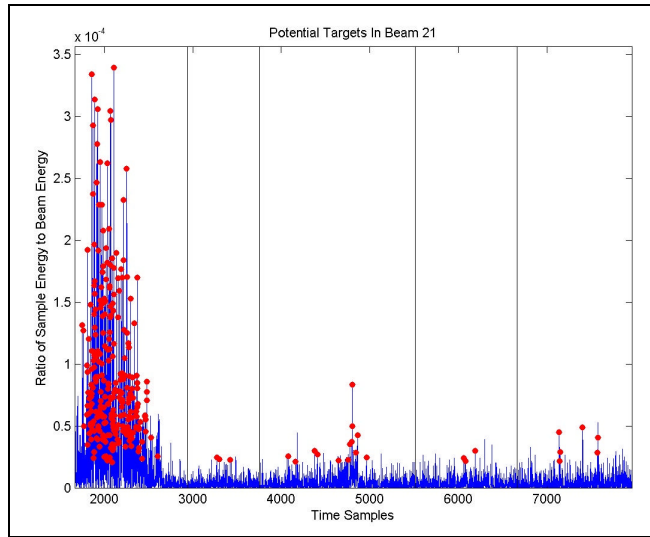
Figure 5.21. Normalized Magnitude of the Selected Points with Target Separation from Ping mud4000 Beam 21, 6x Cutoff.

5.1.5 <u>Refining Potential Targets Extents and Centers</u>

Figure 5.22 shows the data selected as a potential seafloor return in beam 24 of mud4000 with a 6.0x time limit that was mentioned in the previous section. Recall that the cumulative fourth order signal strength curve had a tail with a flatter slope than the main return. It is shown in this figure that the noise is beginning to increase significantly toward the right of the picture, and that it is selected as part of the seafloor return. To limit the target extent, a line is created based on the points at 20% and 80% of the cumulative fourth order signal strength of the selected points grouped in this potential target. This line is extended to intersect the 0% and 100% levels. The times of these intersections are chosen to be the target starting and ending points respectively. These times are shown as black vertical bars in Figure 5.22. It is then assumed that all samples contained in the segment bounded by these two times are part of the target return.

137
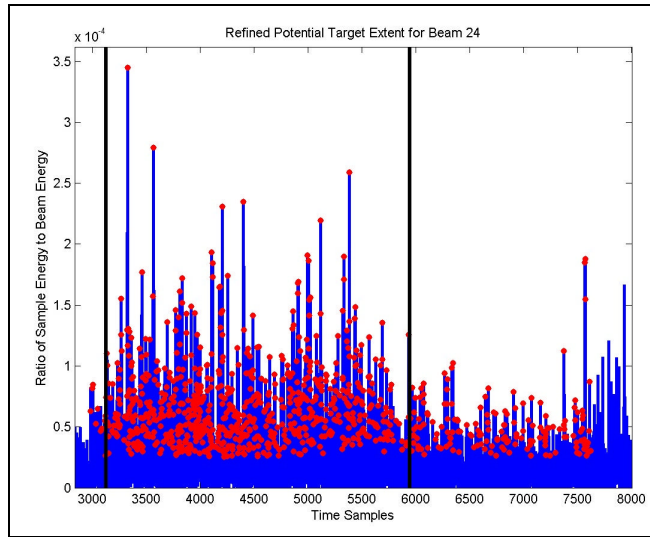
Figure 5.22. Normalized Magnitude of the Selected Target with Target Extent Limiting from Ping mud4000 Beam 24, 6x Cutoff.

Figure 5.23 through Figure 5.26 show the NB data selected as the seafloor echoes for sand3688 and mud4000. For the purpose of comparison, these figures follow the same order as those of the selected point returns for these pings (Figure 5.15 through Figure 5.18). None of these plots exhibit any noise problems except at the outer three beams on either side of nadir where the time limits cut off at least some of the seafloor returns. All of them exhibit the u-shaped pattern characteristic of multibeam sonar echoes from a horizontal seafloor. While the results shown for the 4.5x and 6.0x time limits are similar, the extents of the seafloor echoes are different for the different time limits. For pings with lower signal to noise ratios than those shown here, the estimated seafloor echo extents from the 6.0x time limit are too large, and errors that prohibit accurate seafloor detection are generated.
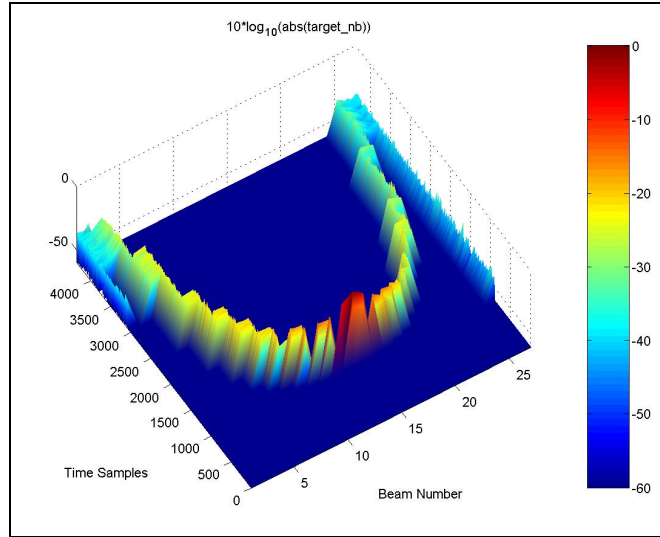
Figure 5.23. Normalized Magnitude in dB of the Selected Targets from Ping sand3688, 4.5x Cutoff – 3D View.
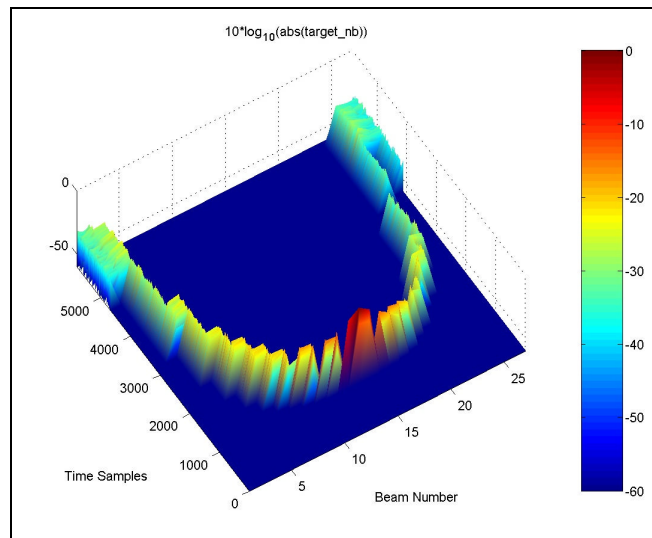
Figure 5.24. Normalized Magnitude in dB of the Selected Targets from Ping sand3688, 6x Cutoff – 3D View.
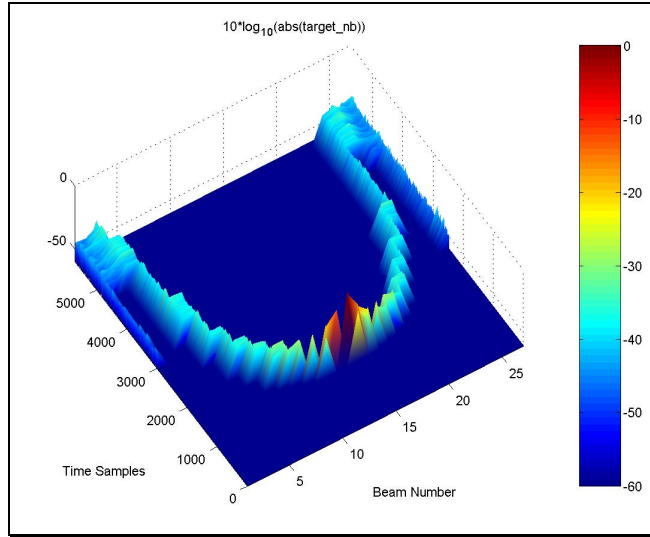
Figure 5.25. Normalized Magnitude in dB of the Selected Targets from Ping mud4000, 4.5x Cutoff – 3D View.
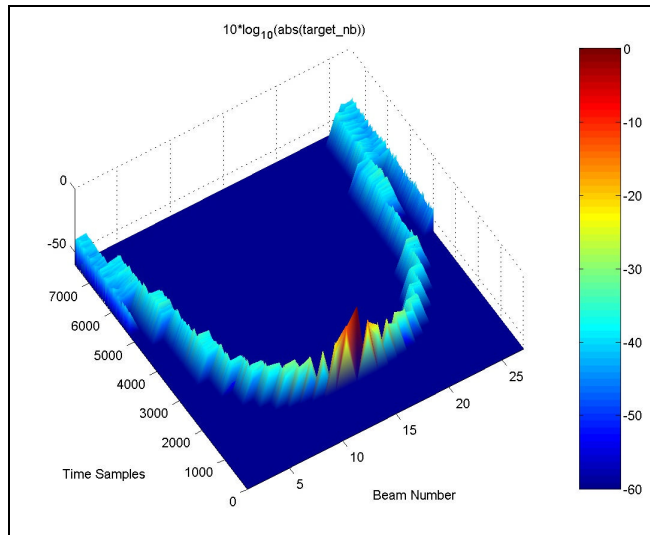
Figure 5.26. Normalized Magnitude in dB of the Selected Targets from Ping mud4000, 6x Cutoff – 3D View.

Figure 5.27 and Figure 5.28 show the normalized cumulative NB magnitude squared of the selected seafloor targets for the mud4000 data with 4.5x and 6.0x time limits respectively. Comparison with the plots in the previous section shows that the noise tail in beam 24 has been removed. The results for this particular ping show no remaining problems.
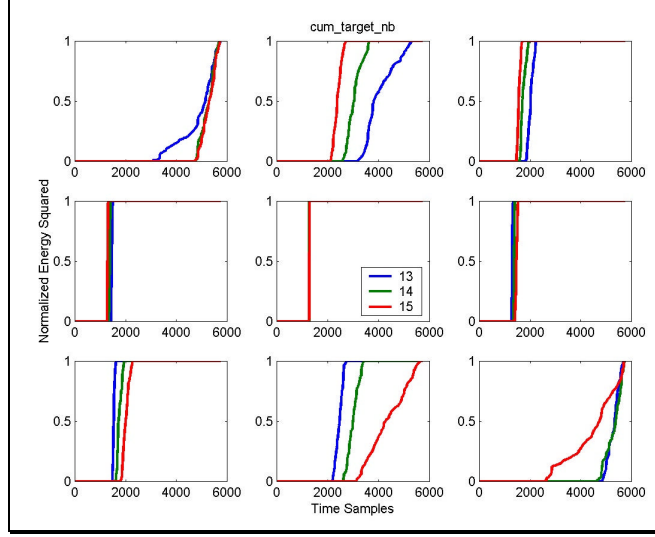
Figure 5.27. Normalized Cumulative Magnitude Squared of the Selected Targets from Ping mud4000, 4.5x Cutoff.
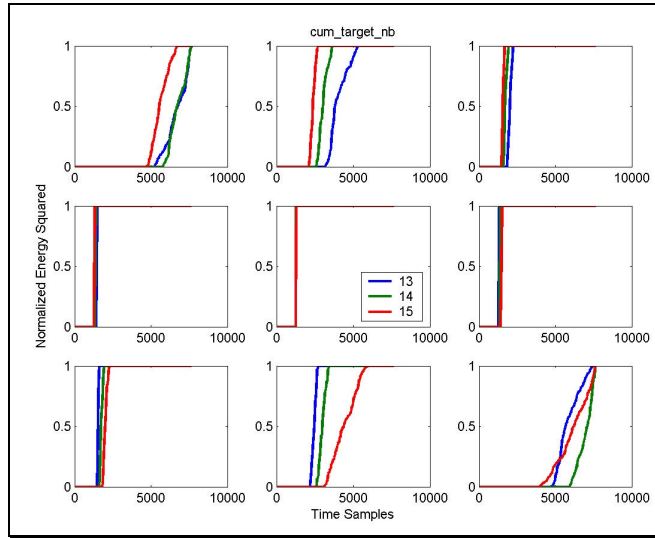
Figure 5.28. Normalized Cumulative Magnitude Squared of the Selected Targets from Ping mud4000, 6x Cutoff.

In order to estimate a single point for each beam to represent the location of the seafloor for that beam, an amplitude-squared weighted summation method is employed. The equation for this method is

$$MeanTargetTime = \frac{\sum NB_i^2 \cdot time_i}{\sum_i NB_i^2} \qquad (6.1)$$

141

for each beam. The results of this calculation are shown in Figure 5.29 and Figure 5.30

for mud4000 and sand3688 with 4.5x time limits. Both of these figures show reasonable

results for beams 4 through 24.
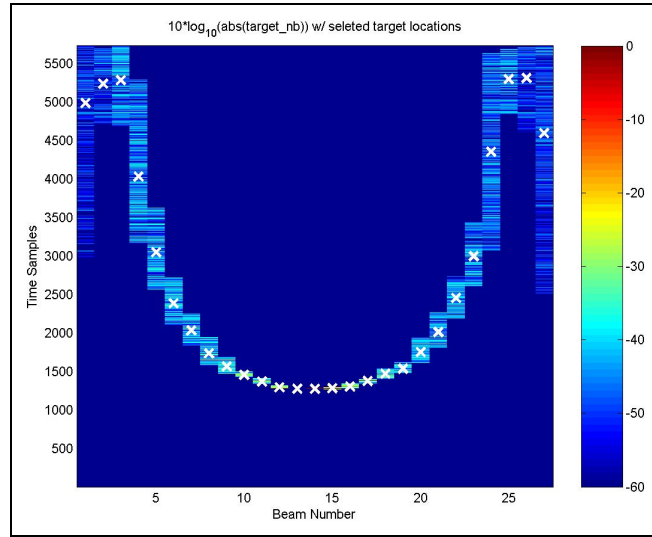
Figure 5.29. Normalized Magnitude in dB of the Selected Targets with Estimated Target
Centers from Ping mud4000, 4.5x Cutoff. (The estimated seafloor target centers are
shown with white *x*'s.)
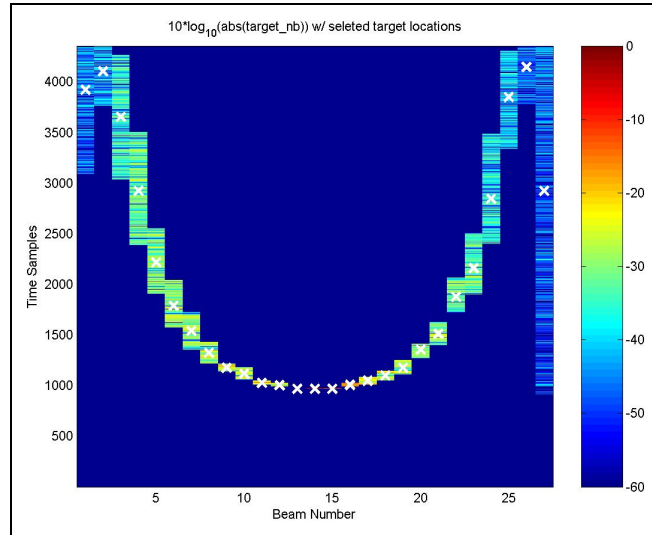
Figure 5.30. Normalized Magnitude in dB of the Selected Targets with Estimated Target
Centers from Ping sand3688, 4.5x Cutoff. (The estimated seafloor target centers are
shown with white *x*'s.)

5.1.6   Seafloor Estimate using a Minimum Energy Spring Model

Finally, after these various processing stages, a bathymetric profile is produced for each of these pings.   The remaining step is to convert the (time, angle) data into rectangular coordinates, (x, y, z) (rough positional format – ideal towed body orientation with no movement). In the case of the NB data from along-track beam pairs and nominal towed body orientation, all along-track components (x) of the beam maximum response axes have been removed. This reduces the problem to a simple conversion between polar and rectangular coordinates in two dimensions (y, z). The estimated bathymetric profiles for mud4000 and sand3688 are shown in Figure 5.31 and Figure 5.32 respectively. The selected points that survived the dual-normalized thresholding process are shown for each beam along its theoretical maximum response axis. Additionally, the estimated seafloor target centers are shown with a solid black line. The estimated extent of the seafloor target returns are shown as two black dots on each beam. This illustrates the difficulty of estimating the seafloor position in the outer beams using a magnitude only process. The targets in the three outer beams on either side of nadir were removed from the seafloor estimate in the final results (Section 5.3) based on the fact that their seafloor return extents extended beyond the 4.5x time limit used. For data sets covering more varied seafloors than those shown here, a more robust technique will be required.
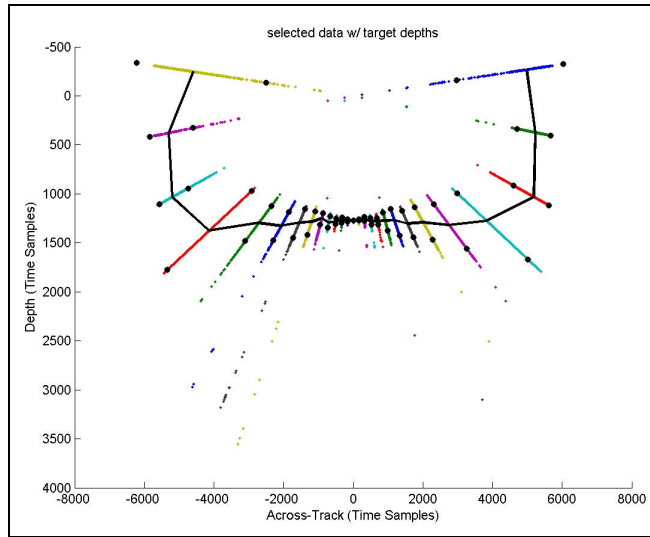
Figure 5.31. Selected Points with Estimated Selected Target Centers and Extents from Ping mud4000, 4.5x Cutoff – Rough Positional Format.
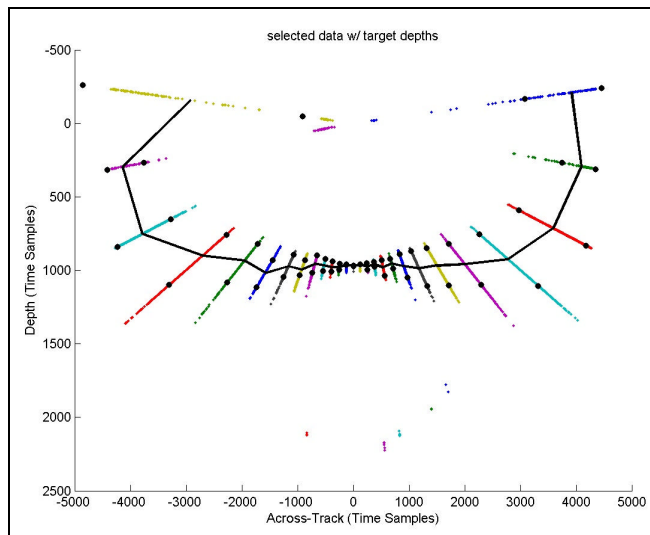
Figure 5.32. Selected Points with Estimated Selected Target Centers and Extents from Ping sand3688, 4.5x Cutoff – Rough Positional Format.

Recall from a few sections ago that all targets containing more than 25% of the fourth order signal strength of the selected points in each beam are retained. In the two cases above only one target on each beam met this criterion. However, the '25%' limiting criterion allows up to three targets to be retained on each beam. Figure 5.33 shows all targets meeting the 25% criterion for mud4000 with a 4.5x time limit when sidelobe suppression is not included in the detection process. The same type of result

144

would have occurred if there had been a few strong targets in the water column. In this case, there are two targets on both beam 9 and beam 19.
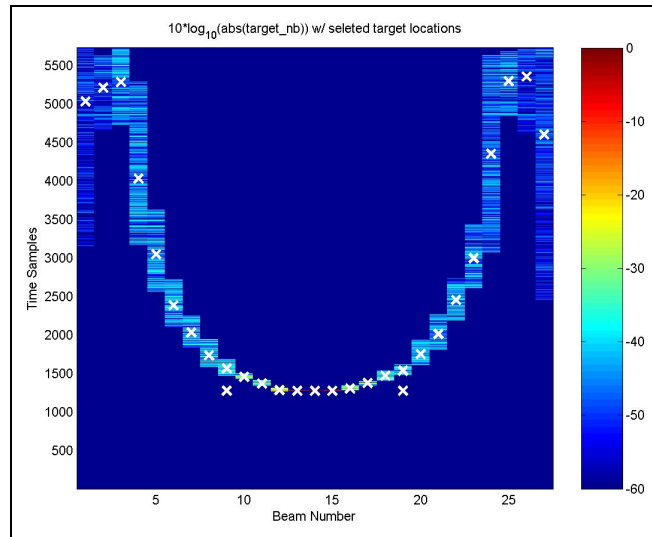
Figure 5.33. Normalized Magnitude in dB of the Targets with Estimated Target Centers from Ping mud4000 w/o Sidelobe Suppression, 4.5x Cutoff. (The estimated seafloor target centers are shown with white *x*'s.)

The estimated potential target centers are shown in rough positional format in Figure 5.34. In order to estimate correctly which targets compose the seafloor return, the assumption is made that the seafloor should provide a relatively spatially continuous echo. That is to say, if a beam has three estimated target centers and one of them lies near the single estimated target center in each adjacent beam but the other two estimated target centers of the first beam do not, it is quite likely that the former target center on that beam is the correct one. For instance, if the measurements were collected over a swath of planar seafloor, the collection of estimated target centers most closely matching a straight line would be desired. This process is achieved analytically using a minimum energy spring model. In such a model, the value assigned to a line segment connecting estimated target centers in adjacent beams is proportional to the square of its length. If the assigned values are summed across all beams for all potential paths, the path with the

145

lowest total value is assumed to represent the seafloor. By this process, the two target centers lying in the water column are removed to create the seafloor estimate shown in Figure 5.35. As expected, this is essentially identical to seafloor estimate of mud4000 shown above.

Figure 5.34. Selected Points with Estimated Potential Targets Centers from Ping mud4000 w/o Sidelobe Suppression, 4.5x Cutoff – Rough Positional Format.

Figure 5.35. Selected Points with Estimated Selected Target Centers and Extents from Ping mud4000 w/o Sidelobe Suppression, 4.5x Cutoff – Rough Positional Format.

5.1.7   <u>Acoustic Backscatter Estimate of Targets Selected to Compose the Seafloor</u>

In addition to obtaining a bathymetric estimate of the seafloor from the VSS data, the echo magnitude and shape are used to learn about the seafloor sediment type. It is often desirable to obtain specific values of the acoustic backscatter for this purpose. However, this proof of concept study looks only at the relative backscatter strength of the sample data sets.

Figure 5.36 and Figure 5.37 show the relative acoustic backscatter estimates of the seafloor for sand3688 and mud4000 versus (a) across-track distance and (b) angle from nadir. This is accomplished by calculating the mean of the square of the NB values composing the seafloor target for each beam. Since this is a fourth order signal (NB^2), backscatter values are calculated by taking five times the base ten logarithm of the mean values. Recall that the values for the three beams on either end are not valid for these sample pings. Both curves decrease sharply in magnitude away from nadir. However, mud4000 exhibits a significantly lower relative backscatter strength in the outer beams than sand3688 does. This angular dependence is an identifying characteristic which could be used to classify material types. Part (b) of each figure compares the measured data to standardized acoustic backscatter curves [APL94] for a frequency of 30kHz, where the standardized curves have been normalized to their respective maxima. The sand3688 data seems to match the *medium sand* curve. The mud4000 data does likewise for the *very fine sand* curve in the near-specular region. However, in the other regions, the measured data yields acoustic backscattering strengths lower than those for any grain size in the standardized curves. This most likely is due to a difference in the definition of

how the acoustic backscattering strength estimate is defined here and in the standardized
curves.
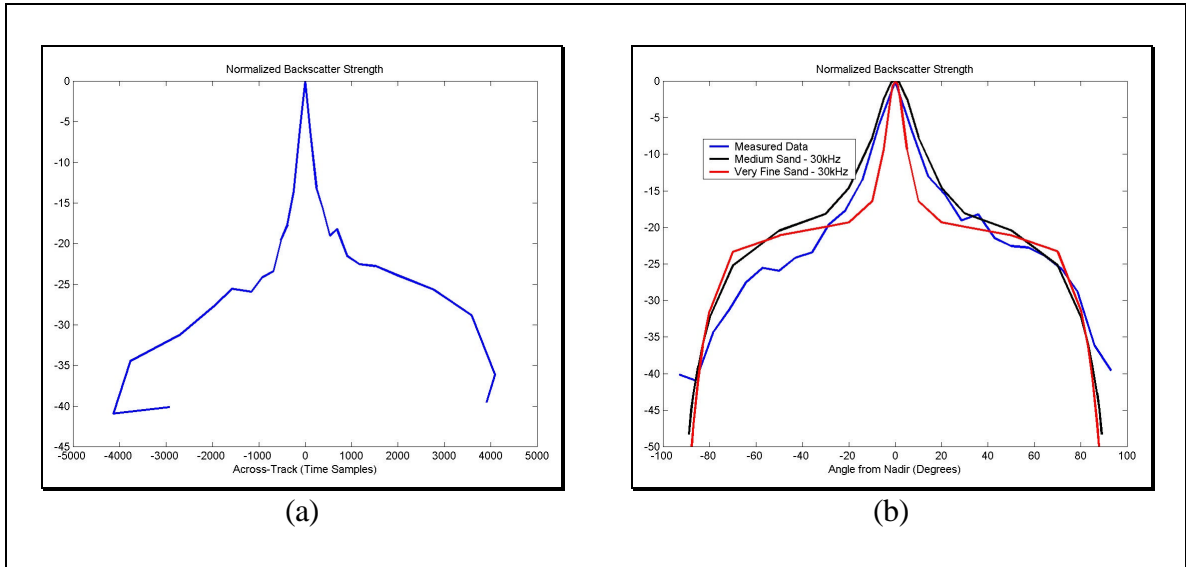
Figure 5.36. Normalized Magnitude in dB of the Estimated Acoustic Backscatter
Strength of the Selected Targets from Ping sand3688, 4.5x Cutoff: (a) vs. Across-Track
Distance, (b) vs. Angle from Nadir.
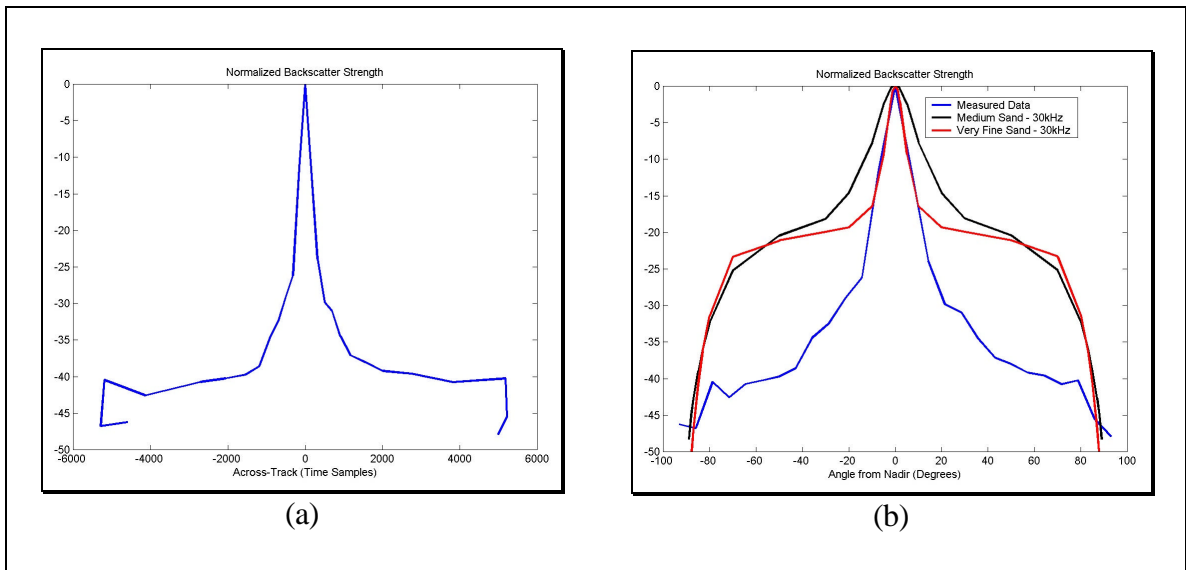
Figure 5.37. Normalized Magnitude in dB of the Estimated Acoustic Backscatter
Strength of the Selected Targets from Ping mud4000, 4.5x Cutoff: (a) vs. Across-Track
Distance, (b) vs. Angle from Nadir.

5.2   Position Corrections

5.2.1   Specific Measured Values Compensated For

There are fifteen towed body orientation and sound speed characteristics that were recorded during the collection of the pings in sample data sets 019 and 022 used in this report. These are plotted in Appendix C. None of these were taken into account in the calculations of Section 5.1. The towed body depth, the towed body pitch, the towing speed and the acoustic sound speed are used for the full data sets. The correction for towed body depth is straightforward and is applied when the seafloor relief estimates of the previous section are converted into depths (time into distance). The towing speed is used to calculate the forward motion of the towed body between pings. The other two parameters are necessary for ray tracing as discussed in the following section.

5.2.2   Ray Tracing

Thus far the assumption has been made that the transmitted signals follow straight paths through the water, i.e. the water is homogeneous. However, a sound speed profile (Figure 5.38) recorded during the data set collection exhibits a negative gradient. It has been extended to the surface and infinite depth using the slopes of the uppermost and lowermost segments respectively, which were both zero in this case. This extension allows for an estimation of the sound speed profile in regions for which data is not available, e.g. all regions of more than fifty meters depth. The assumption has been made that this sound speed applies to all locations in the survey area, i.e. the water column is a horizontally layered medium. The other curve in this figure is the mean harmonic sound

149

speed assuming that the towed body is situated at 9.2 m depth with a local sound speed of 1538.5 m/s. The mean harmonic sound speed is the mean sound speed to any depth along a vertical path, i.e. perpendicular to the layers [Mou04].
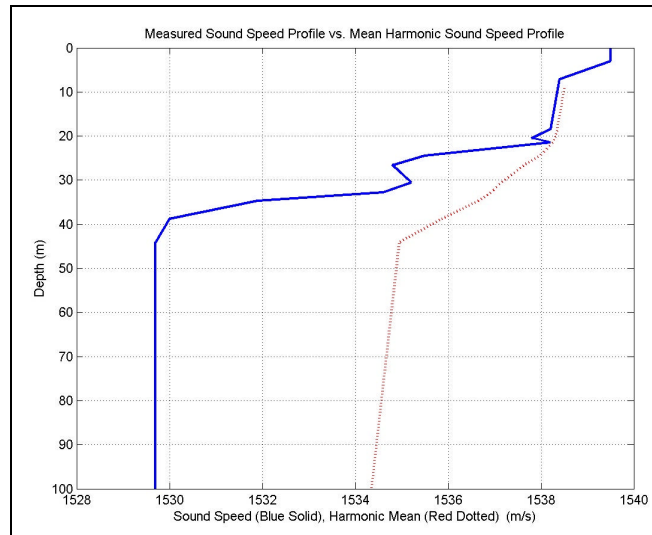
Figure 5.38. Measured Sound Speed Profile and Mean Harmonic Sound Speed Profile for Data Sets 019 and 022 – Starting at 9.2 m Depth and 1838.5 m/s Sound Speed.

This sound speed profile suggests that the rays launched below the horizontal plane containing the array axis will be bent toward nadir. This would make the seafloor estimates deeper and closer to nadir than previously calculated. This is shown in simulation for beams 2 through 14 in Figure 5.39 using the sound speed profile shown above. As expected, the seafloor estimates are pulled down and to the left compared to the straight path solutions. In other words, the uncorrected seafloor estimate of a horizontal seafloor will tend to curl towards the sea surface at its ends. This effect will be demonstrated in the following section. The beam angles used assumed a nominal towed body orientation. If there is any towed body pitch, the initial ray angles from nadir will be increased. This will result in increased distortion in addition to moving the estimated seafloor targets fore or aft of nadir.
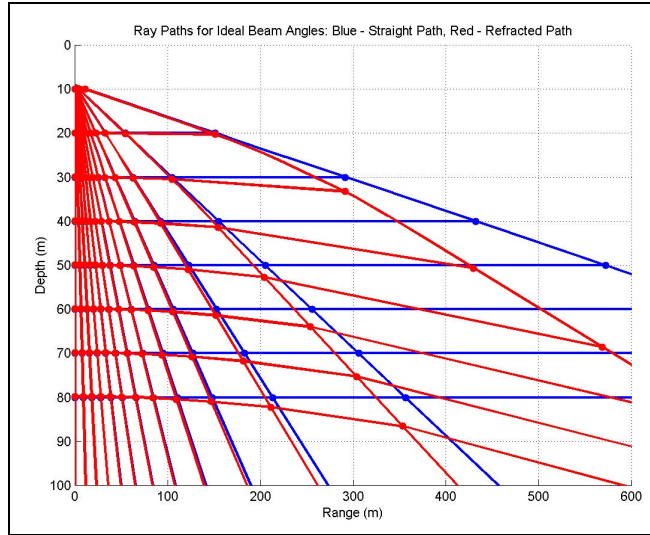
Figure 5.39. Simulated Ideal and Actual Ray Paths for the Measured Sound Speed Profile for Data Sets 019 and 022 – Starting at 9.2 m Depth and 1538.5 m/s Sound Speed.

5.3   Bathymetry and Acoustic Backscatter Imagery

Here at last are the results that have been pursued. Figure 5.40 and Figure 5.41 show the bathymetric results of applying the seafloor detection algorithm and corrections discussed previously to sample data sets 019 and 022 respectively. These contain ping numbers 3515 through 3699 and 4070 through 4254 respectively – 185 pings in each group. Initial results show a hillside for data set 019 and a relatively flat area for data set 022. They also show some errant results in the form of extreme outliers. The causes of these outliers are discussed in the following section. The bathymetry for data set 019 retains beams 4 through 24 (150° swath), but the bathymetry for data set 022 retains only beams 5 through 23 (136° swath) because the same form of noise corruption that is seen in the outlying seafloor estimates shown below distorts the results in beams 4 and 24 for data set 022.
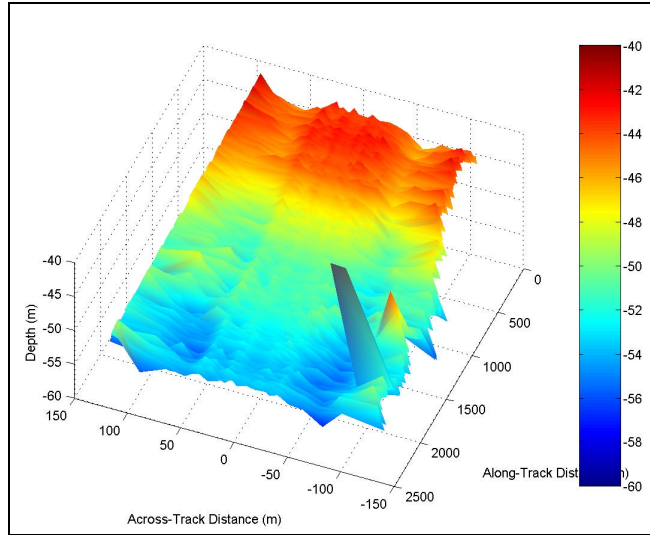
Figure 5.40. Bathymetry of Data Set 019 with Outliers, 4.5x Cutoff – 3D View.
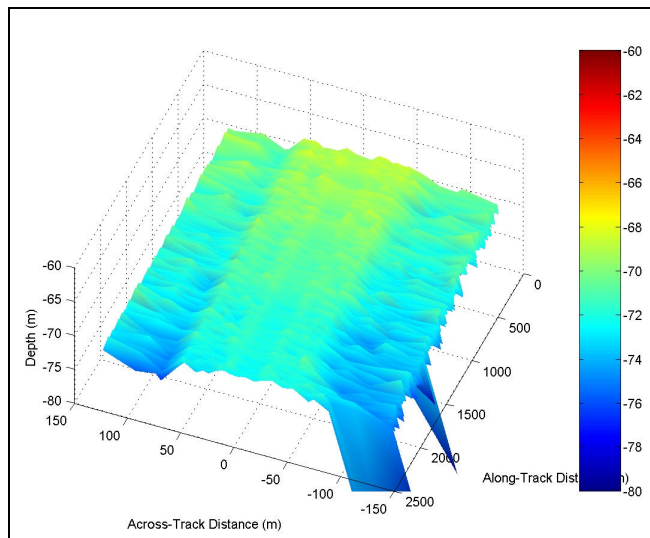
Figure 5.41. Bathymetry of Data Set 022 with Outliers, 4.5x Cutoff – 3D View.

The worst outliers are removed using depth thresholds. The remaining outliers are removed by looking for points with depth differences varying by more than a few meters from the mean depth for the adjacent beams from that ping. The cleaned bathymetry is shown in Figure 5.42 through Figure 5.45 for both data sets in both the standard and overhead views. This data looks smooth within fifty meters of nadir. The rougher estimates further from nadir are the result of the low resolution nature of the seafloor returns in these outer beams. One systematic error that appears in these figures

is the appearance of a trench on either side of nadir that follows along the direction of travel. The returns on these particular beams occur slightly before the seafloor-to-surface-to-seafloor multiples of the nadir reflection are seen by the beams' sidelobes. These returns are not separable by the current detection algorithm and pull the seafloor estimates down in these areas. One other seafloor feature that is clearer in the overhead view of the bathymetry for data set 019 is the appearance of several small hills at the base of the main slope just beyond 1500 m from the start. Note that in the case of these two data sets the nose of the towed body is always slightly above horizontal. This is the cause of the slightly forward positions (with respect to nadir) of the outer beam seafloor estimates.
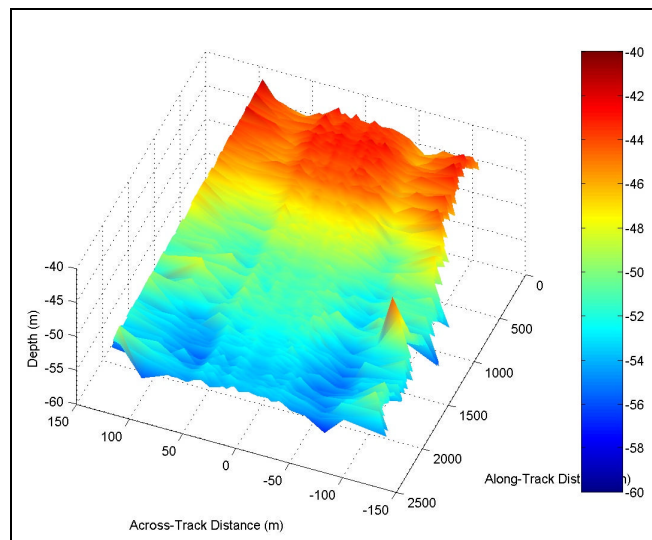
Figure 5.42. Bathymetry of Data Set 019, 4.5x Cutoff – 3D View.
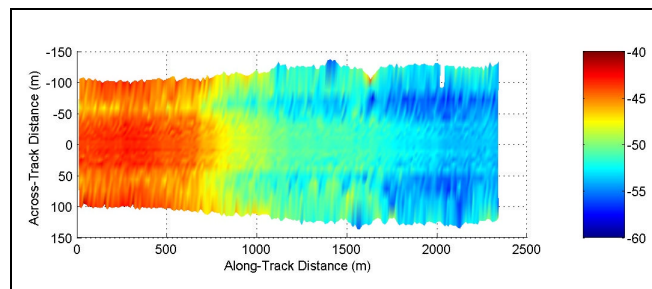
Figure 5.43. Bathymetry of Data Set 019, 4.5x Cutoff.

153
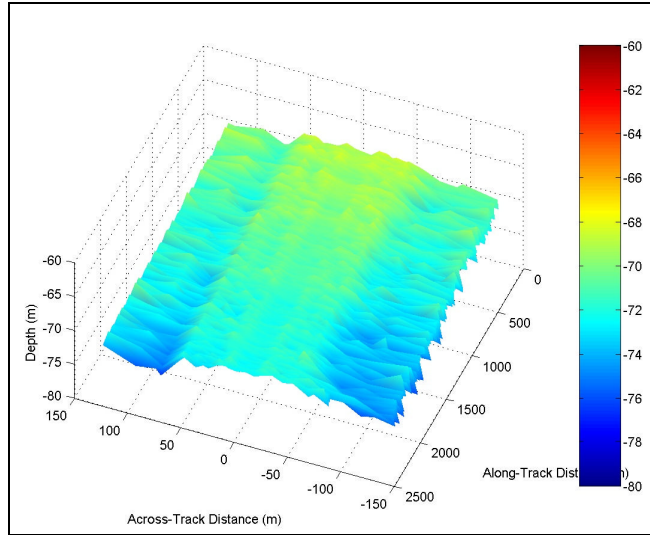
Figure 5.44. Bathymetry of Data Set 022, 4.5x Cutoff – 3D View.
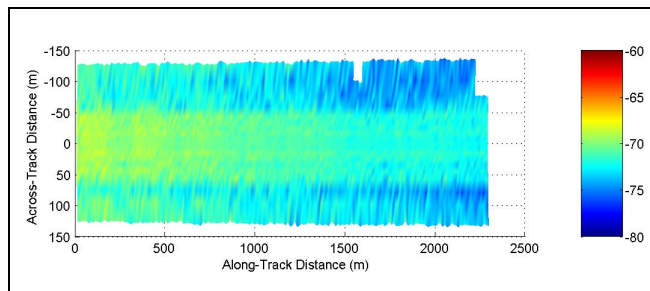
Figure 5.45. Bathymetry of Data Set 022, 4.5x Cutoff.

Figure 5.46 through Figure 5.49 show the relative seafloor acoustic backscatter for both data sets in both 3D and conventional overhead, i.e. sidescan sonar, views. Data set 022 has a relatively homogeneous set of returns indicative of a consistent sediment type. The backscatter from data set 019 is of greater interest. Recall those small hills that were seen in the bathymetry, these appear to have significantly different acoustic characteristics. Although they do not appear here, there were some targets in the water column in this area that may have been schools of fish. The bathymetric and acoustic backscatter characteristics in these regions may be altered by these targets as well. Additionally, there appears to be boundaries between regions of different sediment types in the direction of towed body travel. The maximum response from data set 019 was 5.3

dB stronger than the maximum response from data set 022 after the spreading loss correction.
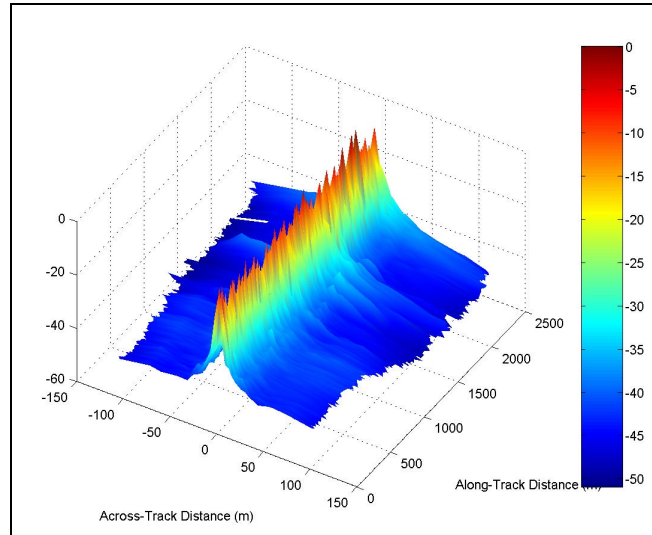
Figure 5.46. Seafloor Acoustic Backscatter of Data Set 019, 4.5x Cutoff – 3D View.
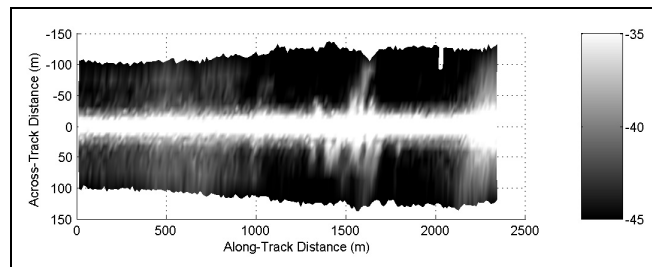
Figure 5.47. Seafloor Acoustic Backscatter of Data Set 019, 4.5x Cutoff.
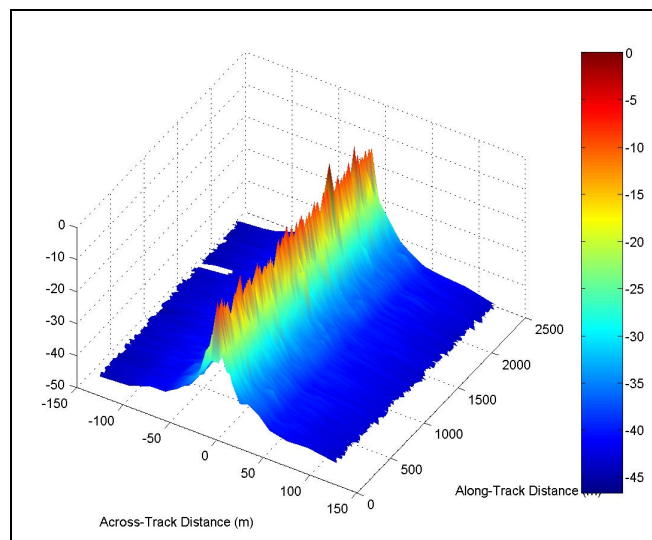
Figure 5.48. Seafloor Acoustic Backscatter of Data Set 022, 4.5x Cutoff – 3D View.
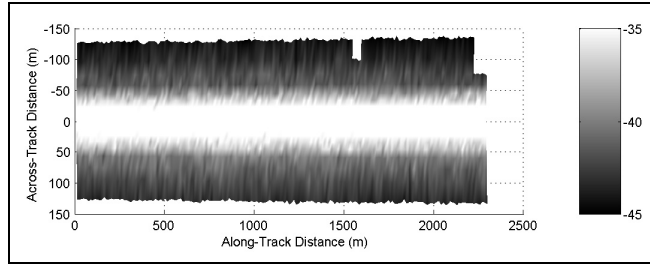
Figure 5.49. Seafloor Acoustic Backscatter of Data Set 022, 4.5x Cutoff.

5.4   Problematic Pings

5.4.1   Target and Noise Separation

Two distinct types of detection errors produced the outliers shown in the bathymetry of the previous section. The outliers which appeared to be significantly deeper than the seafloor actually was, are the result of an inability to separate the seafloor echoes from the long range noise. Figure 5.50 shows the NB data for ping 4253 from data set 022. While the seafloor return is visually detectable out to the time limit, it is apparent that there is also noise of the same order of magnitude as the signal near the time limit. This is even more evident in Figure 5.51, which shows the points selected as potential target returns, and in Figure 5.52, which shows the extents of the targets selected to represent the seafloor. Because of the large variance caused by the high noise level, the estimated target extent extends beyond the time limit for several beams

156
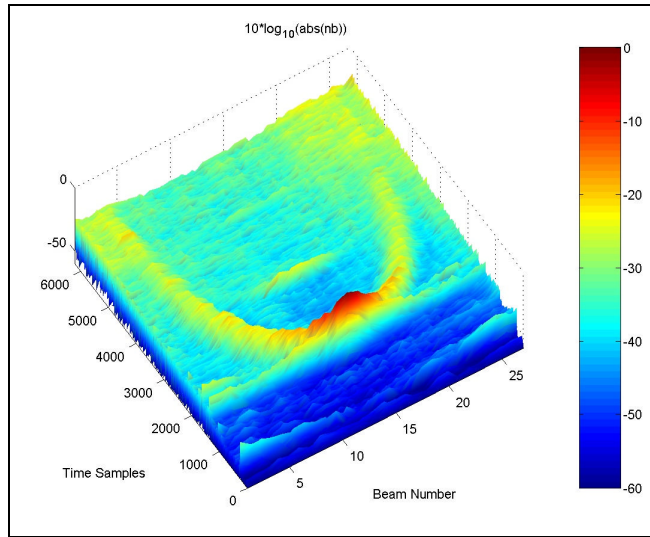
Figure 5.50. Normalized Magnitude in dB of the NB of Ping 4253, 4.5x Cutoff – 3D View.
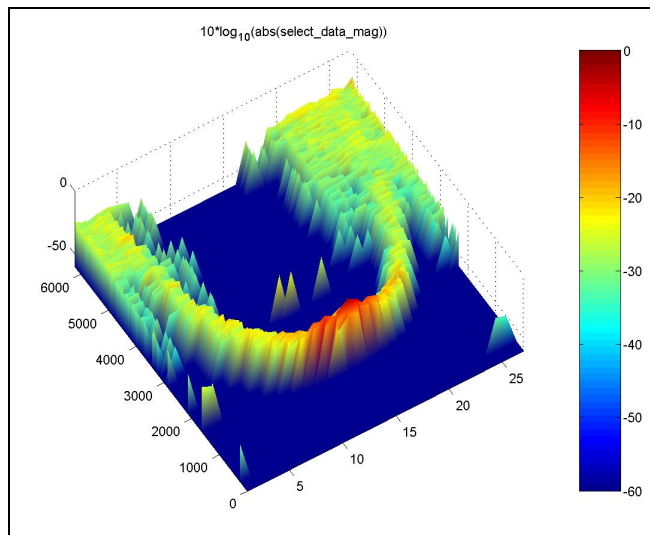
Figure 5.51. Normalized Magnitude in dB of the Selected Points from Ping 4253, 4.5x Cutoff – 3D View.
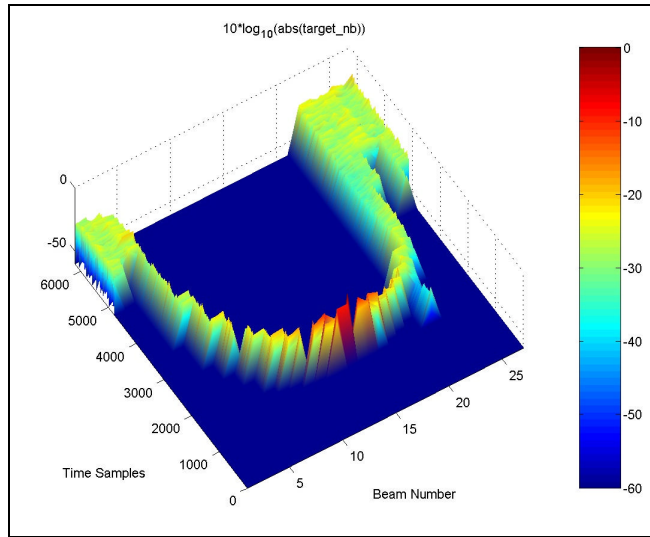
Figure 5.52. Normalized Magnitude in dB of the Selected Targets from Ping 4253, 4.5x Cutoff – 3D View.

Figure 5.53 shows the points selected as part of the seafloor target for beam 22 of ping 4253. The separation between the seafloor return and the long range noise is clearly visible. However, since there is no long gap in the selected points, all of these selected points were included in a single target. The standard deviation of this data is so high that the refined target extent limits are outside of the visible region of the figure. The bimodal shape of the selected return could be used as a flag for either rejection or further processing. Unfortunately, the bimodal shape is not always are distinct as it is in this case.
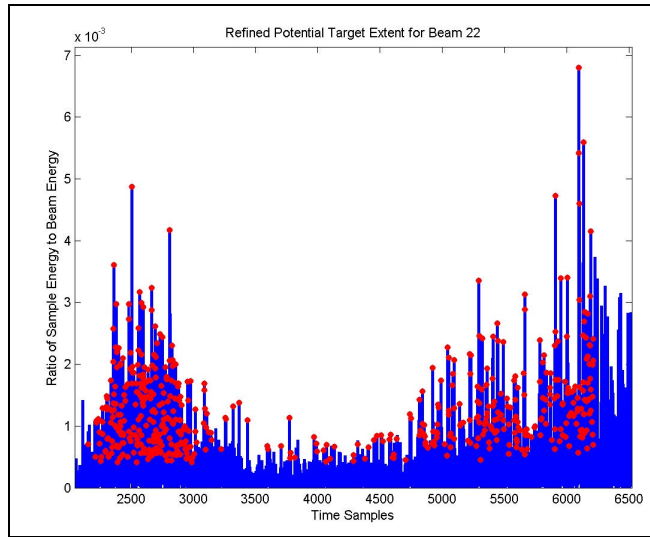
Figure 5.53. Normalized Magnitude of the Selected Target with Target Extent Limiting from Ping 4253 Beam 22, 4.5x Cutoff.

Figure 5.54 and Figure 5.55 show how this inability to separate the seafloor targets from noise affects the bathymetry estimate. Figure 5.54 shows that there are two potential seafloor targets in both beams 20 and 21. Clearly, one of these is the result of increased noise at long ranges. In beams 22 through 24 the noise cannot be distinguished from the seafloor return by this detection method. Thus, the errant results are created.
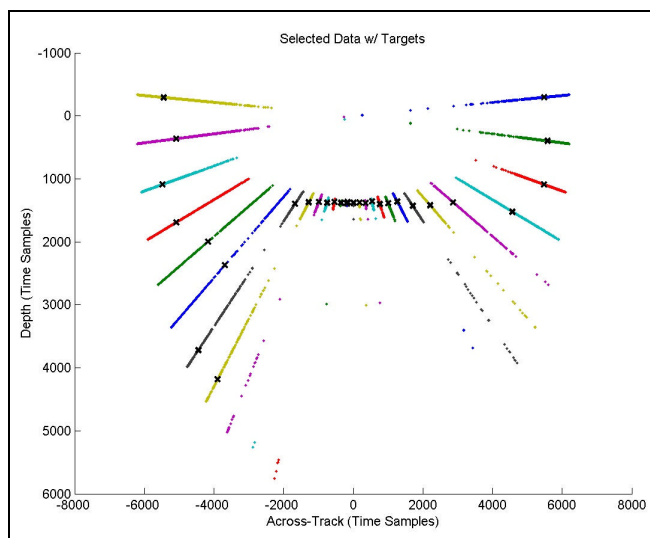
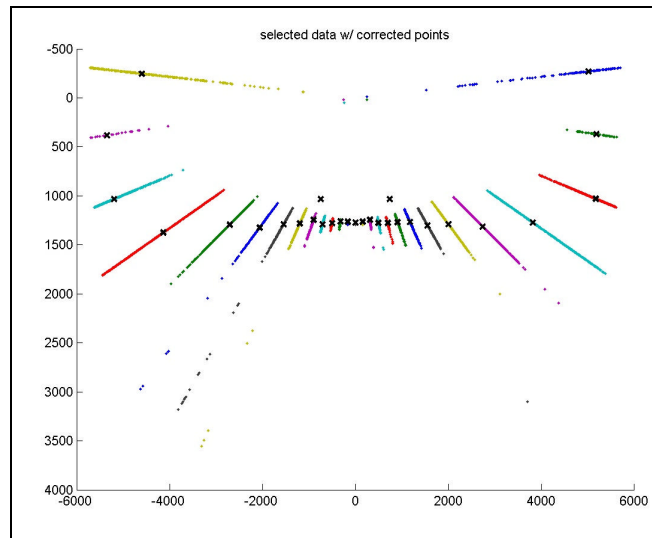Figure 5.54. Selected Points with Estimated Potential Targets Centers from Ping 4253, 4.5x Cutoff – Rough Positional Format.

159
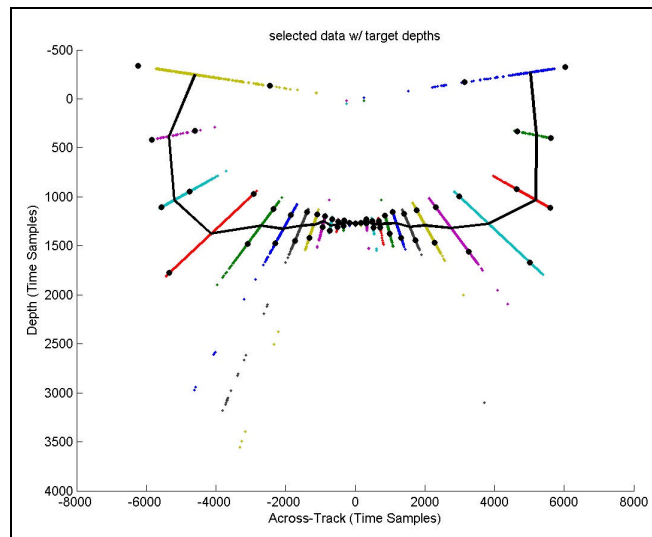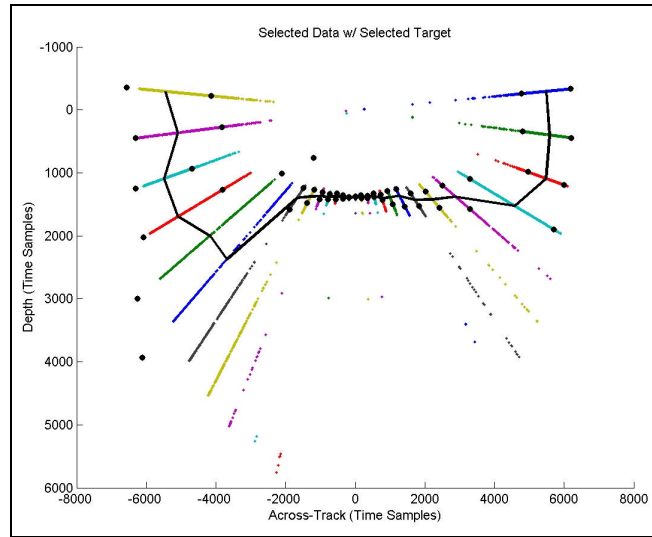
Figure 5.55. Selected Points with Estimated Selected Target Centers and Extents from Ping 4253, 4.5x Cutoff – Rough Positional Format.

5.4.2 Minimum Energy Spring Model

The other bathymetric outlier that was seen in the initial bathymetry estimates is caused by a different type of error. In this case, it is an echo multiple that causes the error. Figure 5.56 through Figure 5.58 illustrate how the seafloor-to-surface sidelobe returns are mistaken by the detection algorithm for seafloor returns. The sidelobe returns of the surface reflections themselves are not a problem because they have been severely reduced by the spreading loss corrections. One fascinating feature seen in Figure 5.56 is a seafloor-to-towed_body-to-seafloor reflection of the near nadir beams (around time sample 1900). This multiple reflection occurs in several pings in this region.
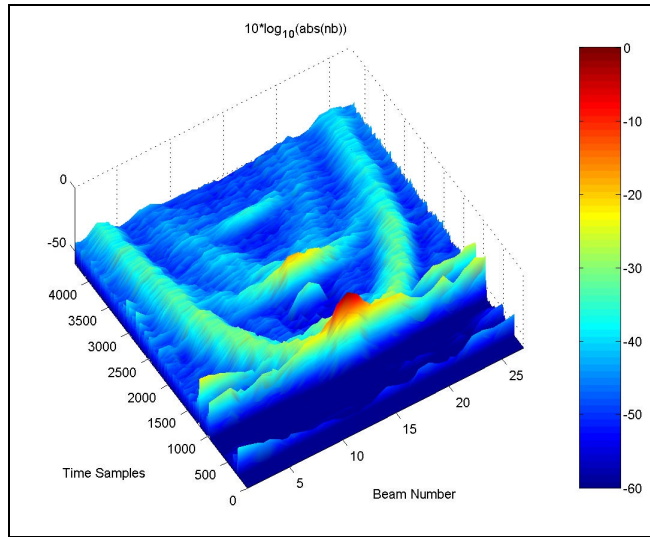
Figure 5.56. Normalized Magnitude in dB of the NB of Ping 3671, 4.5x Cutoff – 3D View.
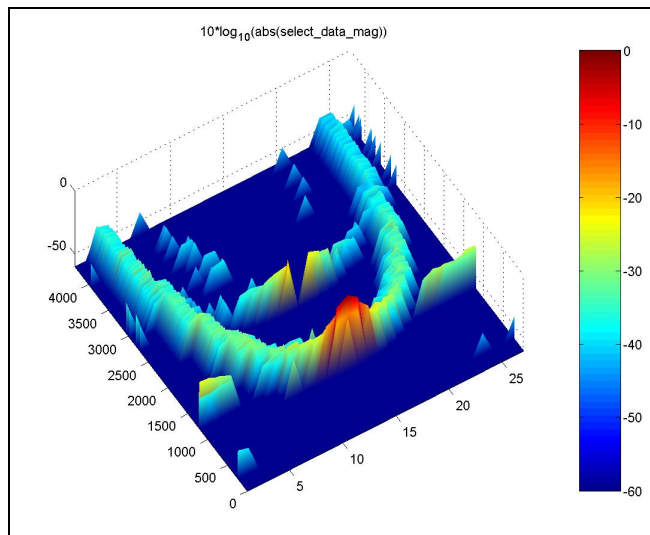
Figure 5.57. Normalized Magnitude in dB of the Selected Points from Ping 3671, 4.5x Cutoff – 3D View.
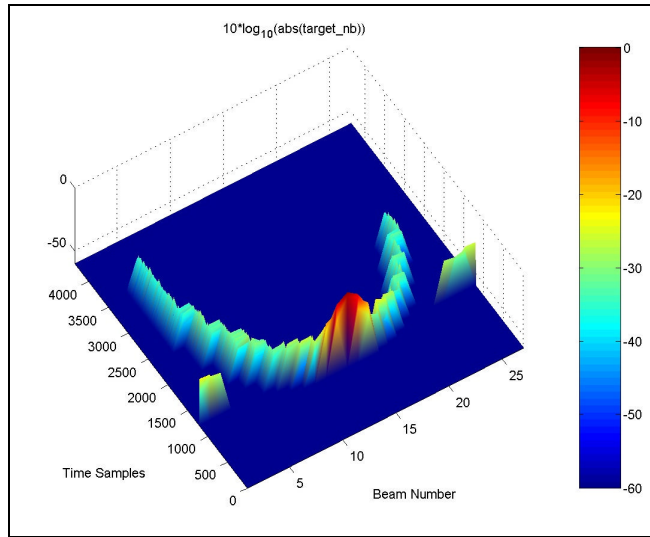
Figure 5.58. Normalized Magnitude in dB of the Selected Targets from Ping 3671, 4.5x Cutoff – 3D View.

The seafloor detection algorithm chooses the seafloor-to-surface multiples rather than the seafloor echoes because of a blind application of the minimum energy spring model to beams that contain targets from the sidelobes of the seafloor-to-surface returns in addition to targets from the main lobe seafloor returns (Figure 5.59). Figure 5.60 shows the resulting minimum energy path.
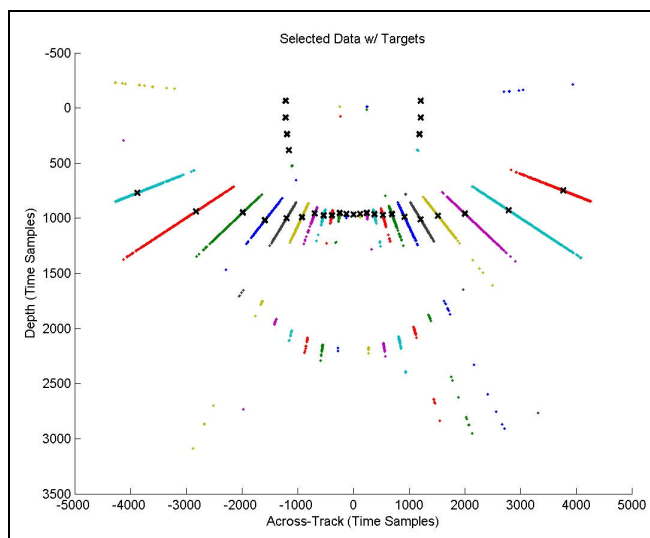
Figure 5.59. Selected Points with Estimated Potential Targets Centers from Ping 3671, 4.5x Cutoff – Rough Positional Format.
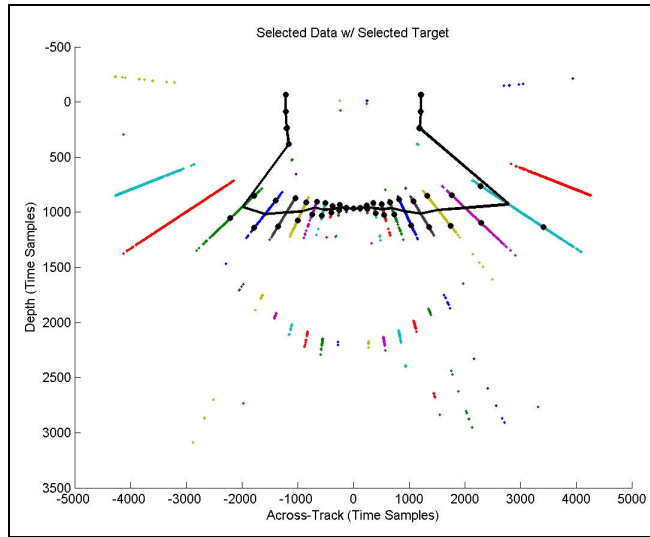
Figure 5.60. Selected Points with Estimated Selected Target Centers and Extents from Ping 3671, 4.5x Cutoff – Rough Positional Format.

5.5   Comparison with Data From an Alternate Source

For the sake of comparison, bathymetry and backscatter covering the same area as the latter portion of data set 022 has been obtained from an alternate source [G+0?]. This data was recorded using a 95 kHz Kongsberg Simrad EM1002 multibeam echo sounder. The depth accuracy was stated to be better than 0.5% of the water depth (better than 0.4 meters in this case). This was determined from the towed body track shown in Figure 5.61. Unfortunately, the alternate source did not contain any information about the area covered by data set 019.
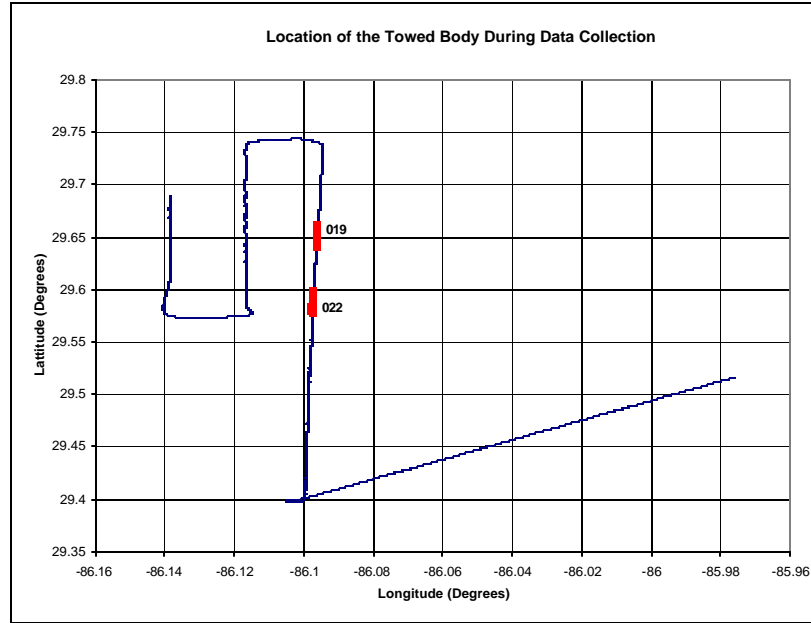
Figure 5.61. Towed Body Track.

In Figure 5.62 the estimated bathymetry from data set 022 is overlaid on the alternate source data. This comparison shows a constant offset between the two surfaces. Assuming that the alternate bathymetry is correct and the near-nadir (specular) beams are the mostly likely to be correct of the bathymetry estimated from VSS data, the estimated bathymetry from data set 022 is lowered by 2.8 m as shown in Figure 5.63. This aligns the near-nadir beams with the alternate bathymetry. Figure 5.64 shows only the near-nadir beams with the alternate data in order to better show the alignment between the two data sets.

This offset agrees with that of rough positional format plots in Chapter 4. In these rough positional format figures the sidelobes of the surface return seem to extend to some point above the surface. Figure C.2 records the altitude of the towed body, which agrees relatively well with the VSS data where it isn't corrupted. Harris, Avera and Bibee [HAB02] explain that some of this error is the result of assuming that the towed body is motionless when estimating depth from the pressure gauge. The increased static pressure

164

from the forward towed body motion acts as bias to the depth estimates. They estimated the total offset error from the bias and potential calibration issues of the pressure reading to be roughly 1.7 meters for the VSS data set. It is possible that the relatively constant towed body pitch offset of four degrees (nose up) could affect the depth measurement (Appendix C). Some of the remaining offset error might result from a tidal shift in the water depth on the day that the sample data sets were collected.
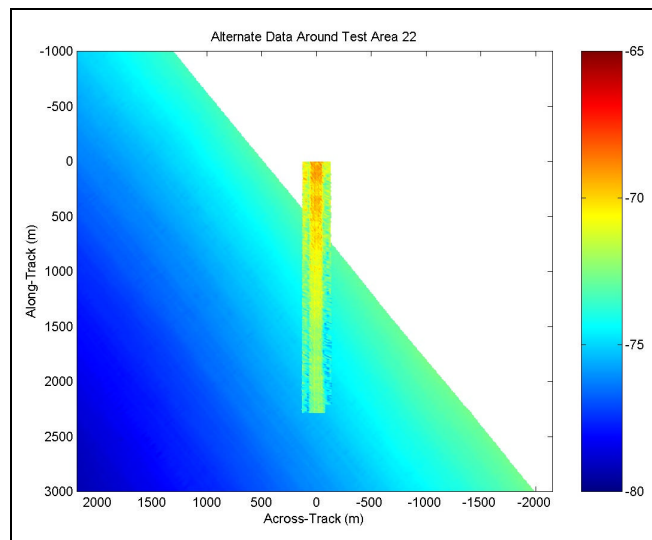
Figure 5.62. Alternate Bathymetry Around Area 022 with the Estimated Bathymetry from Data Set 022.
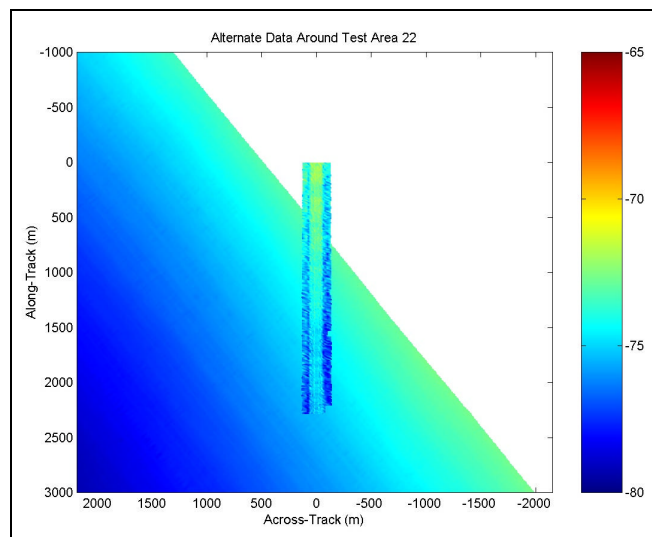
Figure 5.63. Alternate Bathymetry Around Area 022 with the Estimated Bathymetry from Data Set 022 – Shifted.
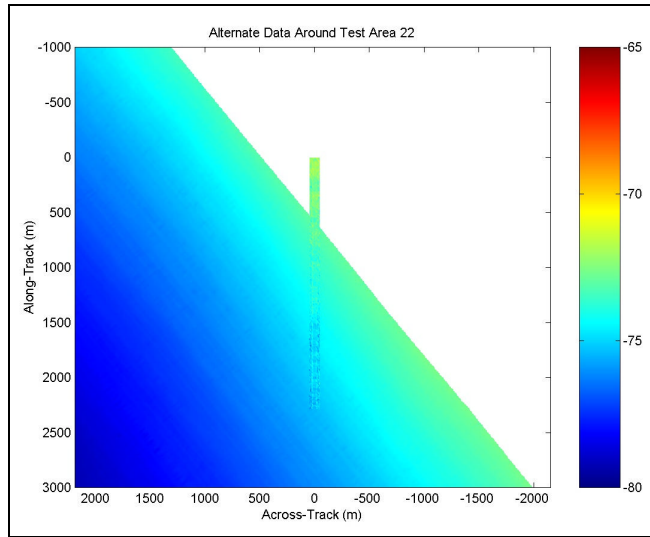
Figure 5.64. Alternate Bathymetry Around Area 022 with the Estimated Bathymetry from Data Set 022 – Shifted, Near-Nadir Beams only.

Figure 5.65 shows the relative seafloor acoustic backscatter from the alternate data source for the same area around sample data set 022 that is used in the backscatter figures. This area contains relatively uniform seafloor acoustic backscatter characteristics, which agrees with the seafloor acoustic backscatter estimates for sample data set 022.
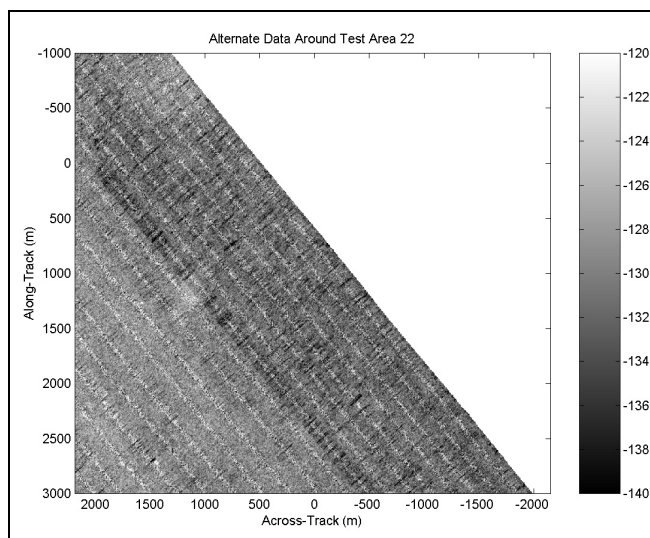
Figure 5.65. Alternate Relative Seafloor Acoustic Backscatter Around Area 022.

5.6 <u>Summary</u>

In addition to desirable target returns from objects such as the seafloor, the sea surface and water column targets; several undesirable target returns were included in the data. These included the echoes sensed by sidelobes of beams with main lobes pointed in other directions and several multipath returns including seafloor-to-surface, surface-to-seafloor, seafloor-to-sonar-to-seafloor, seafloor-to-surface-to-seafloor and seafloor-to-surface-to-seafloor-to-surface-to-seafloor returns. For the purposes of this research, only the seafloor returns were of interest, and the detection algorithm was designed accordingly. This task was simplified by the fact that the sample data sets used for implementation contained relatively flat seafloors with minimal water column targets. The robustness of this algorithm to operation in other types of environments is unknown.

A magnitude-only seafloor detection algorithm for NB data generated from along-track beam pairs is employed. This algorithm eliminates the effects of amplified noise at large ranges by limiting the detection process to signals arriving prior to 4.5 times the arrival time of the strongest near-specular return. Under the assumption of ideal conditions over a horizontal seafloor, this allows swath widths of 75° from nadir. Subsequently, significant seafloor returns are brought into the same order of magnitude while the noise floor is reduced by applying an energy squared normalization to the data of each beam and a maximum signal strength normalization to the data from each time sample. Following these normalizations, a signal/noise threshold is set at roughly one percent (-20dB) of this dual-normalized beam energy squared. The surviving potential target returns are restored to their original NB values for further processing.

The algorithm employed detects targets within each beam independently. The potential target returns from each beam are grouped by comparing their first difference time separation to the standard deviation of the potential target returns in that beam and a constant of 500 samples (≈ 20m). Thresholding is used on these grouped target returns to retain no more than three strong targets from any one beam. The time (range) extents of these potential targets are then refined in order to remove any noise tails that exist within them. Finally, a center of mass estimate is used to estimate the potential target time of arrival.

In order to determine which of these potential targets are actually from the seafloor, a minimum energy spring model is employed to find the collection of target echoes (one per beam) which represent the most linearly continuous shape. This condition of spatial continuity is considered to be one of the most unique characteristics of target echoes from the seafloor. Subsequently, simple corrections are applied to these estimated seafloor target locations using other recorded data such as towed body depth and pitch and a sound speed profile.

Two sample groups of pings were analyzed by this process to obtain bathymetry and mean relative seafloor acoustic backscatter within the estimated seafloor target return extents. The bathymetry shows both sloped and relatively flat areas including areas that are possibly some small hills. The trenches that appear in the bathymetry parallel to the direction of travel are an artifact of the magnitude-only detection process. The acoustic backscatter reveals some large amplitude variations in the vicinity of the small hills, suggesting that they are different in material type from the surrounding seafloor medium. There is also the appearance of boundaries between bordering regions of different

sediment types. This shows the potential the VSS to produce a rough estimate of the seafloor texture in much the same manner that a sidescan sonar would, while operating at a much higher forward speed in the range of 10 to 14 m/s. A final comparison of some of this data with that from an alternate source did reveal that there appears to be an offset problem with the towed body depth estimate resulting primarily from the effects of hydrodynamic forces on the pressure sensor used to estimate towed body depth. However, this detection algorithm demonstrates the concept that seafloor relief and texture are obtainable with this system over swath widths of roughly 140°.

CHAPTER 6

CONCLUSION

6.1   Summary of the Completed Research

This document has focused on increasing the swath width of environmental information, e.g. bathymetry and acoustic backscatter imagery, that is obtainable from the volume search sonar (VSS) of the AQS-20 mine countermeasure system, beyond 90°. This was accomplished by using pulse compression, a narrow-beam monopulse technique and a seafloor detection algorithm designed specifically for the VSS data set to increase the signal-to-noise ratio. A combined processing gain of about 17.3 dB was obtained in the SNR from the pulse compression and the NB monopulse technique.   Potential additional increase in SNR resulting from the seafloor detection process has not been quantified.

The use of a 37.5 kHz transmission pulse center frequency produces minimal across-track scalloping and along-track sidelobes among frequencies in the range 25 kHz to 50 kHz according to the simulation results of Chapters 2. The simulation results of Chapters 3 illustrate that the stepped FM transmission pulse is a useful approximation to the optimal linear FM chirp. This allows for an increase in the system range resolution through the use of pulse compression techniques.

The configuration of the receive beam geometry allows for the use of both along-track and across-track beam pairs with monopulse techniques, which are used to improve angle of arrival estimates. Due to the simplicity of their spatial configuration, the along-track beam pairs were chosen for use in this proof of concept research. Because the beams in each along-track pair share a common phase center, no phase information is available in the monopulse results for these beam pairs to indicate that a target is present. Thus, the data from the narrow-beam (NB) monopulse technique was chosen for use in the seafloor detection process due to its superior magnitude response compared to the other two monopulse techniques reviewed.

The seafloor detection algorithm selects a portion of data likely to contain the seafloor echoes; normalizes and thresholds this data to separate the signal from noise; groups the remaining signal components into potential targets on each beam, irrespective of the other beams; produces weighted estimates of the central arrival time of each potential target; and selects the most linearly continuous collection of targets across the beams as the seafloor echo. These estimated seafloor echo times of arrival are corrected for several factors including: refraction, and towed body depth and pitch. Seafloor acoustic backscatter estimates are also made within the detected time intervals of the seafloor echoes. The resulting acoustic backscatter images indicate lines of separation between regions of different acoustical properties, showing the potential of this system to assess bottom texture while operating at a forward speed of 10 to 14 m/s. This detection process was tested with data from two regions containing relatively flat seafloors and negligible water column targets, and the accuracy of the results has not been quantified. However, this work demonstrates that it is possible to obtain seafloor relief and texture

over a swath width of roughly 140° using the VSS of the AQS-20 mine countermeasure system, which is a significant extension of the 90° swath width achieved in the previous work [H^{+}01], [H^{+}02].

6.2   Future Considerations

For a full bathymetric solution, corrections must be applied for additional towed body parameters, e.g. roll and yaw, shown in Appendix C. While the roll is relatively small with only a few tenths of a degree of variation, the yaw is a few degrees in magnitude, and its correction may serve to better align some of the small hills seen on the seafloor in Section 5.3. Additionally, corrections for the towed body location from the towed body track shown in Figure 5.61 could be applied to earth reference the data.

Using data from conjugate-product (CP) and difference-over-sum (DS) monopulse techniques applied to across-track beam pairs will allow for a combined magnitude and phase based seafloor detection algorithm. Using detection algorithms on data from both along-track and across-track based algorithms potentially provides three seafloor profiles for each ping, as shown in the VOL SR NB simulation results in Figure 6.66. While the areas of the seafloor ensonified by these three profiles do overlap (implying that they are correlated), the detection techniques using CP or DS data for the outer profiles should improve the spatial resolution of the seafloor detection, which will reduce this correlation.
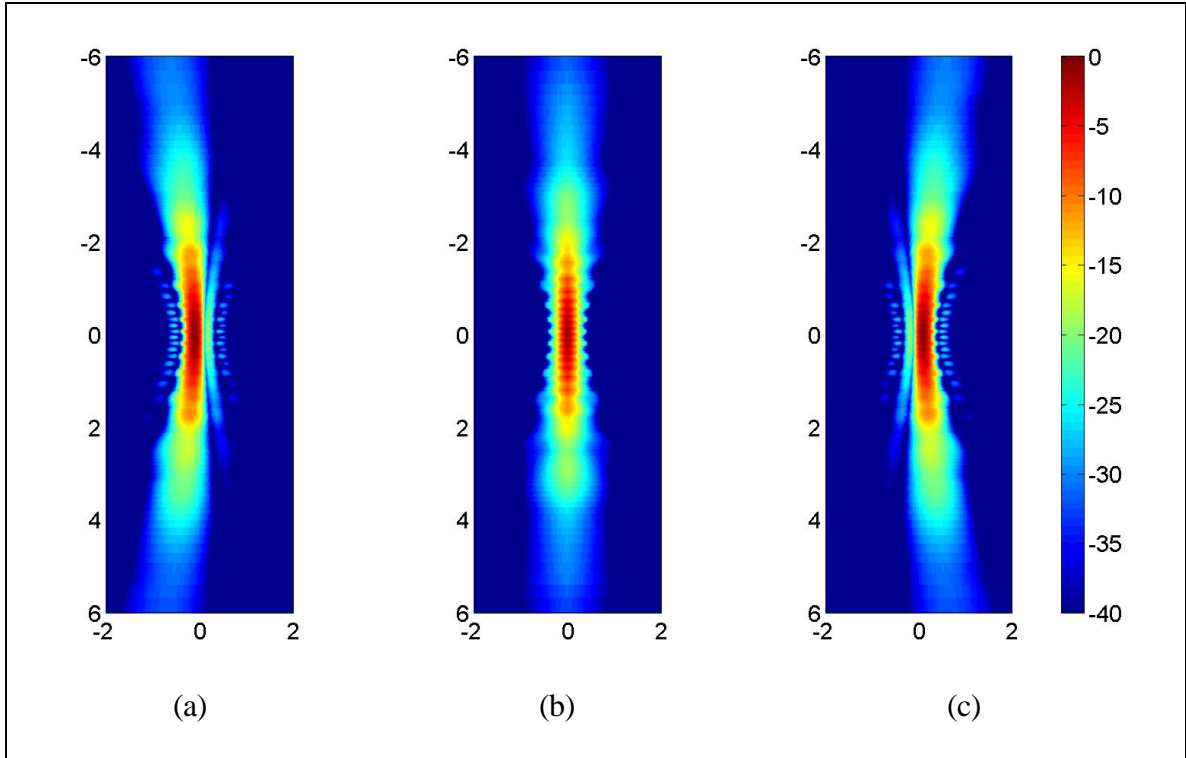
Figure 6.66. Normalized Narrow-Beam Footprints on a Horizontal Plane at Unit Distance from the Transducer for VOL SR (Viewed from Above) – Units are in Multiples of the Transducer Altitude, Forward ≡ Right – 37.5 kHz: (a) Rear Across-Track, (b) Along-Track, (c) Forward Across-Track.

The NB-expression difference term gain is not limited to the value of 0.50 used throughout this research (equation (4.7)). The results of using gain values of 0.75 and 0.96 in addition to the standard value of 0.50 are shown in Figure 6.67 for SR and LR modes. The half-power NB beamwidths are 9.2°, 7.2° and 6.0° for SR mode and 7.0°, 5.9° and 5.0° for LR mode for increasing values of difference term gain where the *forward* and *rear* beamwidths are 10.6° and 7.2° for SR and LR modes respectively. A gain of 0.75 provides for a -20 dB sidelobe level in SR mode, and a gain of 0.96 provides for a sidelobe level of -10 dB in SR mode and -20 dB in LR mode. The unwanted side effect of using the higher difference term gain is an increase in sensitivity by a few dB in directions outside the main lobes of both the rear beam and the forward beam

173
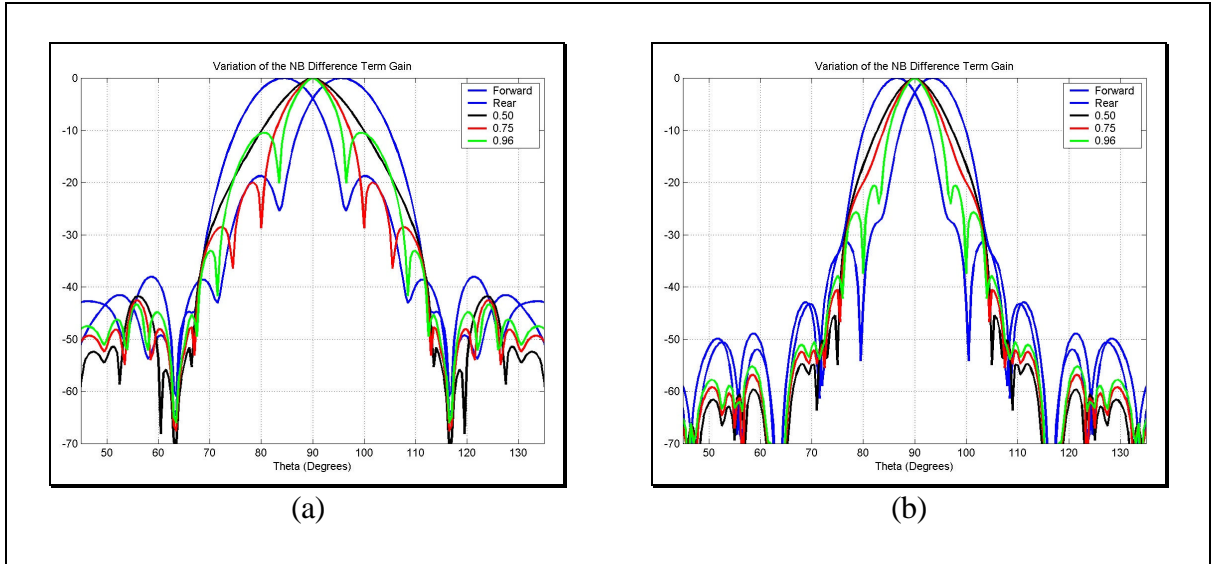
Figure 6.67. Central Along-Track Slice ($f = 0°$) of the Normalized Narrow-Beam Beam Pattern for Various Difference Term Gains – Along-Track (Beams 14 & 41) (Nadir At $(q = 90°, f = 0°)$), Cylinder Along 180° to 0° Axis – 37.5 kHz: (a) VOL SR, (b) VOL LR.

It is possible to obtain phase detection information from the along-track beam pairs by displacing the effective phase centers of the rear beams from those of the forward beams. This is accomplished by reversing the non-symmetrical along-track element weights (Table 1.3) for the rear beams with respect to those used for the forward beams, which separates the effective phase centers of the forward and rear beams. The spherical cross-section simulation phase shown in Figure 6.68 for the central along-track beam pair using the CP and DS monopulse techniques illustrates the results of this technique. The small change that this modification creates in the amplitude pattern is negligible from a proof of concept viewpoint.
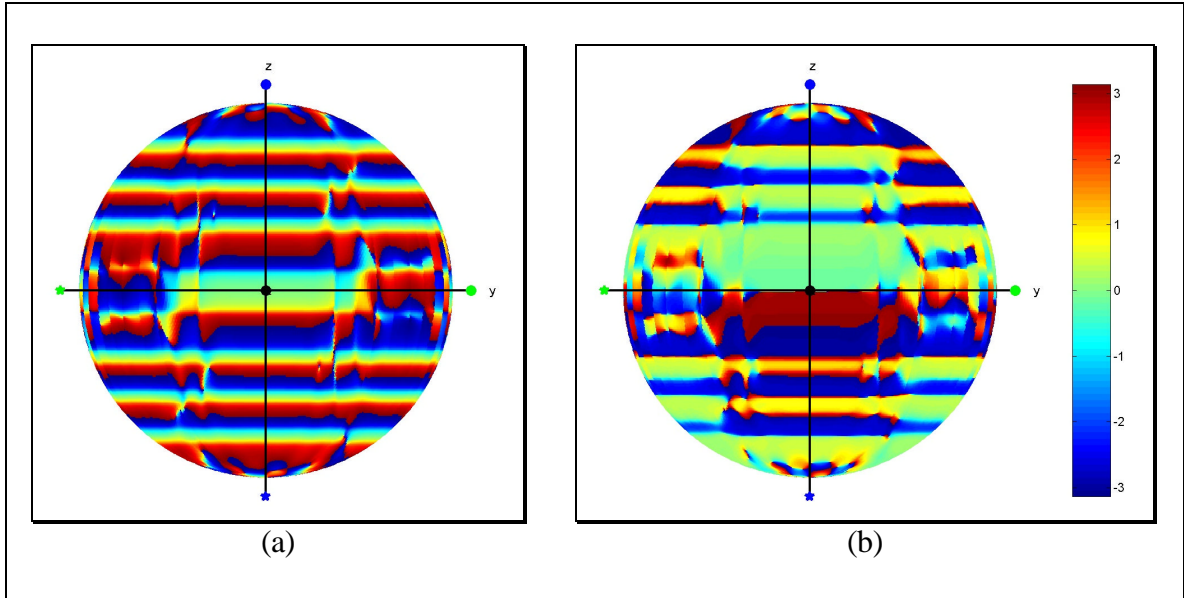
Figure 6.68. Along-Track Weighting Reversal – Spherical Cross-Section Phase in Radians – Along-Track (Beams 14 & 41), VOL SR – 37.5 kHz: (a) Conjugate-Product (b) Difference-Over-Sum.

The phase transitions in these plots are not as definitive as those of the across-track beam pairs (Figure 4.28, Figure 4.38 and Figure 4.39). However, the CP central phase slope and the DS central p-radian phase shift did not exist for the along-track beam pairs without reversed along-track weighting (Figure 4.21 and Figure 4.35). The application of a phase based detection algorithm to this data would, in theory, further reduce the correlation between the three seafloor profiles generated from a single ping.

This research has focused on obtaining seafloor characteristics from the VSS of the AQS-20 mine countermeasure system. However, additional information about the seafloor, the sea surface and objects in the water column could be obtained by using all five sonar subsystems.

APPENDIX A

THEORETICAL DERIVATION OF THE BEAM PATTERNS USED IN CHAPTER 2

A.1 <u>Theoretical Derivation of the Pressure Field in the Far Field of a Rectangular Piston Transducer in the VSS Orientation</u>

Contained herein is the theoretical derivation of the far-field beam pattern equations used in the simulations of Chapter 2. It is important to note that the beam pattern is a measure of acoustical intensity. However, unless otherwise stated, the remainder of this derivation is actually for the far-field pressure. The normalized beam pattern is calculated by simply converting the normalized squared pressure into a dB scale. Calculation of the far-field pressure is accomplished by combining the effect of each rectangular transducer used to create any given beam. The pressure pattern of each rectangular transducer itself is derived by integrating the pressure produced by a point source across the physical area of the transducer face. The calculations are performed using spherical coordinates where q is defined as the angle from the positive z-axis and f is defined as the angle in the xy-plane from the positive x-axis in the direction of the positive y-axis.

The far-field pressure of a monochromatic point source is shown in equation (A.1). In this case it is assumed that the medium is homogeneous, isotropic and lossless.

$$P_{POINT\_SOURCE} = G \cdot \exp\left(j\left(wt - \vec{k} \bullet \vec{r}\right)\right)$$ (A.1)

The gain, G, contains the physical parameters of the system. Since the pressure pattern will be normalized, only the relative magnitude of G is consequential in this case. The time varying component, $\exp(jwt)$, of the pressure pattern is likewise of little interest and will be dropped throughout the remainder of this derivation (w is radial frequency and t is time). The spatial component, $\exp\left(-j\vec{k} \bullet \vec{r}\right)$, of the pressure pattern is defined by the dot product of the wavenumber vector, $\vec{k}$, and the position vector, $\vec{r}$. The wavenumber vector is defined as the product of the magnitude of the wavenumber ($|\vec{k}| = 2p/l$ where l is the wavelength) and the unit vector in the direction of propagation. The direction of propagation is defined in this case along the line through some arbitrary origin in the direction of interest defined by the angle pair (q, f). The position vector is defined as the vector from the same arbitrary origin to the location of the point source. This changes equation (A.1) into the form shown in equation (A.2).

$$P_{POINT\_SOURCE} = G \cdot \exp\left(-j\vec{k} \bullet \vec{r}\right) = G \cdot \exp\left(-j\left(k_x x + k_y y + k_z z\right)\right)$$ (A.2)

Where $\vec{k}$ has been broken into rectangular coordinate components.

As stated previously, the pressure pattern of a rectangular transducer can be calculated by integrating the point source pressure over the transducer's surface. For mathematical convenience, the transducer array is orientated with its central axis on the z-axis and symmetry about the xy-plane. The transducer staves are symmetrically spaced about the positive x-axis. Further details of the transducer array configuration are found in Section 1.2. A sample transducer orientation is shown in Figure A.1 for the transducer array. The set (r, q_p, f_p) define the geometrical center, p, of the transducer with

respect to the origin. Because the transducers are located around a cylindrical surface, the normal to the transducer, $\vec{N}$, is equivalent to the radial component of the line from the origin to P, $r[\sin(\boldsymbol{q}_p)\cos(\boldsymbol{f}_p)\hat{x} + \sin(\boldsymbol{q}_p)\sin(\boldsymbol{f}_p)\hat{y}]$. Because of this $\boldsymbol{f}_N$ is the same as $\boldsymbol{f}_p$. The transducer is considered to have a major dimension b and a minor dimension a.
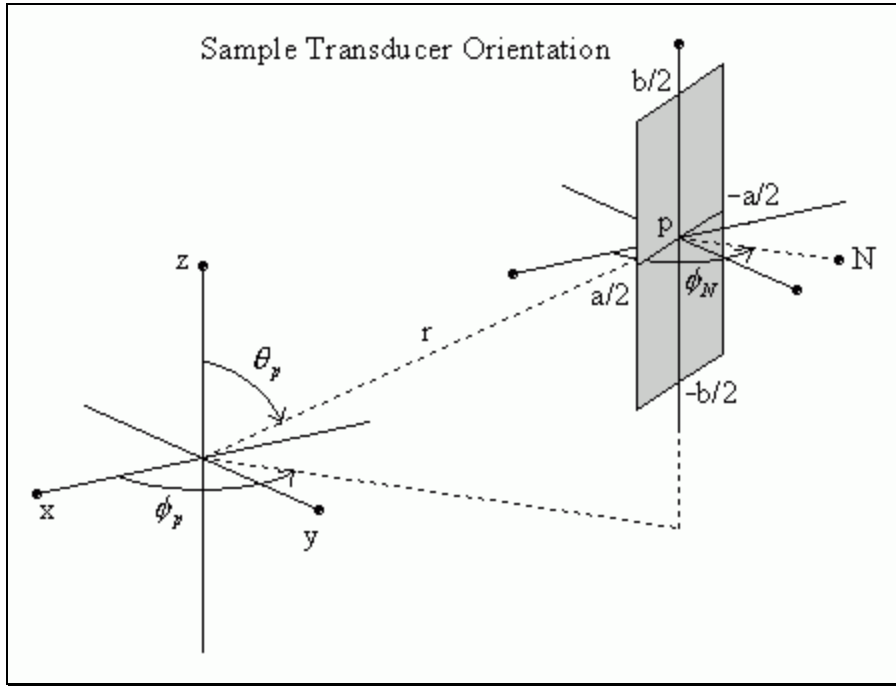
Figure A.1. Sample Transducer Orientation.

Figure A.1 shows that the x and y components of the transducer face are dependent on each other and independent of the z component. The position vector of the center of the transducer is

$$\vec{r}_p = x_p\hat{x} + y_p\hat{y} + z_p\hat{z} = r\sin(\boldsymbol{q}_p)\cos(\boldsymbol{f}_p)\hat{x} + r\sin(\boldsymbol{q}_p)\sin(\boldsymbol{f}_p)\hat{y} + r\cos(\boldsymbol{q}_p)\hat{z} \qquad \text{(A.3)}$$

Using direction cosines this reduces to

$$\vec{r}_p = r\cdot\ell_p\cdot\hat{x} + r\cdot m_p\cdot\hat{y} + r\cdot n_p\cdot\hat{z} \qquad \text{(A.4)}$$

Thus from Figure A.1 the position vector to any point on the transducer is defined to be

$$\vec{r} = \left[r \cdot \ell_p - (y - r \cdot m_p) \tan(f_N) \right] \hat{x} + [y] \hat{y} + [z] \hat{z} \tag{A.5}$$

where the x-component is now a function of the variation of the y-component about the point p. This allows integration of the surface in y and z. The limits of integration in the z dimension are simply $z_p \pm b/2$. In the y dimension they are the slightly more complex $y_p \pm (a/2) \cos(f_N)$. This can be seen in Figure A.2, which shows a sample transducer location viewed from the positive z-axis. The wavenumber vector will be scanned over all space ($0 \le q \le p, -p \le f \le p$ radians) and has the form

$$\vec{k} = |\vec{k}| \left[\sin(q) \cos(f) \hat{x} + \sin(q) \sin(f) \hat{y} + \cos(q) \hat{z} \right] = |\vec{k}| \left[\ell \hat{x} + m \hat{y} + n \hat{z} \right] \tag{A.6}$$

where direction cosines have been used to simplify notation. Note also that a unit area of the transducer face is defined to be $(dy / \cos(f_N)) \cdot dz$ because the transducer does not lie in the yz-plane.
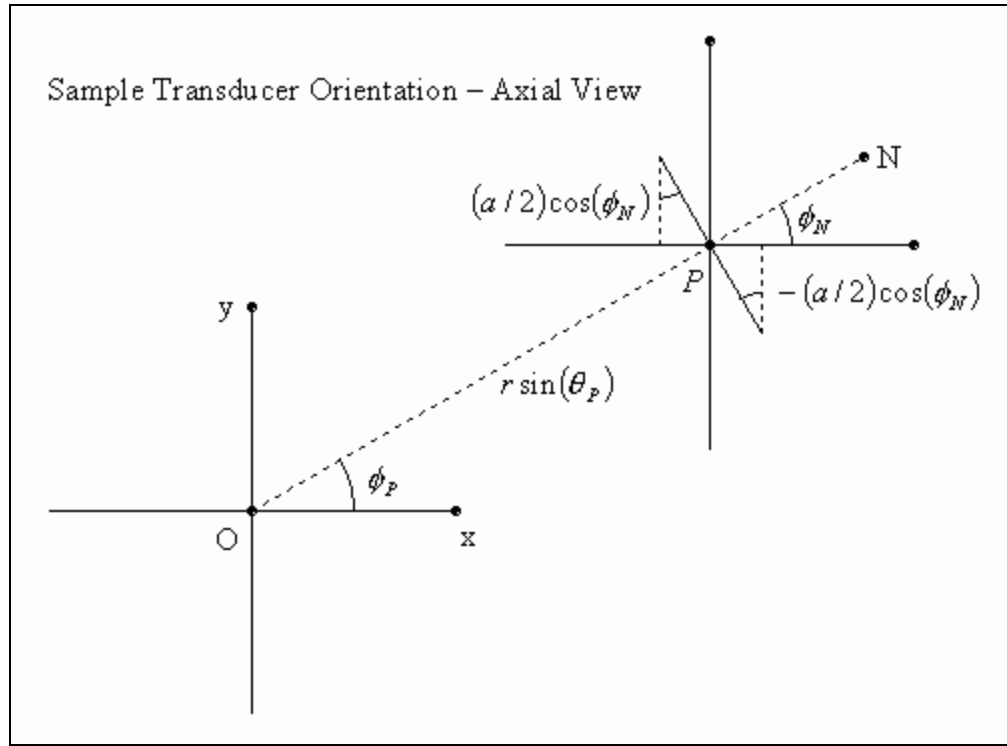
Figure A.2. Sample Transducer Orientation – Axial View.

Thus the pressure pattern can be defined to be

$$P(\boldsymbol{q},\boldsymbol{f}) = \int_{r \cdot n_p - b/2}^{r \cdot n_p + b/2} \int_{r \cdot m_p - (a/2)\cos(\boldsymbol{f}_N)}^{r \cdot m_p + (a/2)\cos(\boldsymbol{f}_N)} P_{POINT\_SOURCE} \frac{dy \cdot dz}{\cos(\boldsymbol{f}_N)}$$

(A.7)

where the effective pressure from the point source is

$$P_{POINT\_SOURCE}(\boldsymbol{q},\boldsymbol{f}) = G \cdot \exp\left(jk\left(\left[r \cdot \ell_p - (y - r \cdot m_p)\tan(\boldsymbol{f}_N)\right] \cdot \ell + y \cdot m + z \cdot n\right)\right)$$

(A.8)

Because the y and z components are independent, this integral can be split as shown in equation (A.9) and reduced.

$$P(\boldsymbol{q},\boldsymbol{f}) = \frac{G \cdot \exp\left(jkr\left(\left[\ell_p + m_p \tan(\boldsymbol{f}_N)\right] \cdot \ell\right)\right)}{\cos(\boldsymbol{f}_N)}$$
$$\cdot \int_{r \cdot n_p - b/2}^{r \cdot n_p + b/2} \exp(jkzn)dz \cdot \int_{r \cdot m_p - (a/2)\cos(\boldsymbol{f}_N)}^{r \cdot m_p + (a/2)\cos(\boldsymbol{f}_N)} \exp(jky(-\tan(\boldsymbol{f}_N)\ell + m))dy$$

(A.9)

$$P(\boldsymbol{q},\boldsymbol{f}) = \frac{G \cdot \exp\left(jkr\left(\left[\ell_p + m_p \tan(\boldsymbol{f}_N)\right] \cdot \ell\right)\right)}{\cos(\boldsymbol{f}_N)}$$
$$\cdot \left\{ \frac{\exp\left(jk(r \cdot n_p + b/2)n\right) - \exp\left(jk(r \cdot n_p - b/2)n\right)}{jkn} \right\}$$
$$\cdot \left[\frac{\exp\left(jk\left[r \cdot m_p + (a/2)\cos(\boldsymbol{f}_N)\right]\left[-\tan(\boldsymbol{f}_N)\ell + m\right]\right)}{jk\left[-\tan(\boldsymbol{f}_N)\ell + m\right]} \right.$$
$$\left. - \frac{\exp\left(jk\left[r \cdot m_p - (a/2)\cos(\boldsymbol{f}_N)\right]\left[-\tan(\boldsymbol{f}_N)\ell + m\right]\right)}{jk\left[-\tan(\boldsymbol{f}_N)\ell + m\right]} \right]$$

(A.10)

$$P(\boldsymbol{q},\boldsymbol{f}) = \frac{G \cdot \exp\left(jkr\left(\left[\ell_p + m_p \tan(\boldsymbol{f}_N)\right] \cdot \ell\right)\right)}{\cos(\boldsymbol{f}_N)}$$
$$\cdot \frac{\exp(jk(b/2)n) - \exp(-jk(b/2)n)}{jkn} \cdot \exp\left(jkrn_p n\right)$$
$$\cdot \left\{ \begin{array}{l} \exp\left(jk(a/2)\cos(\boldsymbol{f}_N)\left[-\tan(\boldsymbol{f}_N)\ell + m\right]\right) \\ -\exp\left(-jk(a/2)\cos(\boldsymbol{f}_N)\left[-\tan(\boldsymbol{f}_N)\ell + m\right]\right) \end{array} \right\} \cdot \frac{\exp\left(jkrm_p\left[-\tan(\boldsymbol{f}_N)\ell + m\right]\right)}{jk\left[-\tan(\boldsymbol{f}_N)\ell + m\right]}$$

(A.11)

$$P(\boldsymbol{q},\boldsymbol{f}) = G \cdot \exp\left(jkr\left(\left[\ell_p + m_p \tan(\boldsymbol{f}_N)\right] \cdot \ell\right)\right) \cdot \frac{2\sin(k(b/2)n)}{kn} \cdot \exp\left(jkrn_p n\right)$$
$$\cdot \frac{2\sin(k(a/2)\cos(\boldsymbol{f}_N)\left[-\tan(\boldsymbol{f}_N)\ell + m\right])}{k\cos(\boldsymbol{f}_N)\left[-\tan(\boldsymbol{f}_N)\ell + m\right]} \cdot \exp\left(jkrm_p\left[-\tan(\boldsymbol{f}_N)\ell + m\right]\right)$$

(A.12)

The sinc function is defined to be sinc(x) = sin(πx)/(πx). Thus,

$$P(\boldsymbol{q},\boldsymbol{f}) = G \cdot \exp\left(jkr\left(\left[\ell_p + m_p \tan(\boldsymbol{f}_N)\right] \cdot \ell\right)\right) \cdot b \cdot \text{sinc}(k(b/2\boldsymbol{p})n) \cdot \exp\left(jkrn_p n\right)$$
$$\cdot a \cdot \text{sinc}(k(a/2\boldsymbol{p})\cos(\boldsymbol{f}_N)\left[-\tan(\boldsymbol{f}_N)\ell + m\right]) \cdot \exp\left(jkrm_p\left[-\tan(\boldsymbol{f}_N)\ell + m\right]\right)$$

(A.13)

$$P(q,f) = G \cdot a \cdot b \cdot \text{sinc}((2p/1)(b/2p)\cos(q))$$
$$\cdot \text{sinc}((2p/1)(a/2p)[-\sin(f_N)\cos(f)+\cos(f_N)\sin(f)]\sin(q))$$
$$\cdot \exp(jkr[[\ell_p + m_p \tan(f_N)]\ell + m_p[-\tan(f_N)\ell + m] + n_p n)) \qquad (A.14)$$

$$P(q,f) = G \cdot a \cdot b \cdot \text{sinc}((b/1)\cos(q)) \cdot \text{sinc}((a/1)\sin(q)\sin(f-f_N))$$
$$\cdot \exp(jkr[\ell_p \ell + m_p m + n_p n]) \qquad (A.15)$$

$$P(q,f) = G \cdot a \cdot b \cdot \text{sinc}((b/1)\cos(q)) \cdot \text{sinc}((a/1)\sin(q)\sin(f-f_N)) \cdot \exp(j\vec{k} \bullet \vec{r}_p) \qquad (A.16)$$

Thus the pressure pattern of the transducer is simply the pressure pattern of a rectangular transducer centered at the origin shifted by the translation of the transducer center. This result is valid for any transducer in the given orientation that is not centered on the z-axis expect for the cases that $f_p = f_N = \pm p/2$ radians. In these cases, the integration along y falls apart. To fill in these missing cases, equations (A.7) and (A.8) are rewritten as an integral of x and z and reduced as follows:

$$P(q,f) = \int_{r \cdot n_p - b/2}^{r \cdot n_p + b/2} \int_{-a/2}^{a/2} G \cdot \exp(jk(x \cdot \ell + y \cdot m + z \cdot n))dx \cdot dz \qquad (A.17)$$

$$P(q,f) = G \cdot \exp(jkrm_p m) \cdot \int_{r \cdot n_p - b/2}^{r \cdot n_p + b/2} \exp(jkzn)dz \cdot \int_{-a/2}^{a/2} \exp(jkx\ell)dx \qquad (A.18)$$

$$P(q,f) = G \cdot \exp(jkrm_p m) \cdot \frac{\exp(jk(rn_p + b/2)n) - \exp(jk(rn_p - b/2)n)}{jkn}$$
$$\cdot \frac{[\exp(jk(a/2)\ell) - \exp(-jk(a/2)\ell)]}{jk\ell} \qquad (A.19)$$

$$P(q,f) = G \cdot \exp(jkrm_p m) \cdot \frac{2\sin(k(b/2)n)}{kn} \cdot \exp(jkrn_p n) \cdot \frac{2\sin(k(a/2)\ell)}{k\ell} \qquad (A.20)$$

$$P(q,f) = G \cdot a \cdot b \cdot \text{sinc}(k(b/2p)\cos(q)) \cdot \text{sinc}(k(a/2p)\sin(q)\cos(f))$$
$$\cdot \exp(jkr[0\ell + m_p m + n_p n]) \qquad (A.21)$$

$$P(q,f) = G \cdot a \cdot b \cdot \text{sinc}((b/1)\cos(q)) \cdot \text{sinc}((a/1)\sin(q)\sin(f-f_N)) \cdot \exp(j\vec{k} \bullet \vec{r}_p) \qquad (A.22)$$

Thus the pressure pattern for any rectangular transducer having its major axis parallel to, but not on, the z-axis is defined by equation (A.16).

A.2 Combination of the Rectangular Elements Pressure Patterns into the

Applicable Beam Patterns

The next step is to combine the effects of several transducers. It is assumed that each transducer operates only in the half space on the side of the transducer away from the array center. This is accomplished in simulation by modifying equation (A.16) such that

$$P_{HALF\_SPACE}(\boldsymbol{q},\boldsymbol{f}) = P_{FULL\_SPACE}(\boldsymbol{q},\boldsymbol{f}) \cdot \frac{\mathrm{Re}\left(\sqrt{\boldsymbol{p}/2 - |\boldsymbol{f} - \boldsymbol{f}_N|}\right)}{\sqrt{\boldsymbol{p}/2 - |\boldsymbol{f} - \boldsymbol{f}_N|}} \tag{A.23}$$

This forces the beam pattern at more than $\boldsymbol{p}/2$ radians from the transducer normal to be zero. While equation (A.23) is anything but elegant, this method implements faster in MATLAB than a search and replace algorithm used to accomplish the same task. In the case of transducers around a cylindrical array, $\boldsymbol{f}_N = \boldsymbol{f}_p$ and, $|\vec{r}_p|$ is a function only of z. For convenience, the distance along the z-axis between element centers is defined to be h, and the angular spacing in phi-space between element staves is defined to be $\boldsymbol{a}$. The magnitude of the radius, R, of the cylinder is a constant. Figure A.3 shows the element centers of the array used in $(h, \boldsymbol{a})$ space. All of the light grey elements are transmission elements. These are used to create a single transmission beam. Each of the transmission elements is given equal weighting. The dark grey elements are used to create the receive beams. There are fifty four receive beams created for both long-range and short-range modes. Two of these are created for each grouping of receive elements. This pair is symmetrically steered in the positive and negative z directions. The group of receive elements used to create each pair of long-range receive beams consists of the receive elements on sixteen adjacent staves except for the end groups, which use only fourteen

staves. The short-range receive beams use only the central five receive elements on each stave. In each case, the same set of weighting factors are applied to the receive elements of each stave and the staves are also weighted with respect to each other.
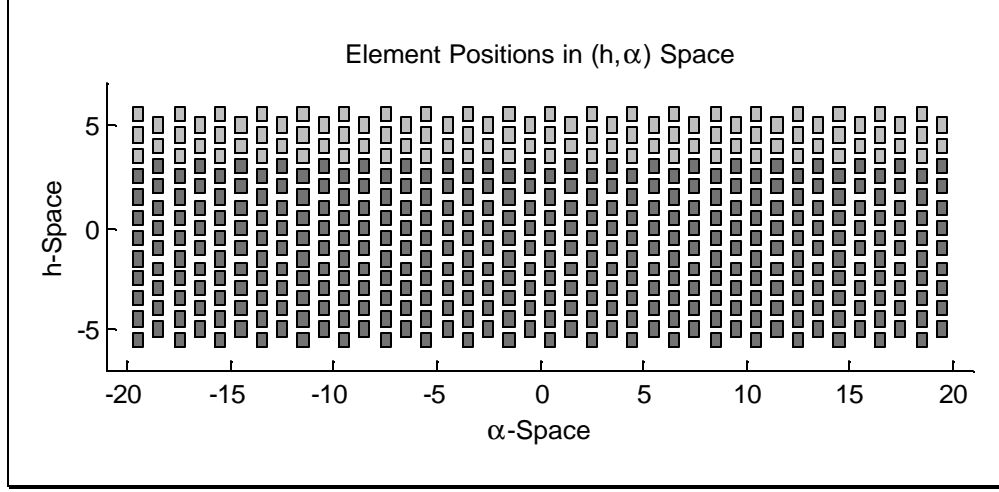
Figure A.3. Element Positions in $(h, \mathbf{a})$ Space.

Since there is a single transmission beam, which has uniform weighting and no steering, the transmission pressure pattern is calculated first. Figure A.3 shows that the transmission array is symmetrical in h space about $4.5\,h$. This $4.5\,h$ shift if removed in the calculations in order to place the reference point at the transmission array's phase center. Since all of the elements on a single stave have are identical expect for their z value, a stave with two transmission elements reduces to

$$
\begin{aligned}
P_{T2}(\mathbf{q}, \mathbf{f}) \;=\;& G \cdot a \cdot b \cdot \mathrm{sinc}((b/\mathbf{1})\cos(\mathbf{q})) \cdot \mathrm{sinc}((a/\mathbf{1})\sin(\mathbf{q})\sin(\mathbf{f}-\mathbf{f}_p)) \cdot \frac{\mathrm{Re}\!\left(\sqrt{p/2-|\mathbf{f}-\mathbf{f}_p|}\right)}{\sqrt{p/2-|\mathbf{f}-\mathbf{f}_p|}} \\
& \cdot \exp\!\left(jk\left(R\cos(\mathbf{f}_p)\ell + R\sin(\mathbf{f}_p)m - 0.5hn\right)\right) + \exp\!\left(jk\left(R\cos(\mathbf{f}_p)\ell + R\sin(\mathbf{f}_p)m + 0.5hn\right)\right)
\end{aligned}
\tag{A.24}
$$

$$
\begin{aligned}
P_{T2}(\mathbf{q}, \mathbf{f}) \;=\;& G \cdot a \cdot b \cdot \mathrm{sinc}((b/\mathbf{1})\cos(\mathbf{q})) \cdot \mathrm{sinc}((a/\mathbf{1})\sin(\mathbf{q})\sin(\mathbf{f}-\mathbf{f}_p)) \cdot \frac{\mathrm{Re}\!\left(\sqrt{p/2-|\mathbf{f}-\mathbf{f}_p|}\right)}{\sqrt{p/2-|\mathbf{f}-\mathbf{f}_p|}} \\[2mm]
& \cdot \exp\!\left(jk\left(R\cos(\mathbf{f}_p)\ell + R\sin(\mathbf{f}_p)m\right)\right) \cdot \{\exp(j0.5khn) + \exp(-j0.5khn)\}
\end{aligned}
\tag{A.25}
$$

183

$$P_{T2}(\boldsymbol{q},\boldsymbol{f}) = G \cdot a \cdot b \cdot \mathrm{sinc}((b/\boldsymbol{1})\cos(\boldsymbol{q})) \cdot \mathrm{sinc}((a/\boldsymbol{1})\sin(\boldsymbol{q})\sin(\boldsymbol{f}-\boldsymbol{f}_p)) \cdot \frac{\mathrm{Re}\left(\sqrt{p/2-\left|\boldsymbol{f}-\boldsymbol{f}_p\right|}\right)}{\sqrt{p/2-\left|\boldsymbol{f}-\boldsymbol{f}_p\right|}} \tag{A.26}$$

$$\cdot \left[2\cos(0.5kh\cos(\boldsymbol{q}))\right] \cdot \exp\left(jk\left(R\cos(\boldsymbol{f}_p)\ell + R\sin(\boldsymbol{f}_p)m\right)\right)$$

Likewise, a stave with three elements reduces to

$$P_{T3}(\boldsymbol{q},\boldsymbol{f}) = G \cdot a \cdot b \cdot \mathrm{sinc}((b/\boldsymbol{1})\cos(\boldsymbol{q})) \cdot \mathrm{sinc}((a/\boldsymbol{1})\sin(\boldsymbol{q})\sin(\boldsymbol{f}-\boldsymbol{f}_p)) \cdot \frac{\mathrm{Re}\left(\sqrt{p/2-\left|\boldsymbol{f}-\boldsymbol{f}_p\right|}\right)}{\sqrt{p/2-\left|\boldsymbol{f}-\boldsymbol{f}_p\right|}} \tag{A.27}$$

$$\cdot \exp\left(jk\left(R\cos(\boldsymbol{f}_p)\ell + R\sin(\boldsymbol{f}_p)m\right)\right) \cdot \left\{\exp(jkhn)+1+\exp(-jkhn)\right\}$$

$$P_{T3}(\boldsymbol{q},\boldsymbol{f}) = G \cdot a \cdot b \cdot \mathrm{sinc}((b/\boldsymbol{1})\cos(\boldsymbol{q})) \cdot \mathrm{sinc}((a/\boldsymbol{1})\sin(\boldsymbol{q})\sin(\boldsymbol{f}-\boldsymbol{f}_p)) \cdot \frac{\mathrm{Re}\left(\sqrt{p/2-\left|\boldsymbol{f}-\boldsymbol{f}_p\right|}\right)}{\sqrt{p/2-\left|\boldsymbol{f}-\boldsymbol{f}_p\right|}} \tag{A.28}$$

$$\cdot \left[1+2\cos(kh\cos(\boldsymbol{q}))\right] \cdot \exp\left(jk\left(R\cos(\boldsymbol{f}_p)\ell + R\sin(\boldsymbol{f}_p)m\right)\right)$$

The total transmission pattern is found by summing P_{T2} and P_{T3} over the appropriate staves in $\boldsymbol{a}$ space as is shown in equations (A.29) and (A.30) where $q\boldsymbol{a} \equiv \boldsymbol{f}_p$ and $Q=40$

$$P_T(\boldsymbol{q},\boldsymbol{f}) = \sum_{q=-(Q-1)/2}^{(Q-1)/2} P_{T2} \cdot \mathrm{mod}(q-0.5,2) + P_{T3} \cdot \mathrm{mod}(q+0.5,2) \tag{A.29}$$

$$P_T(\boldsymbol{q},\boldsymbol{f}) = G \cdot a \cdot b \cdot \mathrm{sinc}((b/\boldsymbol{1})\cos(\boldsymbol{q}))$$

$$\times \sum_{q=-\frac{Q-1}{2}}^{\frac{Q-1}{2}} \left[\begin{array}{c} \mathrm{sinc}((a/\boldsymbol{1})\sin(\boldsymbol{q})\sin(\boldsymbol{f}-q\boldsymbol{a})) \cdot \dfrac{\mathrm{Re}\left(\sqrt{p/2-\left|\boldsymbol{f}-q\boldsymbol{a}\right|}\right)}{\sqrt{p/2-\left|\boldsymbol{f}-q\boldsymbol{a}\right|}} \\[2ex] \cdot \exp\left(jkR\sin(\boldsymbol{q})\left[\cos(\boldsymbol{f})\cos(q\boldsymbol{a}) + \sin(\boldsymbol{f})\sin(q\boldsymbol{a})\right]\right) \\[2ex] \cdot \left\{\left[1+2\cos(kh\cos(\boldsymbol{q}))\right] \cdot \mathrm{mod}(q+0.5,2) + \left[2\cos(0.5kh\cos(\boldsymbol{q}))\right] \cdot \mathrm{mod}(q-0.5,2)\right\} \end{array} \right] \tag{A.30}$$

The mathematical expression for the pressure pattern of the receive beams cannot be reduced nearly as much since it lacks spatial symmetry. The spatial weighting coefficients from Table 1.2 and Table 1.3 are contained in the vectors $W_a(q)$ and $W_h(p)$

respectively, where counters p and q increment (along-track and across-track respectively) through the elements used to create each beam pair. The steering angles are $p/2 \mp q_S$, where q_s is a small angle on either side of the xy-plane (8° for SR and 4° for LR). The steering angles cannot be applied to the element patterns themselves but only to separate elements along a stave. The beam pressure patterns for the various receiving configurations are shown below where the beam pair number is i, i_cent is 14, Q is 16 for beam pairs 2 through 26 and 14 for beam pairs 1 and 27, Q_{SHIFT} is 22.5 $((length(W_a)+1)/2+i\_cent)$, P is 5 for SR mode and 9 for LR mode, and P_{SHIFT} is 5 $((length(W_h)+1)/2)$.

$$P_R(q,f) = \sum_q \sum_p \left[\begin{array}{c} G \cdot a \cdot b \cdot W_a(q) \cdot W_h(p) \cdot \text{sinc}((b/\mathbf{1})\cos(\mathbf{q})) \cdot \text{sinc}((a/\mathbf{1})\sin(\mathbf{q})\sin(\mathbf{f}-q\mathbf{a})) \\ \cdot \exp\left(jk \left(\begin{array}{c} R\cos(q\mathbf{a})[\sin(\mathbf{q})\cos(\mathbf{f})]+\sin(q\mathbf{a})[\sin(\mathbf{q})\sin(\mathbf{f})] \\ + p \cdot h[\cos(\mathbf{q})-\cos(\mathbf{p}/2 \mp \mathbf{q}_S)] \end{array} \right) \right) \\ \cdot \dfrac{\text{Re}\left(\sqrt{\mathbf{p}/2-|\mathbf{f}-q\mathbf{a}|}\right)}{\sqrt{\mathbf{p}/2-|\mathbf{f}-q\mathbf{a}|}} \end{array} \right] \quad \text{(A.31)}$$

$$P_R(q,f) = G \cdot a \cdot b \cdot \text{sinc}((b/\mathbf{1})\cos(\mathbf{q})) \cdot \sum_p \left[W_h(p) \cdot \exp\left(jk \cdot p \cdot h[\cos(\mathbf{q}) \mp \sin(\mathbf{q}_S)] \right) \right]$$

$$\cdot \sum_q \left[\begin{array}{c} W_a(q) \cdot \text{sinc}((a/\mathbf{1})\sin(\mathbf{q})\sin(\mathbf{f}-q\mathbf{a})) \cdot \dfrac{\text{Re}\left(\sqrt{\mathbf{p}/2-|\mathbf{f}-q\mathbf{a}|}\right)}{\sqrt{\mathbf{p}/2-|\mathbf{f}-q\mathbf{a}|}} \\ \cdot \exp\left(jk(R\cos(q\mathbf{a})[\sin(\mathbf{q})\cos(\mathbf{f})]+\sin(q\mathbf{a})[\sin(\mathbf{q})\sin(\mathbf{f})]) \right) \\ \cdot \exp\left(-j0.5k \cdot h[\cos(\mathbf{q}) \mp \sin(\mathbf{q}_S)] \cdot \text{mod}(q+0.5,2) \right) \end{array} \right] \quad \text{(A.32)}$$

$$P_{R\_i}(\boldsymbol{q},\boldsymbol{f}) = G \cdot a \cdot b \cdot \text{sinc}((b/\mathbf{1})\cos(\boldsymbol{q}))$$

$$\cdot \sum_{p=-(P-1)/2}^{(P-1)/2} \left[W_h(p + P_{SHIFT}) \cdot \exp\left(jk \cdot (p+0.25) \cdot h[\cos(\boldsymbol{q}) \mp \sin(\boldsymbol{q}_S)]\right) \right]$$

$$\cdot \sum_{q=i-\frac{Q-1}{2}-\bar{i}\_cent}^{i+\frac{Q-1}{2}-\bar{i}\_cent} \left[\begin{array}{c} W_{\boldsymbol{a}}\left(q + Q_{SHIFT} - i\right) \cdot \text{sinc}((a/\mathbf{1})\sin(\boldsymbol{q})\sin(\boldsymbol{f} - q\boldsymbol{a})) \\[6pt] \cdot \dfrac{\text{Re}\left(\sqrt{\boldsymbol{p}/2 - |\boldsymbol{f} - q\boldsymbol{a}|}\right)}{\sqrt{\boldsymbol{p}/2 - |\boldsymbol{f} - q\boldsymbol{a}|}} \\[8pt] \cdot \exp\left(jk\left(R\cos(q\boldsymbol{a})[\sin(\boldsymbol{q})\cos(\boldsymbol{f})] + \sin(q\boldsymbol{a})[\sin(\boldsymbol{q})\sin(\boldsymbol{f})]\right)\right) \\[8pt] \cdot \exp\left(-j0.5k \cdot h[\cos(\boldsymbol{q}) \mp \sin(\boldsymbol{q}_S)] \cdot \text{mod}(q+0.5,2)\right) \end{array} \right] \quad (A.33)$$

The beam patterns is calculated from the beam pressure patterns as follows:

$$B_T(\boldsymbol{q},\boldsymbol{f}) = 20\log_{10}(abs(P_T(\boldsymbol{q},\boldsymbol{f}))) \quad (A.34)$$

$$B_{R\_i}(\boldsymbol{q},\boldsymbol{f}) = 20\log_{10}(abs(P_{R\_i}(\boldsymbol{q},\boldsymbol{f}))) \quad (A.35)$$

$$B_{TR\_i}(\boldsymbol{q},\boldsymbol{f}) = 20\log_{10}(abs(P_{R\_i}(\boldsymbol{q},\boldsymbol{f}) \cdot P_T(\boldsymbol{q},\boldsymbol{f}))) \quad (A.36)$$

APPENDIX B

EXPANSION OF MONOPULSE EXPRESSIONS

This appendix expands and summarizes the monopulse expressions for the conjugate-product (CP), difference-over-sum (DS) and narrow-beam (NB) techniques in the case the beams A and B are complex valued. The symbol $\angle$ means 'phase of', and f_A and f_B are the phases of the signals measured on beams A and B respectively. From Section 1.3.3 the phase comparison classification implies that $|A| = |B|$ and the magnitude comparison classification implies that $f_A = f_B$. As explained in Section 4.1 the along-track beam pairs fit into the magnitude comparison classification, and the across-track beam pairs do not reduce to either classification. However, it will be useful in some instances to note that $|f_A - f_B| < 10° = p/18\,\text{rad}$ in for the across-track beams.

The CP expression is

$$CP = A \cdot B^* = |A||B| \cdot \exp\left(j(f_A - f_B) \right) \tag{B.1}$$

In the case of phase comparison this reduces to

$$CP_{PC} = |A||A| \cdot \exp\left(j(f_A - f_B) \right) = |A|^2 \cdot \exp\left(j(f_A - f_B) \right) \tag{B.2}$$

which is not significantly changed from the general form. However, the magnitude comparison,

$$CP_{MC} = |A||B| \cdot \exp\left(j(\boldsymbol{f}_A - \boldsymbol{f}_A)\right) = |A||B| \tag{B.3}$$

loses all of its phase information.

The DS expression is

$$DS = \frac{A - B}{A + B} = \frac{|A| \cdot \exp(j\boldsymbol{f}_A) - |B| \cdot \exp(j\boldsymbol{f}_B)}{|A| \cdot \exp(j\boldsymbol{f}_A) + |B| \cdot \exp(j\boldsymbol{f}_B)} \tag{B.4}$$

This is reduced as follows:

$$DS = \frac{|A| \cdot \exp(j\boldsymbol{f}_A) - |B| \cdot \exp(j\boldsymbol{f}_B)}{|A| \cdot \exp(j\boldsymbol{f}_A) + |B| \cdot \exp(j\boldsymbol{f}_B)} \cdot \frac{|A| \cdot \exp(-j\boldsymbol{f}_A) + |B| \cdot \exp(-j\boldsymbol{f}_B)}{|A| \cdot \exp(-j\boldsymbol{f}_A) + |B| \cdot \exp(-j\boldsymbol{f}_B)} \tag{B.5}$$

$$DS = \frac{|A|^2 - |B|^2 + |A||B| \cdot \left[\exp(j[\boldsymbol{f}_A - \boldsymbol{f}_B]) - \exp(j[\boldsymbol{f}_B - \boldsymbol{f}_A])\right]}{|A|^2 + |B|^2 + |A||B| \cdot \left[\exp(j[\boldsymbol{f}_A - \boldsymbol{f}_B]) + \exp(j[\boldsymbol{f}_B - \boldsymbol{f}_A])\right]} \tag{B.6}$$

$$DS = \frac{|A|^2 - |B|^2 + 2j|A||B|\sin(\boldsymbol{f}_A - \boldsymbol{f}_B)}{|A|^2 + |B|^2 + 2|A||B|\cos(\boldsymbol{f}_A - \boldsymbol{f}_B)} \tag{B.7}$$

Since the denominator of this expression is never negative, the phase reduces to

$$\angle DS = \tan^{-1}\left(\frac{2|A||B|\sin(\boldsymbol{f}_A - \boldsymbol{f}_B)}{|A|^2 - |B|^2}\right) \tag{B.8}$$

The magnitude does not reduce nearly as much. It can be expressed in the following three forms:

$$|DS| = \frac{\sqrt{\left(|A|^2 - |B|^2\right)^2 + 4|A|^2|B|^2\sin^2(\boldsymbol{f}_A - \boldsymbol{f}_B)}}{|A|^2 + |B|^2 + 2|A||B|\cos(\boldsymbol{f}_A - \boldsymbol{f}_B)} \tag{B.9}$$

OR

$$|DS| = \frac{\sqrt{|A|^4 + |B|^4 - 2|A|^2|B|^2 + 4|A|^2|B|^2\sin^2(\boldsymbol{f}_A - \boldsymbol{f}_B)}}{|A|^2 + |B|^2 + 2|A||B|\cos(\boldsymbol{f}_A - \boldsymbol{f}_B)} \tag{B.10}$$

$$|DS| = \frac{\sqrt{|A|^4 + |B|^4 + 2|A|^2|B|^2 \left[2\sin^2(f_A - f_B) - 1\right]}}{|A|^2 + |B|^2 + 2|A||B|\cos(f_A - f_B)}$$

(B.11)

$$|DS| = \frac{\sqrt{|A|^4 + |B|^4 - 2|A|^2|B|^2 \cos(2[f_A - f_B])}}{|A|^2 + |B|^2 + 2|A||B|\cos(f_A - f_B)}$$

(B.12)

OR from equation (B.10)

$$|DS| = \frac{\sqrt{|A|^4 + |B|^4 + 2|A|^2|B|^2 + 4|A|^2|B|^2 \sin^2(f_A - f_B) - 4|A|^2|B|^2}}{|A|^2 + |B|^2 + 2|A||B|\cos(f_A - f_B)}$$

(B.13)

$$|DS| = \frac{\sqrt{\left[|A|^2 + |B|^2\right]^2 - \left[2|A||B|\cos(f_A - f_B)\right]^2}}{\left[|A|^2 + |B|^2\right] + \left[2|A||B|\cos(f_A - f_B)\right]}$$

(B.14)

$$|DS| = \sqrt{\frac{\left[|A|^2 + |B|^2\right] - \left[2|A||B|\cos(f_A - f_B)\right]}{\left[|A|^2 + |B|^2\right] + \left[2|A||B|\cos(f_A - f_B)\right]}}$$

(B.15)

In the case of phase comparison equation (B.7) reduces to

$$DS_{PC} = \frac{2j|A||A|\sin(f_A - f_B)}{|A|^2 + |A|^2 + 2|A||A|\cos(f_A - f_B)} = \frac{j\sin(f_A - f_B)}{1 + \cos(f_A - f_B)}$$

(B.16)

$$DS_{PC} = j\tan\left(\frac{1}{2}[f_A - f_B]\right)$$

(B.17)

which is an indicator of the relative magnitudes of f_A and f_B. In the case of magnitude comparison, equation (B.4) reduces to

$$DS_{MC} = \frac{|A| - |B|}{|A| + |B|}$$

(B.18)

For the small difference angle, equation (B.9) reduces to

189

$$|DS| \approx \frac{\left\|A\right|^2 - \left|B\right|^2\|}{\left|A\right|^2 + \left|B\right|^2 + 2\left|A\right|\left|B\right|} = \frac{\left\|A\right| - \left|B\right\|}{\left|A\right| + \left|B\right|} \tag{B.19}$$

The NB expression is

$$NB = \left\| A \right| \cdot \exp(j\boldsymbol{f}_A) + \left| B \right| \cdot \exp(j\boldsymbol{f}_B) \right\|$$
$$\cdot \left(\begin{array}{c} \left\| A \right| \cdot \exp(j\boldsymbol{f}_A) + \left| B \right| \cdot \exp(j\boldsymbol{f}_B) \right\| \\ -0.5 \cdot \left\| A \right| \cdot \exp(j\boldsymbol{f}_A) - \left| B \right| \cdot \exp(j\boldsymbol{f}_B) \right\| \end{array} \right) \tag{B.20}$$

The absolute value operations make the magnitude and phase of this expression easily

derivable. The phase comparison case is

$$NB_{PC} = \left\| A \right| \cdot \exp(j\boldsymbol{f}_A) + \left| A \right| \cdot \exp(j\boldsymbol{f}_B) \right\|$$
$$\cdot \left(\begin{array}{c} \left\| A \right| \cdot \exp(j\boldsymbol{f}_A) + \left| A \right| \cdot \exp(j\boldsymbol{f}_B) \right\| \\ -0.5 \cdot \left\| A \right| \cdot \exp(j\boldsymbol{f}_A) - \left| A \right| \cdot \exp(j\boldsymbol{f}_B) \right\| \end{array} \right) \tag{B.21}$$

Considering that

$$[\exp(j\boldsymbol{f}_A) + \exp(j\boldsymbol{f}_B)] \cdot conj[\exp(j\boldsymbol{f}_A) + \exp(j\boldsymbol{f}_B)]$$
$$= 2[1 + \cos(\boldsymbol{f}_A - \boldsymbol{f}_B)] \tag{B.22}$$

and

$$[\exp(j\boldsymbol{f}_A) - \exp(j\boldsymbol{f}_B)] \cdot conj[\exp(j\boldsymbol{f}_A) - \exp(j\boldsymbol{f}_B)]$$
$$= 2[1 - \cos(\boldsymbol{f}_A - \boldsymbol{f}_B)] \tag{B.23}$$

$$NB_{PC} = \left| A \right|^2 \sqrt{2[1 + \cos(\boldsymbol{f}_A - \boldsymbol{f}_B)]}$$
$$\cdot \left(\sqrt{2[1 + \cos(\boldsymbol{f}_A - \boldsymbol{f}_B)]} - 0.5 \cdot \sqrt{2[1 - \cos(\boldsymbol{f}_A - \boldsymbol{f}_B)]} \right) \tag{B.24}$$

$$NB_{PC} = \left| A \right|^2 \cdot \left(2[1 + \cos(\boldsymbol{f}_A - \boldsymbol{f}_B)] - \sqrt{[1 - \cos^2(\boldsymbol{f}_A - \boldsymbol{f}_B)]} \right) \tag{B.25}$$

$$NB_{PC} = \left| A \right|^2 \cdot (2[1 + \cos(\boldsymbol{f}_A - \boldsymbol{f}_B)] - \sin(\boldsymbol{f}_A - \boldsymbol{f}_B)) \tag{B.26}$$

The magnitude comparison results are

$$NB_{MC} = \left\| |A| \cdot \exp(j\boldsymbol{f}_A) + |B| \cdot \exp(j\boldsymbol{f}_A) \right\|$$
$$\cdot \left(\begin{array}{c} \left\| |A| \cdot \exp(j\boldsymbol{f}_A) + |B| \cdot \exp(j\boldsymbol{f}_A) \right\| \\ -0.5 \cdot \left\| |A| \cdot \exp(j\boldsymbol{f}_A) - |B| \cdot \exp(j\boldsymbol{f}_A) \right\| \end{array} \right) \qquad \text{(B.27)}$$

$$NB_{MC} = \left| \exp(j\boldsymbol{f}_A) \right|^2 \cdot \left(|A| + |B| \right) \cdot \left(\left(|A| + |B| \right) - 0.5 \cdot \left\| |A| - |B| \right\| \right) \qquad \text{(B.28)}$$

$$NB_{MC} = \left| \exp(j\boldsymbol{f}_A) \right|^2 \cdot \left(\left(|A| + |B| \right)^2 - 0.5 \cdot \left\| |A|^2 - |B|^2 \right\| \right) \qquad \text{(B.29)}$$

APPENDIX C

TOWED BODY MEASUREMENTS

This Figure C.1 through Figure C.15 contain the towed body orientation and sound speed data recorded during the collection of the pings in sample data sets 019 and 022 in the order that these characteristics were saved to file. The lines show the values measured, and the diamonds show the average value measured during each ping. The values for towed body depth (Figure C.1), towed body pitch (Figure C.3), towing speed (Figure C.11) and acoustic sound speed (Figure C.12) are used to refine the bathymetry in this report. The towed body roll (Figure C.4) is only a few tenths of a degree and is ignored. Corrections for towed body yaw (Figure C.5) are not yet included but will need to be applied since the yaw varies by a few degrees. The towed body altitude (Figure C.2) is corrupted, but it serves as a check for the estimation of the seafloor position below the towed body. The towed body course (Figure C.9) and heading (Figure C.10) will be important for refining the positions of the data. There are currently no plans to use the pitch, roll and yaw rates or the x, y, and z acceleration data (Figure C.6, Figure C.7, Figure C.8, Figure C.13, Figure C.14 and Figure C.15 respectively).
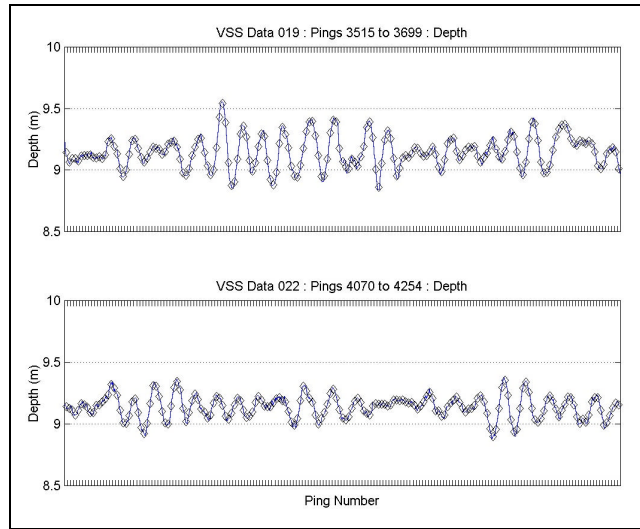
Figure C.1. Towed Body Depth.
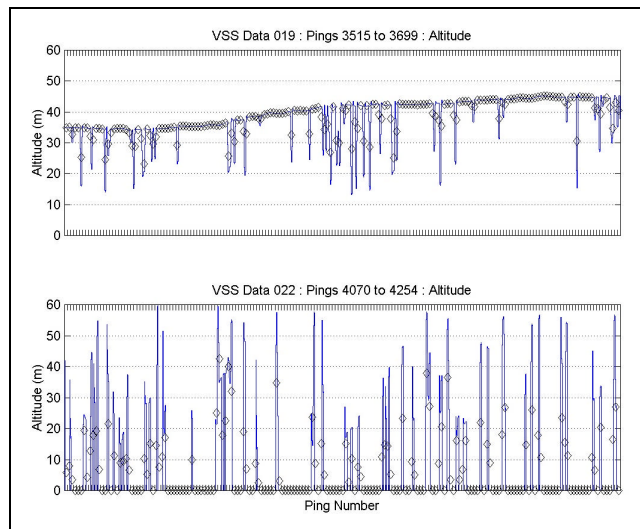
Figure C.2. Towed Body Altitude – Corrupted Data.

Figure C.3. Towed Body Pitch.
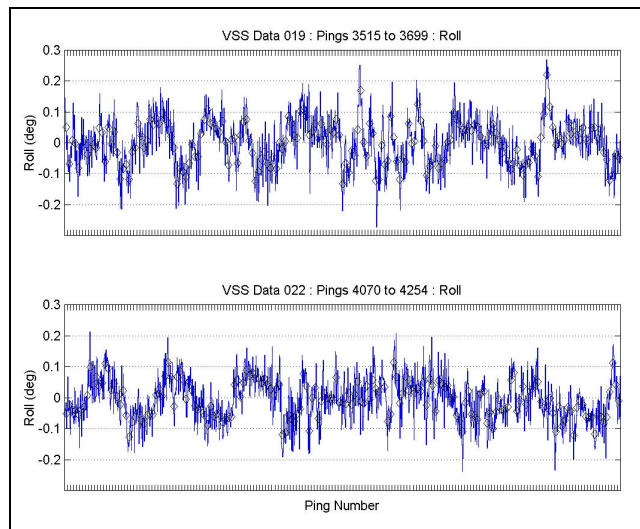
Figure C.4. Towed Body Roll.
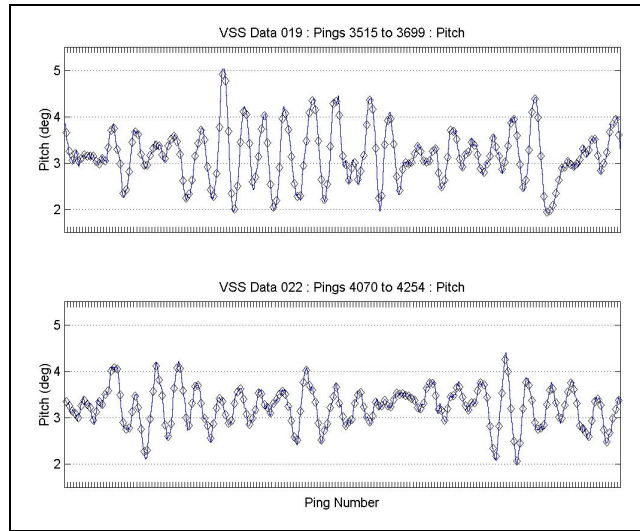
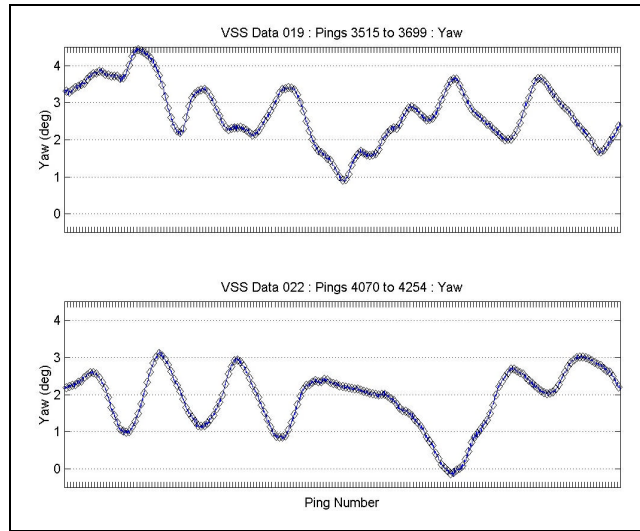Figure C.5. Towed Body Yaw.
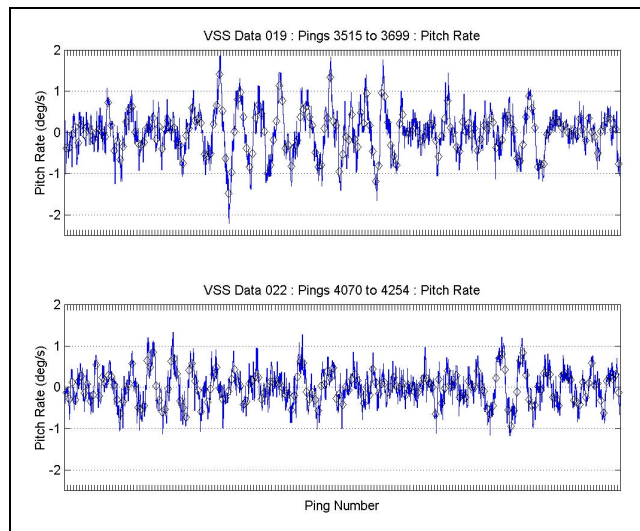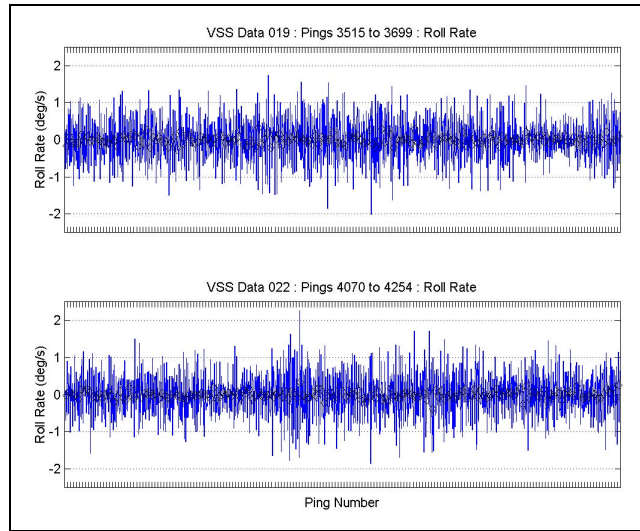

Figure C.6. Towed Body Pitch Rate.

Figure C.7. Towed Body Roll Rate.

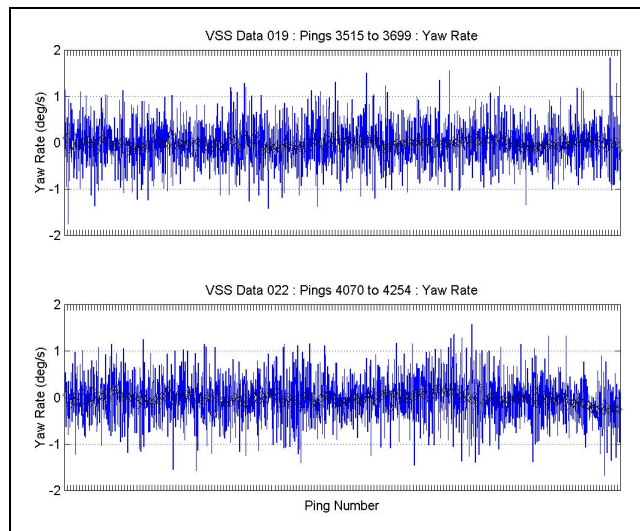Figure C.8. Towed Body Yaw Rate.
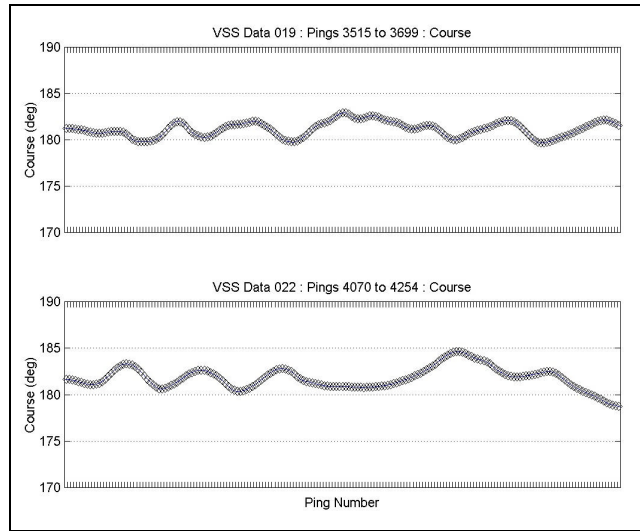
Figure C.9. Towed Body Course.
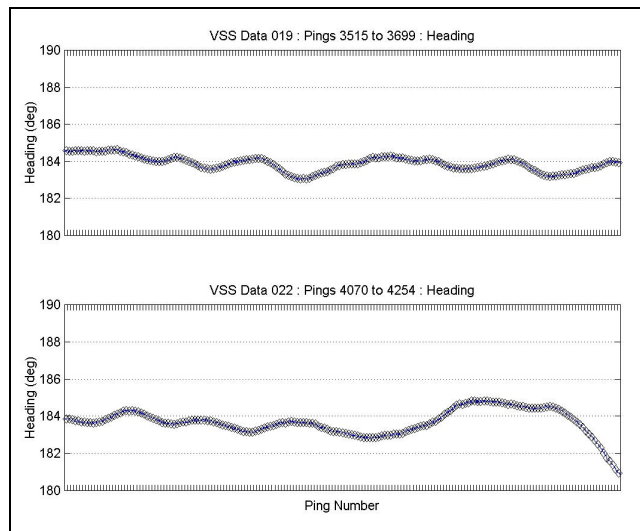
Figure C.10. Towed Body Heading.

197
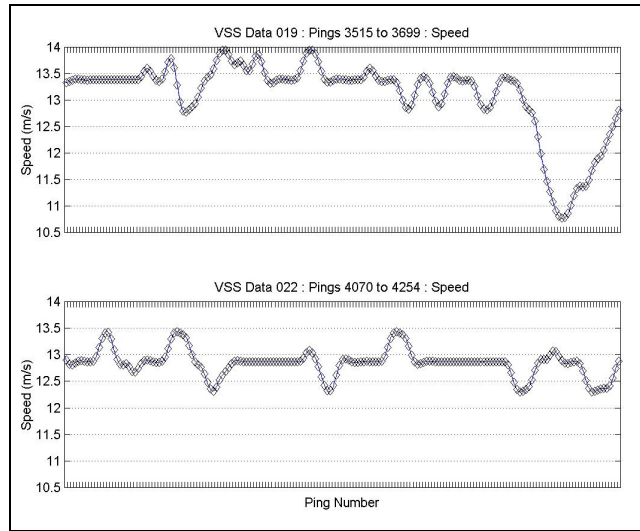
Figure C.11. Towing Speed.
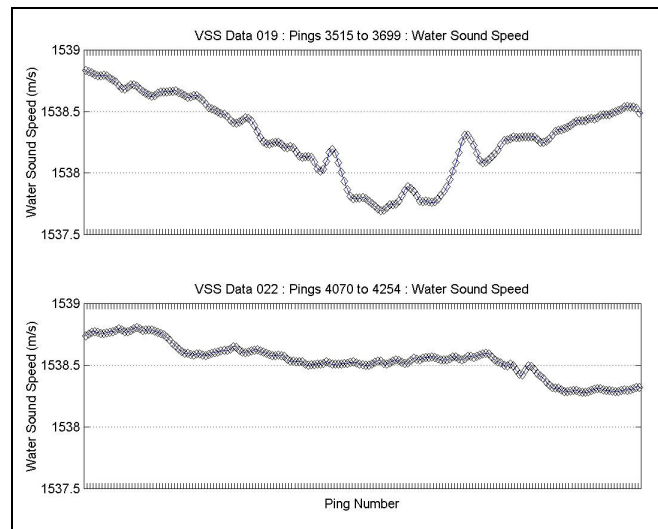
Figure C.12. Acoustic Sound Speed.
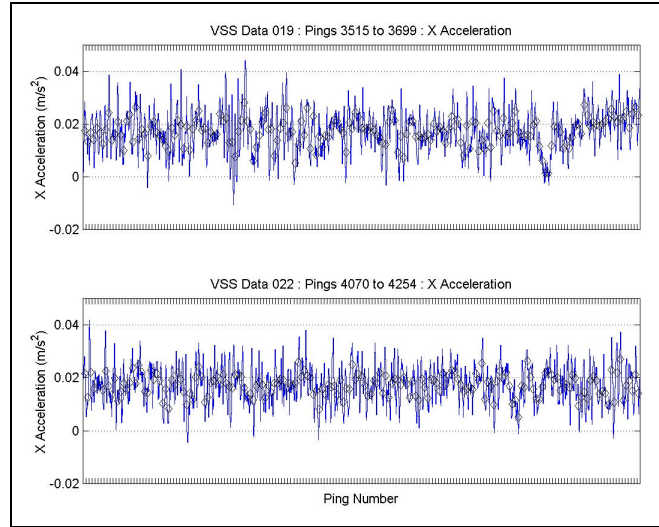
Figure C.13. Towed Body X-Acceleration.
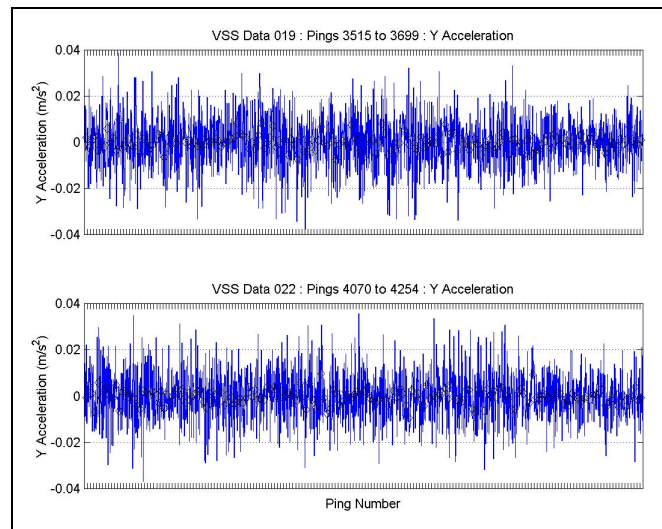
Figure C.14. Towed Body Y-Acceleration.
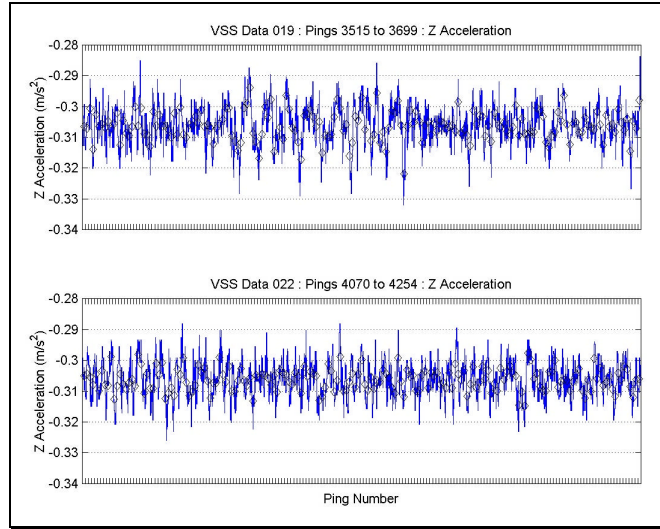
Figure C.15. Towed Body Z-Acceleration.

REFERENCES

[AM88]   D. Alexandrou and C. de Moustier. Adaptive Noise Canceling Applied to Sea Beam Sidelobe Interference Rejection. *IEEE Journal of Oceanic Engineering*, Vol.13, No.2, April 1988, pp.70-76.

[APL94]   Applied Physics Laboratory – University of Washington (APL-UW), *APL-UW High Frequency Ocean Environmental Acoustic Models Handbook*, Technical Report, APL-UW TR 9407, AEAS 9501, APL-UW, Seattle, Washington, USA, October 1994.

[Bar74]   D. K. Barton, Ed. *Radars, Volume 1 – Monopulse Radar*. Artech House, Dedham, MA, USA, 1974. ISBN:0890060304.

[BB72]   G. V. Borgiotti and Q. Balzano. Analysis and Element Pattern Design of Periodic Arrays of Circular Apertures on Conducting Cylinders. *IEEE Transactions on Antennas and Propagation*, Vol.AP-20, No.5, September 1972, pp.547-555.

[BCH91]   D. K. Barton, C. E. Cook and P. Hamilton, eds. *Radar Evaluation Handbook*. Artech House, Boston, 1991. ISBN:0890064881. [Ch.7.1-7.2.4].

[Ber86]   Leo L. Beranek. *Acoustics*. Acoustical Society of America, 1986 [Printed by American Institute of Physics, New York, 1990]. [pp.101-106].

[Bib04]   L. D. Bibee. *Joint Inversion of Through-the-Sensor Data for Mine Countermeasure Environmental Characterization*. Marine Geosciences Division, Naval Research Laboratory, Stennis Space Center, MS, 2004.

[Bor83]   G. V. Borgiotti. Conformal Arrays. In A. W. Rudge et al., editors, The Handbook of Antenna Design: Volume 2, Peter Peregrinus Ltd., London, 1983, Chapter 11. [Ch.11.3-11.5].

[Bra00]   R. N. Bracewell. *The Fourier Transform and Its Applications, 3rd ed.* McGraw-Hill, Boston, Massachusetts, USA, 2000. ISBN:0073039381.

[Car43]   P. S. Carter. Antenna Arrays Around Cylinders. *Proceedings of the I.R.E.*, Vol.31, No.12, December 1943, pp.671-693.

[CB67]   C. E. Cook and M. Bernfeld. *Radar Signals An Introduction to Theory and Application*. Academic Press, New York, 1967. [Ch..1, 6, 8.5-8.6 and 9.7].

[Coo60]   C. E. Cook. Pulse Compression – Key to More Efficient Radar Transmission. *Proceedings of the IRE*, Vol.48, No.3, March 1960, pp.310-316.

[Coo63]   C. E. Cook. Transmitter Phase Modulation Errors and Pulse Compression Waveform Distortion. *Microwave Journal*, Vol.6, No.5, May 1963, pp.63-69. [Reprinted in D. K. Barton, Ed. *Radars, Volume 3 – Pulse Compression*. Artech House, Dedham, MA, USA, 1975, pp.91-97. ISBN:0890060320.]

[Dav83]   D. E. N. Davies. Circular Arrays. In A. W. Rudge et al., editors, *The Handbook of Antenna Design: Volume 2*, Peter Peregrinus Ltd., London, 1983, Chapter 12.

[DS93]   A. N. Denisenko and O. A. Stetsenko. Analysis of the Effect of Frequency Distortion on the Characteristics of LFM Signals. *Telecommunications and Radio Engineering*, Vol.47, No.11, Nov 1992, pp.114-118. Originally Published in *Radiotekhnika*, No.9, 1992, pp.50-54.

[Fre60]   A. Freedman. Sound Field of a Rectangular Piston. *Journal of the Acoustical Society of America*, Vol.32, No.2, February 1960, pp.197-209.

[Fre70]   A. Freedman. Farfield if Pulsed Rectangular Acoustic Radiator. *Journal of the Acoustical Society of America*, Vol.49, No.3 (Part.2), March 1971, pp.738-748.

[GM00]   T. C. Gallaudet and C. P. de Moustier. On Optimal Shading for Arrays of Irregularly-Spaced or Noncoplanar Elements. *IEEE Journal of Oceanic Engineering*, Vol.25, No.4, October 2000, pp.553-567.

[G$^+$0?]   J. V. Gardner, et al. Shelf-Edge Deltas and Drowned Barrier-Island Complexes on the Northwest Florida Outer Continental Shelf. *Geomorphology*, in press.

[HAB02]   M. Harris, W. Avera and D. Bibee. Tow Body Depth Verification. Ocean's 2002 Conference and Exhibition (*Oceans Conference Record,* Vol.2), Mississippi, USA, October 2002, pp.1199-1202.

[HAB04]   M. Harris, W. Avera and D. Bibee. *AQS-20 Environmental Data Collection from Sensor to Decision Aid*. 2004 Mine Countermeasures & Demining Conference, 9-11 February 2004, Canberra.

[Han83]   R. C. Hansen. Planar Arrays. In A. W. Rudge et al., editors, *The Handbook of Antenna Design: Volume 2*, Peter Peregrinus Ltd., London, 1983, Chapter 10. [pp.154-155].

[Har78]   F. J. Harris. On the Use of Windows for Harmonic Analysis with Discrete Fourier Transform. *Proceedings of the IEEE*, Vol.66, No.1, January 1978, pp.51-83.

[Hen87]   T. L. Henderson. Wide-Band Monopulse Sonar: Processor Performance in the Remote Profiling Application. *IEEE Journal of Oceanic Engineering*, Vol.OE-12, No.1, January 1987, pp.182-197.

[HHT85a] J. C. Herper, A. Hessel and B. Tomasic. Element Pattern of an Axial Dipole in a Cylindrical Phased Array, Part I: Theory. *IEEE Transactions on Antennas and Propagation*, Vol.AP-33, No.3, March 1985, pp.259-272.

[HHT85b] J. C. Herper, A. Hessel and B. Tomasic. Element Pattern of an Axial Dipole in a Cylindrical Phased Array, Part II: Element Design and Experiments. *IEEE Transactions on Antennas and Propagation*, Vol.AP-33, No.3, March 1985, pp.273-278.

[HL89]   T. L. Henderson and S. G. Lacker. Seafloor Profiling by a Wideband Sonar: Simulation, Frequency-Response Optimization, and Results of a Brief Sea Test. *IEEE Journal of Oceanic Engineering*, Vol.14, No.1, January 1989, pp.94-107.

[Hor59]   J. W. Horton. *Fundamentals of Sonar, 2nd Ed*. United States Naval Institute, Annapolis, Maryland, USA, 1959. [pp.176-179].

[H$^+$01]   M. M. Harris, et al. Aquiring Bathymetry Data With The VSS Sonar On The AQS-20 Mine Hunting System. *Second Australian-American Joint Conjerence on the Technologies of Mine Countermeasures*, Sidney, Australia, March 2001, pp.?.

[H$^+$02]   M. M. Harris, et al. Environmental Data Collection from the AQS-20. *Proceedings of Fifth International Symposium, Technology and the Mine Problem*, U.S. Naval Postgraduate School, Monterey, California, USA, April 2002, pp.?.

[Koc83]   V. N. Kochemasov. Formirovanie signalov s lineinoi chastotnoi moduliatsiei [Generation of LFM Signals]. Radio i sviaz, Moskva [Moscow], 1983. [in Russian].

[KPDA60] J. R. Klauder, A. C. Price, S. Darlington and W. J. Albersheim. The Theory and Design of Chirp Radars. *The Bell System Technical Journal*, Vol.XXXIX, No.4, July 1960, pp.745-808.

[K$^+$00]   L. E. Kinsler, et al. *Fundamentals of Acoustics, 4th Ed*. John Wiley & Sons, Inc., New York, 2000. ISBN:0471847895. [pp.453-454].

[LL65]   S. W. Lee and Y. T. Lo. On the Pattern Function of Circular Arc Arrays. *IEEE Transactions on Antennas and Propagation*, Vol.13, No.4, July 1965, pp.649-650.

[Lur02]   X. Lurton.   *An Introduction to Underwater Acoustics Principles and Applications*.   Praxis Publishing Ltd, Chichester, UK, 2002.   [Ch.8.4 – Multibeam Echo Sounders].

[MA91]   C. de Moustier and D. Alexandrou. Angular dependence of 12-kHz seafloor acoustic backscatter. *Journal of the Acoustical Society of America*, Vol.90, No.1, July 1991, pp.522-531.

[MC98]   H. Medwin and C. S. Clay. *Fundamentals of Acoustical Oceanography*. Academic Press, San Diego, CA, 1998.

[MG02]   C. de Moustier and T. C. Gallaudet.   Detection of Sonar Induced Measurement Uncertainties in Environmental Sensing: A case Study with the Toriodal Volume Search Sonar. In N. G. Pace and F. B. Jensen (eds.), *Impact of Littoral Environmental Variability on Acoustic Predictions and Sonar Performance*, Kluwer Academic Publishers, Netherlands, 2002.

[Mor76]   S. D. Morgera. Signal Processing for Precise Ocean Mapping. *IEEE Journal of Oceanic Engineering*, Vol.OE-1, No.2, November 1976, pp.49-57.

[Mou88]   C. de Moustier.   State of the Art in Swath Bathymetry Survey Systems. *International Hydrographic Review*, Vol.65, No.2, July 1988, pp.25-54.

[Mou93]   C. de Moustier.   Signal Processing for Swath Bathymetry and Concurrent Seafloor Acoustic Imaging. In J. M. F. Moura and I. M. G. Lourtie, editors, *Acoustic Signal Processing for Ocean Exploration*, Kluwer Academic Publishers, Netherlands, 1993, pp.329-354.

[Mou04]   C. de Moustier. Lecture 16 - Sound Refraction in the Water Column. *34th UNB OMG / UNH CCOM Multibeam Sonar Training Course*, Ottawa, Ontario, Canada, May 2004, 48pp.

[MPG71]   A. D. Munger, J. H. Provencher and B. R. Gladman. Mutual Coupling on a Cylindrical Array of Waveguide Elements. *IEEE Transactions on Antennas and Propagation*, Vol.AP-19, No.1, January 1971, pp.131-134.

[MS84]   S. D. Morgera and R. Sankar. Digital Signal Processing for Precision Wide-Swath Bathymetry. *IEEE Journal of Oceanic Engineering*, Vol.OE-9, No.2, April 1984, pp.73-84.

[Off58]   C. B. Officer. *Introduction to the Theory of Sound Transmission With Application to the Ocean*. McGraw-Hill Book Company, New York, 1958.

[Ols47]   H. F. Olson. *Elements of Acoustical Engineering, 2nd Ed.* D. Van Nostrand Company, New York, 1947. [pp.31-40].

[Nut81]   A. H. Nuttall. Some Windows with Very Good Sidelobe Behavior. *IEEE Transactions on Acoustics, Speech, and Signal Processing*, Vol.ASSP-29, No.1, February 1981, pp.84-91.

[Que70]   W. C. Queen. The directivity of Sonar Receiving Arrays. *The Journal of the Acoustical Society of America*, Vol.47, No.3 (Part.1), March 1970, pp.711-720.

[Ray99]   Raytheon Systems Company, Naval and Maritime Systems. *AN/WLD-1(V) Variable Depth Sensor (VDS) Subsystem, Volume IB: Technical Description*. Portsmouth, RI, 1999, 40pp.

[RC68]   K. Ruttenberg and L. Chanzit. High Range Resolution by Means of Pulse to Pulse Frequency Shifting. *EASCON '68 Record*, Annual Publication, pp.47-51.

[RD82]   T. Rahim and D. E. N. Davies. Effect of directional elements on the directional response of circular antenna arrays. *IEE Proceedings, Part H: Microwaves, Optics and Antennas*, Vol.129, No.1, February 1982, pp.18-22.

[Rho59]   D. R. Rhodes. *Introduction to Monopulse*. McGraw-Hill Book Company, New York, 1959.

[Rih64]   A. W. Rihaczek. Radar Resolution Properties of Pulse Trains. *Proceedings of the IEEE*, Vol.52, No.2, February 1964, pp.153-164.

[RPS77]   R. L. Rolleigh, J. G. Pruitt and R. H. Stokes. Vertical side-lobe suppression in cylindrical arrays. *Journal of the Acoustical Society of America*, Vol.61, No.2, February 1977, pp.397-402.

[RW61]   H. O. Ramp and E. R. Wingrove. Principles of Pulse Compression. *IRE Transactions on Military Electronics*, Vol.MIL-5, No.2, April 1961, pp.109-116. [Reprinted in D. K. Barton, Ed. *Radars, Volume 3 – Pulse Compression*. Artech House, Dedham, MA, USA, 1975, pp.75-82. ISBN:0890060320.]

[She84]   S. M. Sherman. *Monopulse Principles and Techniques*. Artech House, Boston, 1984. ISBN:0890061378.

[SK79]   R. H. Stokes and G. A. Koeler. Analysis of acoustic fill time effects on cylindrical arrays. *The Journal of the Acoustical Society of America*, Vol.66, No.5, November 1979, pp.1420-1426.

[Ste27]   H. Stenzel.   Über die Richtwirkung von Schallstrahlern.   *Elektrische Nachrichten Technik*, Band.4, Heft.6, 1927, pp.239-253.   [H. Stenzel.   Over the directive effect of sound emitters.   *Electrical ones realign technology*, Bound.4,   Booklet.6,   1927,   pp.239-253.]   (Translated   using http://babelfish.altavista.com/babelfish/tr)

[Swe53]   G. W. Swenson, Jr.   *Principles of Modern Acoustics*.   D. Van Nostrand Company, New York, 1953. [pp.110-118].

[Too82]   J. C. Toomay.   *Radar Principles for the Non-Specialist*.   Lifetime Learning Publications, Belmont, California, 1982. ISBN:0534979432. [Ch.5].

[Tra66]   Tracor, Inc.   *Introduction to Sonar Technology*.   Bureau of Ships – Navy Department, NAVSHIPS 0967-129-3010, Washington D. C., 1966 (US Gov. printing office: 1966 0-211-710). [pp.74-79].

[VT02]   H. L. Van Trees.   *Optimum Array Processing: Part IV of Detection, Estimation, and Modulation Theory*.   John Wiley & Sons, New York, 2002. [Ch.4].

[Weh95]   D. R. Wehner. *High Resolution Radar, 2nd Ed*. Artech House, Boston, 1995. [pp.92-95,114-119,132,142-161,196-215,236-237].

[Wei99]   E. W. Weisstein.   *CRC Concise Encyclopedia of Mathematics*.   CRC Press, New York, 1999.

[YT97]   L. Yang and T. Taxt.   Multibeam Sonar Bottom Detection Using Multiple Subarrays.   *Oceans '97 MTS/IEEE Conference Proceedings,* Vol.1, Halifax, NS, Canada, October 1997, pp.932-938.

[YTA97]   L. Yang, T. Taxt and F. Albregtsen. Bottom Detection for Multibeam Sonars with Active Contours.   *Oceans '97 MTS/IEEE Conference Proceedings,* Vol.1, Halifax, NS, Canada, October 1997, pp.943-950.